Technology for Brain-Machine Interfaces

by

Timothy Lars Hanson

Department of Neurobiology
Duke University

Date: _____

Approved:

_____
Miguel A.L. Nicolelis, Supervisor

_____
Sidney A. Simon, Chair

_____
Craig S. Henriquez

_____
Michael L. Platt

Dissertation submitted in partial fulfillment of the requirements for the degree of
Doctor of Philosophy in the Department of Neurobiology
in the Graduate School of Duke University
2013

Abstract

Technology for Brain-Machine Interfaces

by

Timothy Lars Hanson

Department of Neurobiology
Duke University

Date: _____

Approved:

_____
Miguel A.L. Nicolelis, Supervisor

_____
Sidney A. Simon, Chair

_____
Craig S. Henriquez

_____
Michael L. Platt

An abstract of a dissertation submitted in partial fulfillment of the requirements for the degree of Doctor of Philosophy in the Department of Neurobiology in the Graduate School of Duke University
2013

Abstract

Brain-machine interfaces (BMIs) use recordings from the nervous system to extract volitional and motor parameters for controlling external actuators, such as prosthetics, thereby bypassing or replacing injured tissue. As such, they show enormous promise for restoring mobility, dexterity, or communication in paralyzed patients or amputees. Recent advancements to the BMI paradigm have made the brain – machine communication channel bidirectional, enabling the prosthetic to inform the user about touch, temperature, strain, or other sensory information; these devices are hence called brain-machine-brain interfaces (BMBIs).

In the first chapter an intraoperative BMI is investigated in human patients undergoing surgery for implantation of a deep brain stimulation (DBS) treatment electrodes. While the BMI was marginally effective, we found high levels of behavioral and tremor tuning among cells recorded from the surgical targets, the subthalamic nucleus (STN) and ventral intermediate nucleus (VIM) of the thalamus. Notably, this tremor or behavior tuning was not mutually exclusive with oscillatory behavior, suggesting that physiological tuning persists even in the face of pathological oscillations. We then used nonlinear means for extracting tremor tuning, and found a significant population, consistent with double-frequency or co-modulation to tremor within the basal ganglia. Synchrony was then assessed over long and short timescales between pairs of neurons, and it was found that tremor tuning implies synchrony: all units exhibiting tremor tuning showed synchrony to at least one other unit.

BMBIs rely on a host of both scientific knowledge and technology for effective function, and this technology is currently in intensive research. In this dissertation two technologies for BMBIs, corresponding to the two directions of communication, are designed, described, and tested. The first one is a high compliance, digitally controlled, high-side current-regulated microstimulator for intracortical microstimulation (ICMS). The device is validated on the bench, tested in monkeys, and used for multiple experimental setups. Due to careful control of parasitic charge injection, the microstimulator is ideally suited for interleaving stimulation and recording as employed in some BMBIs.

The second technology described is a wireless, scalable, 128 channel neural recording system. The device features aggressive digital filtering to maximize signal quality, has spike sorting and compression on the transceiver, can be fully configured over the air through a custom wireless bridge and client software, and can run for over 30 hours on one battery. This system has been tested in a monkey while in its home cage, where the wireless system permitted unfettered, continuous recording and continuous access to a simplified BMI. A full description of the development and device is described, as well as results showing convincing 1D and suggestive 2D BMI control.

Perfection is achieved, not when there is nothing more to add, but when there is nothing left to take away. – Antoine de Saint-Exupery

↺

Wit and puns aren't just decor of the mind; they are essential signs that the mind knows it's on, recognizes its software, and can spot bugs in its own programming. – Adam Gopnik

↻

The basal ganglia is the dark basement of the brain. – apocryphal, S. A. Wilson-Kinnier

Contents

Abstract **iv**

List of Tables **xii**

List of Figures **xiii**

List of Abbreviations and Symbols **xviii**

Acknowledgements **xxii**

1 Introduction **1**

1.1 Review of previous work 3

1.2 Stimulation 4

1.3 Recording 13

1.3.1 Summary 21

1.4 Recording Systems 22

1.4.1 Amplification 22

1.4.2 Integration 24

1.5 BMI 27

1.6 Parkinson's Disease, Essential Tremor, and DBS 43

1.6.1 Anatomy of the Basal Ganglia 44

1.6.2 Physiology of the Basal Ganglia 53

1.6.3 Pathophysiology of the Basal Ganglia in PD 60

1.6.4 Treatment of PD through DBS 71

1.6.5 Conclusions 76

2 Population Analysis of Human Subcortical Neurons in Parkinson's Disease 78

2.1 Abstract 78

2.2 Introduction 79

2.3 Materials and Methods 80

2.3.1 Patient characteristics and operative plan 81

2.3.2 Electrode arrays and electrophysiological recording 82

2.3.3 Voluntary motor task 82

2.3.4 Neuronal tuning to target and movement 84

2.3.5 Directional tuning 86

2.3.6 Tremor sensitivity 87

2.3.7 Oscillatory neurons 87

2.3.8 Neuronal synchrony 89

2.3.9 Efficacy of neuronal recordings for kinematic predictions . . . 91

2.4 Results 92

2.4.1 Neuronal tuning to target and movement 93

2.4.2 Directional tuning 97

2.4.3 Properties of multiunits 99

2.4.4 Tremor sensitivity 99

2.4.5 Oscillatory behavior 100

2.4.6 Neuronal synchrony 105

2.4.7 Efficacy of neuronal recordings for kinematic predictions . . . 108

2.5 Discussion 109

2.5.1 Subcortical encoding of behavior 109

2.5.2 Elusive relationship between oscillatory activity and tremor . 111

2.5.3 Network synchrony: genesis or indicator of tremor? 112
2.5.4 Subcortical recordings in BMI applications 113

3 Microstimulator 115

3.1 Abstract 115
3.2 Introduction 116
3.3 Methods 119
3.3.1 Microstimulation system 119
3.3.2 Software control 119
3.3.3 Stimulus isolation units 121
3.3.4 Electrodes 124
3.3.5 Assembly and Testing 125
3.4 Results 126
3.4.1 Bench-top testing 126
3.4.2 In Vivo testing 128
3.4.3 Efficacy in Nervous Tissue 133
3.5 Conclusion 134
3.6 Acknowledgment 135

4 Wireless recording system 137

4.1 Abstract 137
4.2 Introduction 138
4.3 Methods 138
4.3.1 Revision 1 139
4.3.2 Revision 2 143
4.3.3 Revision 3 145
4.3.4 Revision 4 147

4.3.5 Revision 5 . . . 149
4.3.6 Revision 6 . . . 150
4.3.7 Revision 7 . . . 150
4.4 Software . . . 151
4.4.1 Transceiver firmware . . . 154
4.4.2 Bridge firmware . . . 163
4.4.3 Sorting Client . . . 165
4.5 Testing . . . 168
4.5.1 1D BMI . . . 169
4.5.2 2D BMI . . . 172
4.6 Discussion . . . 172
5 Discussion **181**
A Co-author papers **187**
A.1 The muscle activation method: an approach to impedance control of brain-machine interfaces through a musculoskeletal model of the arm 187
A.2 Primate reaching cued by multichannel spatiotemporal cortical microstimulation . . . 189
A.3 Unscented Kalman filter for brain-machine interfaces . . . 191
A.4 A brain-machine interface instructed by direct intracortical microstimulation . . . 193
A.5 Future developments in brain-machine interface research . . . 195
B Yushin **197**
B.1 Description . . . 197
B.2 Reflection . . . 198
B.3 Images . . . 199
Bibliography **209**

Biography **244**

B.4 Publications 244

B.5 Poster Presentations 246

List of Tables

1.1 Mutual information in terms of SNR 42

2.1 Pairwise Classifications for Single Units 94

2.2 Behavioral tuning of subcortical neurons 95

2.3 Tremor tuning of subcortical neurons 99

2.4 Oscillatory units 101

2.5 Heterodyne tremor tuning 104

2.6 Pairwise neuronal synchrony 105

2.7 Comparison of synchrony (cross-correlation method) and tremor tuning (PEPH method) 107

3.1 Microstimulator Specifications 118

4.1 Wireless recording system specifications 173

4.2 Wireless power consumption breakdown 174

List of Figures

1.1 Jose Delgado with a bull controlled by his stimoceiver. 10

1.2 Salcman's floating microwire electrodes. 18

1.3 Early integrated recording system 25

1.4 1024 channel integrated recording system 26

1.5 Basmajian's EMG based biofeedback 28

1.6 Schmidt's precise 1D BMI 32

1.7 Recording setup used by Schmidt. From (Schmidt, 1980). 32

1.8 Simplified BG 45

1.9 BG rate hypothesis 45

1.10 Diagram of striatal projections 46

1.11 Diagram of MSN 48

1.12 Diagram of striatal projections 49

1.13 Wooly fibers and climbing fibers within the SNr 50

1.14 Schematic representation of afferents in the GPi 51

1.15 Schematic representation of STN projections to GPe 52

1.16 LFP Oscillations in the BG in ON and OFF conditions 62

1.17 Changes in LFP oscillations in PD STN ON and OFF drugs 66

1.18 Conflict effect on decision times in normal, PD, and STN DBS patients 70

1.19 Improvement in tremor score following bilateral STN DBS. From (Krack et al., 1997). 71

1.20 Efficacy of M1 HF optical stimulation in rat model of PD. 73

2.1 DBS recording overview 83

2.2 Example PETHs 96

2.3 Separation between single unit response to target appearance and movement time. 97

2.4 Mean normalized PETHs for all responsive units 98

2.5 Example peri-event phase histograms 100

2.6 Distribution of peak frequencies for the spike train autopower function 101

2.7 Example ISI histograms for highly oscillatory neurons 102

2.8 Spike train autopower plots 103

2.9 Comparison of spike train autopower and hand acceleration autopower 104

2.10 Plots of $\zeta(t)$ for three highly synchronous neurons 106

2.11 Cross-correlation coefficient for three highly synchronously neuron pairs 107

2.12 Dependence of offline BMI predictions on neuron ensemble size 108

3.1 Schematic overview of software control of the microstimulator. 120

3.2 Schematic overview of one stimulator channel. 121

3.3 Detailed schematic of one-half of the voltage-controlled high-side current source 122

3.4 Isolated monitoring circuit. 124

3.5 Photograph of a populated PCB featuring four bipolar channels . . . 125

3.6 Microstimulator output waveforms 126

3.7 Microstimuator rise and fall times 127

3.8 Expected vs. actual pulse amplitude for several current settings and resistive loads. 128

3.9 Microstimulator pulse width and charge imbalance 128

3.10 Stimulator artifact in rasters 129

3.11 Stimulator artifact in rasters 2 130

3.12 Stimulation artifact duration 131
3.13 Stimulation artifact duration 2 132
3.14 Microstimulation effect on recorded aggregate firing 133
3.15 EMG response to microstimulation 134
4.1 Frequency response of LMV1032-6. Gain is 2, as expected. 140
4.2 Nordic flowchart 141
4.3 Layout of revision 1 of wireless headstage 141
4.4 Assembled version 1 headstage 142
4.5 Direct Form II IIR filter 143
4.6 Blackfin Direct Form I IIR filter 143
4.7 Revision 2 144
4.8 Revision 2 EMG 145
4.9 Revision 3 wireless headstage 146
4.10 Revision 3 PCB 147
4.11 Revision 4 PCB 148
4.12 Revision 5 PCB 150
4.13 Revision 6 'Bridge' PCB 151
4.14 Revision 6 transceiver PCB 152
4.15 Revision 7 'Bridge' PCB 153
4.16 Revision 7 'Bridge' Assembled 154
4.17 Revision 7 transceiver PCB 155
4.18 Revision 7 wireless Assembled 156
4.19 Integrator and AGC 158
4.20 LMS noise cancellation 159
4.21 IIR programmable filtering 160

4.22 Template matching . . . 161
4.23 Transceiver Packetization . . . 162
4.24 Transceiver Framing . . . 163
4.25 Wireless Overview . . . 166
4.26 Sorting Client: waveforms . . . 167
4.27 Sorting Client: rasters . . . 168
4.28 Firing rate kernel . . . 169
4.29 Headcap system . . . 170
4.30 Wireless system mounted in headcap . . . 170
4.31 Home cage wireless recording and behavioral setup . . . 171
4.32 128 channel wireless recording . . . 176
4.33 Example 1D BMI behavior . . . 177
4.34 1D BMI latency to target . . . 177
4.35 1D BMI distance to target . . . 178
4.36 1D BMI cursor occupancy . . . 178
4.37 2D BMI cursor occupancy . . . 179
4.38 2D BMI latency to target . . . 179
4.39 2D BMI distance to target . . . 180
B.1 Yushin pick and place robot. . . . 200
B.2 Back of robot. . . . 200
B.3 Control computers. . . . 201
B.4 Robot was bolted to steel I-beams from a Durham scrapyard. . . . 201
B.5 Work table assembled of pressure-treated 4x4 lumber. . . . 201
B.6 Robot head camera, cannula, and laser . . . 202
B.7 Robot head wiring . . . 202

B.8 Y-axis servo 203
B.9 Z-axis servo. 203
B.10 Hall effect sensor simulator 204
B.11 Vacuum pump. $25. 204
B.12 Vacuum manifold. $2 205
B.13 Positive pressure regulator 205
B.14 Parker Automation servo controllers. 205
B.15 Y axis ballscrew 206
B.16 Wires destroyed by liquidating crew were repaired or replaced. . . . 206
B.17 Software control of robot 207
B.18 Destination part location and rotation GUI in planning program. . . 207
B.19 Destination part location, rotation, and optical calibration GUI in Yushin. 208

List of Abbreviations and Symbols

Abbreviations

ADC	Analog to digital converter
AGC	Automatic gain control
ALS	Amyotrophic lateral sclerosis
AM	Amplitude modulation
ASCII	American Standard Code for Information Interchange
ASIC	Application specific integrated circuit
BMBI	Brain-machine-brain interface
BMI	Brain-machine interface
CDF	Cumulative density function
COTS	Commercial off the shelf
CRC	Cyclic redundancy check
CS	Conditioned stimulus
DAC	Digital to analog converter
DBS	Deep brain stimulation
DHCP	Dynamic host configuration protocol
DMA	Direct memory access
DOF	Degrees of freedom
DSP	Digital signal processor
DUCN	Duke University center for neuronengineering

EDA	Electronic design automation
EEG	Electroencephalography
EM	Expectation maximization
EMG	Electromyography
ESD	Electrostatic discharge
ET	Essential tremor
FET	Field effect transistor
FIFO	First in first out
FIR	Finite impulse response
FPGA	Field programmable gate array
FR	Firing rate
FSK	Frequency shift keying
GSM	Groupe Spcial Mobile, Global System for Mobile Communications.
GUI	Graphical user interface
HLSL	High level shader language
HML	Heavy polyimide enamel insulation
ICMP	Internet control message protocol
ICMS	Intracortcial microstimulation
IIR	Infinite impulse response
IP	Internet protocol
IRQ	Interrupt request
ISI	Interspike interval
JPSTH	Joint peri-stimulus time histogram
JTAG	Joint test action group
LDO	Low drop-out regulator

LFP	Local field potential
LMS	Least mean squares
MAC	Media access control
MAP	Multi-acquisition processor
ML	Maximum likelihood
MOS	Metal oxide semiconductor
MPEG	Moving Picture Experts Group
MUX	Multiplexer
MWA	Microwire array
NEF	Noise efficiency factor
NMOS	N-channel metal oxide semiconductor
OOK	On-off keying
PCA	Principal component analysis
PCB	Printed circuit board
PCI	Peripheral component interface
PD	Parkinson's disease
PEPH	Peri-event phase histogram
PETH	Peri-event time histogram
PHY	Physical layer of ethernet
PI	Proportional integral (controller)
PLL	Phase locked loop
PMOS	P-channel metal oxide semiconductor
PTN	Pyramidal tract neuron
PV	Population vector
RMS	Root-mean squared
SAA	Sum absolute and accumulate

SDRAM	Synchronous dynamic RAM
SEQ	Flag used in TCP
SLP	Service location protocol
SNR	Signal to noise ratio
SPI	Serial peripheral interface
STN	Subthalamic nucleus
SUA	Single unit activity
SUNY	State University of New York
TCP	Transmission control protocol
UDP	User datagram protocol
USB	Universal serial bus
VIM	Ventral intermediate thalamus

Acknowledgements

I would like to thank my advisor, Miguel Nicolelis, for supporting me and giving me the freedom me scratch the itch to modernize our recording system – an itch that caught me spring 2007 and has not abated since. I would also like to thank Dr. Dennis Turner, for conducting the DBS surgeries, and providing helpful energy; Misha Lebedev, for his enthusiasm, astute scientific comments, and encouragement; Joseph O'Doherty for his collegial hard work, openness to sharing, advice, and friendship; Ana Oliveria, for her insightful, critical brain, friendship, tolerance (she is a fellow conspirator without which this would have been more depressing than it was); my mother, for instilling the passion to persevere, and for providing support from up north; my father, for providing advice and experience without which this construction would have taken twice as long; and my brother, for going on wonderful, illuminating and rejuvenating trips both large and small.

Within the lab, I would like to thank the large group of people I have been privileged to share friendship, knowledge, and time with. In loosely chronological order: Erin Phelps, Jose Carmena, Hyun Kim, Aaron Sandler, Weiying Drake, Kristin Dewey, Rui Costa, Shih-Chieh Lin, Hao Zhang, Eric Thompson, Mike Weist, Janaina Pantoja, Romulo Fuentes, Craig Roberts, Kafui Dzirasa and too many more to remember. Within the monkey lab I am indebted to the banter and intelligence of Nathan Fizsimmons, the help, hard work, and friendship of Ian Peikon and Ben Grant; fantastic philosophical discussions with Jesse Winans and Solaimon Shokur;

NY wit of Je Hi An; the help of Peter Ifft and Andrew Tate; the statistical chops of Andrew Fuller, without which the DBS work was lost; the enthusiasm, friendship, and baking skills of Katie Zhuang; the help of David Schwartz and Wenwen Bai; and Zheng Li's impeccable mathematical prowess. None of us could have made any progress without the concerted, organized efforts of Susan Halkiotis, Gayle Wood, Terry Jones, Tamara Philips, and Laura Oliveira, who keep the lab running smoothly and effectively. Nor could we have done it without Jim Meloy and Gary Lehew; I would like to thank Jim for making the (many revisions of, naturally) 3D printed monkey headcap and battery systems, and Gary for both designing the electrodes so pivotal to the lab's work as well as helping me with my cars and providing all around excellent technical advice.

In the broader Duke community, I would like to thank my friends and fellow triatheletes David Kahler, for the many swims and escapades, and Viviane Callier, for both the swims and richly philosophical jaunts in through the woods of Uwharrie. As for swimming, the Duke club has been a valuable daily source of escape and exercise, the swimmers companions for many good trips, and the workouts persistent remindera that continued effort brings continued performance (or at least a continued hunger). Johanna Schuster-Craig, Marc Reibold, Gabi Wurmitzer, Caroline Kita, Christophe Fricker, Timothy Senior and others orbiting the German department have been good friends and intellectual companions; Fahad Bishara, Tracy Gill, and many others have been good friends and shared the Durham living experience over the years. I've had many good discussions with my technophile friends Max Hodak and Sharif Razzaque, and am glad to be connected to the forefront of biomediacal technology through them.

Most if not all this work was done with and on open-source software, and so I am indebted to the continued selfless work of thousands of programmers throughout the globe. Indeed, I must thank all the American taxpayers for making this work

possible! The following grants have supported me during my time at Duke: NIH 5T32-GM008441-13 and 5T32-GM008441-14 training grants, NIH DP1OD006798, NIH (NICHD) RC1HD063390, DARPA N66001-06-C-2019, DARPA N66001-02-C-8022.

1

Introduction

My efforts in the laboratory of Miguel Nicolelis have been aimed at furthering the field of brain-machine interfaces (BMIs). As the name suggests, a BMI connects brains with machines, with the ultimate goal of replacing or helping paralyzed individuals interact with the world, amputees control their prosthetic in a natural way, or for alleviating disease states. Deep brain stimulation (DBS), a common and effective treatment for the symptoms of Parkinson's disease (PD) can also be considered a brain-machine interface, albeit a simple unidirectional one. Though the propose may appear divergent, DBS shares many of the underlying electrophysiology and neuroanatomy underlying motor brain-machine interfaces (Benabid et al., 2011).

The hypothesis behind the field of motor BMIs is that if you can record volitional control signals where they originate – in the CNS and, more specifically, the cortex – then it should be possible to decode these signals and use them to control a communication interface or prosthetic.

This hypothesis or task can be broken down into sub-tasks:

- Neural recording – the outgoing communication channel from the brain. In the Nicolelis lab we use electrophysiology, though optical methods are rapidly

advancing. Recording from neurons involves electrode technology, surgical procedures, biocompatability, electrode mounting and connection; all issues and techniques that are vitally important and will be briefly reviewed.

- Neural stimulation – the incoming communication channel to the brain. While optogenetics is presently revolutionizing this field, my work has focused on electrical stimulation of nervous tissue, mainly intracortical microstimulation (ICMS).

- Processing. This involves amplification, digitization, filtering, and sorting, and has been the focus of my work. A wireless solution to these problems is proposed, described, and tested in Chapter 4.

- Decoding. Mathematical transforms, like the Weiner filter and Kalman filter (and variants) have been used successfully to decode motor commands and volitional signals. I spent quite some time on this, and eventually decided that the impoved fidelity (processing gain) of increased algorithmic sophistication was not worth the concomitant complexity and code fragility.

- Prosthetic fabrication and control. While essentially important, this is largely outside the scope of our lab.

The structure of this dissertation will be as follows. The remainder of this chapter will roughly and chronologically cover past literature regarding microstimulation, electrodes, technology for recording from electrodes, and a broad background behind Parkinson's disease, it's etiology, and treatment. The intention is to embed the DBS recordings, microstimulator, and recording hardware in a broader scientific and engineering context. While the work presented in the following chapters does not investigate electrodes, this seems to be the limiting step in BMI technology and one that I hope to work on in the future, and so a literature review is carried out.

Chapter 2 documents initial work which hoped to implement a BMI during intraoperative recording from patients being implanted with DBS treatment electrodes. While the Parkinsonian patients never did control a realtime BMI, the data we obtained proved informative of synchrony, oscillations, and behavioral tuning within the targeted subthalamic nucleus (STN) and ventral intermediate (Vim/Vop) thalamus, and reflects in a more nuanced way on the idiopathic etiology of PD. Chapter 3 then details the design and testing of computer-controlled high resolution microstimulation hardware. Chapter 4 describes the development, structure, and testing of a 128-channel wireless neural recording system which has been used to allow monkeys continuous access to a BMI while housed in their home cage. Preliminary results from this experiment are presented. Chapter 5 synthesizes problems and future directions in neuroprosthetic and Parkinson's research. Appendix A includes the other papers which I have co-authored, and Appendix B details the robot built to fabricate the hardware needed for the lab.

1.1 Review of previous work

Science and technology have played a very tightly coupled role; much science has been directed by the technology available, and much technology has been driven by scientific understanding of the physical and biological world. For example, optical stimulation (Boyden et al., 2005) has permitted more controlled probing of the pathology of Parkinson's disease (Gradinaru et al., 2009), two-photon imaging (Denk et al., 1990) permits deeper and more precise observation of synaptic plasticity (Grutzendler et al., 2002, 2011); sometimes technology precedes scientific understanding, which seems to be the case for DBS. We still do not fully understand how or why DBS works, though there are several plausible theories (Gubellini et al., 2009; Hashimoto et al., 2003; Plaha et al., 2008). Indeed, science and technology seem to be created via the same iterative, experimental, cumulative, refining algorithms

for building and verifying structures – only (very roughly) technology operates on physical structures, and science on ideas.

I belabor this point as the present science of BMIs is limited by technology, and a large part of the work described here deals with creation of technology designed to move us closer to a clinical application of neurally controlled prosthetics.

1.2 Stimulation

A BMI can be thought of as having two communication channels – efferent via recording, and afferent via stimulation. As stimulating the brain is technically simpler (a current or voltage source and electrodes are all that are required), it has been a tool for experimentation for well over a century. Fritsch and Hitzig (1870) were of the first to use intracortical stimulation to probe the brains of dogs; it was a great leap forward from the vivisectionists and those who "stimulated" (cauterized) the cortex with potash. Though their cardboard batteries and bipolar DC stimulation was technologically simple, the reasoning derived from it was not, as they were the first to reveal how quickly the brain perishes without blood in comparison to the peripheral nerves and muscles, the first to show that the cortex, but not the striatum, is responsive to electrical stimulation, and that there is a pre-central [1] organized map of forelimb movements.

Shortly thereafter Bartholow tried a similar, albeit even less controlled, experiment on Mary Rafferty. Mary had epithelioma which spread to necrose the cranium above the central suclus on both sides of the midline to the point that the brain dura could be seen pulsing within the scull. In the course of cleaning out the ensuing infections, needles had been poked through the dura, leading Bartholow to reason that stimulating electrodes could be introduced with little harm. He then, with dubious patient disclosure and consent, tried several attempts of gross, one-battery

[1] Back then it was called the Rolandic fissure.

DC current-uncontrolled bipolar stimulation, and was able to induce contralateral arm movements, speech, and eventually a seizure. Upon application of more voltage, Mary went into grand mal seizures and 20 minute coma; the patient, likely due to a combination of infection, stroke, and epilepsy kindled by the electrical stimulation, died three days later (Bartholow, 1874). While the he had intended to resolve if DC (then called "galvanic") or AC (then "faradic") current is better for stimulation, he only proved that controlled current was *absolutely essential*. Though the experiment was a disaster, Bartholow did prove that human cortex was as electrically excitable as the dog; this and other studies marked a time when medical practice was shifting from intuition and observation to treatment directed by empiricism and science, especially from work on laboratory animals (Harris et al., 2009).

Wilder Penfield and Boldrey continued this work by applying ICMS to 163 patients being treated for seizures, brain tumors, or other central neurological problems. In experiments that might not pass IRB approval today (despite their modern neurosurgical procedures), they meticulously mapped the effect of ICMS proximal to the central sulcus, fleshing out the cortical map of human motor control and somatosensation, and leading to the idea of a cortical "homunculus"(Penfield and Boldrey, 1937).

Later Penfield and Perot were to carry this technique further during the treatment of temporal lobe seizures. Electrical stimulation of the cortex was a direct and effective method for locating the source of a seizure to be surgically removed, and a necessary step for avoiding eloquent cortex. As their procedures required removing the whole side of the cranium, Penfield was able to stimulate large parts of the brain during the operations. This included the primary somatosensory and motor cortices for calibrating current levels, a procedure used in our laboratory and others today (Fitzsimmons et al., 2007). Within 1,288 surgeries, of which 520 where for the treatment of temporal lobe epilepsy, 40 patients showed "experiential responses"

elicited by ICMS to the temporal lobe. The descriptions of these are fantastic – vivid and dreamy memories, art, music (a lot of music!), childbirth, counting, and autobiographical stories.

Penfield and Perot's pioneering stimulation studies led to some important conclusions. All experiential responses were within the realm of visual and auditory interpretation, which meant this function was localized to the non-dominant temporal lobe. (The dominant lobe is concerned with speech, but most interestingly ICMS there produces not speech but aphasia; c.f. stimulation to the non-dominant lobe actively recalls memories.) Also quite remarkable was that removal of all or parts of the temporal lobe to hopefully cure the epilepsy did *not* interfere with the recall of the same memories elicited by ICMS there, strongly suggesting that storage and access of the memories are separate. This despite the fact that the temporal lobe is the only region of brain that ICMS is capable of forcing this type of recall. Penfield noted that despite the likely large number of activated neurons in the cortex, only one coherent idea resulted from these "gentile pulse trains"[2] at a time, implying that there is sufficiently strong inhibition in the cortex to enable mutual exclusion. Finally, the neurologist observed that stimulated memories leave behind a temporal "facilitation", in that memories are likely to be highly related in a sequence of stimluations, even over a distance of several centimeters and a quarter of an hour. That is, despite the wide possible breadth of memories ICMS might elicit from different locations in the temporal lobe (all possible remembered experience), most of what his patients reported followed a theme. For example, one patient had ICMS induced hallucinations that all involved some aspect of grabbing – a man grabbing a rifle from a cadet at a parade, a man snatching his hat from a hat-check girl, himself pulling a stick from a dog's mouth (Penfield and Perot, 1963).

[2] He repeats this phrase several times, apparently in an effort to diffuse worries that he was electrocuting the patients.

While these stimulation experiments did much to elucidate the function of the cortex (and brain in general, in a great many other studies), it does not generally refine whether the cortex uses spatial or contextual/temporal coding of information. The line deliminating multisensory and interpretive temporal corticies is sharp, yet many different stimulation sites elicit the same memory further anterior. The coding seems mixed, and evidence supporting both continues today.

As Penfield did with his numerous human patients, the primary initial animal-experiment use of electrical stimulation was to determine the behavioral function of a brain region. Doty summarizes the rich and fascinating literature documenting these investigations. For example, ICMS to extrastriate cortex can elicit insect-grasping responses in macaque monkeys, after which they will carefully examine their hands to see what was caught. The same experiment was tried in humans; after ICMS elicited a catching movement, the patient reported wanting to grab "that butterfly". Similarly complex behavior follows by stimulation of the rostral thalamus in humans in the language dominant hemisphere, which caused a patient to utter "Now one goes home" or "Thank you", albeit with no memory of speaking. In opossums, stimulation of the hypothalamus can elicit mating behaviors, but only if another opossum or furry object is present. Stimulation in the periaqueductal gray will induce fear behavior in rats, but none the less the rats will self-administer this stimulus repeatedly, so long as its intensity does not exceed a certain value (Doty, 1969); this same behavior is apparent, without the need for electrophysiology, in humans.

In cats, stimulation of the lateral hypothalamus induces both hunger and the complex behavior required to eat[3] (Wyrwicka and Doty, 1966). Other locales can induce not hunger or feeding, but prey-catching attack behavior where cats will solve

[3] "In one experiment, the meat in the bowl was replaced with a banana. Upon stimulation [to the lateral hypothalamus] the cat quickly approached the bowl, sniffed the banana, turned away (in some disgust and frustration!), searched the chamber again, returned to the banana etc, but would not eat the banana."

puzzles in order to get access to a rat (Roberts and Kiess, 1964).

A more fundamental locale for motivation discovered by Olds and Milner: their rats would repeatedly press a lever to obtain stimulation to the septal region of the limbic system (Olds and Milner, 1954). Doty later observed that "Stimulation at most sites in the limbic system has the still mysterious ability to organize motor activity in any fashion required to produce more of the activity or to avoid it, as the case may be." This discovery, while used practically to motivate experimental animals (Shinkman et al., 1974; Talwar et al., 2002), reflects rather deeply on the simplifying principles used to structure, organize, and interpret behavior (Hofstadter, 2007).

In these cases the stimulation serves as an overpowering command or as a reinforcement, a signal which is very nonspecific in information content (a uniform series of pulses or uniform frequency, up until this point) but specific in location. In terms of BMIs, we are more interested in relaying sensory information, e.g. from a prosthetic, which implies both time and spatial information. Initial work on sensory ICMS was in terms of Skinner's operant conditioning (Skinner, 1938). Stimulation of nearly any part of the central nervous system (CNS) can serve as a conditioned stimulus (CS) for classical conditioning, excluding the ventral nucleus of the thalamus (motor thalamus, discussed below in regard to DBS) and the cerebellum (Doty, 1969; Nielson et al., 1962). As the dura is extremely sensitive to mechanical and electrical stimulation (Doty, 1969; Harris et al., 2009), it was initially not completely proven that ICMS acted directly on the brain and not through the peripheral nervous system (PNS)[4]. By severing the trigeminal and most other cranial nerves, and by paralyzing the motor targets of the CS ICMS in classically conditioned cats, Doty and colleagues conclusively proved that the cortex was the direct site of the CS (Doty

[4] For example, initial work by Loucks (1935) used an induction coil to stimulate; this coil vibrated ever so slightly when excited, which the experimental animals could feel.

et al., 1956), and such conditioning did not require motor activity.

Such a CS is akin to a sense in that the brain can trigger or modify behavior based upon it. Furthermore, macaque monkeys can spatially discriminate electrical stimulation over the entirety of the cortex at widely varying frequencies and currents, 30-100 Hz, 0-700 μA (Doty et al., 1956) or 2-100 Hz and currents as low as 100 μA (Doty, 1965). This makes ICMS a highly suitable means of conveying information directly to the brain, though it does not bypass the state-dependence and complexity of the sensory system, as the thresholds for stimulation throughout the brain were found to strongly vary with arousal. Namely, ICMS to precentral cortex that was below threshold and elicited no movement would begin to elicit movement if the unconditioned stimulus (a shock) was applied or a loud unfamiliar sound (a truck horn) was sounded (Doty, 1965). This may be useful, though: it shows ICMS can be ignored much like other somatosensation.

Microstimulation has been used to verify learning on a much smaller scale in a pioneering study by Bures and colleagues. Using low-frequency DC ICMS at very low currents of 10-50 nA, which permitted simultaneous stimulation and recording from the *same neuron*, they stimulated neurons in most of the major brain areas. By applying this stimulation shortly after presentation of an audio tone, they were able to train a few neurons to respond with both increased and decreased firing rate to the tone. That is, they trained neurons to respond to sound, though admittedly most of their successes were in the inferior colliculus (Bures and Buresova, 1967). This amounts to Hebbs rule, verified in vivo.

A strong caveat in Bures and Buresova's study is that there was no behavioral control, so there was no way to tell if the auditory stimulus was reacted or attended to. The authors themselves admit that some tuning observed may have resulted from attending to, then habituating to, the tone used. A similar, and much more successful, study was later done which linked auditory cortical recorganization /

retuning to presentation of an auditory tone not via stimulation of the neuron itself, but rather by paired microstimulation of the nucleus basalis, a partially acetylcholine releasing center of the rat brain (Kilgard and Merzenich, 1998).

On a much larger scale Jose Delgado built upon the work of Doty and colleagues in a spectacular demonstration of electrical stimulation. In one experiment Delgado stood in a Spanish bullring in the path of a charging bull; using his "stimoceiver", which wirelessly delivered current through electrodes to the bull's caudate, he abruptly stopped the animal and made it turn and walk away (Delgado, 1971). See Figure 1.2. The stimoceiver is similar to the work described in Chapters 3 and 4 – it could record EEG signals from patients or experimental animals, and deliver stimulation current, all wirelessly. Delgado used his stimoceiver clincially in a number of patients implanted with depth electrodes in the amygdala to diagnose behavioral and affective epilepsy. His electrodes, 15 contacts on a 1.2mm diameter shaft, spaced at 3mm, are similar though coarser than those used presently for DBS surgeries; unlike DBS, however, he recorded and stimulated at the same sites. Stimulation to these could produce "pleasant sensations, elation, deep, thoughtful, concentration, odd feelings, super relaxation, colored visions, and other responses", and also a remarkable increase in volubility in one patient (Delgado et al., 1968)[5].

Since then, ICMS has been used extensively as an investigational and technological tool in the striate cortex (V1, area 17) for the purposes of creating a visual prosthetic for the blind both in macaques (Bartlett et al., 2005) and humans (Dobelle et al., 1974), or the middle temporal visual area (MT, V5) for biasing motion perception (Salzman et al., 1990), or biasing switching between reflexive and controlled

[5] His work in monkeys is perhaps more remarkable: by implanting electrodes in the thalamus, he could repeatedly get the monkey to walk from one side of the cage; stimulation to the posterior ventral thalamus induces targeted & organized rage in monkeys; stimulation to the medial caudate just behind the frontal lobes makes an alpha monkey tolerant and less aggressive. When this function was enabled by pressing a button in the monkeys cage, the monkey most harassed learned to press the button to halt the α males aggressive behavior. (Delgado, 1964)

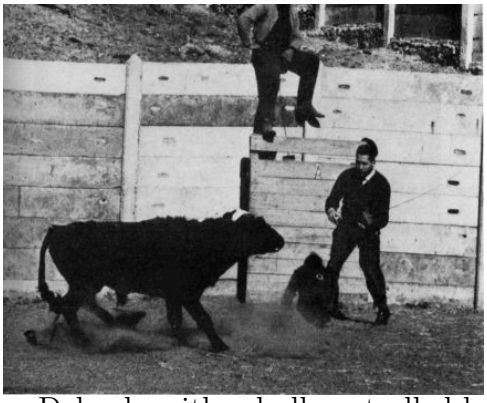

FIGURE 1.1: Jose Delgado with a bull controlled by his stimoceiver.

saccades (Isoda and Hikosaka, 2007), or in the lateral interparietal area (LIP) for biasing decision making (Hanks et al., 2006), or affecting face recognition in inferior temporal cortex (IT) (Afraz et al., 2006). In somatosensory cortex (S1, area 3b), ICMS has been shown to simulate mechanical perception of flutter (Romo et al., 2000, 1998), which is uniquely interesting because it proves that stimulating cortical neurons is sufficient for sensory discrimination, and hence as a basis for a sensory BMI. In rats, single 2 nC pulses of ICMS to the barrel cortex are detectable and discriminable at 80%; longer repetitions of pulses increase efficacy (Butovas and Schwarz, 2007).

Further proof that ICMS is salient and discriminable[6] occurred with the demonstration of the Roborat in the lab of John Chapin. Here rats were trained to go left, right, or straight based on radio-controlled ICMS to their barrel cortex (Talwar et al., 2002), and were rewarded for proper behavior using microstimulation to the medial forebrain bundle, a part of the limbic system that is strongly reinforcing for behavior (Olds and Milner, 1954). Optical stimulation has proved capable of providing the same CS to mice (Huber et al., 2008). In the congenitally deaf and those with cochlear, vestibulo-cochlear nerve damage, or neurofibramatosis (hence unable

[6] but not necessarily equivalent to physiological somatosensation; the only true way to tell is to try this in humans.

to use a cochlear hearing implant) (O'Driscoll et al., 2011), microstimulation to the inferior colliculus has been shown to permit speech understanding provided there are additional lip-reading cues(Lim et al., 2009). To be discussed more later, microstimulation can be used to locate pyramidal tract neurons by antidromic stimulation of the cervical spinal cord; this is often used in motor control studies to verify the identity of recorded neurons (Evarts, 1968; Schmidt et al., 1978; Wyler et al., 1980a).

As mentioned above, the broad aspect of sensory information is it's ability to modify or inform behavior. That's quite general, though: sensory information can also enable the brain to make inferences about the environment, or inferences about the sate of the body; sensory information is usually reactive feedback to ongoing motor commands, not a one-time CS. Within the Nicolelis laboratory, we've been working on using ICMS to enable these more specific aspects of somatosensation. In 2007 Nathan Fitzsimmons used different pattens of ICMS to cue left/right food pellet reaching in owl monkeys, proving when all other things were controlled (charge delivery, frequency, pulse duration), the cortex is capable of discriminating different *patterns* of stimulation (Fitzsimmons et al., 2007); see also Appendix A.2. In this experiment the owl monkeys did not immediately generalize their previous extensive vibrotactile cuing training, suggesting that ICMS either *not* equivalent to flutter as in (Deco et al., 2009), or area 3b of somatosensory cortex works differently than area 1. Alternately, owl monkeys could just be less intelligent.

Subsequent work by Joseph O'Doherty showed that ICMS cuing could be successfully incorporated into a closed-loop BMI. Indeed, ICMS learning was more rapid than initial tactile learning in one monkey; this might not be surprising as the regions targeted by ICMS mapped to the digits and palm of the hand, so the rhesus monkey could generalize previous mechanical vibration training. Despite what Doty (1969) reported, ICMS to posterior parietal region (PP) was ineffective, or at least much less effective than S1. See also Appendix A.4.

Yet this was still cuing, and not an real sensation – a real sensation both informs about properties of the world, and is often contingent on motor behavior. Dr. O'Doherty showed this recently in a brain-machine-brain interface, or BMBI. In the experimental task, the monkeys had to select one rewarded of three targets by artificial texture, provided by ICMS. By interleaving 50 ms period of stimulation with 50 ms periods of recording, the BMBI could both use a Kalman filter to decode the motor commands and deliver ICMS sensory information. Characteristics of exploration behavior were present in both hand- and brain-control sessions, suggesting that the prosthetic was being used in a familiar, closed sensorimotor loop (O'Doherty et al., 2011b). Pushing the field further, O'Doherty most recently showed that different variances of ICMS could be discriminated by a monkey, suggesting that the communications channel afforded by ICMS goes beyond amplitude and frequency into the timing of individual pulses. (O'Doherty et al., 2012).

To review, brain stimulation, and in particular ICMS, has been used for a host of purposes, including:

- Determining the function of brain structures in both humans and animals.
- Motivating experimental animals.
- Probing the mechanisms of learning.
- Providing information to the CNS in the form of conditioned stimuli (CS).
- Providing information in the form of artificial sensation for visual, auditory, or motor neuroprostheses.
- Antidromic activation of projecting fibers.
- Treating Parkinson's disease & essential tremor.

1.3 Recording

The second part of my work was focused on the opposite direction of communication: recording. The history of neural recording has been nearly as long as that of stimulation, and possibly even more broad; I will focus on the historical detail relevant to this thesis.

The need for a many-channel recording system is necessitated and contingent upon having a number of recordings sites; the desire to fabricate many-channel microwire arrays (MWAs) is circularly dependent on being able to record from them, both possibilities that have opened relatively recently (Nicolelis and Ribeiro, 2002). Hence the history of MWAs and recording systems have been tightly linked.

For the first 70-odd years of electrophysiology, almost all recording was done with one or a few electrodes, for which individual tube amplifiers sufficed (Gesteland et al., 1959). Original electrodes were simply short sections of fine wire, often varnished for insulation (Fritsch and Hitzig, 2009). These and present macro-electrodes, such as those used to deliver DBS currents, are both simpler to make and more reliable due to the much larger area, so there has been less technological focus and refinement on them.

The first microelectrodes were constructed by heating fine borosilicate glass tubing in the middle and pulling it to a fine tip. These glass pipettes have tips around 1 μm in diameter offered a resistive connection to the electrolyte and hence a good means for intracellular recording. They remain in extensive use, but their $> 10M, \Omega$ resistance plus 10 pF parasitic capacitance strongly filters recordings above 1.5 kHz, making extracellular action potentials disappear into background noise. Metal probes have a largely capacitive connection to saline due to the electrode-electrolyte interface, hence their impedance decreases with frequency, and are ideally suited for recording extracellular action potentials (Gesteland et al., 1959).

In the 1950's Hubel was of the first to begin using fine varnished microelectrodes; some of his later success with Torsten Wiesel (e.g.(Hubel and Wiesel, 1963)) is due to their ability to record high-quality extracellular action potentials from awake, behaving animals. Their electrodes were made of tungsten, the second stiffest metallic element (steel has a tendency to fracture near very fine tips), and electropolished to a fine point. These electrodes are then coated with a thin layer of lacquer, and $\approx$5 μm of their tip exposed to yield a recording site with an impedance of 500 kΩ - 10 MΩ at 5kHz. (Hubel, 1957). A stiffer glass-insulated improvement upon this type of electrode using tungsten (Collias and Manuelidis, 1957) or platinum (Guld, 1964) is reliable and has been in continuous application since its invention.

Around the same time, John Cunningham Lilly began developing the first true microwire array, albeit using micrpopettes that could slide freely in their housing so as to rest lightly and non-invasively on the pial surface. Twenty-five micropipettes were arrayed on a 2 mm grid, each with a tip opening of 100 μm, and were filled by capillary action to connect to Ag/AgCl electrodes. These electrodes were fed to a bank of vacuum-tube amplifiers, which notably employed common-mode rejection (Nicolelis, 2011), fed in turn to a series of glow tubes that would dim with positive electrode potential. At the time there were only physical means of recording (paper and film), so Lilly used a high-speed camera to photograph these glow tubes during his recordings. The resulting 3500 feet of film was nearly impossible to analyze in an age with only a few computers (Lilly, 1950). Later work mentions implanting 610 channels over 19 cm^2 of a monkey's cortex, and though he was only able to record from 25 at one time, he was able to observe in the thousands of feet of data different speeds of evoked potentials in the high-resolution electrocorticogram (ECoG) and sharp delineations between e.g. arm and leg representation in motor cortex [7].

[7] Lilly summarized the problems of MWA recording quite astutely: "One of the large difficulties in correlating structure, behavior, and CNS activity is the spatial problem of getting enough electrodes,

The next advancement of MWA technology was borrowed, like all good advancements. Kensall Wise used silicon lithography techniques to make SiO_2 coated gold electrodes with 2 μm fine, sharp points. However, the recording site could not be more than 50 μm from the 100 μm thick supporting silicon substrate, hence could only record superficially (Wise et al., 1970). Still, the promise of integrating electrodes and amplifiers on the same silicon substrate was realized early. A few years later PCB lithography was used to make a planar microelectode array (MEA) for recording from cultured heart cells (Thomas et al., 1972), a technique which is continued in modern slice recording.

As Lilly realized (and avoided by recording from the pial surface), microelectrode arrays should be as fine as possible to minimize damage to the tissue, but still need to be rigid enough to penetrate the pia. This is necessary as not only is the pia difficult to dissect out, but it contains many of the capillaries that supply the cortical surface. One obvious solution is to glue electrodes together into a more rigid bundle, an idea which led to the "sweet" electrode. In this scheme, 7 or more 25 μm teflon-coated Pt-Ir wires are glued to a connector with colloidal silver solder, inserted through 26 gauge hypodermic tubing, twisted together, and bunched with saliva. Then they are coated with dextrose melted at 148 °C, desiccated, and inserted into the rat brain, where extracellular spikes appear within a few days and last 2-3 months. These electrodes have a 1 kHz impedance of $\approx 500k\Omega$ (Chorover and DeLuca, 1972). Much of this technique has been copied in our lab and others, notably the silver epoxy, but not the saliva (presumably the 148 °C sterilized it, but the proteins likely make it antigenic). This technique has been further expanded upon and refined for floating arrays (Westby and Wang, 1997).

and small enough electrodes, *in* there with minimal injury. Still another problem is getting enough samples from each electrode per unit time, over a long enough time, to see what goes on during conditioning or learning [...] As for the problem of the investigator's absorbing the data – if he has adequate recording techniques, he has a lot of time to work on a very short recorded part of a given monkey's life."

Shortly thereafter Salcman and colleagues attacked the MWA design problem "rationally". Using again teflon-coated $25\mu m$ Pt-Ir (90%/10%) wires, stiffened and insulated by heat fusing with a glass micropipette and backfilled with cyanoacrylate, they were able to record the same apparent neuron for over 90 days (Salcman and Bak, 1973). To better understand the task of extracellular recording, they then developed an analytical mechanical model of this electrode in the cortex as subjected to accelerations from head movement and shear stress from connection through a wire, and determined that their tethering through a $25\,\mu m$ insulated gold wire should result in $10\,\mu m$ instantaneous movement of the electrode tip through the cortex in response to a 1 mm surface displacement, likely causing $2\,\mu m$ passage through tissue (Goldstein and Salcman, 1973). This movement is almost acceptable for extracellular recording, as the gradient for extracellular AP recording is $\approx 7.5\,\mu v/\mu m$, meaning movements of a few μm can change spike shape. Larger movements can destroy recording quality: a separable cell with SNR of 3:1 will disappear into the background hash with an electrode movement of $15\,\mu m$ or more[8] (Salcman and Bak, 1973).

Later electrodes by Salcman removed the glass micropipette insulator in favor of a pure $25\,\mu m$ iridium electrically sharpened, gold-coated electrode attached via microwelding to a $25\,\mu m$ gold lead wire. Pure iridium, with a Young's modulus of 521 GPa, is stiffer than tungsten with (406 GPa), hence Ir wires can be made the thinnest and least invasive of any wire MWA[9]. With the dura dissected away, penetrating the pia with a electrosharpened wire requires 50-200 μg; 2mm of $25\mu m$ Ir wire has a buckling strength of $\approx$900 μg [10]. The penetrating microwire is welded

[8] High-quality single tungsten wire recording contests this assertion, as others have been able to record the same spike over 50 μm of vertical penetration, and very large (Betz?) cells for 0.6 mm (Vibert and Costa, 1979)

[9] Platinum wires are usually alloyed with iridium to make them stiff enough to penetrate.

[10] For reference: if an electrode can penetrate the skin of a reasonably fresh red grape, it can penetrate the pia mater of rhesus monkeys; if it can penetrate canned pineapple against the grain, it is likely too thick (personal communication, Anonymous, at SfN)

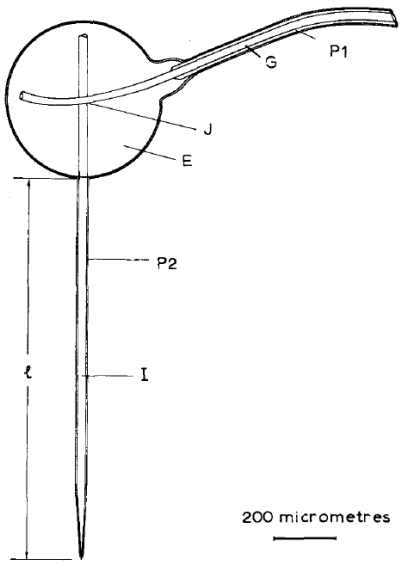

Fig. 1 Design of the parylene-coated gold and iridium microelectrode
The electrode consists of a pure iridium shaft (I) microwelded to an ultraflexible lead of pure gold (G). The lead has been previously coated with 12 μm of Parylene-C (P1). The weld joint (J) is encased in a ball of fast-curing epoxy resin (E). The entire assembly received a second coat of Parylene-C (P2). See text for further details

FIGURE 1.2: Salcman's floating microwire electrodes.

to an ultraflexibe gold tether, and this joint encased in a ball of epoxy which later serves and a handle for insertion – see figure 1.3. The whole device is then insulated with vacuum deposited parylene C, pinhole-free with a dielectric strength of 700 V/μm (Salcman and Bak, 1976). Each of these electrodes are individually inserted, which allows the surgeon to avoid vasculature but does not permit large numbers of implantations. Note also that, despite the high levels of expertise and technology, recording quality on these intial electrodes declined within 40-50 days, possibly due to organic polarization of the iridium-electrolyte interface which lead to a concomitant decline in electrode impedance. Later versions apparently had much better longevity of 37 months, as desired; these were of the first electrodes to be explicitly targeted for neuroprosthetic research (Schmidt, 1980).

As Salcman's individually floating arrays offered and improvement in longevity,

but their construction is quite complicated, and without commercialization they were not used again (to the best of my knowledge). This seems to be a common theme in neuroengineering: researchers may create substantially advanced technology, but unless it is dramatically better in quality or simplicity than existing technology, or goes into commercial production, the simplest effective technology remains. For example, Verloop and Holsheimer (1984) describe a simple MWA formed from wires stretched parallel in a jig and epoxied together or (Williams et al., 1999) which is highly copied and commercially available from Tucker-Davis technologies.

The next advancement came from MIT, where Kuperstein and Whittington demonstrated a MWA fabricated on a thin sliver of molybdenum foil useful for both high-density, precise localization of recorded neurons (microelectrodes diverge a bit when pushed into the cortex, so precise location in an animal is difficult). This work and others proved the utility of such lithographically patterned MWAs, leading to Khalil Najafi and Kensall Wise to fabricate the first "Michigan" probe using a deep boron diffusion layer to protect silicon from back-etching, thereby allowing chemical etchants to thin relatively thick silicon wafers into a precisely defined needle-like probe. This critical etching step allowed the silicon probe to be $\approx$15 μm thick (Najafi et al., 1985), solving the earlier beam problem, and permitting silicon electrodes and electronics to be fabricated in the same step (BeMent et al., 1986), including with amplifiers and multiplexers (Najafi and Wise, 1986) for reducing microphonic noise (Csicsvari et al., 2003), and later assembled into 64-channel three-dimensional structures (Hoogerwerf and Wise, 1994). While crystaline silicon is generally brittle, thin films of silicon are remarkably tough and flexible – about six times as strong as bulk silicon, allowing the lead wires to be made of silicon too (Najafi and Hetke, 1990).

In the most common integrated circuit processing practice crystaline silicon wafers are patterned with doped regions, insulators, and metal layers in a repeating pattern

to make many identical chips; these chips are diced or separated from the wafer using a special very fine-kerf diamond saw. Normann and colleagues realized that this dicing saw, followed by an acid etch step (exactly as used to sharpen metal microelectrodes) could be used to mechanically, rather than lithographically, create a silicon microelectrode array. After initial semi-failed attempts using p-n-p junctions to insulate the individual spikes of p-doped conductive silicon, they switched to frit glass insulation using kerfs of the diamond dicing saw to separate electrodes, and the modern "Utah" array was born (Jones et al., 1992) [11].

Initial tests of these arrays in cat S1, V1, and auditory cortex were less than sanguine. Of 12 implanted Utah arrays, all but one showed some degree of fibrous encapsulation, likely from invagination from either the dura or arachnoid. These arrays are tethered using 25 μm polyester-insulated gold wire to limit the mechanical coupling between the scull and brain (not only does the brain accelerated within the cranial volume, but it swells and contracts on a diurnal cycle). The tether permits the brain to eject the Utah array, which it did to completion in one array, leaving the cortex below with no evidence of implantation or scarring. Two other arrays were totally removed from the leptomeningeal space. Histology revealed that in all implants the dura adhered strongly to the bone flap, and in turn the fibrous encapsulation of the Utah array adhered to the dura: the implant was effectively affixed to the scull, not tethered (Rousche and Normann, 1998).

Through an undisclosed "longitudinal development series" which included 39 array implants in 18 monkeys, the quality of the Utah array was markedly improved. By changing the insulation from silicon nitride or polymide to parylene-C and, perhaps most critically, placing a layer of sterile Gore-Tex above the individual arrays before replacing the dura, the electrode was not so thoroughly rejected. Recording

[11] Additive, rather than subtractive, construction can also be used to create silicon electrodes. Innovative new work shows that vapor-liquid-solid growth can fabricate electrodes as fine as 4 μm (Kawano et al., 2010).

quality persisted for at least 70% of the electrode arrays to 82, 172, and 154, and 569 days; one monkey reportedly could be recorded out to 1264 days (3.4 years) (Suner et al., 2005).

Phillip Kennedy took an alternative approach to recording from neurons: rather than inserting metal to get close to them, he use a bit of cat sciatic nerve to get neurons to grow *toward* the electrodes (Kennedy, 1989). This bit of sciatic nerve was placed inside a glass micropipette in which several fine gold wires were glued; the nerve released neurotrophins, causing the neuropil (axons and dendrites, but no cell bodies) to extend into the cone, leading to good and reliable recording approximately 6 months post implantation (Kennedy et al., 1992). The cone electrode has been successfully used in clinical human BMIs, to be discussed below.

The final electrode technology worth mentioning is the oblique or inverted method of implantation. Normally when recording from the cortex, electrodes are implanted through the superficial layers into the deeper layers, as this is both easiest and disrupts the minimum amount of tissue. An alternative, developed by Kruker and colleagues, is to implant from the opposite direction, e.g. from the white matter. Using very fine polymide-insulated 12.5 μm Ni-Cr-Al wire in rabbit and marmoset V1 cortex, they were able to record stable action potentials for up to 711 days, during which recording quality did not degrade. The authors surmise that the small diameter of the wire and long length of free wire running through the brain provided a sufficient degree of friction so that tissue does not move near the electrode tip (Porada et al., 2000), thereby reducing mechanically stimulated immune response. Later work proved that this method could be used to record from arrays of 64 channels in ventral motor cortex of monkeys for 7 years, a point at which the primary failure mode was the connectors, not the electrodes or insulation (Kruger et al., 2010).

Within the Nicolelis lab, there has been a continuous evolution of MWA technology and assembly technique. Prior my arrival at Duke, arrays were assembled

by affixing individual straight segments of wire to small PCBs. These PCBs were soldered directly to the headstage connector and could be arrayed vertically to form a 2D array of 16 to 96 individual channels (Nicolelis et al., 2003). In lieu of Utah or Michigan arrays, other labs have similar sensible construction techniques (Verloop and Holsheimer, 1984) or (Williams et al., 1999). Gary Lehew's arrays offer basically indefinite recording from owl monkeys and > 4 year longevity in rhesus monkeys (that is, clear SUA is recorded on many electrodes for at least 4 years, though the identity of those cells may change over time); other labs have verified the longevity of similarly constructed MWAs to 800 days (Liu et al., 2006). The most recent arrays, as used in the experiments of Chapters 3 and 4, include 2 or 3 microwires per shaft (65 μm and 40 μm or three 50 μm), and are moveable in groups of three or four shafts.

1.3.1 Summary

The above review very roughly outlines the many and varied attempts at using arrays of electrodes to record from the central nervous system. The net impression is that many different technologies offer nearly equivalent levels of performance, which has been verified in a controlled study (Ward et al., 2009). Microwire arrays to offer slightly worse SNR than single electrode recordings (Kelly et al., 2007), but they more than make up for this in high bandwidth simultaneous recordings across a neural population (Friston, 2002). As improved signal quality would dramatically simplify the recording system, future directions of this field will be presented in the discussion.

1.4 Recording Systems

1.4.1 Amplification

In comparison to the complex issues surrounding assembly, biocompatibility, and longevity of electrodes, electrical recording of extracellular action potentials is not inherently daunting. The needed bandwidth is not too high, and all that is required is low input-referred noise (Gesteland et al., 1959). Amplifier passband should be between 100 and 7.5 kHz, with the highpass to remove ten-times larger LFP, and the lowpass to remove noise beyond the band in which spike energy is concentrated. Electrodes have a thermal noise of $E = 0.1219\sqrt{R \times B}\mu V_{rms}$, where B = bandwidth in Hz and R = resistance in $M\Omega$, which equates to 10 μV from a 1 MΩ electrode at 7.5 kHz bandwidth (Schmidt, 1984b). FET input op-amps have an equivalent noise source resistance of 15 kΩ, so sufficient noise performance is not difficult to achieve with commercially available integrated circuits.

Placing the amplifiers very close to the recording sites minimizes the capacitance of the electrode leads; as the electrode-electrolyte tissue is a capacitor with a value of $0.2pf/\mu\,m^2$ (Robinson, 1968) electrodes have a typical capacitance of 5-20pf and any load capacitance serves as a (degrading) voltage divider. Immediate pre-amplification also reduces microphonic pickup due to wire movement. As a result, nearly all electrophysiology setups place the initial amplifier or headstage as close to the recording site as possible.

Spike sorting and data recording is a considerably more challenging task; original sorting was done via custom analog window-comparators tuned for the cell under study (Olds, 1967), or switched sequenced amplifiers; one particularly ingenious method used photodetectors taped to the screen of an oscilloscope (Schmidt, 1984b). The advent of the computer simplified the problem tremendously, and by the early 80's the standard methods for spike sorting had been well established: template

matching, PCA, spike amplitude, peak-to-peak amplitude, Fourier analysis, curve fitting, spike area, and RMS value (Schmidt, 1984a). Given sufficient signal-to noise on the neural traces, any of these methods will work well, but only a few parameters are needed for adequate separation: maximum voltage, minimum voltage, and the time between them (Vibert and Costa, 1979). Chapter 4 describes a system which uses template sorting, chosen mainly because it maps well to the computational resources of the hardware, and because it it most familiar to the end-users.

As mentioned, obtaining acceptable gain, passband, and input noise parameters is not too difficult with discrete semiconductors or commercial off the shelf (COTS) components (Obeid et al., 2004a). Miniature and integrated bioamplifiers, however, face a number of challenges, including:

- Nulling electrode offsets. The electrode - electrolyte interface acts as a half-cell, hence can be polarized to 1 V with as little as 10 nA. Hence amplifiers must have zero DC gain. This is frequently accomplished by capacitively coupling the amplifier input.

- Positioning highpass poles. Capacitively coupling the input provides a high-pass, but given that only very small on-chip capacitors ($0.001pf/\mu m^2$ (Obeid et al., 2003)) can be made, the associated resistors must have very high resistance. One clever solution is to use deep-ohmic PMOS transistors as high value resistors (Mojarradi et al., 2003), or MOS-bipolar pseudoresistors (Harrison and Charles, 2003; Perelman and Ginosar, 2007), very long transistors (Dabrowski et al., 2003), or even diodes forward-biased so that dV/dI effects a high value resistor (Dorman et al., 1985). Larger capacitors can be realized by nitride films (Dorman et al., 1985) or by exploiting the Miller effect (Dabrowski et al., 2003).

- Low noise. PMOS transistors, which have lower 1/f (flicker) noise than their

NMOS counterparts, are generally used here. To maximize transconductance (gain) they are biased for weak inversion and made wide to further optimize noise (Harrison and Charles, 2003). Cascode current sources can be used in the rest of the amplifier, as these shunt their own current sources (Wattanapanitch et al., 2007). An alternative approach is to use chopper-stabilization of the amplifier (Dagtekin et al., 2001), which has the added benefit of electrode offset rejection.

- Low power. A fundamental trade-off in amplifier design is that between power, bandwidth, and noise, so much so that a metric, the noise efficiency factor (NEF) is typically specified for a given design. In his thesis, Wattanapanitch (2007) proposes a very low power bioamplifier with a NEF of 2.7, and furthermore cleverly permits reducing bias current for lower recording power when background neural noise is high. It is also possible to vary bias current based on required bandwidth (Mojarradi et al., 2003). Other work has NEFs of 1.8 (Holleman and Otis, 2007), 4 (Harrison and Charles, 2003), 10 (Mohseni and Najafi, 2004), or greater (Obeid et al., 2003).

The recording system described in Chapter 4 uses a commercially available amplifier and multiplexer chip based on (Harrison and Charles, 2003), which feature a low input-referred noise of 2.2 μ, V_{rms} [12]. Many other lower-power designs exists, as mentioned above, but in the interest of time, effort, and expertise custom amplifiers were not investigated.

1.4.2 Integration

Research in the integration of electrodes, neural amplifiers, sorting, and telemetry seems to be lead by Najafi, Wise, and colleagues. As mentioned above, placing

[12] The research version of this amplifier seems to have much lower power (80 μ, W than the commercially available chip ($400\mu, W/chan$)

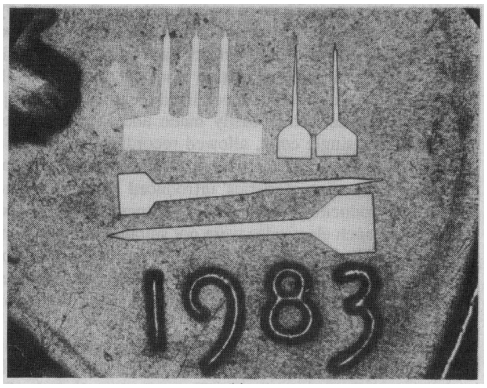

FIGURE 1.3: Early recording system with amplifiers on the electrodes. From (BeMent et al., 1986)

amplifiers as close as possible to the recording site has distinct advantages, which led initial work to put enhancement-mode NMOS preamplifiers on a micromachined silicon electrode (Najafi et al., 1985). Figure 1.3 shows examples of these silicon electrodes with integrated circuitry. These amplifiers featured a gain of 100, a bandwidth of 15 kHz, and recording of 10 sites through 3 leads via on-chip multiplexing (Najafi and Wise, 1986). Later versions had an unfortunately high input-referred noise of 15 μ, V_{rms} but consumed a modest 2.5 mW for 8 channels (Ji and Wise, 1992).

As early as 1995 these amplifiers were multiplexed, digitized, and telemetered using an bidirectional inductive link (Akin et al., 1995). This system allowed transdermal transmission of 2 digital channels of neural activity from a peripheral nerve recorded via a 32 site silicon sieve electrode, within a 4 x 4 mm package consuming 90 mW of power[13] (Akin et al., 1998). The same group created a 1024 site 3D integrated recording system using Michigan-style planar silicon probes vertically mounted to a carrier board and spike sorting DSP (Bai and Wise, 2001; Wise et al., 2004). The system, shown in Figure 1.4, can digitally record, stimulate, and teleme-

[13] Given the very advanced level of this work, and its transparent utility to others, I wonder what has happened to the technology – it was at least 10 years before others.

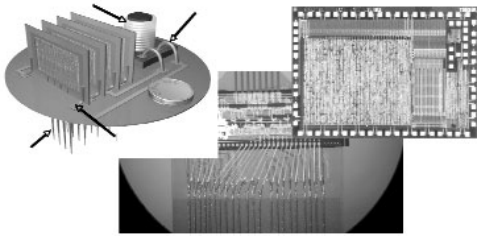

FIGURE 1.4: .

1024 channel silicon integrated recording system. Vertical silicon electrodes & preamplifiers are mounted by electroplating nickel between opposed contacts on the base and vertical silicon. From (Wise et al., 2004)

ter from any 128 of the 1024 recording sites. Spike sorting here is simple thresholding with 2 channels broadband transmission per 64 electrode sites (Sodagar et al., 2006); spikes are compressed to 18 bits of address and voltage (Sodagar et al., 2007). Later work extends recording to 256 simultaneous channels (Olsson and Wise, 2005) using parameterized spike sorting inspired by (Vibert and Costa, 1979) at only 5.4 mW. To my limited knowledge, this system has not been used in a monkey, but similar devices have provided stable recording for over a year in rats.

Their most recent work is frankly far beyond my own modest efforts. In a single 1.4 x 1.55 cm package consuming 14.4 mW they can amplify, sort (detect threshold crossings and maximum amplitude), and telemeter 64 channels (Sodagar et al., 2009). These systems have had limited adoption, however, due to the expensive mixed MEMS / CMOS fabrication steps required, and the relatively low yield of functioning chips (Michel Maharbiz, personal communication).

Many other groups have been working on wireless recording systems; a literature review seems to be an enormous amount of duplicated effort. At Duke Obeid et al. (2004b) have demonstrated a wireless recording of 12 broadband system using 802.11 (WiFi) using 4 W of power; later work consumes 2.3 W (Parthasarathy et al., 2006) or was extended to include signal processing for BMI applications (Darmanjian et al., 2005). Integrated amplifiers (Obeid et al., 2003) and a discrete analog front end (Obeid et al., 2004a) have been developed here, as well as a 96-channel FPGA-

based wireless recording system (Rizk et al., 2007) that is fully implantable (Rizk et al., 2009). This last work is highly similar to that presented in Chapter 4, except the analog section of Rizk's design is much higher power (300 mW), the outgoing bandwidth is lower (1 Mbps), sorting is not done on the transceiver, and no digital filtering is performed on the raw signal traces.

Other innovative approaches include using optical means to deliver power via GaAs/AlGaAs photodiodes (Song et al., 2005) and transmit data (Song et al., 2009); saving neural data to compact flash (Linderman et al., 2006; Santhanam et al., 2007); making the recordings system light enough to mount on homing pigeons (Vyssotski et al., 2006); using completely passive sensors based on RF backscatter (backscatter is used for e.g. airport security scanners) (Schwerdt et al., 2011; Towe, 2007); ultra low-cost systems (Ativanichayaphong et al., 2008; Rolston et al., 2009a); mounting a custom spike sorting & radio power/data system on the back of a Utah array (Harrison et al., 2009; Kim et al., 2009); 1000 channel active surface recording (Maschietto et al., 2009); and time-division multiplexed encoding neural potentials into a video stream for wireless transmission (Szuts et al., 2011). Ultra wide-band radios are presently quite popular due to FCC regulations and the need for high bandwidths in wireless systems without spike sorting (Chae et al., 2009; Fan et al., 2011; Miranda et al., 2010).

1.5 BMI

The idea of a brain-machine interface is possibly as old as neuroscience, or at least as old as science-fiction. People have wanted to control things directly with their minds, circumventing the musculoskeletal system and presumably the attendant fatigue[14] and power limitations. That desire is elevated to a proper need in the case of amputation and paralysis, whence the normal end-effector of volition must be replaced by

[14] This despite the fact that fatigue may largely be centrally mediated (Hilty et al., 2011)

something else. The natural choice is closest point in the broken signal chain: either the mixed peripheral nerves exiting the spinal cord, the spinal cord itself, pyramidal tract neurons in the motor cortex, or other CNS targets. This document will only deal with signal sources within the CNS, primarily within motor cortices.

Before controlling something with your neurons it must be determined if the firing of individual neurons themselves could be controlled. Olds was the first to demonstrate this form of operant conditioning of individual neurons chronically recorded from rats. Cells were recorded from the pontine nucleus and hippocampus; the rat was given food or self-reinforcing ICMS to the hypothalamus whenever the neuron bursted for 250 ms above a normal spontaneous range, contingent on a light trigger signal. The rat was able to operantly condition FR changes in all neurons recorded. However the threshold for bursting would need to vary over the course of an experiment, as the FR for these neurons would vary by a factor of 2-5 over a period of several hours, and exhibited sinusoidal oscillations on the order of 10-20 minutes, depending on the structure recorded (Olds, 1967).

Earlier work by Basmajian showed that this was unsurprisingly true in people as well, here via recording intramuscular EMGs. A motor unit, (the group containing an anterior horn cell in the spinal cord, its axon, and all the muscle fibers on which the terminal branches of the axon end) can be discriminated much like cortical cells by extracellular fine electrodes inserted through the skin (in this case, 25 μm Karma alloy, NiCrAl, normally used in strain gauges). Three to five units from one electrode could be voluntarily recruited by the patient after a half-hour period of training, and through simple feedback (an oscilloscope and speaker), each could be controlled independently. The author was impressed by how quickly and reliably learning occurred: "The controls (are) learned so quickly, are so exquisite, are so well retained after the feedbacks are eliminated that one must not dismiss them as tricks" (Basmajian, 1963).

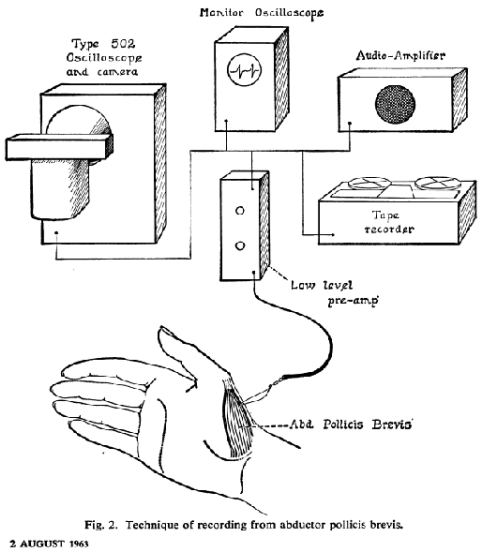

FIGURE 1.5: Setup used by Basmajian for EMG biofeeback studies. From (Basmajian, 1963).

These early results have pivotal importance on the nascent field of brain-machine interfaces, as it proved that individual control of motor units – hence likely the pyramidal tract neurons that activate them – is both possible and precise. Eberhard Fetz proved that this was true by training monkeys to increase the firing rate of precentral cortical neurons recorded in the classical fashion, through a single acute electrode penetration. With audio and visual feedback (like Basmajian) the monkeys quickly (mean 6.5 minutes) learned to increase the firing rates of 65% the recorded neurons, and these increases usually involved movement such as elbow flexion or wrist pronation/supination (Fetz, 1969). This results were unlikely to be purely the result of sensory feedback, as shown by extinction trials, and the presence of specific movements suggests that it is not an overall result of global attentional or motivation. This last point was verified using bilateral electrodes (Wyler et al., 1980c).

Fetz subsequently showed that these operant responses could be dissociated from the habitual or normal associated muscle contraction (Fetz and Finocchio, 1971, 1972), further suggesting that individual precentral units are independent channels

of efferent information. A more extensive study showed that when a single electrode was able to record two or more units at the same time, each could be independently conditioned for high or low firing rate. As would be expected, these neighboring cells usually (but not always) exhibited correlated firing rate changes (Fetz and Baker, 1973). Later work found that 80% of simultaneously recorded neurons did *not* show covarying firing rates, consistent with Lemon and Porter's finding that neighboring cells respond to widely separated peripheral fields (Lemon et al., 1976); even yet fully two thirds of them show tight 1ms synchrony(Wyler, 1985). The discoveries led to what was arguably the first cortically-driven BMI (Humphrey et al., 1970), in which operant responses from small groups of motor cortex units were used for real-time prediction of simple arm movements; despite the stated neuroprosthetic purpose, it did not garner nearly the publicity of later BMIs.

Around the same time Wyler, under the tutelage of Fetz, hypothesized that epilepsy might be possible to control through biofeedback and operant conditioning. In monkeys in which precentral epilepsy was induced by placing alumina on the cortical surface, the researchers were able to record three classes of neurons based on the temporal structure of their epileptiform bursts and presence of ISIs shorter than 10ms (precentral neurons rarely exhibit ISIs less than 10ms except during vigorous movement or sleep). Cells with highly structured, stereotyped burst could not be conditioned; less stereotypical bursts could be conditioned, though not to repress bursting (Wyler and Fetz, 1974; Wyler et al., 1975).

The work let Wyler to ask if ISIs themselves could be operantly conditioned; this reflects, albeit loosely, on the idea that both the time and the rate of individual spikes matters (Rieke et al., 1999). Though to the best of my knowledge this has not been duplicated, they were unable to train monkeys to control ISIs (Wyler and Robbins, 1979); indeed, they discovered that the ISI distribution or PTNs was likely to be bi- or tri-modal during movements unrelated to the neuron's tuning, but as the monkey

gained volitional control over the cell, the distribution became *more gaussian*. With some neurons, variance of this gaussian could be controlled by the monkey, but only to a point. As the few cases of control were associated with apparent isometric contraction of the associated muscles, (as observed by all studies of operant control in motor cortex up to this point), next they sectioned the dorsal cervical spinal cord. This markedly decreased the fidelity of volitional control. When only contralateral C5-7 ventral roots were sectioned, PTNs could no longer be statistically controlled, leading the authors to conclude that high fidelity control of FR in precentral neurons requires afferent feedback from the spinal cord, and usually peripheral movements (Wyler et al., 1980b). As a further control, they then eliminated audio and visual feedback; monkeys were able to control PTN FR independent of sensory feedback, consistent with the essential feedback coming from the spinal cord and periphery (Wyler and Robbins, 1980). The inability to train ISIs is also consistent with feedback from the periphery, as individual ISIs are destroyed during the conversion of spikes to force to spikes; indeed, even if the CNS computes via precise spike timing volitional control of ISI PTNs is useless, as muscles (and the skeletal system) are agnostic to the feature.

A final study by Wyler further buttressed the hypothesis of spinal cord control: by implanting a stimulating electrode in the pyramids at the level of the brainstem he was able to measure antidromic latency on the recorded neurons. Surprisingly, slow PTNs, those with latency > 2 ms, were nearly all well controlled in the operant-conditioning task; fast (< 2 ms, 1.2ms mean latency, presumptive Betz cells) had a more highly variable firing rate and ISI, and were *less* well controlled (Wyler et al., 1980a). While this experiment is highly suggestive, it needs to be verified in a more typical FR-only operant conditioning task.

Such a study was conducted by Schmidt and colleagues using the floating chronic iridium microelectrodes mentioned earlier (Carmena et al., 2005; Salcman and Bak,

1973, 1976). During recordings spanning two years, they found that 77% of single units and 65% of multiunits could be brought under volitional control by the monkeys. As they were only recording one neuron, this was a one dimensional BMI, with a row of 8 lights and 8 target annular rings serving as the target-acquisition task. The cursor in this case was controlled by the firing rate of individual neurons, using an analog threshold and RC filter. Systematic variance of the target hold time and smoothing τ led to a peak bitrate (in the case of 4 targets, 2* targets/sec; 8 targets: 3* targets/sec, assuming 100% success) of 3.85 bits/sec, which nearly equals the 4.29 bits/sec that the monkeys achieved when using a manipulandum (Schmidt et al., 1978). For comparison, a human can convey $\approx$2.7 bits/sec using single-channel surface EMG; a trained monkey can convey 3 bits/sec (Schmidt, 1980). As before, they found successful conditioning was always associated with specific repeatable limb movements, e.g. finger and shoulder movements, frequently isometric against the primate chair. An antidromic pyramidal tract electrode was implanted in one of the three monkeys used, and latencies were 1.2-1.3 ms for conditioned units; direct comparison with Wyler's results are difficult, but a positive result is generally stronger than a negative: fine control of M1 PTNs is possible, even easy for well-trained monkeys. This led the authors to conclude that these signals were eminently suitable for neuroprosthetics (Schmidt, 1980) with some ensuing media hysteria (Marbach et al., 1982; O'Neill, 1980).

To the best of my knowledge, this initial work in BMIs under the heading of operant conditioning was left fallow until 1999, when Miguel Nicolelis, John Chapin[15], Karen Moxon and colleagues at SUNY Downstate demonstrated the first modern BMI. Here neurons recorded using microwire arrays in M1 and ventrolateral thalamus (VL, has major afferents to motor cortex) were used to control a one DOF robot arm that could retrieve droplets of water. To convert the firing of up to 46 neurons to

[15] also known as my boss and former boss.

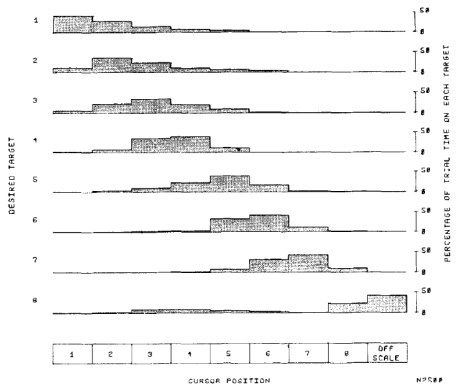

FIG. 2. Firing rate distributions of a conditioned cortical pyramidal tract neuron for the eight different targets. The firing frequency was divided into eight equal zones to activate the appropriate cursor light. The range of each cursor position was 4.83 spikes/s. Firing rates greater than 38.6 spikes/s went off-scale and were included in the last bin of the histograms.

FIGURE 1.6: Illustration of precise control achieved by Schmidt & his monkeys. From (1978).

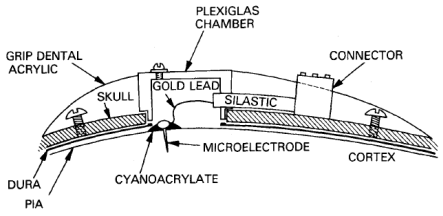

FIGURE 1. Implant arrangement for intracortical chronic recording microelectrodes (with permission of Academic Press, from Ref.5).

FIGURE 1.7: Recording setup used by Schmidt. From (Schmidt, 1980).

the one dimensional control signal, recurrent artificial neural networks and linear methods regressed ensemble activity to recorded forelimb movements the rat made while manually controlling the robot (Chapin et al., 1999). This bit of supervised learning[16] was a large departure from operant conditioning in that much of the learning was now done by the computer. This was as much a technological limitation as scientific, for up until this point neither the microwire (Nicolelis et al., 1997), electronic recording, or computer technology did not exist for these experiments.

Shortly thereafter Wessberg et.al (2000) showed that the 1D BMI task in rats could be extended to full 3D hand endpoint predictions in owl monkeys. Super-

[16] Supervised in the sense that both the input and output of a transform is known, so the task is to infer the transform.

vised learning via a Wiener filter or artificial neural network were used in real-time to reconstruct the path of the monkey's arm[17] from 50-100 neurons, which then commanded the trajectories of local and remote haptic robots. Most interestingly, the reconstructions were accurate despite the facts that the variance on the monkey's reaching movements was quite high, the movements were often ballistic, and movements were not overtrained & stereotyped – thereby proving that the decoding generalized to normal arm trajectories (Wessberg et al., 2000).

Around the same time Phillip Kennedy reported on his initial work using the cone electrode in ALS (Kennedy and Bakay, 1998) and brainstem stroke locked-in patients. The electrodes worked as in monkeys and two patients were able to control a one-bit (on-off) or 1D + select BMI for typing on a computer screen. Kennedy found that pure increases of firing rate within the recorded neurites were more effective than bidirectional modulations, as would be expected from the motor system (muscles exert force in one direction), hence the BMI was not only one dimensional but one directional. To permit typing the keyboard cursor simply wrapped when it got to the right of the screen (Kennedy et al., 2000). One patient was able to dissociate neurite activity from eyebrow EMG, as Fetz did, but this begs the question of why non-invasive surface EMG was not used if it could provide the same information[18]. Work with these patients must have been slow, as they were sick and had many complications (ulcers, peripheral neuropathy)(Chapin and Moxon, 2000); the same issues came up in our work with PD patients.

Later work with the cone electrode in human patients showed promise for decoding speech. As detailed in an recent article (Bartels et al., 2008), the cone electrodes

[17] Using shape-tape – loops of fiber optic that measure bending by light loss around curves (another enabling technology).

[18] The same issue holds for EEG BMI studies, where adaptive noise cancellation often must be used to remove the order-of-magnitude larger head EMG signals (Schalk et al., 2000). If the EMG signals are so large, why not just use them? Furthermore, EEG control peaks at around 0.25 bits/sec (Blankertz et al., 2003), an order of magnitude lower than surface EMG on one muscle

were implanted rather deep (5-6mm) into the speech motor cortex of patients, and telemetered with a bipolar, inductively powered, FM radios. The received broadband signals were sorted into 56 spike clusters on two channels[19] and fed through a Kalman filter to produce two control axes. As with the rats at SUNY, this was supervised learning – Kennedy asked the patients to imagine making a series of simple vowel sounds that can be characterized by trajectories through a 2D format space, from which he trained the Kalman filter to produce the corresponding sounds at will (Guenther et al., 2009). Normal speech contains plosives and fricatives in addition to the formants of vowels, but still this is a promising start.

Returning to monkeys, Serruya et. al. (2002) showed that monkeys could be rapidly trained to use a relative few (7-30) motor cortex neurons to directly control a 2D computer cursor under visual feedback; this result was extended to decoding movement direction (classification) using ML methods as well as continuous linear decoders on as little as 1 minute of data (Serruya et al., 2003). Taylor et. al. (2002) extended this result to three spatial dimensions with a monkey reaching to 8 spatial targets arranged at the corners of a cube. The population vector (PV) algorithm was used to decode movements in this experiment, followed by an ad-hoc but apparently effective "co-adaptive" algorithm. This employed what were effectively cross-validation and semi-supervised methods to update individual tuning vectors (Helms Tillery et al., 2003). Work by our lab has shown the PV method to be inferior to other methods, like the Kalman filter (Li et al., 2009), and indeed Taylor et al reflected that raw PV without adaptive update yielded poor predictions.

Jose Carmena and colleagues in the Nicolelis lab shortly thereafter published work in a realtime 3D reaching and grasping BMI (Carmena et al., 2003). In these expiermiments, monkeys first learned to control a video game in which cursor position

[19] This seems excessive, as we normally sort 4 units maximum per channel; Kennedy's justification was that the Kalman filter with a ridge-regression normalization step will correctly merge or reject clusters despite excessive sorting.

was controlled by a 2D joystick, and cursor size was controlled by grip force; once the monkeys mastered the task, a Wiener filter was trained on the data and used to directly control the video game. Ultimately the joystick itself was removed, and the monkeys had to make reaching movements with only neural activity. In comparison to previous work by Schmidt and Wyler, after a while monkeys ceased use their muscles at all, as EMG recordings were silent. Carmena also looked at prediction quality by area, and found a mixed but distributed coding of the task information between M1, PMd, PP, and S1, and SMA. These neurons were analyzed for tuning changes between pole and brain control, and remarkably this too was modulated by area. In brain control it was found that most neurons progressively grouped around the same preferred direction, a result I find quite interesting[20]. Carmena et al (2003) showed that when control signals were passed through a robot, the monkeys were able to compensate for the resultant nonlinearities and delays, and could control it as a prosthesis would be controlled. This control was stabilized through visual feedback and distributed coding, as though the correlation between the firing of individual neurons and movement parameters was nonstationary over 30 minute periods, aggregate predictions were stable (Carmena et al., 2005).

The next major advance was built on the observation that the parietal reach region (PRR) of the posterior parietal cortex (PPC) encodes reaches in visual coordinates. Musallam et. al. (2004) recorded the medial intraparietal section of PRR, and were able to rapidly – in 200 to 1100 ms – decode the intended discrete reach of a monkey from a small set of neurons (<= 16). The decoder in this case was an adaptively updated database indexed by wavelet-transformed firing rates.

Using a similar probabalistic model, Santhanam et. al. (2006) were able to

[20] If all neurons are tuned to approximately the same direction, then how is the orthogonal direction controlled? One must be careful in making extrapolations from this, as the cursor movement is controlled by the firing of the neurons themselves, and so regressing firing rate of one neuron to the aggregate firing of many neurons may just be extracting the first principal component of the ensemble activity.

quickly decode the intended reach target from 96 microwires recorded in PMd. The peak sustained channel rate in these experiments was 6.5 bits per second, or approximately 15 words per minute, which is 68% higher than reported by Schmidt (1978) nearly thirty years earlier – despite the fact that they had over 100 times as many neurons. This strongly nonlinear scaling (if all neurons were independent, then 100 neurons should convey 385 bits/second) is, I think, more a limitation of feedback and training than of the motor system itself.

Donoghue and colleagues later showed a 2D BMI in a human rendered teraplegic by spinal cord stroke. Using 96 channels from a Utah array chronically implanted in hand/arm precentral gyrus, the BMI user was able to perform reasonably reliable pursuit tracking and center-out tasks, as well as typing and generally using a computer (Hatsopoulos et al., 2005; Hochberg et al., 2006). This study served as conclusive proof that motor cortex was an active and functional source of volitional signals in paralyzed humans, despite Wyler's observations that the quality of control markedly decreased without the ventral horn (Wyler et al., 1980b). Despite the work, EMG and eye saccade controls remain non-invasive and far more reliable (Birbaumer and Cohen, 2007).

A swell of interest and related work followed (Lebedev and Nicolelis, 2006) (see also Appendix A.5), some of it innovative and other more capitalizing on the sci-fi public appeal of BMIs. Most studies fit within the category of incremental improvements in the quality or bandwidth of brain-computer communication, though some surprising results can be found.

As described in the first section of the introduction, electrodes are a common bottleneck in electrophysiological systems, particuarly BMIs. Mehring et. al. (2003) showed that LFPs – which are much more stable than SUA against electrode changes, immune response, or micromotion – are equal to single-unit recordings in terms of predictive capability. Wood et. al. (2004) addressed the problem of stability a

different way, by putting the sorting of SUA within the optimization step. They show a modest increase – 14% – with optimized machine sorting of cells versus human sorting. Another alternative is to simply *not* sort the data, and instead include all threshold crossings on a given electrode channel into one unit (Won and Wolf, 2004). This does not seem to be a well-motivated idea, as described before, for neurons recorded from the same channel can have different tunings.

A second limiting step in BMIs is the decoder, and efforts to improve noisy predictions have investigated many supervised, semi-supervised, and unsupervised learning techniques. As in the original BMI work within the Chapin lab, Single recurrent networks have been used to effectively predict multiple kinematic parameters (Sanchez et al., 2005). This study used the data from (Carmena et al., 2003) and showed that a large proportion of the output variance is predicted by a few neurons, a result that remains disputed (Narayanan et al., 2005). Probabilistic methods, like particle filters, have been shown to be 3-5 times better than optimal linear control, and 7-10 times better than population vector (Brockwell et al., 2004). Within the Nicolelis lab, we have developed a more principled and computationally efficient method for BMI predictions using an unscented Kalman Filter (Li et al., 2009) and see also Appendix A.3; 'unscented' in this case refers to accurate modeling of nonlinear tuning and state-transition functions. Other nonlinear techniques within the literature include support vector machines (Byron and Jennie, 2010), permitting an assessment of which neurons the brain was changing to support learning, or spiking neural net decoders (Dethier et al., 2011). Yet other BMI researchers have focused not in improving the quality of control, but rather the quantity of data required to train it, by using immediate, bootstrapping visual feedback (Wahnoun et al., 2004), or by eliminating distracting 'noise' units (Wahnoun et al., 2006).

The third region subjected to engineering improvement is the robot or output of the BMI. As BMI signals are to this date still quite noisy, it makes sense to embed

object-interaction intelligence within the robot. This falls under 'shared control', an idea Hyun Kim investigated in the Nicolelis lab; in his experiment a haptic robot with gripper was partially controlled by the brain, and partially controlled by sensors in the robot arm. The robot emulated the "infant palmar grasp reflex", helping the robot arm to pick and release objects (Kim et al., 2006). The Schwartz laboratory used a similar form of shared control in an experiment where a (presumably very well-motivated) monkey had to learn to control a robotic arm for feeding itself. Rather than controlling the joint angles directly (which would be very non-intuitive, as they did not use an anamorphic arm), a population vector decoder was used to direct the robot endpoint, and the food gripper automatically opened / closed based on position (Velliste et al., 2008).

As part of his doctoral research, Hyun Kim addressed another limitation of robotic output: real-world tasks require a mixture of stiff, position-based control (e.g. writing on paper) and pliant, force-based control (handling an egg); up until this point, all BMIs have been one or the other but not both. His clever solution was to emulate the actual arm through a musculoskeletal model in which the simulated muscles were directly controlled. The experiment showed that a cortical BMI could control both impedance and kinematics simultaneously (Kim et al., 2007); see also Appendix A.1. This work has been elaborated and verified in another laboratory (Fagg et al., 2007).

Far better than a robot or a musculoskeletal model would be to use the patient's arms directly. This is possible through functional electrical stimulation (FES), where muscles are directly electrically stimulated, with control of the current through a simplified BMI. The Fetz laboratory has demonstrated a FES BMI in a simple wrist flexion / extension task (Moritz et al., 2008); as in other BMI studies, this reported that control was robust irrespective if or how the recorded neuron was previously associated with movement.

The final area of optimization is brain area target: while M1 or premotor cortices may be the apparent best source of volitional signals, not all control is motor. The cingulate cortex has been successfully used to demonstrate a BMI (Marzullo et al., 2006), as well as human frontal cortices exposed during DBS surgeries (Ojakangas et al., 2006), suggesting that likely a great many places in the brain can successfully be used to control a BMI, which is in accord with original studies showing that most all parts of the brain can be operantly conditioned.

Several researchers flipped BMI around and used it to investigate motor learning – that is, using the tool to improve our knowledge of the brain and not just to improve the tool. Within the Nicolelis lab, studies show that cortical modulations increase during early BMI control sessions (Zacksenhouse et al., 2007), possibly working like LMAN in songbird vocal learning. Jose Carmena and colleagues repeated training of a BMI across multiple days using a fixed decoder (Ganguly and Carmena, 2009), thereby showing progressive motor learning over the course of weeks, proving that a stable control mapping can be learned (though perhaps not elucidating exactly how this is learned). The group later found evidence supporting internalization of a motor model for BMI control (Ganguly et al., 2011); this model co-existed with that used by the monkey to control its limb normally. By perturbing such an internalized BMI model, further experiments showed that functional reorganization followed a rapid and reversible timecourse, with individual neurons learning reoriented tuning curves within a single training session (Jarosiewicz et al., 2008).

Notably absent from the literature is an investigation of multidimensional operant conditioning, or conditioning of multiple populations for independent, orthogonal control directions. Such a study would avoid the issue that true supervised learning, as used in many recent BMIs, is not possible in the intended target audience of amputees and paralyzed individuals: they want new axes of control, not duplicates of existing axes. More fundamentally, such an experiment would permit watching

the cortex infer what groups of neurons do, and permit observation of how it learns to control sets of neurons (or *if* it can learn arbitrary multidimensional operant control). One would imagine that, as pyramidal tract neurons map semi-directly to muscles, control is learned in the same way that normal motor control is learned: via experimentation and under visual feedback. Some work by the lab supports this hypothesis (Zacksenhouse et al., 2007), but it deserves a more thorough investigation; it could be that the motor cortex learns quickly or employs gradient-descent methods. Earlier work conflates learning with performance, as neurons are regressed against decoded performance instead of the firing profile needed to obtain reward, making it difficult to see what and how the cortex is assigning credit and modifying tuning.

In all these BMI experiments high bit-rate or spatial fidelity has been difficult to achieve. In the last four years of my graduate work it has been my intuition that this is because the supervised-learning models require, effectively, high-dimensional inference of the decoder matrix (or matrices in Kalman filters). Jose Carmena's results (Ganguly and Carmena, 2009) provide evidence to the contrary, but we still haven't seen a reliable, low noise BMI; in the Nicolelis lab, control has a SNR of 6-10 db (3:1 amplitude ratio) at a bandwidth of $\approx$ 2 Hz, equivalent to 3.2-6.4 bits/sec (*).

This rate is too low for a practical prosthesis, as it is only marginally better than surface EMG control from two muscles. I've attempted to attack a number of parameters that affect the quality of control, mainly:

- Training time. Give the monkey unfettered, 24/7 access to the BMI to maximize use and learning.
- Motivation. Provide the BMI in the best environment available to him.
- Number of channels. The recording system scales to and above the total number of electrodes we presently have implanted in one monkey (768).

- Simplicity. The BMI is a tool, hence its transformation matrix should be easily invertible for learning.

The conclusion of these desiderata was the wireless system; but prior that work, deep brain stimulation and microstimulation were investigated, so they will be described first.

(*) For the curious, here is the math for determining the bit-rate of conveyed by one gaussian random process about another in terms of the signal-to-noise ratio between the two. Assume x is the known signal to be predicted, and y is the prediction.

Let's define $SNR(y) = \frac{Var(x)}{Var(err)}$ where $err = x - y$. Note this is a ratio of powers; for the conventional SNR, $SNR_{dB} = 10 * log_{10}\frac{Var(x)}{Var(err)}$. $Var(err)$ is also known as the mean-squared-error (mse).

Now, $Var(err) = \sum (x - y - e\bar{r}r)^2 = Var(x) + Var(y) - 2Cov(x, y)$; assume x and y have unit variance (or scale them so that they do), then

$$\frac{2 - SNR(y)^{-1}}{2} = Cov(x, y)$$

We need the covariance because the mutual information between two jointly Gaussian zero-mean variables can be defined in terms of their covariance matrix. Here Q is the covariance matrix,

$$Q = \begin{bmatrix} Var(x) & Cov(x, y) \\ Cov(x, y) & Var(y) \end{bmatrix}$$

$$MI = \frac{1}{2} log \frac{Var(x)Var(y)}{det(Q)}$$

Table 1.1: Mutual information in terms of SNR

SNR	Amp. ratio	MI (bits)
10	3.1	1.6
20	10	3.3
30	31	5.0
40	100	6.6
90	31e3	15

$$Det(Q) = 1 - Cov(x, y)^2$$

Then

$$MI = -\frac{1}{2} log_2 \left[1 - Cov(x, y)^2\right]$$

or

$$MI = -\frac{1}{2} log_2 \left[SNR(y)^{-1} - \frac{1}{4} SNR(y)^{-2}\right]$$

This agrees with intuition. If we have a SNR of 10db, or 10:1 (power ratio), then we would expect to be able to break a random variable into about 10 different categories or bins (recall stdev is the sqrt of the variance), with the probability of the variable being in the estimated bin to be 1/2. (This, at least in my mind, is where the 1/2 constant comes from - if there is gaussian noise, you won't be able to determine exactly which bin the random variable is in, hence log_2 is an overestimator.)

Here is a table with the respective values, including the amplitude (not power) ratio representations of SNR.

Note that at 90dB, you get about 15 bits of resolution. This makes sense, as 16-bit DACs and ADCs have (typically) 96dB SNR. Good.

Now, to get the bitrate, you take the SNR, calculate the mutual information, and multiply it by the bandwidth (*not* the sampling rate in a discrete time system) of the signals. In our particular application the bandwidth is between 1 and 2 Hz, hence we're getting 1.6-3.2 bits/second/axis, and 3.2-6.4 bits/second for our normal

2D tasks.

1.6 Parkinson's Disease, Essential Tremor, and DBS

Parkinson's disease is a prevalent, idiopathic, progressive neural degenerative disorder which clinically manifests through bradykinesia (slow movements), akinesia (no movement), tremor at rest, muscular rigidity, and abnormal postures or postural instability. Symptoms also may be non-motor, including speech disorders, depression, and dementia (Mink, 1996). Physically, Parkinson's disease is primarily characterized by the death of dopaminergic neurons from the substantia nigra pars compacta (SNpc); symptoms normally do not appear until 50-80% of these neurons have disappeared (Benabid et al., 2009). Death of SNpc neurons is tightly correlated with the presence of α-synuclein immunoreactive Lewy bodies within the nucleus, pathology which later spreads to the remainder of the basal ganglia and into the neocortex (Braak et al., 2003). The mean age of incidence of PD is around 60 years, though 10-15% of patients have much earlier onset due to hereditary[21] (Lohmann et al., 2009) or environmental factors.

Dopmanimergic neurons from the SNpc project to and synapse upon all of the basal ganglia, with a predominant efferent projection to the striatum (the putamen and caudate, split by the internal capsule). The striatum, and basal ganglia in general, are also intimately involved in the etiology of Huntington's disease, in which medium striatal neurons (MSN), neurons which project from the striatum to globus pallidus, are lost. Symptoms of Huntington's disease are nearly opposite that of PD: chorea (dance-like movement that mimic voluntary purposeful movements), dyskinesia (uncontrolled and short-duration movements), tics, and dementia (Mink, 1996). As the basal ganglia are critical for understanding and treating these diseases,

[21] Within the Amish population in the northeastern United States, the incidence of PD is three times the national average

their anatomy and structure will be first reviewed, followed by their still-contentious normal and pathological function .

1.6.1 Anatomy of the Basal Ganglia

The basic anatomy of the basal ganglia is shown in figure 1.8. The striatum is the primary input to the BG, and consists of the cytoarchitecturally similar caudate and putamen. These have neurons which project to the internal and external segments of the globus pallidus, GPi and GPe respectively[22]. The GPi and substantia nigra pars reticulata (SNr), despite the two names, are structurally very similar, and constitute the output nuclei of the BG. They send inhibitory GABA-ergic axons to the thalamus, superior colliculus, and pedunculopontine nucleus of the brainstem, and thereby effect motor behavior, albeit indirectly. The projection from striatum to GPi is classically called the 'direct' pathway, and second 'indirect' pathway exists from the striatum, through the GPe, subthalamic nucleus (STN), and then to the output GPi/SNr (Parent and Hazrati, 1995b).

The classical direct/indirect pathway leads to a neat explanation for the primary symptoms of Parkinson's disease (rigidity, bradykinesia, akinesia) in terms of rate modulations in the involved structures. Figure 1.9 shows this hypothesis graphically.

As shown in the figure, a loss of dopaminergic afferent to the striatum leads to decreased firing in GPi projections, and increased firing in the GPe projections. This in turn decreases GPe activity, and increases GPi/SNr inhibitory output, thereby inhibiting the cortex through the centromedian, ventral anterior and ventrolateral thalamic relays, and hence inhibiting motor behavior. In Huntington's disease the signs of these changes are reversed: loss of medium striatal neurons leads to increased pallidal activity and decreased excitation of the STN, leading to less GPI/SNr

[22] In older literature these are referred to the MPS (medial pallidal segment) or MGP (medial globus pallidus) for the GPi and LPS/LGP for the GPe (Penney and Young, 1983)

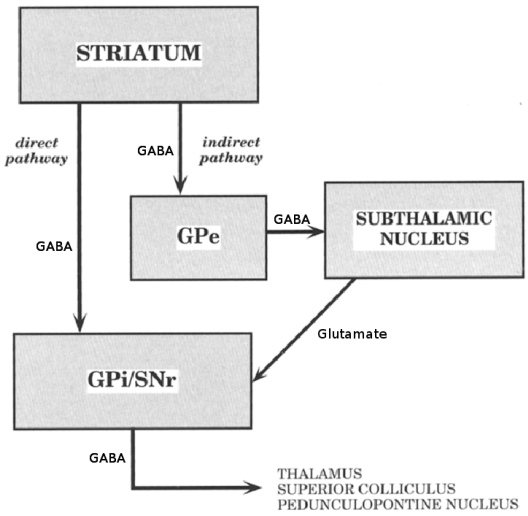

FIGURE 1.8: Simplified schematic of the basal ganglia. From (Parent and Hazrati, 1995b).

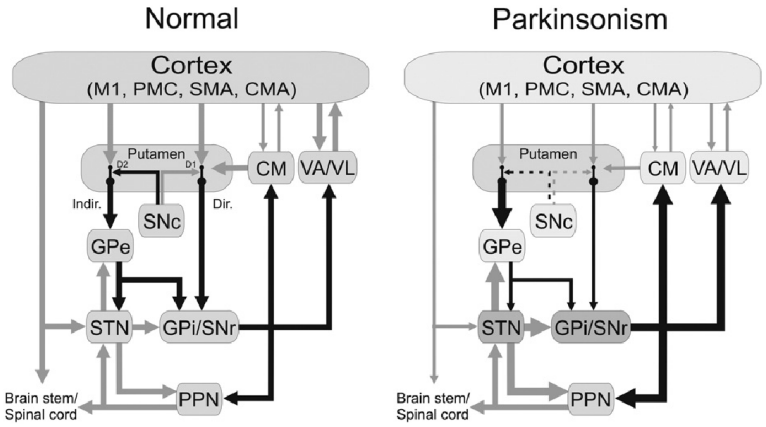

FIGURE 1.9: Rate modulations in Parkinson's disease. Gray arrows are excitatory (glutamate), black arrows are inhibitory (GABA). From (Wichmann and Dostrovsky, 2011).

GABAergic inhibition of VA/VL, and ultimately exposing thalamic neurons to respond indiscriminately to all sorts of inputs and hence leading to hyperkinesia.

The classical direct/indirect pathway, while terse and effective in its ability to explain some features of Parkinson's and Huntington's disease, has limited anatomical and functional support. Most glaringly, STN inputs from the GPe spare regions

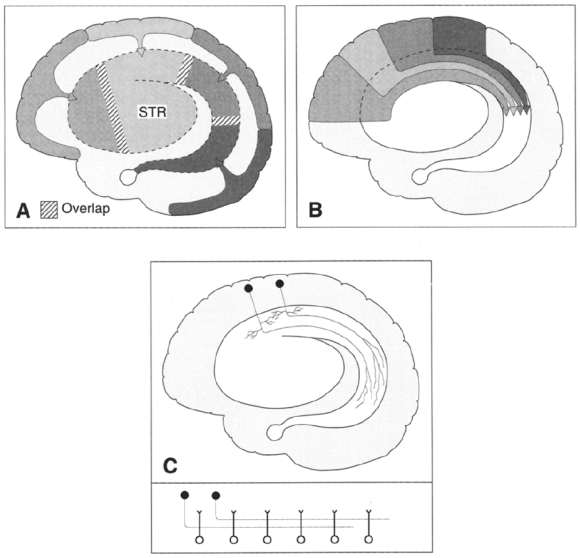

FIGURE 1.10: Diagram of striatal projections. A, original overlapping-subdomian hypothesis. B, modern hypothesis, where projections from cortex form non-overlapping parasagitally elongated domains in the caudate and putamen. C, simplified diagram of cortical projection axons. From (Parent and Hazrati, 1995a).

projecting to the GPi/SNr; they constitute separate, parallel, pathways (Parent and Hazrati, 1995b). Furthermore, the hypothesis ignores the complexity, precise organization, and presence of multiple feedback loops in the basal ganglia, to be overviewed below.

As mentioned above, the striatum consists primarily (95%) of medium spiny neurons; these neurons are exclusively GABAergic (Mink, 1996). The dendritic fields of MSNs lie in semi-coronal parallel planes at right angles to the incoming massive cortical afferents, similar to the structure seen in the cerebellum; these cortical afferents are partially collaterals from the pyramidal tract. Excepting primary visual and auditory cortex, nearly all of the cerebral cortex projects into the striatum, with the incoming axons synapsing a relatively few times onto many MSNs in passage (Parent and Hazrati, 1995a). See Figure 1.10 for a diagram.

The vast reduction in neuron numbers from the cortex to the striatum – between 40:1 and 100:1 in mammals (Morris et al., 2003) – has lead to suppositions that

there is overlap or recombination between multiple projection domains, possibly as a means of merging disparate information sources from the cortex and forming novel representations thereof. In fact, the actual projection is discrete and patchy, with association, sensorimotor, and limbic cortical areas projecting in a segregated manner onto at least three different distinct striatal regions. In cortical regions of close functional similarity, namely the frontal and supplementary eye fields, projection domains may be interdigitated but do not mix (Parent and Hazrati, 1995a).

The striatum itself is not homogeneous, but consists of regions heavily and lightly stained for acetylcholine, corresponding to the striosomes and matrix, respectively. Approximately 2% of striatal neurons are large aspiny neurons, which appear to be interneurons that use acetylcholine as their neurotransmitter. Medium spiny neurons are bistable, and can switch between hyperpolarized (-80 mV) and polarized (-50 mV) states (Wilson and Kawaguchi, 1996); this bistability seems to be mediated by the large aspiny cholinergic neurons in the striosomes (Mink, 1996), although dopaminergic control has not been ruled out. Striosomes and the surrounding matrix receive differential projection from the cortex: cortico-striatal neurons in the infragranular layers (V-VI) project principally to striosomes, while supragranular (I-IV) axons project to the matrix. Single cortical regions project to multiple striosomes, as labeled by anterograde tracers, but these multiple modules can send afferents to single sites in both the GPe and GPi (Flaherty and Graybiel, 1994). Projections from the thalamus, mainly the centromedian / parafasicular nuclei, synapse onto morphologically distinct synapses from those of cortical afferents. Finally, individual MSN receive axon collaterals from neighboring MSNs, as well as nitric oxide releasing interneurons (Parent and Hazrati, 1995a). See Figure 1.11.

Dopamine within the striatum plays a pivotal role in supporting normal neural activity, synaptic plasticity (Prescott et al., 2009), and motor learning (Lehericy et al., 2005), though understanding of the last remains incomplete. There are two

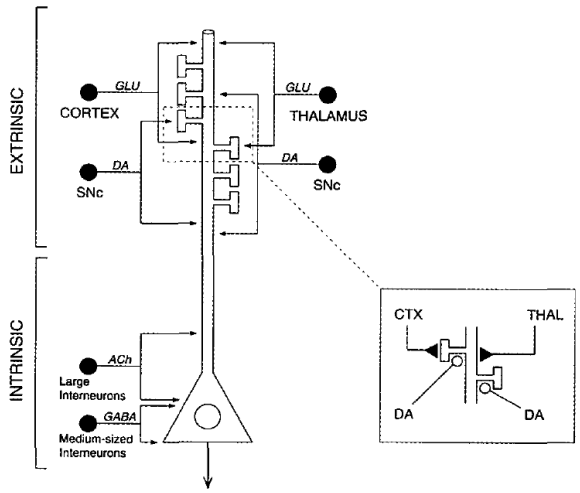

FIGURE 1.11: Diagram of afferents to a medium spiny neuron in the striatum. From (Parent and Hazrati, 1995a).

classes of dopamine receptors in the striatum, D1 and D2, and they appear to both be involved in LTD; in contrast LTP is D1 dependent, and is enhanced by the block of D2 receptors (Centonze et al., 2001). Synaptic plasticity appears to be mediated through NMDA receptors, with dopamine and glutamate receptors highly colocalized (Ariano et al., 1997), though dopamine cannot directly depolarize the cells (Calabresi et al., 2000). Furthermore, cortico-striatal synapses have spike-timing dependent plasticity (STDP) which is also gated by dopamine (Pawlak and Kerr, 2008).

Nitrous oxide, enkephalin, dynorphin, substance P, and other signaling molecules have strong and specific roles as well in the striatum. Dynorphin is expressed in the direct (GPi) pathway along with the D1 receptor and is involved in behavioral sensitization; enkephalin in expressed in striatal matrix neurons along the indirect (GPe) pathway, is colocalized with D2 receptors, and has been indirectly linked to recovery of motor function (Albin et al., 1989; Steiner and Gerfen, 1998). Matrix neurons expressing substance P project mainly on GPi or SNr, while striosome neurons expressing the same neuropeptide project to the SNpc.

Efferents from striatum are anatomically highly organized and layered as well.

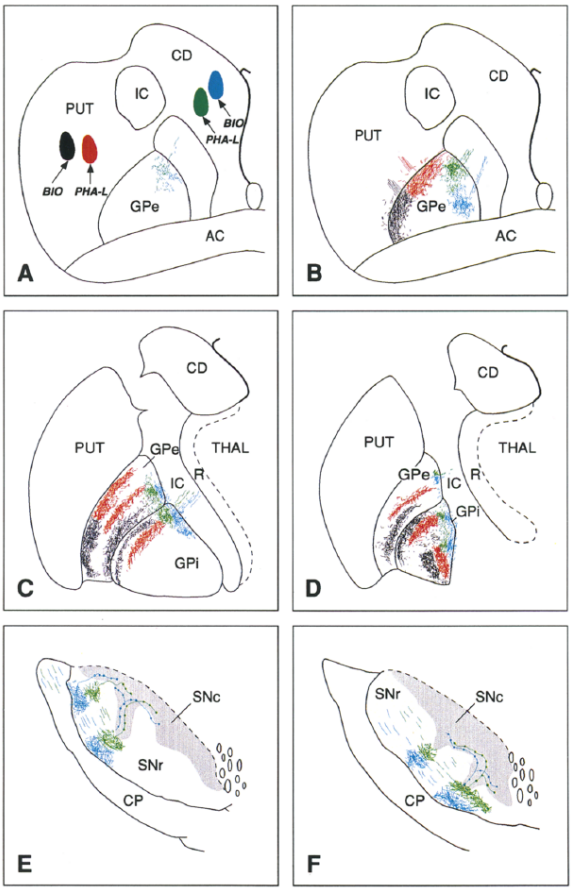

FIGURE 1.12: Diagram of striatal projections derived from computerized camera lucida drawings. A, anterograde injection sites. B C D, labeled projections in the pallidus, moving rostral to caudal. E F, labeled projections in the substantia nigra showing broad axonal arborization in the pars reticulata, and varicosities within the pars compacta. For more detail see (Parent and Hazrati, 1995a).

Much like their input, projections impinge at right-angles to parallel dendritic planes within the palladium. For yet unclear reasons, single labeled regions of the striatum arborize *twice* upon target structures in the globus pallidus and substantia nigra in longitudinally oriented terminal fields that cover nearly the entire rostrocaudal extent of the structures – see Figure 1.12.

Within the GPi and SNr, structures that are cytoarchitecturally the same but are split by the internal medulary lamina, striatal afferents form wooly fibers on neurons there, again in a tightly organized rostral-caudal sequence. Within the SNr, these

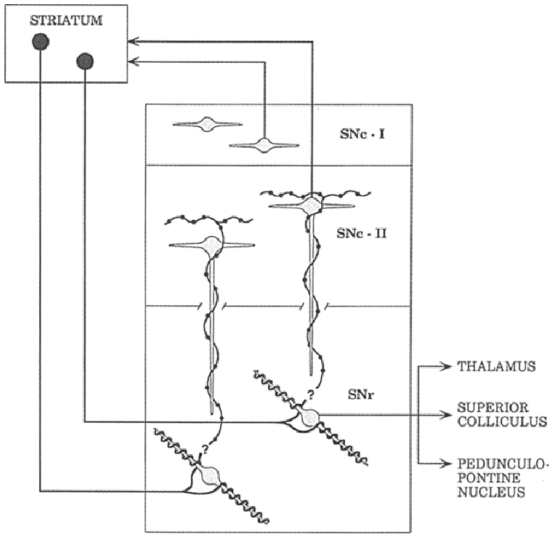

FIGURE 1.13: Wooly fibers and climbing fibers within the SNr. The former are shown encircling proximal dendrites at the bottom, the latter ascending to compacta cells in the middle. All neurons are inhibitory, GABAergic. For more detail see (Parent and Hazrati, 1995a).

axon collaterals form climbing fibers – again much like in the cerebellum – which impinge upon dopaminergic neurons within a subsection of the SNpc, as depicted in figure 1.13. In the Gpi, striatal fibers form wooly fibers twice, and in distinct populations from corresponding GPe neurons, as shown in Figure 1.14. In this way striatal regions may directly and indirectly effect four groups of GPi output neurons. This distinct nature of the projections strongly weigh against simplified 'direct' and 'indirect' pathways (Parent and Hazrati, 1995b).

The GPi/SNr, in turn, sends inhibitory GABAergic axons to the ventrolateral / ventral anterior motor thalamus and to the brainstem, both ipsi- and contralateral, with about 70% of these collateralized to at least two areas. In the brainstem, collaterals project to the pons adjacent and within to the pedunculopontine nucleus, and in turn to the reticulospinal or extrapyramidal motor system (Mink, 1996). Further BG collaterals innervate the centromedian / parafasicular nuclei of the thalamus, which project back to the striatum (and not to the cortex), or back to the SNpc

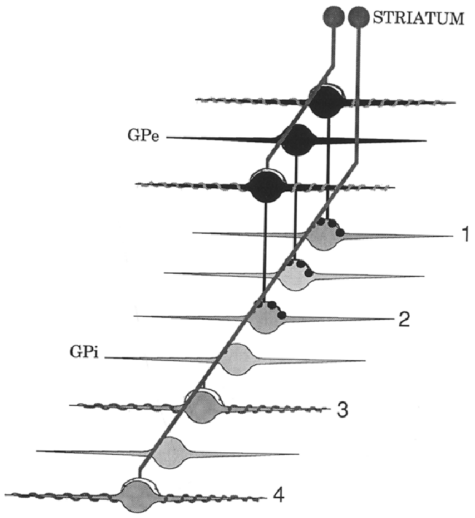

FIGURE 1.14: Schematic representation of afferents in the GPi. Striatal axons arborize twice in both GPe (black cells) and GPi (gray cells); GPe cells in turn synapse upon GPi cells rostrocaudally distinct from those targeted by striatal cells from the same region. From (Parent and Hazrati, 1995b).

(Parent and Hazrati, 1995a).

The Subthalamic Nucleus

The final, and pivotal, region within the basal ganglia is the subthalamic nucleus. As it has proven to be a very effective target for DBS treatment, the STN has been subject to intense study for the past two decades. The region is conserved in mammals, though functionally different in primates, as only in primates does the STN receive direct cortical afferents and pyramidal collaterals (Georgopoulos et al., 1983). Furthermore, in primates the many projections to GPi, GPe, and SNr are more distinct and segregated; in rodents, these projections are highly collateralized (Parent and Hazrati, 1995b), though this anatomical finding remains disputed (Levesque and Parent, 2005). In the rat the STN is small hence difficult to study, only 25,000 neurons, whereas in humans it numbers around 500,000 (Florio et al., 2001). These neurons are almost completely excitatory, glutamergic projection neurons, with very few inhibitory interneurons in the nucleus itself. STN neurons arborize in laminar planes

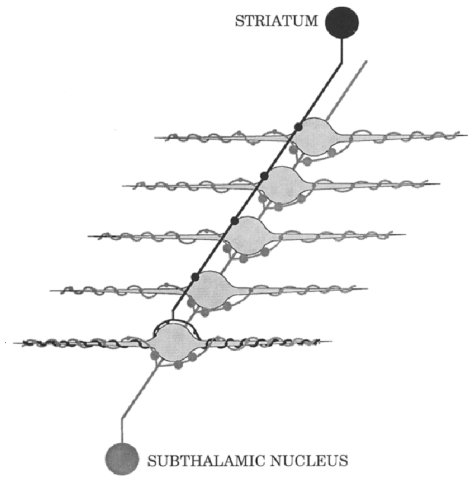

FIGURE 1.15: Schematic representation of STN projections to GPe, showing breadth and strength of projection. From (Parent and Hazrati, 1995b).

in the pallidus, parallel to and in register with striatal inputs, on both the internal and external segments (Carpenter et al., 1981). Projections to GPe are particularly broad, which the STN is reciprocally connected to, allowing activation of large populations of pallidal neurons –see Figure 1.15. GPe reciprocally projects collaterals to STN, organized in rostrocaudal arrays, with strong GABAergic synapses on proximal dendrites that are capable of driving rebound excitation (Bevan et al., 2002). There is a consistent functional organization in this reciprocity: interconnected neurons in the subthalamic nucleus and GPe innervate the same neurons in GPi (Shink et al., 1996). Anterograde tracing finds few if any projections from GPi to STN, however (Carpenter et al., 1981).

In primates the dorsolateral subthalamic nucleus recieves extensive afferents from M1, premotor corticies (SMA, PMd/v) (Monakow et al., 1978), FEF (Hamani et al., 2004), relatively few (if any) projections from postcentral / S1 (Wichmann and Dostrovsky, 2011), along with proprioceptive input (DeLong et al., 1985). The STN is somatotopically organized, with at least two functional divisions rostral/caudal: dorsal STN corresponds to movement and motor function, whereas rostral STN cor-

responds to associative and limbic function (DeLong et al., 1985). Ventromedial STN receives topographic afferents from the frontal and supplementary eye fields (Parent and Hazrati, 1995b). Somatotopy in both regions is partially destroyed in PD, with receptive fields becoming more bilateral (Hamani et al., 2004).

Synthesis

The anatomy of the basal ganglia is far richer, more nuanced, and *organized* than simplistic box-and-arrow models may suppose. Of particular note are the crystal-like parallel dendritic planes and perpendicular axons in both the striatum and pallidus, the prevalence and importance of collaterals in nearly all the structures (Parent et al., 2000), the multiple parallel pathways in the striosomes / matrix or dual projections into the pallidus, and the high degrees of asymmetry in synaptic strength between woolly, climbing fiber, and varicose arborizations. Any model or understanding of how the basal ganglia functions normally and in Parkinson's disease should take into account this anatomical complexity; box-and-arrow propagation of sign models do not suffice.

1.6.2 Physiology of the Basal Ganglia

In accord its role in the pathology of motor diseases, the basal ganglia is known to be tightly involved in motor behavior; however, the extent and nature of that role is still an active area of research. As with anatomy, regions will be addressed in approximate synaptic order.

Cells within the striatum have a low static firing rate of 0 - 1 Hz (Crutcher and DeLong, 1984a), and as mentioned can switch between hyperpolarized and polarized states depending on interneurons and convergent cortical input (Mink, 1996). While both muscle, load, sensory, and proprioceptive modulations have been observed in the firing rates of striatal cells, more cells are related to the direction of movement

than muscle activation when force and movement direction were dissociated in an arm task (Delong et al., 1984). This is consistent with timing, too: cells in the striatum fire both before and *after* M1 and EMG activity, or are driven by sensory input (Crutcher and DeLong, 1984b). Recordings from the striatum have found a variety of firing profiles, with proportions of cells firing before, during, and after a cue in a delayed-cue task (Romo et al., 1992). In a spontaneous movement task, a largely disjoint group of cells (to those responding in the cued task) was found to increase activity 0.5-5 s before movement. Other cells were found to have sustained preparatory activity for up to 80 s in a delayed go / nogo task; yet others responded to task cue, independent of modality; others only responded only if sensory input was in the context of a movement (Schultz and Romo, 1992). Cholinergic interneurons (large aspiny) fire in response to sensory cues as well, with a relatively constant firing rate of 3-6 Hz, but have no relation to movement (Mink, 1996).

The heterogeneity of responses, with correlations to both motor and cognitive features, does not lead to a clear role of the striatum; proposed theories include computing the behavioral contingencies of reward (Hollerman et al., 2000), the scaling of force and velocity (Turner and Desmurget, 2010), or the selection and sequencing of competing motor programs (Mink, 1996). The last is supported by long-train microstimulation to the striatum. Whereas short train stimulation occasionally induces myclonus, longer bouts of microstimulation to the posterior striatum induces complex, abnormal behavior: finger licking and biting, dyskinesias, and grooming; more anterior (putative associative regions) results in hyper or hypomanic or stereotyped behaviors (Worbe et al., 2011).

Timing evidence suggests that the striatum does not play a role in the early phases of a movement, which is consistent with cooling studies, kainic acid lesions, and microstimulation. Furthermore, the striatum does not seem to receive spindle afferents; proprioceptive information as seen in response to passive movement seems

largely relative to joint angle (Crutcher and DeLong, 1984a).

In comparison to the striatum, cells in the globus pallidus have a higher tonic firing rate of 80-100 Hz and can both increase and decrease firing rate in relation to movement (Georgopoulos et al., 1983). Within the GPe most cells show high firing rate with frequent long pauses, while a smaller subset of neurons have a lower mean firing rate interrupted by very high frequency bursts. Cells within the GPi all show a high mean firing rate with shorter pauses and infrequent bursts. These pauses are presumably effected by inhibitory striatal input. Somatotopy is mixed within both structures, with a relatively higher representation of proximal muscles and movement, not muscle activation (Delong et al., 1984). As in the motor cortex, there have been found linear relationships between movement direction and distance, though in the pallidus tuning is not nearly as deep (Georgopoulos et al., 1983). Other studies have found the relation of pallidal discharge to specific muscles and single joints, both contralateral and ipsilateral (Iansek and Porter, 1980). Passive response to movement is evident in both segments of the pallidus, again mostly relative to a single joint and not muscle spindle afferent (DeLong et al., 1985) or touch (Iansek and Porter, 1980).

The substantia nigra pars reticulata is the sister output nucleus of the GPi, with similar cell properties and firing rates. One third of all cells there are related to visually-evoked saccades, with no response to saccades in the dark (Hikosaka and Wurtz, 1983a); a further third of cells there responded to saccades to remembered target location (Hikosaka and Wurtz, 1983c), and a fraction of the remainder responded to auditory and sensory cues (Hikosaka and Wurtz, 1983b). The SNr projects inhibitory afferents to the superior colliculus, hence decreased SNr discharge results in disinhibitition in the SC and initiation of saccades. The region has also been implicated in simultaneous head orienting (neck muscle) movements (Mink, 1996).

The STN, with its broad connectivity within the BG, has a variety of cell response

types. Cells are tonically active, with a resting rate of 20 Hz, and predominantly increase firing rate with respect to arm or leg movement (Wichmann et al., 1994). As mentioned above, these motor-related cells are located in the dorsolateral STN, while the ventromedial thalamus is associative and oculomotor, with a smaller region dedicated to limbic function (Parent and Hazrati, 1995b). In the dorsolateral STN there is a somatotopic representation of motor space, with the lower extremity dorsal and face / eyes ventral. In accord with strong motor cortex afferent, movement-related response is much stronger in the STN than the pallidus, with approximately half to three quarters of recorded neurons correlated to movement direction, amplitude, and peak velocity (Georgopoulos et al., 1983), and with a preponderance of proximal muscle representation (Wichmann et al., 1994). Unlike neurons in the striatum and pallidus, subthalamic cells respond strongly to muscle palpitation. As mentioned, there are few if any interneurons in the STN, and cells in normal subjects show a low degree of cross-correlation (Wichmann et al., 1994).

The exact function of the STN, especially given it's role in treatment, is still under debate. When the STN humans or other primates is lesioned, either experimentally or through stroke, violent hemiballismus results (involuntary, stereotyped large-amplitude movements limited to one side of the body) (Florio et al., 2001; Lee et al., 2005). Other effects of infarction of the STN include agitation, manic behavior, and logorrhoea (incoherent talkativeness) (Rodriguez-Oroz et al., 2011). This severe behavior gradually decreases with time, suggesting that plasticity or learning compensates for the loss of excitatory GP input (Guridi and Obeso, 2001). Hemibalismus is illuminating on the strength and nature of synaptic innervation of GPe/GPi: while 48% of STN axons are collateralized to both GPi/GPe, and 21% to GPe, GPi, and SNr (Hamani et al., 2004), the relative exitatory influence on GPi must be greater, since loss of excitation will decrease GPi firing, leaving the motor thalamus disinhibited. Were the primary effect to be in the GPe, decreased inhibitory GPe activity

would disinhibit GPi, inhibiting motor thalamus, at least according to a rate model.

Of particular note is the strong reciprocal connection of GPe to the STN (Shink et al., 1996); not only do pallidal cells oscillate spontaneously when isolated in vitro due to membrane properties (Bevan et al., 2002), but models have shown that this tight loop is particularly prone to oscillation (Holgado et al., 2010). Oscillations, and their relationship to tremor and other symptoms of PD, will be discussed further below.

Function of the Basal Ganglia

An understanding of the normal function of the basal ganglia is useful if not vital to understand the pathology of Parkinson's disease, Huntington's disease, and others. While there has been a long line of research on the BG, no one definitive theory has adequately explained all (or even most) functions, either normally nor pathologically. This difficulty may be traced to the confusing and obscuring aspects of the disorganization resulting from disease, and the necessary bias for recording from PD patients and not normal humans (Mink, 1996).

S. A. Kinnier Wilson is credited with being of the first to realize the link between pathology of the BG (as opposed to the corticospinal system) and dysfunction in PD, HD, and other movement disorders, and hence the basal ganglia's normal role in the command and control of movement. He hypothesized that movement disorders in HD were the result of the cortex responding without discrimination to afferent input (Kinnier wilson, 1925) – that is, the cortex serves as a very general-purpose associative memory, and the basal ganglia keeps the vast spread of auto-associations from reacting blindly to the sensory world. In the intervening 90 years, this hypothesis not been disproved, though the theory has been elaborated and morphed by new data. In Kinnier's day it was thought that the pyramidal system was inherently plastic, whereas the extrapryramidal system was static and archaic; yet now it seems that

BG is critical in guiding learning.

The most common, and perhaps best supported, theory behind basal ganglia function is that it serves to select one from many competing motor programs (Mink, 1996). This is consistent with the gross, common symptoms of PD and HD – inability to initiate movements in PD, and inability to inhibit chorea in HD, and the fact that some movement disorders can be controlled by selective sensory input (Albin et al., 1989). The theory takes into account several salient features of the basal ganglia, namely the highly convergent projections from cortex → striatum → pallidus, which can be used to compute behavioral contingencies to determine which motor programs to enable; such contingencies are seen in the context-dependent sensory responses seen in the striatum. In this motor-selection theory the direct pathway is used to disinhibit desired movement, and the indirect pathway to inhibit competing programs and control the direct pathway (Shink et al., 1996). A malfunction of inhibition is particularly apparent in micrograpahia, where PD patients' handwriting becomes progressively smaller during the course of writing, presumably due to competition from alternative letters, words, and sentences (Mink, 1996). It also seems consistent with ataxia due to rigidity, as PD patients are unable to inhibit long-latency (cortical loop) stretch reflexes following instruction, unlike normal controls (Berardelli et al., 1983).

The motor selection theory suffers from a number of counterfactual evidence, much like almost every other theory surrounding the BG. Lesions of the GPi improve dyskinesias without inducing hemibalismus, with minimal effects on motor function in PD patients (Brown, 2003); they remain an effective surgical treatment for the disease. Secondly, changes in pallidal activity mostly lag *behind* movement initiation (Israel and Bergman, 2008). Thirdly, paradoxical kinesis – a surprising ability to move following sensory impetus, as seen with encephalitis lethargica patients in Oliver Sacks' Awakenings, and generally seen as indicative of inhibition

malfunction – appears to be a general property of the motor system, and is largely unchanged in PD (Ballanger et al., 2006).

One overriding feature of the BG is the strong convergence / divergence (Morris et al., 2003), which with the advent of new computational learning theories and data showing dopamine looks like an ideal error-reinforcement signal (Hollerman et al., 2000), led to the idea that the BG performs reinforcement driven dimensionality reduction (RDDR) (Bar-Gad et al., 2003). In reinforcement learning, an animal or 'agent' progressively learns the value of actions contingent on 'state' based on a scalar, episodic reward signal (Barto and Sutton, 1998). There is substantial and growing evidence that the BG implements a form of reinforcement-learning, especially the the anterior forebrain pathway (AFP) in songbirds, which is a homolog of the BG. Data from mammals is less clear, but growing: striatal neurons change response prior cortical neurons in a learning task, and the degree of striatal firing variance is correlated with performance in a reinforcement-learning task (Graybiel, 2005). Furthermore, dopamine regulates the impact of the cerebral cortex on the subthalamic nucleus-globus pallidus network (Magill et al., 2001), as would be required by the theory. Note this is not dissimilar to the motor selection, as reinforcement learning inherently involves selection of actions based on value and salience, as verified in numerical models of the BG e.g. (Prescott et al., 2006).

Some have extended/reinterpreted reinforcement learning to mean dopamine modulates model complexity (Parush et al., 2011) – that is, dopamine organizes actions by controlling the tradeoff between reward gain and behavioral cost. If the dopamine disappears, this model would imply that the basal ganglia becomes randomly organized (Heimer et al., 2006), which is consistent with both the literature and our own data.

Another salient feature is that Parkinson's patients have difficulty with long, complex movements (Brown, 2003), and are prone to repetitive, habitual actions

following levodopa treatment, which is more consistent with *sequencing* than selection. The BG role as a behavior sequencer is plausible, except that evidence weighs against habits residing in the striatum or other BG structures: when monkeys were overtrained on a repetitive task and tested with both random and stereotyped movements, the kinematics but not habits of movement were effected by MPTP lesion (Desmurget and Turner, 2010).

The basal ganglia's consistent role in learning and scaling led to a final theory that it serves as a 'vigorous tutor' (Turner and Desmurget, 2010). This is somewhat a superset of reinforcement learning, as intensity scaling is both an essential feature of motor control (how far do you want to throw the stick, jump etc.), and when applied to broader behavioral or cognitive strategies, supports preference scaling and selection[23]. It is also consistent with the nature of BG dysfunction – problems occur not when the output structures are lesioned (indeed, this is therapeutic), but when the striatal input or *learning* structure begins to fail (Turner and Desmurget, 2010).

The theory explains several consistent features of GPi lesion: unchanged reaction time (the BG is not involved in movement selection), unchanged on-line error correction (this must be cortical), unchanged habitual motor actions (habit does not have substrate in the BG), but consistent movement velocity and acceleration reduction, without changes in linearity or direction. Bradykinesia /akinesia is, after all, a primary symptom of PD. Micrographia is also neatly explained – rather than having many competing actions as above, the action gain simply goes down. It is also consistent with a hallmark feature of PD, inability to voluntarily control grip force or reflex scaling, as discussed in the "Piper Rhythm" section below. Finally, pallidotomy is associated with an impaired ability to learn new stimuli sequences

[23] This argument sounds unfortunately broad, like saying that multiplication and addition can support all arithmetic.

(Brown et al., 2003) and probabilistic classification learning (Sage et al., 2003). This is confirmed in a patient with surgical lesion of both STN and GPi, effectively eliminating all output of the BG; the only clear deficit was the complete inability to learn implicit sequences (Obeso et al., 2009).

1.6.3 Pathophysiology of the Basal Ganglia in PD

Classical hypotheses place Parkinson's and Huntington's disease on opposite ends of basal ganglia dysfunction. In hyperkinetic disorders, such as HD, chorea (dance-like movements) and atheosis (writhing-like movements) are supressed by D2 receptor antagonists and exacerbated by dopamine agonists. Early HD, when chorea is most prominent, is characterized by a selective loss of enkephalin-staining neurons projecting to the GPe. In the rate model, this corresponds to a relative increase in GPe firing, inhibiting GPI/SNR neurons, disinhibiting motor thalamus and cortex. Hypokinetic disorders, primarily Parkinson's disease, are exacerbated by D2 receptor antagonists and ameliorated by DA agonists as well as anti-cholinergics. Here the rate model posits that GPi/SNr firing increases due to disinhibition from D1/substance P striatal projections (Farshchi et al., 2006). The rate model is also consistent with recording from dystonia patients, where it was found that GPi firing rate was inversely correlated with dystonia severity (Starr et al., 2005).

Though several rate models have been proposed over the years, they all seem to suffer from contradictory experimental evidence. Perhaps most damning, thalamotomy does not result in worsening of Parkinsonism, as would be expected if enhanced GPi/SNr inhibition was the root cause of akinesia/bradykinesia in PD. Likewise, GPi lesions *do* cause bradykinesia in normal monkeys, despite the loss of inhibitory output. Clinical pallidotomy has been shown to be primarily effective in alleviating l-dopa induced dyskinesias (in this case involuntary movements, like tic or chorea) – again exactly the opposite of what the model would predict (Israel and

Bergman, 2008). As would be expected from HD above, GPe lesion should cause hypokinetic disorders – but it does not (Wichmann and Dostrovsky, 2011).

Examination of firing rate changes are confounded by the fact that they very based on subject awareness and arousal, and in the case of intraoperative recording, anesthesia and other drugs (Wichmann and Dostrovsky, 2011). We have observed this effect in our patients, as seen in Figure 2.5. Further negative evidence comes from data showing synchrony can increase by a factor of 100 in the pallidus of animal models of PD, while the firing rate itself decreases only slightly (Mallet et al., 2008a).

The failure of any rate models to explain all or most clinically observed data, and growing evidence for markedly increased levels of synchrony and oscillations in PD, led to suppositions that these were correlative or causative of pathology.

Synchrony & Oscillations

Synchrony and oscillations in the basal ganglia are both prevalent and heavily studied in relation to PD, yet despite the intense scrutiny, a scientific consensus as to their cause, significance, and role has yet to be reached. For the purposes of discussion, researchers have co-opted the frequency bands of EEG for discussion of LFP oscillations found within PD patients and models, which are: theta 4-8Hz, alpha 8-13Hz, beta 13-30Hz, gamma => 30Hz. Adherence to these bands is loose and supplemented with actual frequencies where appropriate. What follows is a review of *some* of the conflicting evidence regarding synchrony and oscillations in PD, with as much organization as can be managed – a full review is impossible, as there are literally thousands of papers (with at least 260 reports on PD back in 2004 (Benabid et al., 2005)), and collating reams of contradictory evidence is difficult.

One prominent theory behind oscillations in the basal ganglia is that, when broken into two ranges $> 30Hz$ and $< 30Hz$, the two are inversely affected by both movement and dopmaine treatment, with $< 30Hz$ decreased by movement and levodopa

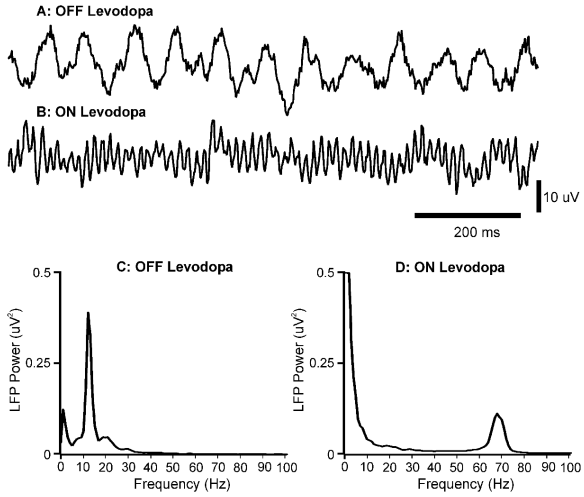

FIGURE 1.16: Oscillations in the BG in ON and OFF conditions. A,B: raw LFP traces. C,D: power spectral density of the LFP. From (Wichmann and Dostrovsky, 2011).

and $> 30Hz$ increased (Brown, 2003). See figure 1.16 for example data showing the strong effect of levodopa on BG LFP[24]. This effect has been confirmed in MPTP (1-methyl-4-phenyl-1,2,3,6-tetrahydropyridine) lesioned monkeys, where administration of this potent dopamine neuron targeting neurotoxin causes intermittent tremor band (theta) and double tremor band (alpha) oscillations in both the basal ganglia and motor cortex (Bergman et al., 1994; Raz et al., 2000).

With DBS, the dominant EMG frequency shifts from $\approx 12Hz$ to 40 Hz, as in the Piper rhythm, leading Cassim et. al. (2002) to suggest DBS treatment is consistent with the low-high frequency hypothesis. The "low-frequency system" would impair movement, and would be blocked either by dopaminergic stimulation or focal destruction of GPI or STN, thus explaining the good results of pallidotomy. The "high-frequency system" would promote movement, oscillations would be involved in keeping "sumbolic movements" active (as in the temporal binding hypothesis), and would be artificially enhanced by high frequency stimulation of either nucleus (Cassim et al., 2002).

[24] In at least some patients

Litvak et. al. (2011) got conflicting results – dopaminergic medication modulated the resting beta network, by *increasing* beta coherence between the subthalamic region and prefrontal cortex. They found that higher frequency oscillations ¿ 45Hz in the STN LFP were not consistent with a cortical source, and cortical oscillations were only weakly modulated by ON and OFF medication conditions (Litvak et al., 2011). This might have been because the patients were at rest – not moving – and beta band coupling between STN and CTX drops before and during movement (Cassidy et al., 2002), though this study did support some effect of medication on changes in oscillation frequency. Others have found differences in ON drug side-effects depending on STN LFP frequency and coherence: those with impulse control problems had primarily theta-alpha activity (mean 6 Hz) coherent with frontal regions, those with dyskinesias (mean 8 Hz) coherent with motor cortex (Rodriguez-Oroz et al., 2011), though this remains unverified.

Despite this EEG-LFP coherence data, beta oscillations are resolved by ablation of the cortex (Cassim et al., 2002), in both normal and 6-OHDA lesioned rats, suggesting that GPe-STN is *not* an inherent oscillator. This concurs with slice studies showing that STN neurons themselves do not exhibit the broad synchrony or oscillations supposed in pathology [25](Wilson et al., 2006). Further support for cortical-sourced oscillations comes from the observation that STN neurons primarily fire in the positive phases of cortical EEG (Cassim et al., 2002). On the other hand, modeling studies indicate GPe-STN is capable of robust oscillations across a broad range of synaptic connectivity strengths (Holgado et al., 2010) and other rat 6-OHDA models indicate that oscillations become hardwired and independent of brain state hence capable of driving activity in the rest of the BG (Mallet et al., 2008a).

Coherence between cortex and STN is exaggerated in Parkinson's disease (Sharott et al., 2005). This seems to be the result of neuroplasticity, as in rats it takes > 4

[25] Though, this is slice – Chapter 2 presents the opposite result in humans.

days for beta oscillations to appear following excitotoxic leasion; acute disruption of D1/D2 activity with antagonists does not enhance cortical or STN beta oscillations (Mallet et al., 2008b). However, in an inducible and reversible dopamine enhancement or depletion via dopamine transport (DAT) knockout mouse, dopamine withdrawal induced an immediate increase in synchrony and change in LFP power spectrum, and increased dopamine induced hyperkinesia concomitant with decreased synchrony (Costa et al., 2006).

In monkeys exposed to chronic and progressive dopamine depletion, synchronized oscillatory activity only emerged late in the experiment, as occurs in the normal progression of PD. Early in the depletion process, inhibitory responses in the pallidium disappeared, concomitant with bradykinesia; only later in the disease, when bradykinesia was severe, did exaggerated beta-frequency oscillations occur (Leblois et al., 2007), implying that the oscillations are sequelae of a failure in plasticity and not causal of motor symptoms; the more likely culprit is the lack of proper motor coding. This is consistent with D1/D2 antagonist results, but not the DAT knockout mouse, above.

Synchrony and burst discharge in STN and GPi increases following administration of dopamine-agonist apomorphine (APO), which implies that synchrony is an *anti-pathological* state. As expected, APO *decreases* limb tremor, but it also decreased the proportion of cells in both nuclei responding to active, passive, and tremorous limb movements, which is counter the reduction in dyskinesia (Levy et al., 2001).

Synchrony seems correlated or involved in tremor, too. Synchronized high-frequency oscillations, 15-30Hz, between individual STN neurons were observed in 28 out of 37 pairs in five patients who had tremor in the operating room and none of 45 pairs in three patients who did not; this is in accord with out findings in chapter 2, where all cells synchronous to at least one other neuron were also co-modulated with tremor. In comparison to the APO result of the preceding paragraph, dopamine

treatment also supressed LFP HFOs, synchrony between STN neuron pairs, and synchrony between tremor cells; movement also decreased synchrony between STN pairs (Levy et al., 2002).

Intuitively, synchrony and LFP oscillations are inherently related, as in order to observe broad periodic fluctuations in the LFP, many local neurons must have synchronized firing at the same frequency. This is not a tight correspondence, though, as Heimer et al (2006) find that synchrony and oscillations can exist independently.

In another study, *only nonlinear* techniques were capable of extracting the relationship between STN LFP and hand acceleration in 48 PD tremor patients; in our study (Chapter 2), nonlinear techniques were also found to be successful in extracting spike-tremor correlation, whereas no linear trend was found between oscillation frequency and peak tremor frequency. Strangely, in that study phase-dynamics modeling revealed that hand acceleration lagged LFP oscillations by one or two periods, which is far longer than the 15-25 ms conduction delay from the cortex to the muscles (Tass et al., 2010). Other studies have shown that STN and GPi firing at tremor frequency locks *only transiently* to peripheral tremor (Hurtado et al., 1999), again consistent with the heterodyne results in Chapter 2. Yet other studies using magentoencephalography (MEG) with beamforming techniques shows that M1 and EMG are predominantly coherent at double-tremor frequency (and not the actual tremor frequency), and find that the contralateral cerebellum, in addition to premotor, sensory, and posterior parietal cortices are all involved in the double-tremor synchronization (Timmermann et al., 2003).

Improvement in bradykinesia and rigidity is proportional to the suppression of excessive oscillations, irrespective of the frequency that synchronization occurs (Kuhn et al., 2009). This indicates that there is a wide variety of synchronization responses – see figure 1.17 – and levodopa may actually increase the oscillation power in some patients. Other studies show that the percentage of neurons exhibiting oscillatory

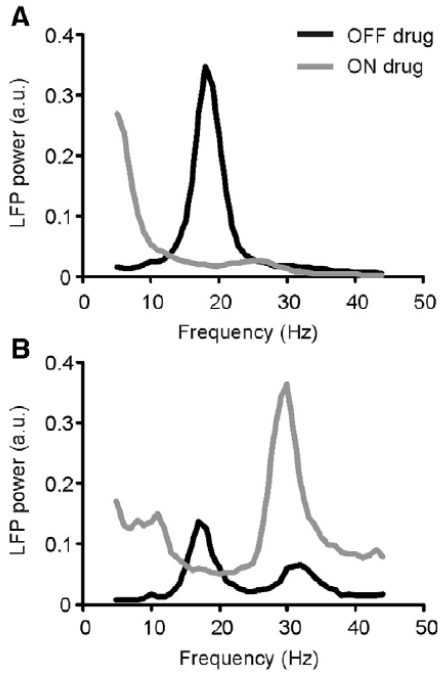

FIGURE 1.17: Changes in LFP oscillations in PD STN ON and OFF drugs. A and B, power spectral density from two different patients, showing both beta suppression by levodopa (A), and gamma enhancement (B). From (Kuhn et al., 2009).

firing in the beta range correlates with motor symptom improvement following drug administration (Kuhn et al., 2009). But this does not necessarily imply causality – the levodopa is the likely cause, or increased movement may be the cause of an oscillation decrease, as occurs in normal individuals (Weinberger et al., 2009). Yet another study indicates that plasticity in the SNr is critical for the propagation of oscillations, and this plasticity is modulated by levodopa and serves to restore motor function and quench oscillations simultaneously (Prescott et al., 2009).

The net effect of all these synchrony / oscillation studies is, quite frankly, a bit confusing – and this is less than 10% of the literature available. It is clear that oscillations and synchrony are important and common features of PD, with generally increased beta band oscillations and synchrony in the diseased state, but the exact nature and frequency seem highly idiopathic sequelae of pathology, and hence a

relatively insensitive or low-utility metric for understanding disease. Closed-loop DBS shows that oscillations may be a good therapeutic target, however, as will be discussed below.

The Piper Rhythm

An interesting but contentious corollary to gamma-frequency oscillations in the basal ganglia is the Piper rhythm. This refers to the observation that during isometric muscle contractions, motor units synchronize at 40-60Hz. This frequency is much too high to be supported directly by a feedback loop involving the muscle spindles, and it appears in different muscles with remarkably different mechanical resonance properties, hence is very likely centrally mediated (Hagbarth et al., 1983). Indeed, magnetoencephalographic recordings from humans support a cortical source of the piper rhythm (Brown et al., 1998). This rather universal feature has led some to propose that the Piper rhythm is a means of binding multiple muscles involved in the same movement together (Brown, 2000), which matches gamma-band EEG coherence between co-activated cortical areas (Cassim et al., 2002). Alternately, the Piper rhythm may just be an effective method for driving of motor units in the spinal cord, or a non-causative artifact of other mechanisms (Hari and Salenius, 1999).

The Piper rhythm is well in the gamma band, which is enhanced by both STN DBS and levodopa treatment, hence it is tempting to suppose that reinstating the Piper rhythm is the mechanism of motor treatment. There is some evidence to support this: as the Piper rhythm is particularly evident in isometric tasks, PD patients in which this is decreased (Cassim et al., 2002) show difficulty in force control, which is a symptom observed relatively early in the disease (Turner and Desmurget, 2010). Indeed, PD patients with gamma EEG suppression are unable to use either subconscious nor conscious load cues to normalize velocity when lifting objects (Fellows et al., 2006).

Like other theories behind oscillation, there is counterfactual evidence and further complexities. High frequency stimulation of the STN would be expected to ameliorate this through reinstatement of the Piper rhythm, but it does not: DBS may improve dexterity and mobility, but it does not let a patient match force output to object being manipulated. Quantitatively, STN DBS actually antagonizes uncontrolled and excessive grip force (Fellows et al., 2006).

Inhibition & Conflict

Deep brain stimulation of the STN has a intricate, if loopy, relationship with impulse control disorders (ICD). While DBS of the GPi treats tremor and akinesia of PD, it does not allow for a reduction in the levodopa dosage (Bronstein et al., 2011); STN DBS does allow for a reduction in the levodopa dosage, but the side-effects of STN DBS often include ICD. It would seem that either you cannot win, or any (scalar) adjustments along the dopamine dysregulation spectrum include both therapeutic and harmful effects. Either way, both the STN and dopamine system seem involved in both impulse and conflict inhibition.

Impulse control disorders are one of the worst side effects of levodopa or dopamine agonist treatments in PD; they including punding [26], hobbyism, chronic gambling, and hypersexuality (Rodriguez-Oroz et al., 2011). Also along the spectrum of dopamine dysregulation disorders is attention-deficit disorder (ADD). These are often treated with the amphetamine or ritalin, which block the monoamine transporter and increase extracellular concentration of dopamine, allowing for heightened concentration: once you select a task, you stick with it for longer (Prescott et al., 2006). This correlates well with undesirable ICD side effects of levodopa treatment in PD, albeit here patients stick to the wrong task.

Yet casting behavior down to a single simplified axis is often inaccurate and

[26] complex, prolonged, purposeless, stereotyped behavior often observed in methamphetamine users

information-destroying. For example, STN DBS often causes weight gain in patients (Chestek et al., 2007), which could be seen as a sign of inability to control consumptive urges. However, a more likely explanation is that patients can eat, or are more 'motivated at life'. Rats with a STN lesion show no increase in food, ethanol, or cocaine consumption (Chestek et al., 2007), and rats with bilateral fiber-sparing lesion of STN show enhanced persevereance at food-related tasks, again *without* increased consumption (Baunez et al., 2002).

As mentioned above, lesion of STN in primates causes hemiballismus. The same effect is not seen in rodents (Florio et al., 2001), possibly because they lack direct projection from motor cortex to STN; instead, lesions induce specific deficits in discrimination and delayed response. In a task where a rat had to detect a brief flash of light in one of 5 locations, and subsequent a delay press a paddle and nose-poke for water in the corresponding location, STN excitotoxic lesion increased premature responses, but also perseverance at the paddle and reward locations (Baunez and Robbins, 1997). Recordings from STN indicate neurons are active before switching from automatic to volitionally controlled saccades (Isoda and Hikosaka, 2008), which is perhaps another form of inhibiton/habit control. Given observations that lesions of the pedunculopontine nucleus (PPN) increases reaction time in conditioned movements in rats, and that the PPN has strong reciprocal connection to the STN, it was hypothesized that PPN lesion would alleviate premature responses in STN lesioned rats. Furthermore, lesion of the PPN with STN intact normalizes STN and SNr activity in 6 hydroxydopamine (6-OHDA) rat models of PD (Breit et al., 2006). Yet PPN lesion did not reverse premature response, and rather increased reaction time due to akinesia/bradykinesia (Florio et al., 2001). Again, casting behavior to a single axis of 'motivation' often ignores the complexity and contingencies of behavior-generation.

Observations of premature responses in rats in a delayed-response task following

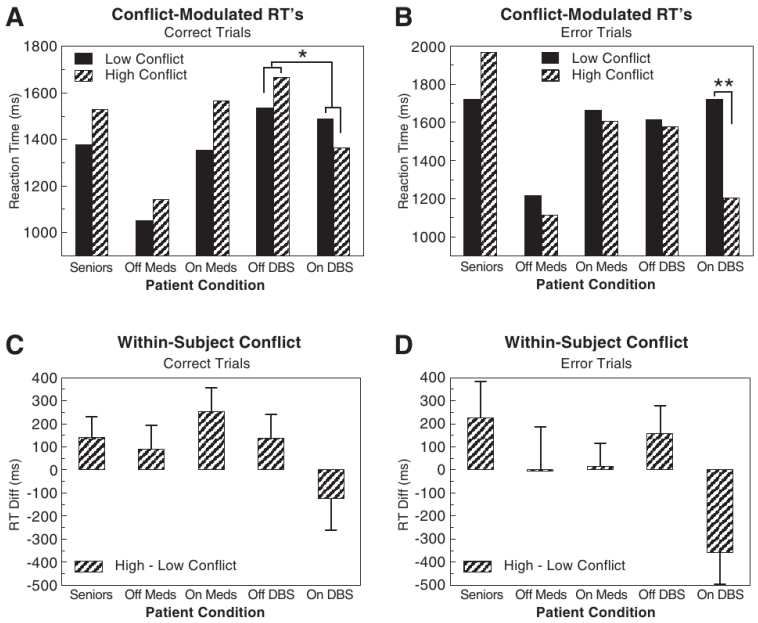

FIGURE 1.18: Conflict effect on decision times in normal, PD, and STN DBS patients. A, Mean reaction times for correct trials and B for error trials for 5 patient states. C, D, within-subject differences in reaction times for correct and error trials. From (Frank et al., 2007).

STN lesions led researchers to theorize that, if the STN has the same role in humans, a similar deficit should be seen in patients being treated with STN DBS. There is strong anatomical support for this hypothesis, as in primates there is a monosynaptic pathway from the medial prefrontal cortex to the STN; breaking this decreases attention and perseverance (Gubellini et al., 2009). Remarkably, this delayed-response deficit was shown to be true by asking PD patients (and controls) to pick between two targets in both high and low conflict situations, where high conflict situations correspond to both choices being nearly equally good or bad. In normal individuals, conflict situations slow reaction times, for the purposes of either obtaining more information or to examine the situation more closely. In comparison, in PD patients with STN DBS, conflict situations *decreased* reaction time – see figure 1.18 (Frank et al., 2007).

It is worth suggesting that this inability to control reaction strength may be

related to an inability to control excessive grip force, another side-effect of STN DBS, as noted in the Piper rhythm section. It may be that accelerated conflict response is the cognitive equivalent of poor force scaling due to STN stimulation; this would make an excellent experiment.

Alternately, cognitive effects may alternatively be the result of poor surgical targeting – in some cases abnormal behavior and ICD is rectified by switching off the ventral contact of the STN lead. This could be from either cognitive (medial-rostral) STN stimulation, or stimulation of the neighboring pedunculopontine nucleus [27] (Rodriguez-Oroz et al., 2011). Indeed, excessive DBS stimulation current induces mirthful, infectious laughter and hypomanic states (Krack et al., 2001), likely due to current spread into the medial-rostral limbic STN.

1.6.4 Treatment of PD through DBS

As noted earlier in the introduction, electrical stimulation of nervous tissue has been extant for a long time; electrical stimulation of the spinal cord has been used to treat pain since the 1950's. A large body of anatomical and pathophysiologial evidence led to the rate hypothesis, as described earlier in this section. The rate hypothesis in addition to observations of clinical hemiballismus led to the supposition that STN lesion could be used to treat PD. This was verified to be true in monkeys rendered parkinsonian by MPTP (Bergman et al., 1990). Shortly thereafter Beabid made the fortuitous discovery that HFS to VIM suppressed tremor in PD patients (Benabid et al., 1991), and that the treatment was safe (Pollak et al., 1993a). These two combined indicated that the STN was likely a good target for DBS as well, which was demonstrated true in 1993, again by Benabid and colleages (Pollak et al., 1993b). STN DBS is remarkably effective at treating both tremor and akinesia (Figure 1.19,

[27] Which is not a suitable DBS target – LFS of the PPN induces feelings of well being and modest improvements in motor function, HFS appears to have no effect (Gubellini et al., 2009).

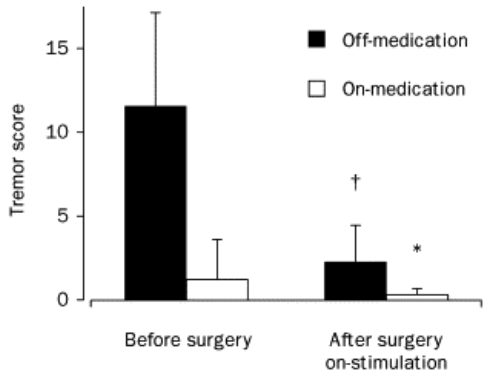

FIGURE 1.19: Improvement in tremor score following bilateral STN DBS. From (Krack et al., 1997).

and for reducing the need for large dosage of levodopa, which as mentioned have unfortunate ICD side-effects (Krack et al., 1997). The strong beneficial effects in $\approx 80\%$ of patients outweighs the negative consequences of treatment, including cognitive decline, speech difficulty, apathy (Bronstein et al., 2011), instability, gait disorders and depression (Rodriguez-Oroz et al., 2005).

DBS is very much a case of technology leading science: though it was effective, it took many years to develop a theory of *why*, and even yet some degree of mystery remains. DBS seems to have the same effect as lesioning the whole structure, which generally suggests that HFS enacts a reversible STN lesion. Recording and metabolic measurements of the treated region is briskly counterfactual to this; DBS does not silence the STN (Carlson et al., 2010).

Instead, evidence suggests that DBS effects an 'information-lesion' whereby aberrant or pathological activity from the basal ganglia is blocked by highly regular stimulus-locked discharge from STN projection neurons; this synchonized activity is preferentially transmitted due to temporal summation (Mallet et al., 2008b). The constant firing causes a null output of the globus pallidus which is then ignored by the rich thalamic and cortical circuits that can hence 'take over' (Israel and Bergman, 2008). The information-lesion theory is consistent with metabolic studies, which

show that DBS decreases the activity of STN neurons and re-normalizes activity in the SNr while decreasing activity in the GPe (Salin et al., 2002). It is also consistent with studies showing that HFS increases synchrony in GPe/GPi (Hashimoto et al., 2003) as required for a 'null output' of the BG. However, in normal rats STN HFS induces dyskinesias, unlike lesion[28] (Hamani et al., 2004) which are blocked by glutamate antagonists in the SNr (Boulet et al., 2006). This leads to a sliding-scale information-lesion model: dopamine depletion decreases the susceptibility to STN induced dyskinesias (Albin et al., 1989), or it could be that movement, even if dyskinetic, happen to be better than no movement in PD.

This hypothesis is in turn called into question by a clever and careful deconstruction of a 6-OHDA rat model of PD using optogenetic methods. While HFS of the STN alleviated hemiparkinsonianism, inhibitory optical stimulation of STN neurons had no therepeutic effect. This led the authors to propose that electrical stimulation may act through glia in the STN; yet optically activating glia also failed to have therepeutic effect, even though firing in the STN was silenced. Next excitatory optical stimulation was tried in the STN, which again elicited no effect. Finally they targeted projection fibers using the Thy1 promoter in the STN with excitatory optical stimulation, which had remarkable and reversible effect on the hemiparkinsonism. In alignment with electrical stimulation, high-frequency optical stimulation had therapeutic effect, whereas low-frequency stimulation exacerbated symptoms. Histology revealed that these Thy1 stimulated neurons were from M1 layer V; direct optical stimulation in M1 had similar positive effects – see figure 1.20 (Gradinaru et al., 2009).

The optogenetic results have support from controlled studies of microstimulation. A general principle of electrical stimulation is that fibers of passage are stimulated far before soma and dendrites (McIntyre et al., 2004) – the chronaxie, or duration of

[28] STN lesion only induces hemiballismus in monkeys, not rats – this is *not* the same as a lesion

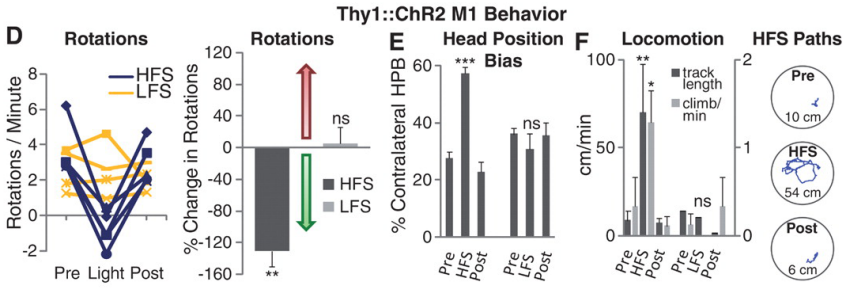

FIGURE 1.20: Efficacy of M1 HF optical stimulation in rat model of PD. Hemiparkinsonian rats have bradykinesia / akinesia on one side, hence rotate around that side. E, Unidirectional rotations are resolved by HFS but not LFS. E, head bias is resolved and F, locomotion restored by HFS to M1. From (Gradinaru et al., 2009).

a stimulus at twice the threshold voltage needed to elicit a response, is 40 times lower for axons than for cell bodies in the cerebrum. This has been verified through direct current injection into soma vs. extracellular current (Nowak and Bullier, 1998a) and NMDA dendrite/soma/proximal axon block controls (Nowak and Bullier, 1998b). Thus the effect of STN DBS might be mediated through motor cortex projection fibers in the STN.

Yet another alternative is that STN DBS may work through inadvertent stimulation of fibers in the zona incerta (ZI), a highly diverse and well connected region (Lin et al., 1990; Nicolelis et al., 1992) which lies ventral the thalamus and dorsal to the rostral STN. Postmortem histology of one long-term DBS patient revealed that efficacious contacts were in the ZI (Sun et al., 2008). Later direct testing of DBS in the caudal (close to STN) ZI yielded excellent results – resting PD tremor was improved by 94.8%, postural tremor by 88.2%, with good control of both proximal and distal tremor, and without development of tolerance typical of thalamic DBS (Plaha et al., 2008).

The role of DBS in changing beta oscillations is itself still quite contentious (Eusebio and Brown, 2009), though there is some intraoperative evidence that STN DBS attenuates beta band power in the LFP (Wingeier et al., 2006). Short-train HFS of

the STN has been shown to decrease STN-cortex coherence for up to 25 s after application (Weinberger et al., 2009). Perhaps the best support of this hypothesis is the recent demonstration of the efficacy of closed-loop DBS. In this groundbreaking study, neurons in M1 and GPi were recorded from MPTP-treated green monkeys, and used to trigger short bursts of HFS stimulation on separate GPi electrodes after a fixed 12.5 ms delay (Rosin et al., 2011). Oscillations in the GPi of the tremorgenic monkeys were in the tremor and double-tremor band $\approx$ 8 Hz, hence this delay corresponds to one full oscillation period; presumably this delay effects a zero in the transfer function of the BG around the double-tremor frequency. Active closed-loop DBS was superior to both HFS and time-shifted DBS controls; clinical devices supporting this activity are presently in testing (Rouse et al., 2011), so deployment of this improved technique may be imminent.

A safer and quite possibly more effective treatment yet may be to use transverse dorsal column stimulation (DCS) to abolish aberrant oscillations in the motor cortex and basal ganglia. Vagus nerve stimulation has been shown effective in treating epilepsy (DeGiorgio et al., 2006; Fanselow et al., 2000; George et al., 2000), and indeed if STN DBS works by stimulating the projecting axons of motor neurons, stimulating the pyramids should have exactly the same effect – only without the need for a craniotomy. Romulo Fuentes and colleagues showed that DCS markedly increases locomotion in both dopamine-deprived DAT-KO mice and 6-OHDA lesioned rats, and effect was correlated with reversal of LFP oscillations in M1. Interestingly, in sham-lesioned rats, DCS caused the animals to move *less*, implying that DCS does not induce movement directly (Fuentes et al., 2009).

Treatment of Essential Tremor through DBS

In Chapter 2 over half of the patients undergoing stereotaxic surgery were being treated for essential tremor (ET), a debilitating disease characterized by higher-

frequency *intention* tremor rather than resting tremor as typical in PD (Deuschl and Elble, 2000). ET is treated by HFS DBS to the ventral intermediate (Vim) / ventralis oralis posterior (Vop) thalamus[29]. The latter is a relay from the cerebellum to the motor cortex (Lenz et al., 2002), and the former is a relay to the supplementary motor cortex (SMA) (Hyam et al., 2011).

While the full etiology in ET is unknown and appears to be largely idiopathic, a prominent theory is that it results from cerebellar degeneration. Loss of cerebellar function would force the patient to rely on visual information to stabilize limb position; as the visual system is much slower and less precise than the proprioceptive system, this leads to phase-margin feedback instability and oscillations (Lenz et al., 2002). Other theories posit that pathology in the inferior olive causes the tremors, as consistent with frequency analysis indicating that the oscillations are centrally generated, and that harmaline, which causes inhibition-rebound in olivary neurons, exacerbates ET (Elble, 1996).

The symptoms of essential tremor overlap with Parkinson's disease, and decision on which subcortical structure is largely based on symptoms and physician / surgeon's experience. Several of the patients in our cohort treated with DBS to VIM had parkinsonian symptoms; we did not discriminate between each disease.

Along this line of argument, there is substantial evidence supporting the idea that ET and PD are different sides of a common pathology. Vim/Vop are effective targets for treating PD tremor as well (Elble, 1996). Lobules 9 and 10 of the cerebellum, considered to be involved in vestibular control of posture (which are highly effected in PD), stain strongly for dopamine (Barik and de Beaurepaire, 1996). Finally, Benabid and colleagues showed, by comparing the relative efficacy of two sister hospitals performing the same Vim DBS procedure with markedly different success rates, that

[29] These are in Hassler nomenclature – there are unfortunately several conflicting nomenclatures for the thalamus (Krack et al., 2002)

the most successful surgeries were those that placed the electrodes closest to CM/Pf thalamus – that is, the part of the thalamus that projects directly back to the striatum, and not from the cerebellum (Caparros-Lefebvre et al., 1999).

1.6.5 Conclusions

DBS was discovered as much by accident as through the scientific method. DBS has been used since the 1950s for localization of lesion targets; in the 1960's was discovered to alleviate tremor; 70s and 80s targeted at the cerebellum for treatment movement disorders or epilepsy (Gubellini et al., 2009). This seems good cause for encouraging further experimentation, despite a lack of perfect scientific consensus on many of the scientific issues. Not discussed here are the many attempts and curing the disease (rather than treating it) by preventing Lewy bodies, protein buildup, or cell death, rather than treating it; nor are discussed treatment through stem cells (Tropel et al., 2006) or gene therapy by inducing striatal expression of neuroprotective neurturin (Eslamboli et al., 2005; Herzog et al., 2007; Kordower et al., 2000, 2006). Though the neuturin studies are promising, they have yet to reach the efficacy of DBS, and due to the fact that the protein stimulates growth, may induce tumors (Marks et al., 2010).

Regarding synchrony and oscillations, my personal opinion is that they are sequelae from a general inability to modulate gain, which is one of the first symptoms of PD. Oscillations are a very general property of feedback systems; the anatomy of the basal ganglia clearly involves several feedback systems, and inability to modulate motor program gain may implicitly cause multilevel oscillations. In Chapter 4 it is described how simple changes to feedback weights enable active filters to become oscillators; likely it is the same within the basal ganglia. Controlling oscillations using closed-loop record/stimulate DBS is a highly attractive therapy, yet given the large variety of synchrony / oscillation results, system identification and pole-annulling

will need to be performed on a per-patient basis.

That said, some consensus as to the function of the basal ganglia, and the method of DBS is coming into focus. The basal ganglia seems tightly involved in learning, consistent with the temporal-difference signal of dopamine, the loss of which causes all sorts of idiopathic synchrony and oscillations, all which collectively 'jam' or further disorganize the cortex / motor system. DBS is effective by dramatically reducing the entropy of the output of the basal ganglia, allowing the remaining motor system to function normally. Stimulation and lesion are not without side-effect, notably inhibition of habitual responses, but this is *not* because the substrate for habit is in the basal ganglia – rather, it is the substrate for correcting and adding habits in a contextualized, organized manner. It could be, by blocking / lesioning the basal ganglia, patients are prevented from learning new things, but this does not matter as by that age all the tasks of daily living – which is what neurologists assess to determine treatment efficacy – are well rehearsed.

The data from Chapter 2 dates from 2006-2007; this section of the introduction from 2012; scientific understanding of the BG in PD has advanced dramatically since then. Had we known what we know now, an the experimental task would have been entirely different; given the anachronism, the following data and analysis must be taken within context.

2

Population Analysis of Human Subcortical Neurons in Parkinson's Disease

2.1 Abstract

Deep brain stimulation (DBS) has expanded as an effective treatment for motor disorders, in turn providing a valuable tool for monitoring spiking activity of subcortical neurons. Until now, the potential utility of subcortical populations of neurons to drive brain-machine interfaces (BMIs) and other neuroprosthetic applications is not completely understood. During DBS procedures in 25 parkinsonian patients, we recorded the single-unit activity of 274 ventral intermediate thalamus (VIM) neurons and 123 subthalamic nucleus (STN) neurons. These subcortical neuronal ensemble recordings were obtained while the patients performed a voluntary motor task that required tracking of a visual target with a cursor controlled by opening and closing the hand. Motor parameters were extracted from both VIM and STN ensembles using BMI decoders. We observed that a substantial number of neurons in both VIM and STN represented target onset, movement onset and direction, and hand tremor via modulations in firing rate. Neurons in both areas were found to exhibit

rhythmic oscillations and pairwise synchrony. Contrary to several previous studies, however, we found no linear relationship between the frequency and spectral sharpness of neuronal oscillations and those of the patients hand tremor. Furthermore, the data indicate that oscillatory neurons and behaviorally tuned neurons form overlapping sets. We also observed the prevalence of increased local synchrony among tremor-associated neurons. We suggest that multielectrode recordings from subcortical structures provide useful signals that can be utilized in a variety of BMI systems for both motor control and the monitoring and suppression of pathological neural activity.

2.2 Introduction

Interest in single-unit recordings from the human brain has grown in recent years, especially in light of the development of brain-machine interfaces (BMIs) for neuroprosthetic control (Chapin et al., 1999; Fetz, 2007; Lebedev et al., 2011; Nicolelis, 2001; Nicolelis and Lebedev, 2009; Patil et al., 2004; Patil and Turner, 2008). Investigators are currently pursuing many potential neuronal sources for BMI motor control signals; invasive single-unit recordings from large ensembles of neurons offer the best quality signals for BMI control(Lebedev and Nicolelis, 2006). While such recordings have been performed in numerous animal studies, human ensemble recordings have been utilized for BMI applications to a much lesser degree (Kennedy and Bakay, 1998; Kennedy et al., 2000, 2004; Patil et al., 2004; Quiroga et al., 2005).

Neurosurgical implantation of deep brain stimulation (DBS) electrodes is a common medical intervention for the treatment of Parkinsons disease (PD) and essential tremor (ET) (Deuschl et al., 2006; Koller et al., 2001; Kumar et al., 2003; Parent and Hazrati, 1995b; Rodriguez-Oroz et al., 2005). For PD patients, the subthalamic nucleus (STN) is the typical implantation target, whereas the ventral intermediate nucleus of thalamus (VIM) is targeted for ET patients. In healthy individuals, both

structures are involved in many aspects of movement regulation and feedback control (Guillery and Sherman, 2002; Parent and Hazrati, 1995b). The role for these structures in movement regulation persists even under pathological conditions; several reports have delineated the activity of individual VIM/STN neurons during voluntary and passive movement, somatosensation, and motor imagery (Abosch et al., 2002; Benazzouz et al., 2002; Lenz et al., 2002, 1990, 1994; Magarinos-Ascone et al., 2000; Magnin et al., 2000; Raeva et al., 1999; Rodriguez-Oroz et al., 2005; Theodosopoulos et al., 2003; Williams et al., 2005). In addition, several reports have examined the single unit activity in these regions with respect to tremor (Amtage et al., 2008; Brodkey et al., 2004; Hua and Lenz, 2005; Lenz et al., 2002, 1994, 1988; Magarinos-Ascone et al., 2000; Magnin et al., 2000; Rodriguez-Oroz et al., 2001; Zirh et al., 1998) and synchronous oscillations (Amirnovin et al., 2004; Levy et al., 2002, 2000). However, the number of simultaneously recorded cells in these studies was low (typically no more than 2 neurons).

Previously, our laboratory demonstrated the feasibility of extracting motor control signals from neuronal ensembles recorded in VIM or STN during DBS surgery (Patil et al., 2004). Subcortical ensemble recordings were utilized to decode task-related modulations of the contralateral hand force during a one-dimensional target tracking task. Demonstration of the feasibility of subcortical BMI was the primary purpose, whereas analysis of neuronal population firing patterns was minimal. In this study, we recorded from up to 23 subcortical neurons simultaneously to elucidate the relationship between neuronal modulations, rhythmic oscillations, and neuronal synchrony during a voluntary motor task. VIM and STN ensembles were recorded in 25 patients asked to produce hand movements to reach visual targets with a computer cursor. Neurons from both subcortical areas were classified by oscillatory behavior, tremor association, and tuning to target, movement, and direction. Neuronal pairs were analyzed for evidence of functional synchrony over both short and long

timescales. Finally, the neuronal ensembles were employed in an offline BMI decoder to reconstruct cursor position.

2.3 Materials and Methods

Intraoperative recordings were conducted in 25 patients undergoing placement of therapeutic DBS implants in either VIM or STN. All studies were approved by the Duke University Institutional Review Board (IRB), and all participating patients understood and signed all required consent forms. All statistical analyses were performed using Matlab (MathWorks Inc.).

2.3.1 Patient characteristics and operative plan

All patients selected for this study underwent either VIM (N=14) or STN (N=11) DBS electrode implantation surgery. Patients whose symptom presentation was dominated primarily by medication-resistant tremor (either essential tremor or severe parkinsonian tremor) were candidates for implantation in VIM, while patients with severe PD (typically akinetic/rigid variant with on/off fluctuations and dyskinesia) were candidates for implantation in STN. Both groups of patients were off their medications prior to and during surgery. Patients first underwent Leksell frame placement, followed by a magnetic resonance imaging (MRI) scan to localize the implantation target. For VIM patients the target was typically estimated according to anterior-posterior commissure (AC-PC) criteria, located approximately 5-6 mm in front of the PC, on the AC-PC line with a lateral measure depending on the width of the third ventricle (typically 12-15 mm). The first pass for VIM was the treatment pass from a frontal burr hole, with the upper 5 mm of the recording track near the border of ventralis oralis posterior (VOP) thalamus and VIM, and the lower 5 mm in VIM and close to ventralis posterior caudalis (VPC) at the most posterior extent. Typically, the upper 5 mm was the best for multineuron recordings, reflecting more

of the slightly anterior motor thalamus. For STN patients the target was calculated by indirect methods, based on the AC-PC and 1 mm axial cuts of spoiled gradient recalled acquisition in the steady state (SPGR) imaging. The target was localized at 11-12 mm from the midline, 2-3 mm posterior to the midpoint of the AC-PC line, and 4 mm below the AC-PC line. Single-unit recordings were first performed to define the borders of the STN, according to standard electrophysiological criteria, with the goal of attaining at least 5.5-6 mm of STN. Typically 2-3 passes were required. For both targets, once single-unit recordings had been performed for localization, a 32-channel Pt/Ir microwire array (Ad-Tech Medical Instrument Corp., 35 μm each) was passed to the appropriate depth via an outer cannula (Levy et al., 2000). After allowing a few minutes for recordings to stabilize, the microwire array was slowly advanced through the cannula. Once the number of clearly distinguishable single units was maximized, the microwire array was left in place. At each electrode depth, the patient was instructed to proceed with the voluntary motor task.

Following completion of the multichannel recording sessions, the microwire array was removed prior to implantation of the DBS treatment electrodes.

2.3.2 Electrode arrays and electrophysiological recording

The 32-channel microwire recordings were performed with a Plexon MAP system (Plexon Inc.). Since this study was performed intraoperatively during electrophysiological mapping of the implantation sites, the recordings for each patient consisted of one or more sessions (up to 8, mean=3.8), between which the electrode depths were altered. For each session, single units were sorted offline using custom software developed in-house. Low-amplitude neuronal discharges that could not isolated as single units were classified as multiunits. Figure 2.1a shows the sorted unit waveforms from a single recording session.

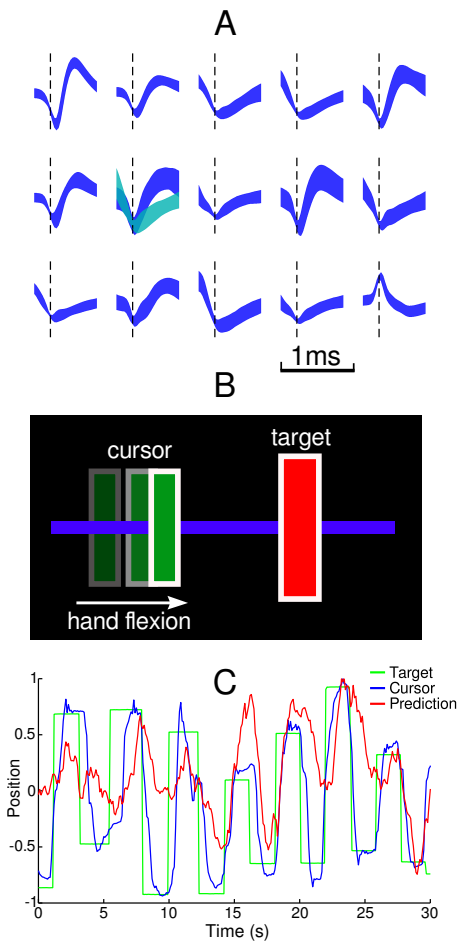

Figure 2.1: (a) Visualization of all 16 sorted units from Patient M (VIM). All captured waveforms are triggered using a linear threshold at t=0 ms. For each unit, the visualized patch represents mean + 1 SD for all captured waveforms. Multiple sorted units from the same channel are shown in different colors. Voltage amplitudes are normalized for display and are therefore represented in arbitrary units. (b) Diagram of the bidirectional hand task. The patient uses opening/closing of the hand to actuate a one-dimensional cursor toward randomly appearing targets. (c) Example offline prediction of hand/cursor position. Prediction was obtained using a linear Kalman filter with a 500 second training period, from Patient M (VIM). 48 units (16 single units, 32 multiunits) were included in the ensemble. Position is given in normalized units.

2.3.3 Voluntary motor task

Patients were placed in a supine, semi-sitting position in front of a computer monitor. A 5DT Systems Data Glove 5 Ultra haptic glove (5DT Inc.) was placed over the hand contralateral to the microelectrode array. This glove was used to measure opening and closing of the hand, sampled at 1 kHz. The recorded signal was used to control the position of a one-dimensional cursor on a video screen, placed directly in front of the patient for high visibility. Patients were trained to open and close their hand in order to acquire targets by moving the cursor into a box placed randomly along a horizontal line (Fig 2.1b). The required target hold time was 200 ms. Once

the target was acquired, the box disappeared for 300 ms before reappearing in a new random position. During the preliminary training/calibration phase, the cursor gain, offset, and target box size were manually adjusted by the experimenters to compensate for variations in physical ability. During the recordings that followed, the length of individual motor task sessions varied depending on electrophysiological recording quality and the level of patient fatigue. Figure 2.1c shows a representative snapshot of the motor task performed by an ET patient. Note the slight 5 Hz tremor that occurred during target hold periods.

2.3.4 Neuronal tuning to target and movement

For all sorted single units and multiunits, peri-event time histograms (PETHs) of neuronal activity (Awiszus, 1997) were generated using one of two event triggers: 1) the appearance of a new target or 2) movement time. PETHs triggered on target appearance were constructed using a window beginning 0.5 s before each event trigger and ending 1.5 s after, whereas a symmetric 2 s window was used for PETHs triggered on movement time. Movement time was defined as the moment at which the cursor crossed the midpoint between initial cursor position (at target appearance) and the endpoint target position. We chose this standard as a robust definition of movement execution in light of patient tremor and occasional incorrect movements. Regardless of reaction time, this event trigger was locked to movement, being in close proximity to the point of maximum hand velocity prior to target acquisition. Trials with anomalous movement times below 200 ms (premature movement) or greater than 1000 ms (inattention) were discarded. Only neurons with at least 50 valid target acquisition trials were chosen for further analysis.

Neuronal tuning (modulation of firing rates correlated to an external parameter) to either target or movement was determined by quantifying the deviation of each PETH from a bootstrap distribution of PETHs generated by uncorrelated trig-

gers. We calculated significance using the one-sample Kuiper's test (Batschelet, 1981; Kuiper, 1962; Zar, 1999), a non-parametric test related to the Kolmogorov-Smirnov (K-S) test (Zar, 1999) but better suited for nonbiased PETH analysis. Unlike the K-S test, Kuipers test is equally sensitive throughout the distribution, a useful property in scenarios in which the locations of the peak modulations are not known a priori. Variations of the K-S test have been employed previously in the significance evaluation of neuronal PETHs . In this study we used Kuipers test to distinguish an observed distribution of event-triggered spike times from the null hypothesis (uniform probability distribution). Kuipers test requires the calculation of the maximum positive and negative deviations of the observed PETH cumulative distribution function (CDF) from a uniform distribution CDF (ramp function); the sum of these two deviations is the statistic V:

$$V = max\lfloor CDF_{sample} - CDF_{uniform} \rfloor + max\lfloor CDF_{uniform} - CDF_{max} \rfloor$$

The Kuiper statistic K is a normalized version of V, taking into account the size of the observed sample size N, in this case the number of binned spikes:

$$K = V(N^{\frac{1}{2}} + 0.155 + 0.24N^{-\frac{1}{2}})$$

To fully account for the non-Poisson effect of intra-trial spike correlation and distinguish the test statistic Kobs from the null hypothesis, we generated a bootstrapped distribution of 1000 simulated Kuiper statistics (K_{sim}). Preliminary analysis determined shuffling of spike timestamps to be an inappropriate control; the process eliminates intra-trial spike correlations from the bootstrap distribution, thereby biasing the evaluation of the observed distribution in favor in significance. Instead, each value of K_{sim} was calculated using a PETH constructed from the original spike timestamps but processed using a distribution of randomized event triggers; the triggers

are drawn uniformly from the recording session. For each sorted unit, the resulting bootstrapped distribution of K_{sim} was used to produce a p-value:

$$p = \frac{(trials\, for\, which\, K^n_{sim} > K_{obs})}{N+1}$$

Units were deemed to be tuned to task events (target or movement onsets) using the threshold $p < 0.05$. In other words, these units exhibited temporal modulations in firing rate relative to newly appearing targets and/or target-directed movements. Tuning strength was defined as the z-score of the observed PETH relative to the bootstrap distribution.

2.3.5 Directional tuning

The directional tuning of each sorted unit or multiunit was defined as the difference in neuronal response for leftward versus rightward movements. Significance of directional tuning was determined using the two-sample Kuiper's test. This test applied the calculation of the maximum positive and negative deviations between the spike CDFs for leftward and rightward movements:

$$V = max\lfloor CDF_{sample1} - CDF_{sample2} \rfloor + max\lfloor CDF_{sample2} - CDF_{sample1} \rfloor$$

The Kuiper statistic K was calculated from V using the same equation as the one-sample Kuipers test, but in the case of the two-sample Kuipers test the effective sample size (N_{eff}) replaced N to account for the combined contributions of the individual sample sizes N1 and N2:

$$N_{eff} = \frac{N_1 N_2}{N_1 + N_2}$$

Two PETHs triggered on movement time were generated one for leftward movements, one for rightward movements. As with the one-sample Kuipers test, each units Kobs statistic was compared to a bootstrapped distribution of Ksim generated from randomized trigger times. Units were deemed to be directionally tuned using the threshold $p < 0.05$. Tuning strength was defined as the z-score of the observed PETHs relative to the bootstrap distribution.

2.3.6 Tremor sensitivity

For all sorted single units, peri-event phase histograms (PEPHs) of neuronal activity were generated using phase of the patients tremor as an event trigger, similar to the approach of Lebedev et al. (1994). Tremor was determined from hand velocity, and tremor periods within the range 100-2000 ms (0.5-10 Hz) were analyzed. To exclude the impact of voluntary movements, hand velocity peaks occurring within 250 ms of a movement trigger were excluded. Each tremor period was defined in units of phase, with neuronal spike activity captured into 100 bins of equivalent phase aperture (3.6 each). The zero phase for each cycle was defined by a local maximum in hand velocity. Only sorted units with at least 500 valid tremor periods were chosen for further analysis.

Each resulting PEPH was a measurement of neuronal firing rate with respect to tremor phase. The one-sample Kuiper's test, in addition to possessing uniform sensitivity, is also rotationally invariant, meaning that the arbitrary choice of zero phase has no effect on the assessment of statistical significance. For analysis of tremor tuning, we generated a bootstrapped distribution of 1000 simulated Kuiper statistics (K_{sim}); eachwas calculated using a PEPH constructed from trials whose binned spike counts were circularly rotated by uniformly random phase offsets. For each analyzed unit, the bootstrapped distribution was used to produce a p-value. Units were deemed to be tremor associated (tuned) using the threshold $p < 0.05$.

Tuning strength was defined as the z-score of the observed PEPH relative to the bootstrap distribution.

2.3.7 Oscillatory neurons

For all sorted units with at least 1000 extracted spikes, we used Welch's method (Oppenheim and Schafer, 1975) with 8 non-overlapping segments to determine the spike train autopower spectral density. The power spectra were smoothed using a 0.5 Hz rectangular sliding window. For each unit the peak autopower frequency was determined in the 1-25 Hz range; frequency content below 1 Hz was discarded for the remainder of the analysis. For the peak frequency, we determined the signal-to-noise ratio (SNR) by dividing peak power by the mean power (assessed from 1 Hz up to the Nyquist frequency of 500 Hz). For the purpose of comparison, the same spectral analysis was performed on hand acceleration traces for all recorded sessions.

Preliminary analysis indicated a functional separation of peak frequencies at about 2.5 Hz. Units with a peak power frequency below 2.5 Hz tended to be dominated by low frequency power and were therefore judged not to be sufficiently oscillatory in a physiologically relevant frequency range. As in previous studies , only units with a peak $SNR > 2$ were classified as oscillatory. Spectral sharpness, or peakedness, of either the spike train or hand acceleration autopower spectra was determined by calculating the maximum power concentrated in a 1 Hz band within the physiologically relevant 2.5-7.5 Hz window. Peakedness was defined as the ratio of the power in this band relative to the total power in the 1-25 Hz band.

In addition to established linear methods, we developed a nonlinear heterodyne method for detecting synchronized activity between each neurons firing rate and associated hand velocity. This method was applied to all sorted units that fulfilled the selection criteria for both target tuning analysis and oscillatory analysis. The spike train and hand velocity recordings were first bandpass filtered (4th order Butter-

worth) between 2-12 Hz, leaving both signals with negligible 0 Hz (DC) energy. The two signals were then multiplied, yielding a third time series from which to extract spectral energy. Because multiplication in the time domain is equivalent to convolution in the frequency domain (and vice versa), any synchronous frequency-modulated components in both neuronal firing rate and hand velocity are transferred to DC. The ratio of spectral energy (Eobs) from 0-0.125 Hz (signal) over that from 0.25-2 Hz (baseline) was considered as a metric of heterodyne synchrony between neuronal activity and hand movement. To provide a control for this estimate, a bootstrap distribution (Esim) was generated by shuffling spike timestamps 1000 times and repeating the above analysis. Since all low frequency information is filtered out prior to multiplication, shuffling timestamps was determined to be a suitable control. For all single units, the resulting bootstrapped distribution was used to produce a p-value. Units were deemed to be heterodyne-tuned to tremor using the threshold $p < 0.05$. Tuning strength was defined as the z-score of the observed spectra relative to the bootstrap distribution.

2.3.8 Neuronal synchrony

The use of simultaneous ensemble recordings allows for the analysis of pairwise synchrony between neurons. To determine the statistical significance of the synchrony between two neurons, we employed the bootstrap procedure introduced by Ventura et al. (Ventura et al., 2005a). This procedure requires the calculation:

$$\zeta(t) = \frac{P^{12}(t,t)}{P^{1}(t)P^{2}(t)}$$

$\zeta(t)$ represents the ratio between the observed probability of near-simultaneous firing of two neurons and the predicted joint probability assuming statistical independence. $\zeta(t)$ can be interpreted as the excess probability ratio of the observed

result with respect to statistical independence.

In this study $P^1(t)$, $P^2(t)$, and $P^{12}(t,t)$ were calculated for all pairs of simultaneously recorded sorted units, using either target or movement as an event trigger. In this context, $P^1(t)$ and $P^2(t)$ are effectively normalized PETHs, while $P^{12}(t,t)$ is the diagonal of a normalized two-dimensional PETH, with each axis corresponding to one of the two recorded neurons. As in the analysis of single unit behavioral tuning, we used a window beginning 0.5 s before and ending 1.5 s after each target trigger. For movement triggering, we used a window beginning 1 s before and ending 1 s after each event trigger. Only neuron pairs with at least 50 valid triggers were chosen for further analysis.

The two-dimensional PETH was smoothed with a two-dimensional Gaussian kernel (σ=20 ms), while $P^1(t)$ and $P^2(t)$ were smoothed with a one-dimensional Gaussian kernel (σ=20 ms). After smoothing, the two-dimensional PETH was compressed into 10 ms square bins, after which it was diagonalized to form $P^{12}(t,t)$. $P^1(t)$ and $P^2(t)$ were simply compressed into 10 ms bins. The excess probability ratio $\zeta(t)$ was then calculated using these constituent probability densities. Following Ventura et al. (Ventura et al., 2005a), 1000 bootstrap simulations of $\zeta(t)$ were produced by using $P^1(t)$ and $P^2(t)$ to generate Poisson spike trains. The result of the bootstrapping procedure is 1000 $\zeta_n(t)$ curves, each corresponding to an observed probability ratio under the null hypothesis statistical independence of the two neurons. For each bootstrap simulation we calculated the statistic G_{sim}, which was defined as the largest area of any contiguous portion of $\zeta_n(t)$ that exceeds the two-tailed 95% confidence bands of the $\zeta_n(t)$ bootstrapped distribution. The bootstrapped distribution was used to produce a p-value, and neuron pairs were deemed to be significantly synchronous using the threshold $p < 0.05$.

Due to nonstationarity in mean firing rates, the $\zeta(t)$ approach to synchrony analysis is largely a measure of long timescale, correlated modulations in the session-wide

firing rate envelope. Rather than correct for trial-to-trial variability as in Ventura et al. (Ventura et al., 2005b), we chose instead to exploit this measure of long timescale neuronal synchrony. For a separate short timescale analysis of neuronal synchrony, we analyzed the cross-correlation peak between pairs of spike trains. Pairs were analyzed if they each contained at least 100 spikes and corresponded to a session with at least 50 targets. The cross-correlation coefficient was first calculated for the observed spike trains of the two neurons, then smoothed using a 5 ms rectangular sliding window. The observed test statistic C_{obs} was defined as the peak coefficient in the +10 ms time lag range. Bootstrap simulations (n=1000) of the two spike trains were generated by convolving the spike trains with a Gaussian kernel (ρ=250 ms) and then generating new spike trains via an inhomogeneous Poisson process. The smoothing filter was used to extinguish correlated high frequency content in the bootstrap distribution, while maintaining low frequency correlation in mean firing rate. Each of these bootstrap simulations was used to produce a cross-correlation coefficient Csim. The bootstrapped distribution was used to produce a p-value, and neuron pairs were deemed to be significantly synchronous using the threshold $p < 0.05$.

To visualize the time dependency of pairwise synchrony, we generated joint peristimulus time histograms (JPSTHs) for neuron pairs, as originally presented by Aertsen et al. (Aertsen et al., 1989). Our JPSTHs were adjusted by subtracting the shift predictor histogram and normalizing (bin-by-bin) by the standard deviation, a procedure referred to by Aertsen as the "true normalization" of the JPSTH.

2.3.9 Efficacy of neuronal recordings for kinematic predictions

BMI algorithms were applied to subcortical neuronal populations to extract behavioral parameters. Several algorithms were tested, including the linear Kalman filter, unscented Kalman filter, and the Wiener filter. Figure 2.1c shows an example offline prediction for a 30 s window of task performance.

Since all three algorithms achieved the same approximate fidelity in preliminary testing, we chose the Wiener filter for further analysis due to its computational simplicity and extensive presence in the BMI literature (Carmena et al., 2003; Patil et al., 2004; Wessberg et al., 2000). Individual Wiener filters were fit by binning neuronal data into 100 ms time slices with 10 causal lags and regressing against recorded hand position. Model training was performed by the random selection of 50% of these time slices; predictions were then made on a distinct random 25%. This process was repeated with 100 draws of fit and predict time slices. Correlation coefficient (R) between predicted hand position and actual hand position was measured for each of the draws; the mean correlation coefficient was reported for each recording session. Offline prediction results are reported for all sessions with at least 50 presented targets.

We generated neuron dropping curves for selected sessions (Wessberg et al., 2000) by drawing random subsets from the neuronal ensemble. For each subset ensemble size N, we performed 1000 draws of random ensemble subset and Wiener filter fit and prediction; the R values for these draws were averaged to form a smooth neuron dropping curve. Following Wessberg et al. (2000), the resulting curve was then fit to the following hyperbolic function to extrapolate the performance results to larger ensemble sizes:

$$R^2 = \frac{cN}{1 + cN}$$

2.4 Results

A total of 25 DBS implantation patients were examined. In these patients we simultaneously recorded from ensembles of up to 23 well-isolated neurons from either VIM or STN, depending on the site of electrode location. Recording sessions varied sub-

stantially in terms of duration and target acquisition rate, as limited by individual patient pathology and motivation. Neurons from these subcortical areas were classified by oscillatory behavior and tuning to target, movement, direction, and tremor. Neuronal pairs were analyzed for evidence of functional synchrony over both short and long timescales. Finally, the neuronal ensembles were employed in an offline BMI decoder to predict cursor position.

STN cells (N=168) exhibited a higher ($p < 0.05$, two-tailed t-test) mean firing rate than VIM cells (N=83): 15.8 + 1.9 Hz and 11.7 + 1.0 Hz, respectively (mean + 1 SE in both cases). In both subcortical areas we found substantial populations of oscillatory neurons, as well as neurons strongly tuned to target, movement, direction, and tremor. At the ensemble level, the vast majority of analyzed cell pairs were found to exhibit functional synchrony. Furthermore, neurons in both subcortical areas tended to show tuning to multiple parameters (Table 2.1) rather than belonging to disjoint sets. For example, the number of VIM cells were tuned to both target and tremor was higher than would be expected under statistical independence (two-tailed Fishers exact test, $p < 0.05$).

2.4.1 Neuronal tuning to target and movement

Both VIM and STN neurons represented target appearance and movement onset (Table 2.2). Of all tested single units tested, 29.2% of 168 VIM cells and 22.9% of 83 STN cells were found to be tuned to target appearance. Both of these percentages represent significant populations (Binomial test, $p << 0.001$ in both cases). Figure 2.2a shows example PETHs for three highly responsive neurons.

Because of the additional reaction-time criterion for analyzing units for movement tuning, fewer single units were analyzed. Of these, 34.7% of 75 VIM cells and 42.3% of 26 STN cells were found to be tuned to movement. Both of these percentages

Table 2.1: Pairwise Classifications for Single Units

VIM CELLS	Target	Movement	Direction	Tremor	Oscillatory	Heterodyne
Target	29.2%(N=168)	32.0%(+)**(N=75)	16.0%(N=75)	9.5%(+)(N=126)	5.1%(N=158)	3.8%(N=158)
Movement	-	34.7%(N=75)	14.7%(+)(N=75)	13.8%(N=65)	1.4%(-)*(N=74)	4.1%(N=74)
Direction	-	-	25.3%(N=75)	12.3%(+)(N=65)	4.1%(N=74)	8.1%(+)(N=74)
Tremor	-	-	-	12.4%(N=169)	2.4%(N=169)	6.3%(+)*(N=126)
Oscillatory	-	-	-	-	21.5%(N=274)	3.8%(N=158)
Heterodyne	-	-	-	-	-	13.3%(N=158)
STN CELLS	Target	Movement	Direction	Tremor	Oscillatory	Heterodyne
Target	22.9%(N=83)	38.5%(+)**(N=26)	11.5%(N=26)	4.1%(N=74)	4.9%(N=81)	2.5%(N=81)
Movement	-	42.3%(N=26)	11.5%(N=26)	12.5%(N=24)	8.3%(N=24)	8.3%(N=24)
Direction	-	-	19.2%(N=26)	0.0%(N=24)	4.2%(N=24)	0.0%(N=24)
Tremor	-	-	-	15.9%(N=82)	1.2%(N=82)	4.1%(N=74)
Oscillatory	-	-	-	-	17.9%(N=123)	6.2%(N=81)
Heterodyne	-	-	-	-	-	17.3%(N=81)

Table 2.2: Behavioral tuning of subcortical neurons

Behavioral Parameter	Unit type	Area	# Units	# Tuned
Target	Single	VIM	168	49** (29.2%)
Target	Single	STN	83	19** (22.9%)
Target	Multi	Both	753	87** (11.6%)
Movement	Single	VIM	75	26** (34.7%)
Movement	Single	STN	26	11** (42.3%)
Movement	Multi	Both	414	48** (11.6%)
Direction	Single	VIM	75	19** (25.3%)
Direction	Single	STN	26	5* (19.2%)
Direction	Multi	Both	414	36* (8.7%)

represent statistically significant populations (Binomial test, $p << 0.001$ in both cases). Figure 2.2b shows example PETHs for three highly responsive neurons. We found a strong positive correlation between the strength of target appearance tuning and that of movement tuning, for both VIM and STN cells. When controlling for the number of session trials, target tuning strength significantly predicted movement tuning strength ($\beta = 0.70$, $p << 0.001$ for VIM; $\beta = 0.71$, $p << 0.001$ for STN). This result is consistent with Table 2.1, which indicates that a larger-than-expected number of neurons in both subcortical areas were tuned to both target and movement.

A portion of the correlation between target tuning and movement tuning may be explained by a tight temporal offset between target appearance and movement time. However, visual inspection of some tuned units indicated a clear decoupling of the neural encoding of target appearance and movement. Sorted raster plots from example neurons are shown in Figure 2.3a,c. From these, we derived the color maps in Figure 2.3b,d, each showing two clear bands of increased spike density. In both panels, the vertical bands are independent of movement time and are clearly related to target appearance (about 450 ms post-appearance). The diagonal bands have a near-unity slope, indicating a clear time-locked relationship between neuronal activity and movement time. For both units, the second peak in firing rate occurred about 300 ms after the defined movement time. From these data it can be concluded that

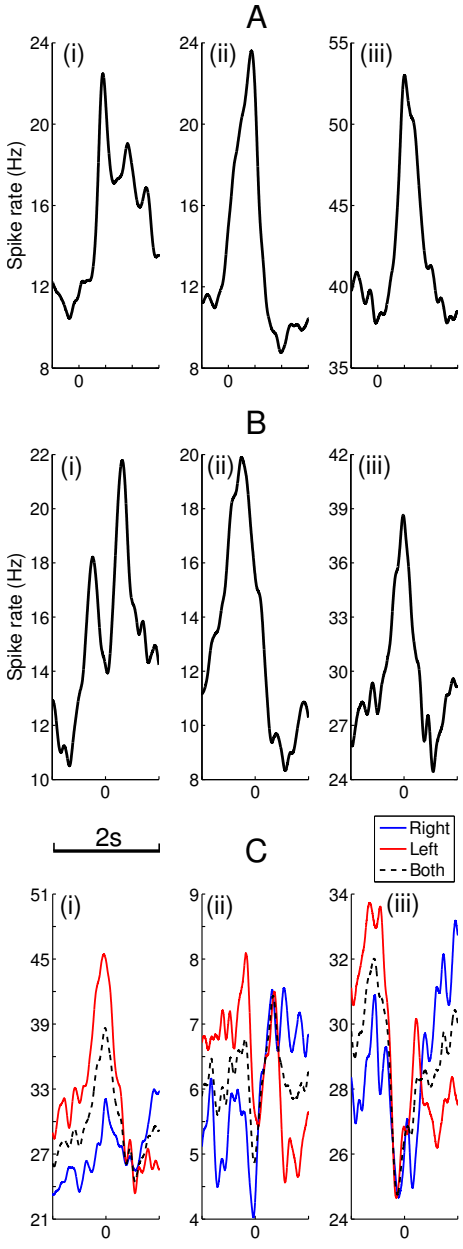

Figure 2.2: Example PETHs, all 2 s long. **A** Strongly tuned units to target appearance; (i) VIM cell, Patient M, 465 trials; (ii) VIM cell, Patient M, 375 trials; (iii) STN cell, Patient H, 310 trials. **B** Strongly tuned units to movement time; (i) VIM cell, Patient M, 390 trials; (ii) VIM cell, Patient M, 310 trials; (iii) STN cell, Patient H, 201 trials. **C** Strongly direction tuned units; (i) STN cell, Patient H, 201 trials; (ii) VIM cell, Patient M, 416 trials; (iii) VIM cell, Patient M, 394 trials. For **A**, reported time is relative to target appearance. For **B** and **C**, reported time is relative to movement time. All plots were smoothed using a Gaussian kernel, σ=40 ms.

these neurons were tuned to both target appearance and movement; they modulated their firing rates in relation to both events.

Modest differences were seen in the aggregate response patterns of VIM and STN cells classified as responsive to either target or movement (Fig. 2.4). Both cell types exhibited a mean response that peaked following target appearance (Fig. 2.4A);

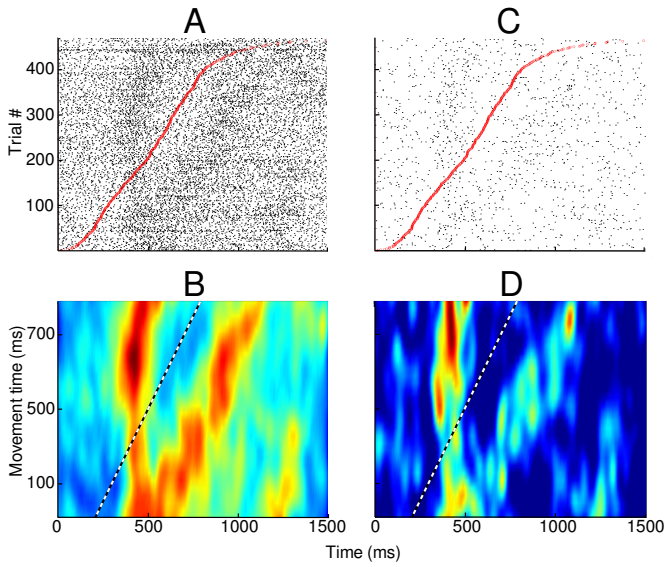

FIGURE 2.3: Separation between single unit response to target appearance and movement time. Time along the X axis is relative to target appearance. Panels **A** and **C** show spike raster plots relative to target appearance, with individual trials sorted by movement time (red circles). Panels **B** and **D** show smoothed color plots for the same two units as **A** and **C**, using the relative timing of all spikes and the movement time of their corresponding trials. The dashed line (unity slope) depicts movement time. For generation of the color plots, the data were smoothed using a two-dimensional Gaussian kernel, with σ=20 ms along the X axis and σ=40 ms along the Y axis. Both units are VIM cells from Patient M.

STN cells peaked later on average. The mean response of the VIM cells peaked immediately before movement while that of the STN cells peaked concurrently with movement (Fig. 2.4B). For both aggregates, the differences between the mean VIM and STN responses were statistically significant (χ^2 test, $p << 0.001$). However, similar proportions of VIM and STN cells were tuned to target appearance; the same was also true for movement tuning (two-tailed Fishers exact test, $p > 0.05$ in both cases).

2.4.2 Directional tuning

Another metric of interest for the behavioral responsiveness of subcortical neurons was directional tuning; Table 2.2 gives the directional tuning results for both single

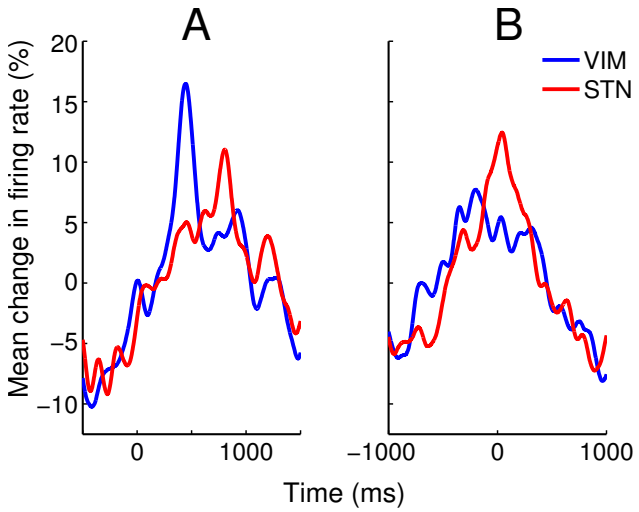

FIGURE 2.4: Mean normalized PETHs for all responsive units (p<0.05) from both subcortical areas using two event triggers: **A** target appearance, and **B** movement time. Reported time is relative to the event trigger. Prior to aggregation, individual PETHs were convolved with a Gaussian kernel (σ=40 ms) and normalized relative to mean firing rate. For both panels, the differences between the mean VIM and STN responses were statistically significant (χ^2 test, $p << 0.001$).

units and multiunits. Of all tested single units, 25.3% of 75 VIM cells and 19.2% of 26 STN cells were found to exhibit directional tuning. Both of these percentages represent statistically significant populations (Binomial test, $p < 0.001$ for VIM, $p < 0.01$ for STN). Figure 2.2c shows example PETHs for three strongly tuned neurons. Similar proportions of VIM and STN cells were tuned to direction (two-tailed Fishers exact test, $p > 0.05$).

Despite the clear separation in the neuronal response to leftward and rightward movements, note the transient regions of convergence that occurred in Figure 2.2c. In Figure 2.2c(iii), for example, the neuronal responses to each direction converged just prior to movement. For many tuned neurons in both VIM and STN, the degree of directional modulation varied throughout the temporal window.

For both VIM and STN cells, we found strong positive correlations between directional tuning strength and the strength of both target tuning and movement

tuning. When controlling for the number of session trials, target tuning strength significantly predicted directional tuning strength ($\beta = 0.16$, $p < 0.05$ for VIM; $\beta = 0.38$, $p < 0.01$ for STN). Similarly, movement tuning strength significantly predicted directional tuning strength ($\beta = 0.24$, $p < 0.01$ for VIM; $\beta = 0.43$, $p < 0.05$ for STN). The latter finding is consistent with the VIM pairwise classification result in Table 2.1.

2.4.3 Properties of multiunits

From Table 2.2, it can be seen that a significant population of analyzed multiunits were tuned to target, movement, and direction (Binomial test, $p < 0.01$ in all cases). A substantial number of these tuned multiunits were found on the same channel as tuned sorted units. Furthermore, when controlling for the number of session trials, the target tuning strength of single units significantly predicted the target tuning strength of same-channel multiunits ($\beta = 0.18$, $p < 0.01$). This suggests the presence of correlated tuning in nearby neurons. Thus, a substantial amount of encoded information has been demonstrated in subcortical multiunits, arguing for the inclusion of these multiunits in future BMI decoding algorithms.

2.4.4 Tremor sensitivity

In order to identify potentially pathological neurons within the recorded subcortical populations, we analyzed the tremor sensitivity of single units using the peri-event phase histogram (PEPH) approach; the results are given in Table 2.3. Of all single units tested, 12.4% of 169 VIM cells and 15.9% of 82 STN cells were found to be correlated to observable hand tremor. Both of these percentages represent statistically significant populations (Binomial test, $p < 0.001$ in both cases). Figure 2.5 shows example PEPHs for three strongly tremor-sensitive neurons. These results demonstrate that for highly tuned units, the dependence of spike rate on tremor

Table 2.3: Tremor tuning of subcortical neurons

Area	Unit type	# Units	# Tuned
VIM	Single	169	21** (12.4%)
STN	Single	82	13** (15.9%)

phase remained stable throughout the recording session (Fig. 2.5a,b,c), even if mean firing rate varied substantially Fig. 2.5a,c. Similar proportions of VIM and STN cells were tuned to tremor (two-tailed Fishers exact test, $p > 0.05$).

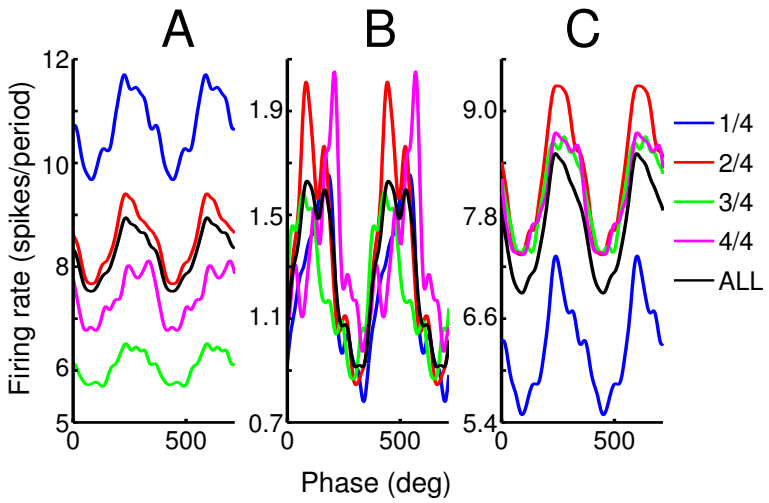

FIGURE 2.5: Example peri-event phase histograms (PEPHs) triggered on hand tremor phase, for strongly tremor tuned units. **A** VIM cell, Patient M, 4478 tremor periods. **B** VIM cell, Patient M, 1259 tremor periods. **C** VIM cell, Patient M, 4642 tremor periods. Zero phase is aligned to local peaks in hand velocity. All panels show individual PEPHs for each temporal quarter of their respective sessions, overlaid with the aggregate PEPH for the session as a whole (ALL). All plots in this figure are smoothed using a Gaussian kernel, $\sigma = 15^\circ$.

For VIM cells (but not STN cells), we found a positive correlation between the strength of tremor tuning and that of directional tuning. When controlling for the number of session trials, directional tuning strength significantly predicted tremor tuning ($\beta = 0.34$, $p < 0.05$). However, we found no relationship between tremor tuning and either undirected target or movement tuning ($p > 0.05$ for all cases).

Table 2.4: Oscillatory units

Area	Unit type	# Units	# Tuned
VIM	Single	274	59 (21.5%)
STN	Single	123	22 (17.9%)

2.4.5 Oscillatory behavior

To explore neuronal oscillations in VIM and STN and their relationship to patient pathology, we inspected the autopower spectra of single unit spike trains for strong frequency peaks. Of all tested single units, the distribution of peak frequencies showed a clear bimodal distribution with a border between low and high-frequency oscillations at about 2.5 Hz (Fig. 2.6). This was particularly true for neurons exhibiting peak $SNR > 2$. The classification results are shown in Table 2.4; 21.5% of 274 VIM cells and 17.9% of 123 STN cells were classified as oscillatory. No difference was seen in the proportions of oscillatory VIM and STN cells (two-tailed Fishers exact test, $p > 0.05$). Figure 2.7 shows example interspike interval (ISI) plots for three highly oscillatory cells. Note that all three ISI histograms exhibit some degree of bimodality, indicative of periodic bursting behavior.

Figure 2.8A shows the smoothed autopower spectra of spike trains for all analyzed single units, with each individually normalized horizontal trace corresponding to a distinct unit. From this figure, one can visually identify some of the highly oscillatory units as well as observe the congruity between multiple units from the same patient. The difference between the mean normalized spectra for VIM and STN cells (Fig. 2.8B) is statistically significant (χ^2 test, $p << 0.001$). From Figure 2.8B, it is clear that STN cells tended to concentrate power at a lower frequency (3 Hz rather than 4 Hz).

The pairwise classification results in Table 2.1 reject the notion that oscillatory neurons and behaviorally tuned neurons form disjoint sets. Furthermore, we found no relationship between spike autopower peakedness and the strength of any of the

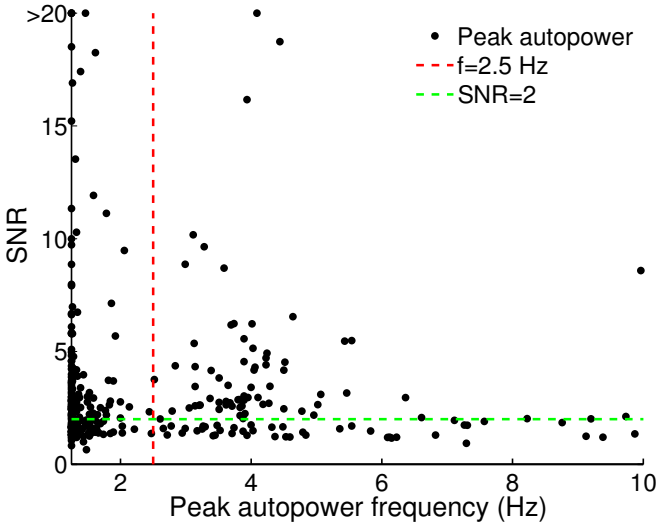

FIGURE 2.6: Distribution of peak frequencies for the spike train autopower spectra of 397 analyzed single units. A clear separation between two subpopulations is clear at about 2.5 Hz. Units with peak frequency above 10 Hz (17.4% of all units) are not shown in this figure; they are distributed with near uniformity in the 10-25 Hz range with SNR mostly below the classification threshold of 2.

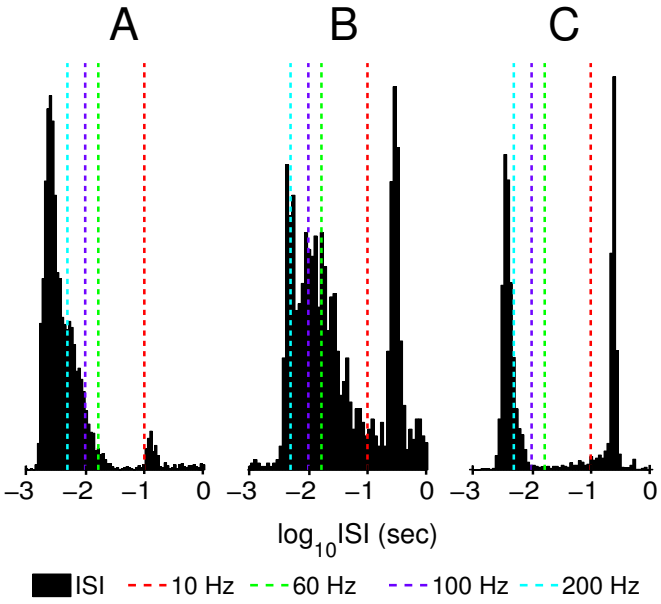

FIGURE 2.7: Example ISI histograms for highly oscillatory neurons. **A** VIM cell, Patient W. **B** STN cell, Patient V. **C** VIM cell, Patient J.

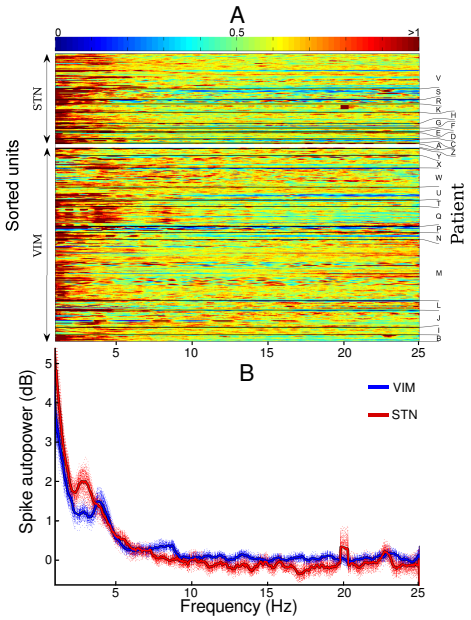

Figure 2.8: **A** Smoothed autopower of spike trains for all sorted units with sufficient spike count. The autopower spectra (determined by Welch's method) of each horizontal trace, corresponding to a distinct unit, has been individually smoothed (using a 0.5 Hz sliding window) and normalized. The horizontal traces are grouped by patient and recording area. The colorbar represents arbitrary units of normalized energy density. **B** Mean autopower spectra from all analyzed VIM and STN cells. Spectra are individually smoothed using a 0.5 Hz sliding window and normalized prior to aggregation. Each of the many dashed traces represents a bootstrap simulation in which only half of all analyzed units are aggregated. The difference between the mean VIM and STN spectra is statistically significant (χ^2 test, $p << 0.001$).

three (target, movement, direction) behavioral tuning metrics ($p > 0.05$ for all cases, for both VIM and STN). The lack of a clear anticorrelation suggests that the sets of behavioral neurons and oscillatory neurons are far from disjoint.

Our next analysis attempted to uncover a relationship between strong oscillatory neuronal patterns and observable hand tremor. However, we did not find any clear relationship. Linear regression analysis revealed no relationship between peak frequency (2.5-7.5 Hz range) of spike train autopower spectra and corresponding hand acceleration autopower spectra ($p > 0.05$ for both VIM and STN). Furthermore, no relationship was found between the sharpness of the two spectra ($p > 0.05$ for both VIM and STN). Figure 2.9 shows overlaid spectra for the spike train autopower

and hand acceleration autopower of three highly oscillatory units. For all three cells (representative of the population as a whole), the peak frequencies do not coincide. On the other hand, we did find a marginally significant (β=0.24, p=0.055) correlation between spike autopower peakedness and tremor tuning strength for VIM cells ($p > 0.1$ for STN cells). These findings call into question the presumed causal linear relationship between the two, suggesting the possibility of an elusive nonlinear relationship.

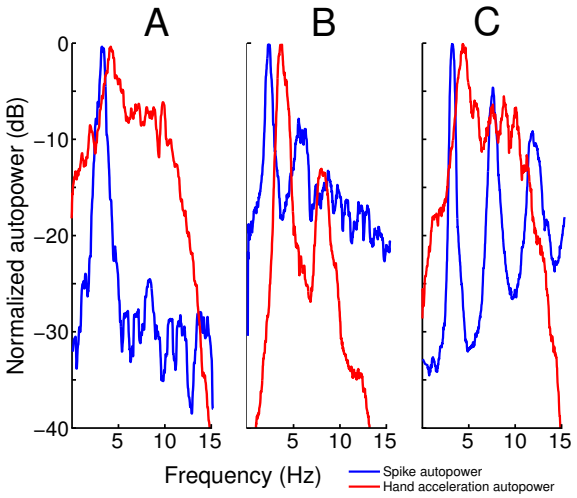

FIGURE 2.9: Comparison of spike train autopower and hand acceleration autopower for three highly oscillatory units. **A** VIM cell, Patient W. **B** STN cell, Patient V. **C** VIM cell, Patient J. Note that for all three cells, peak frequency does not coincide.

Our heterodyne decoding analysis further explored this relationship by applying a nonlinear frequency shifting approach to the autopower spectra. Of 239 analyzed single units, 13.3% of VIM cells and 17.3% of STN cells were found to be tremor associated via heterodyne decoding (Table 2.5). Both of these percentages represent statistically significant populations (Binomial test, $p << 0.001$), but the difference between them is not significant (two-tailed Fishers exact test, $p > 0.05$).

Nonlinear heterodyne encoding, in which the central spectral frequency is shifted,

Table 2.5: Heterodyne tremor tuning

Area	Unit type	# Units	# Tuned
VIM	Single	158	21** (13.3%)
STN	Single	81	14** (17.3%)

may serve to explain the relationship between the oscillatory activity of neurons and observed tremor. Note the similarity in the proportions of tuned neurons in Tables 2.3 and 2.5. Furthermore, in VIM cells we found a strong positive correlation between tremor tuning strength identified using PEPHs and heterodyne tremor tuning strength ($\beta = 0.31$, $p < 0.001$). This relationship was marginally significant in STN cells ($\beta = 0.28$, $p = 0.086$). These findings are consistent with the pairwise classification results in Table 2.1, which for VIM cells indicated a higher than expected joint classification for the two tremor tuning analyses.

2.4.6 Neuronal synchrony

We analyzed neuronal synchrony in pairs of sorted units and investigated how its prevalence and time course varied across subcortical areas; the results are given in Table 2.6. Using the long timescale (ζ) approach, triggered on target appearance, 79.3% of VIM pairs and 90.3% of STN pairs were found to be synchronous. Movement triggering produced similar results: 74.0% of VIM pairs and 91.2% of STN pairs were found be synchronous. All four of these percentages represent significant populations (Binomial test, $p << 0.001$ for all cases). Figure 2.10 shows example $\zeta(t)$ plots for three highly synchronous neuronal pairs.

Using the short timescale cross-correlation approach, 43.0% of VIM pairs and 25.8% of STN pairs were found to be significantly synchronous. Both of these percentages represent significant populations (Binomial test, $p << 0.001$ for both cases). Figure 2.11a shows example cross-correlation plots for three highly synchronous pairs, while Figure 2.11b shows the normalized JPSTH for the same three pairs. Whereas

Table 2.6: Pairwise neuronal synchrony

Parameter	Area	# Analyzed Pairs	# Synchronous
$\zeta(t)$ - Target	VIM	828	657** (79.3%)
$\zeta(t)$ - Target	STN	371	337** (90.8%)
$\zeta(t)$ - Movement	VIM	411	304** (74.0%)
$\zeta(t)$ - Movement	STN	34	31** (91.2%)
Cross-correlation	VIM	1648	708** (43.0%)
Cross-correlation	STN	693	179** (25.8%)

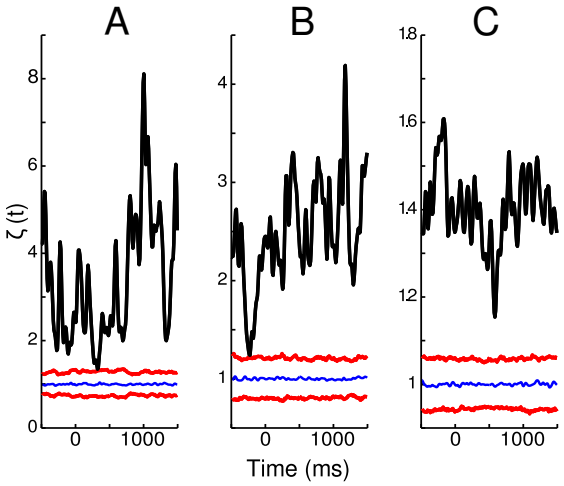

FIGURE 2.10: Example plots of excess joint probability ratio $\zeta(t)$ for three highly synchronous neuron pairs. **A** Pair of STN cells, Patient V. **B** Pair of VIM cells, Patient I. **C** Pair of STN cells, Patient H. For all three panels, the results of bootstrapped $\zeta(t)$ simulations are shown, with mean indicated in blue and 95% confidence intervals (CI) indicated in red. Reported time is relative to target appearance.

Figure 2.11b(i,ii) clearly show temporal synchronization along the diagonal (and off-diagonals), the same result is not visually discernible in Figure 2.11b(iii).

We found highly significant differences between the VIM and STN in terms of the proportions of synchronous pairs. Using the long timescale $\zeta(t)$ approach, a significantly higher proportion of STN pairs were synchronous than VIM pairs, triggered on either target (two-tailed Fishers exact test, $p << 0.001$) or movement (two-tailed Fishers exact test, $p < 0.05$). Interestingly, the result is reversed when considering the short timescale (cross-correlation) approach. Over a shorter timescale, a signifi-

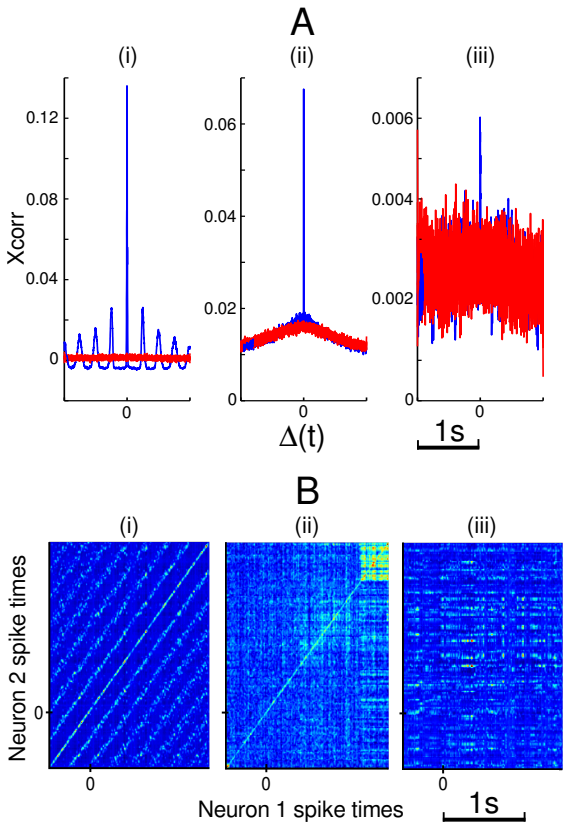

FIGURE 2.11: **A** Example plots of cross-correlation coefficient for three highly synchronously neuron pairs. Bootstrapped simulations of coefficient shown in red. **B** Example normalized JPSTHs for the same three neuron pairs. (i) Pair of VIM cells, Patient I; (ii) Pair of STN cells, Patient H; (iii) Pair of VIM cells, Patient Q. For **A**, reported time is relative to target appearance.

cantly higher proportion of VIM pairs were synchronous than STN pairs (two-tailed Fishers exact test, $p << 0.001$).

It has been reported that the level of tremor in parkinsonian patients is positively correlated to the degree of pairwise synchrony among STN cells . To test the relationship between tremor tuning and local synchrony, we compared the subpopulation of both VIM and STN neurons which were synchronous with at least one other neuron in their respective ensembles (cross-correlation method) to the subpopulation of neurons tuned to hand tremor (PEPH method). Only neurons fulfilling the criteria of both individual analyses were considered. The results are shown in Table

Table 2.7: Comparison of synchrony (cross-correlation method) and tremor tuning (PEPH method)

Tremor tuning (PEPH method)	Synchronized to >1 unit	Not synchronized
Tremor tuned	28	0
Not tremor tuned	137	30

2.7; the observed proportions are significantly different (two-tailed Fishers exact test, $p < 0.01$). Notably, only units synchronized to at least one other unit were tuned to tremor, whereas no unsynchronized units were tuned to tremor.

2.4.7 Efficacy of neuronal recordings for kinematic predictions

We performed offline predictions of cursor motion using the recorded ensembles; the correlation coefficient (mean + 1.96 SE) for each of the sessions is shown in Figure 2.12. Although the predictions varied greatly across sessions and patients, the results compared favorably with the predictive power reported by Patil et al. (2004). The best session for each subcortical area (VIM, STN) was chosen for further analysis, and neuron dropping curves were generated for these two sessions and fitted to a hyperbolic function . Extrapolation of the hyperbolic fit produced estimates of the approximate ensemble sizes required to achieve R2=0.9: 106 VIM neurons or 397 STN neurons.

2.5 Discussion

In this study we analyzed discharges of populations of single neurons recorded in human VIM and STN while patients performed visually guided hand movements. Our results provided further support to our previous proposition that subcortical neurons, if recorded in sufficient quantities, could drive a motor BMI that performs upper-limb movement tasks (Patil et al., 2004). Moreover, we have elucidated characteristics of the activity of subcortical neurons that reflect their representation of motor parameters, as well as characteristics that may be related to pathological states

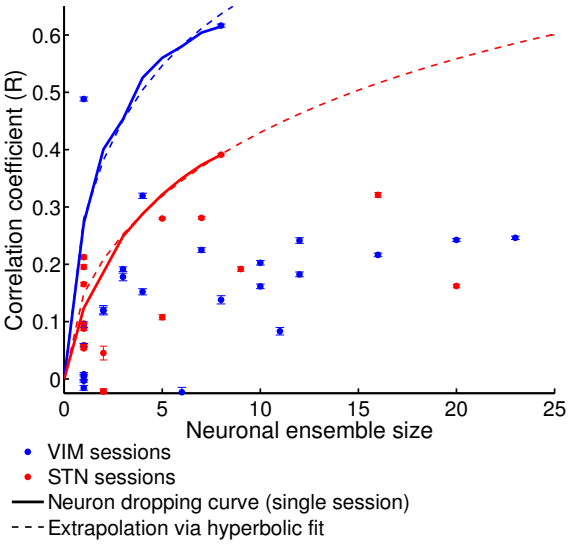

FIGURE 2.12: Dependence of offline BMI predictions on neuron ensemble size. Each data point corresponds to a recording session. Correlation coefficient (R) is indicated as mean + 1.96 SE. The best session for each subcortical area (VIM, STN) was chosen for further analysis. Neuron dropping curves are shown for each of these sessions and fitted to a hyperbolic function (Wessberg et al., 2000). Extrapolation calculations are presented in Results.

tremor sensitivity, oscillations, and pairwise synchrony. Based on these results, we suggest that BMI technology could be used not only to reproduce motor behaviors from subcortical activity, but also to monitor and correct potentially pathological activity such as oscillatory firing and elevated levels of local network synchrony.

2.5.1 Subcortical encoding of behavior

Neurons in both subcortical areas (VIM and STN) were found to encode features of patient motor behavior, both voluntary (hand opening/closing) and involuntary (tremor). With respect to voluntary behavior, a substantial number of neurons were found to be tuned to target appearance, movement onset, and movement direction (Table 2.2). This is remarkable given the simplicity of the target acquisition task and the few hand muscles required for performing it, likely indicating that neurons in both structures are broadly tuned across multiple modalities and muscle groups.

This observation is consistent with previous studies, since it has been reported that STN neurons have large receptive fields that respond to multiple joints (Abosch et al., 2002), with 40% of STN cells tuned to movement in a simple two-dimensional joystick task (Williams et al., 2005). Theodosopoulous et al. found that 42% of cells within the STN responded to passive movement of either arm or leg, and of these, 25% responded to multiple joint movements (Theodosopoulos et al., 2003). Lenz et al. reported that 51% of VIM neurons were tuned to sensory stimuli, with an overlapping 10% of these cells tuned to volitional movements (Lenz et al., 1990).

In some neurons, we were able to clearly visualize the bimodal encoding of target and movement (Fig. 2.3), demonstrating what appears to be linear superposition of two independent rate codes. Furthermore, we observed a significant overlap between tuning to target appearance and to movement onset. Additionally, in both subcortical areas, directional tuning strength was positively correlated to movement tuning strength, indicating that individual neurons encoded both parameters by exhibiting both common mode and differential activity relative to movement onset (Fig. 2.2). Thus, neurons from both subcortical areas exhibited a distributed encoding of task parameters.

Differences in the relative lags for VIM and STN neuronal activation (Fig. 2.4) likely reflect the position of thalamic and STN circuitry in the network hierarchy of motor control (Gradinaru et al., 2009; Guillery and Sherman, 2002; Marsden et al., 2001). The motor regions of thalamus are more involved with intention, with signals arriving prior to motor cortex activation, whereas the collaterals from motor cortex to STN deliver signals at the time of motor activation. This neuroanatomical knowledge, along with the observed multimodality in task parameter encoding, should instruct the future development of custom BMI algorithms for subcortical neurons.

Our analysis of involuntary motor activity (tremor) yielded significant populations of tremor tuned cells (12.4% for VIM, 15.9% for STN); phase histograms demon-

strate clear phase-locking between neuronal activity and tremor periods (Fig. 2.5). However, these results do not distinguish whether these tremor tuned neurons are involved in a pathological mechanism that causes tremor or merely reflect sensory signals indicative of tremor. There is a large range in the published literature with regard to the prevalence of tremor-related cells in these subcortical areas; our STN result falls within this range while our VIM result falls below it. For STN, reported percentages are 11%, 52%, and 19%, (Amtage et al., 2008; Magarinos-Ascone et al., 2000; Rodriguez-Oroz et al., 2001), respectively. For VIM, reported percentages are 34%, 35.6%, and 51%, (Hua and Lenz, 2005; Lenz et al., 1988; Zirh et al., 1998), respectively. Disparities are most likely due to differences in recording parameters and classification methodology. With respect to the latter, these researchers classified tremor tuning using linear coherence between spike train and recorded electromyograms (EMGs) rather than end position.

We found overlap between tremor tuned neurons and those tuned to parameters of voluntary behavior (Table 2.1), and we observed a positive correlation between tremor tuning strength and directional tuning strength (VIM cells only). These results are consistent with Magarios-Ascone et al (Magarinos-Ascone et al., 2000) and Rodriguez-Oroz et al. (Rodriguez-Oroz et al., 2001), both of which reported that a large proportion of tremor-related STN cells were simultaneously related to voluntary movements either through motor or sensory loops. We speculate that the suppression of tremor cell activity using therapeutic DBS may have a side effect of disrupting voluntary motor commands. This result also has an implication for BMI technology, indicating that tremor tuned neurons should not be omitted from the ensemble during decoding.

2.5.2 Elusive relationship between oscillatory activity and tremor

Spike train spectra from VIM and STN neurons tended to possess large amounts of energy at low frequencies, as in 1/f (pink) noise. This power-law distribution has been described for cortical neurons and has been explored as a stochastic process (Davidsen and Schuster, 2002), but alternatively may have been related to slow modulations of patient attention and motivation. This distribution is likely sufficient to explain the 2.5 Hz trough (Fig. 2.6) which separates neurons dominated by 1/f noise from those exhibiting strong oscillations in a tremor-relevant frequency range (2.5-7.5 Hz). Within this range, we observed a substantial population of VIM and STN cells exhibiting strong ($SNR > 2$) oscillations (Table 2.4). Furthermore, we found that the mean autopower spectra for recorded VIM cells had a higher peak frequency than that of recorded STN cells (Fig. 2.8b). This finding is consistent with a higher mean tremor frequency in ET patients; Deuschl et al. (Deuschl et al., 1998) reported 4-12 Hz as the typical range for ET patients and 3-6 Hz as the typical range for PD patients.

Whereas Rodriguez-Oroz et al. (2001) reported that oscillatory cells in STN did not represent movements, we found moderate overlap (Table 2.1) between VIM and STN neurons exhibiting oscillations and those tuned to voluntary behavioral parameters (target, movement, direction). Similarly, we found overlap but no significant correlation between the presence of oscillatory patterns and tremor tuning in both subcortical areas. This finding corroborates the claims of Magnin et al. (Magnin et al., 2000) and Rodriguez-Oroz et al. that in ventral thalamus and STN, respectively, the sets of tremor-related neurons and oscillatory neurons show modest intersection. In other words, not all tremor-related neurons exhibited oscillations, and some oscillatory neurons exhibited no clear association with tremor.

Furthermore, linear methods revealed no relationship between peak spike train

frequency and peak hand acceleration frequency (Fig. 2.9). The prospect still remains for an elusive nonlinear relationship between neuronal oscillations and hand tremor. We hypothesized that for some cells, spike train and tremor co-modulated via different carrier frequencies. Our heterodyne decoding results suggest that a substantial number of cells in both subcortical areas may be tremor tuned in this manner (Table 2.5). Overall, no consensus in the field has been reached regarding the definitive relationship between oscillatory behavior and tremor tuning.

2.5.3 Network synchrony: genesis or indicator of tremor?

A very high percentage of neuronal pairs recorded in both subcortical areas exhibited synchronous behavior, both over long and short timescales (Table 2.6). This is generally consistent with reports of pairwise synchrony in the majority of analyzed STN pairs (Levy et al., 2002, 2000). It should be noted that we observed high levels of functional synchrony in neuronal pairs that were much further apart than the sub-mm separation in the Levy studies. Patients implanted in VIM exhibited significantly higher synchrony over a short timescale (tight temporal locking of spike times), whereas patients implanted in STN exhibited significantly higher synchrony over a long timescale (slow co-modulations in firing rate).

Only cells exhibiting short timescale synchrony with another cell in the ensemble were found to be tremor tuned; no unsynchronized cells were tremor tuned (Table 2.7). This finding corroborates reports that the prevalence of STN pairs synchronized at high frequencies is correlated to the degree of parkinsonian tremor (Levy et al., 2000) and that patients without observable tremor do not exhibit high frequency STN synchrony (Levy et al., 2002). As in the case of individual tremor tuned cells, it remains unclear to what degree network synchrony is tremorgenic or passively indicative of tremor pathology. The efficacy of DBS as a medical intervention suggests the former, in which case applied stimulation would disrupt the activity of unstable

networks.

2.5.4 Subcortical recordings in BMI applications

Our reported offline prediction results from our best VIM and STN sessions are comparable to those reported from selected rhesus macaque cortical regions with the same number of neurons (Carmena et al., 2003; Wessberg et al., 2000). However, hyperbolic extrapolation suggests that we would need to increase our ensemble size by more than an order of magnitude to achieve R2=0.9. Furthermore, there are several reasons to expect that subcortical BMI may require larger ensembles than cortical BMI to achieve the same level of performance: broader/weaker somatotopic and parametric tuning, lower demonstrable levels of volitional control over neuronal activity, and a high level of local synchrony which would degrade expected BMI performance via mutual information (particularly in patients exhibiting pathology).

Future developments in subcortical BMI will require chronic recordings of much larger neuronal ensembles. This will necessitate the design of denser microelectrode arrays for cannula-based implantation with demonstrable long-term safety and recording efficacy. As with cortical implantation in rhesus macaques, chronic recordings of subcortical areas will allow time for stabilization of the electrode-tissue interface and recovery of the implanted tissue from local network disruption.

We have demonstrated that microelectrode recordings in the VIM and STN provide useful information about the properties of single neurons and their relationship to behavior and pathology. In addition to motor control, subcortical BMI offers promise for long-term monitoring of potentially pathological activity such as oscillatory firing and elevated levels of local network synchrony. Furthermore, in parkinsonian patients we propose that a hierarchical combination of cortical and subcortical BMI could be used to decode motor intention and/or motor error (due to tremor, bradykinesia, dyskinesia, etc.). These signals would be used to modulate stimulation

parameters of the implanted DBS or other targets such as the spinal cord (Fuentes et al., 2009). Given the extensive number of DBS patients implanted worldwide, such a closed loop neuroprosthetic would advance neuroscience and neurorehabilitation alike.

3

Microstimulator

3.1 Abstract

Electrical stimulation of nervous tissue has been extensively used as both a tool in experimental neuroscience research and as a method for restoring of neural functions in patients suffering from sensory and motor disabilities. In the central nervous system, intracortical microstimulation (ICMS) has been shown to be an effective method for inducing or biasing perception, including visual and tactile sensation. ICMS also holds promise for enabling brain-machine-brain interfaces (BMBIs) by directly writing information into the brain. Here we detail the design of a high-side, digitally current-controlled biphasic, bipolar microstimulator, and describe the validation of the device in vivo. As many applications of this technique, including BMBIs, require recording as well as stimulation, we pay careful attention to isolation of the stimulus channels and parasitic current injection. With the realized device and standard recording hardware - without active artifact rejection - we are able to observe stimulus artifacts of less than 2 ms in duration.

3.2 Introduction

Numerous studies have shown that electrical microstimulation of neural circuits by injecting small currents from an electrode tip into the nervous tissue may evoke a variety of effects that are often similar to the functional contribution of the stimulated area (Tehovnik et al., 2006). In particular, microstimulation can produce or bias sensations (Bartlett et al., 2005); (Salzman et al., 1990); (Britten and van Wezel, 1998); (Romo et al., 2000, 1998); (Fitzsimmons et al., 2007) (O'Doherty et al., 2011a). This property of bioelectrical stimulation has attracted the attention of neural engineers as the key component of sensory neural prosthetics for the restoration of sensation in patients suffering from sensory disabilities.

Microstimulation has been introduced as a sensory loop in brain-machine-brain interfaces (BMBIs), systems that both translate brain activity into commands to artificial actuators and deliver information to the brain in the form of microstimulation of sensory areas. In experiments conducted in our laboratory, we utilized temporal patterns of cortical microstimulation to create an artificial somatosensory input for the BMI that enacted arm reaching movements(O'Doherty et al., 2009). More recently, our laboratory has demonstrated closed-loop BMBI control for delivering artificial texture feedback through ICMS(O'Doherty et al., 2011a), where precise, rapid, and low-artifact ICMS control was essential to give feedback to the monkey without interfering with recording periods. Here we describe our custom multichannel microstimulator that enabled these BMBIs.

Intracortical microstimulation (ICMS) poses a number of exacting requirements on the experimental system. ICMS requires relatively high voltages (50-100 V) when high impedance (0.5-2 MΩ) electrodes are used (Afraz et al., 2006; Hanson et al., 2008; Nicolelis et al., 2003). Furthermore, the useful stimulation waveform durations are usually very short (10 μs to 100 μs) (Afraz et al., 2006; Bartlett et al., 2005;

Brindley and Lewin, 1968); (Fitzsimmons et al., 2007; Hanson et al., 2008). The waveform most frequently used is a charge balanced, symmetric, biphasic stimulation pulse, where a square cathodic pulse is followed by an anodic pulse of equal amplitude (Grill and Mortimer, 1995). Although the second pulse can reduce the excitation of the tissue, damage to the electrode and tissue is prevented by this charge balancing pulse. The impairing effect of the second pulse can be partially counteracted by a short (100 μs) delay between the two pulses (McIntyre and Grill, 2000)). Due to the variable electrode to tissue impedance, and response of the tissue to charge, cortical stimulation is usually performed with constant current sources (Merrill et al., 2005). In terms of safety, the range of figures quoted here – 100μs pulses of 100 μA/phase – equates to 10nC/phase, well within the regions described by (McCreery et al., 1988). Charge density using our 65μm electrodes is 300 $\mu C/cm^2$/phase, which is also within the safety limits proposed by (Shannon, 1992).

The current, voltage and timing requirements are not difficult to achieve with modern electronic systems, and many commercial products are available that satisfy the conditions. However, for advanced ICMS studies, the complexity of the stimulus train and number of electrodes enforce more rigorous requirements on stimulation technology. There is immediate need for advanced microstimulation systems capable of operating as ICMS feedback systems in BMBIs (Lebedev and Nicolelis, 2006); (Fitzsimmons et al., 2007); (O'Doherty et al., 2009);(Marzullo et al., 2010). These systems require microstimulation in multiple sites in the brain, using multiple electrodes and complex spatiotemporal stimulation patterns (Fitzsimmons et al., 2007; London et al., 2008; O'Doherty et al., 2009), delivered at low latency to enable closed-loop control (O'Doherty et al., 2011a). It is critical for these systems to induce artifacts of minimal duration to adjacent recording sites to maximize recording quality in BMBIs.

Our stimulator is high-side current controlled, which nearly eliminates the charge

Table 3.1: Microstimulator Specifications

Parameter	Value
Compliance	50V(160V max)
Current	800μA
Current resolution	0.2μA
Output impedance	>10MΩ
Leakage current	300pA
Parasitic current injection	30pC/pulse
Charge imbalance	-0.094$\pm$0.56 nC
Channel isolation	15pF
Timing resolution	10μs
Timing latency	5.4 ms$\pm$180 μs
Power	300mW/channel
Size	13 cm x 2.5 cm/channel
Channel count	15 (bipolar/monopolar)

and discharge current of stray capacitance between each isolated channel and animal ground. High-side means that the compliant current source is tied to the voltage rails, not ground; with a low-side current source, the current regulator develops voltage across it depending on electrode impedance, voltage that is presented to the stray capacitance of the microstimulator and experimental wiring. Since currents associated with charging and discharging voltage offsets from stray capacitance must necessarily go through the stimulation electrodes, and ultimately through the ground that connects the animal to wired recording systems, voltage offsets should be minimized for both accuracy and artifact avoidance. High-side current control is, to the best of our knowledge, unique to this design. Further artifact suppression can be achieved through close-proximity bipolar biphasic stimulation, which restricts the spread of electric field within the tissue while remaining efficacious (Fitzsimmons et al., 2007). Finally, the described stimulator is highly flexible: both the current and duration of both phases of the biphasic stimulus waveform can be controlled continuously from a computer with tight synchrony. This computer control permits stimulus trains of arbitrary complexity to be enacted in real-time as needed for a BMBI.

It should be emphasized that the construction and testing of this device was done explicitly for a tethered research environment – that is, where the microstimulator is not mounted on or in the experimental animal – as no commercially available microstimulators were available to permit high temporal fidelity, high flexibility (any pattern can be commanded), high compliance, good current resolution, good channel isolation, minimum parasitic current injection, and a flexible number of channels. Full specifications of the described device are listed in Table 3.1. Given these design criteria the size of the device is large and consumes 300 mW per channel. In comparison, other research into microstimulators such as the clinically-targeted Bion (Kane et al., 2011) are much smaller and lower power, but correspondingly much more expensive, less flexible due to their high level of integration, and not matched for the high compliance voltage required by our electrodes. Integrated ASIC microstimulators such as (Hassell et al., 2007) and (Ghovanloo and Najafi, 2007) offer compliance of 11V or less, which is insufficient to drive current through high-impedance (more than 100kΩ) electrodes; full systems described in (Myers et al., 2006) offer insufficient latency and bandwidth for our experimental requirements. Finally, the current-mirror topology of integrated microstimulators does not guarantee low leakage current, which is critical as DC current will gradually erode the tips of electrodes and damage neural tissue.

3.3 Methods

3.3.1 Microstimulation system

The full microstimulation system is comprised of four principal elements: high-level control programs (web interface, UDP sever), a low-level driver/DMA control program, stimulus isolation channels, and the stimulation electrode array (including lead system). Software control of the microstimulation system is depicted in Figure 3.1.

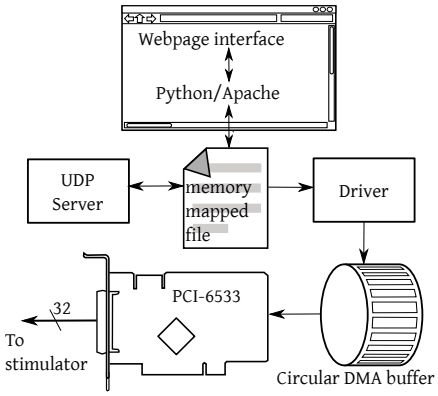

FIGURE 3.1: Schematic overview of software control of the microstimulator.

3.3.2 Software control

Interactive control of the microstimulator is through a custom driver program. This program, which runs on a dedicated computer Linux running a low-latency kernel, services a free running National Instruments PCI-6533 card, which continually outputs 16 or 32 bits of digital data at a clock rate of 100 kHz. These digital data consist of multiplexed control pulses and serial peripheral interface (SPI) commands to set the channel current. Data to be output are read by the PCI-6533 from a circular DMA buffer, the address of which is acquired through a custom Linux kernel module. The driver maintains the DMA buffer via a set of watermarks, placement of which depends on the speed of the computer and its peripheral subsystem. To prevent underflow, typically this is less than 200 samples, which translates to a delay of 2 ms at the 100 kHz clock rate. Between DMA servicing cycles – when the watermark criteria are satisfied – the driver program interprets control commands written to a common memory-mapped file.

Microstimulation commands can either be issued through a python-based web interface, or from a UDP server. The latter allows the stimulator to be controlled through Matlab or from other experimental software, such as the BMI software developed in our lab. The web interface allows easy user control of all parameters

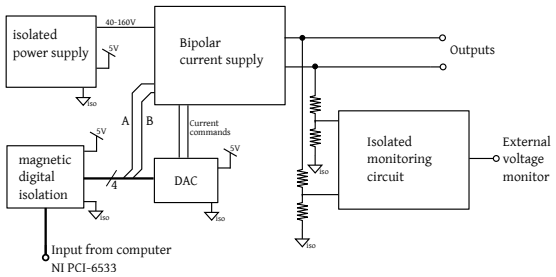

FIGURE 3.2: Schematic overview of one stimulator channel.

of stimulation, e.g. current amplitude, pulse width, frequency, and secondary frequency from any networked computer. The present software implementation allows the stimulation pattern to be a single pulse, a continuous train of pulses, a pulsed stimulation train, a doubly-pulsed stimulation train corresponding to three periods and duty cycles (Hanson et al., 2008), or a stochastic stimulus train derived from a gamma distribution. More complicated stimulus programs can easily be added to the driver program to provide more sophisticated feedback. In the experiments described in (O'Doherty et al., 2011a), where 50ms of BMI decoding alternated with 50ms of microstimulation, we minimized kernel overhead and tightened DMA watermarks so that the latency from BMI command to stimulation, including UDP transmission over ethernet, was $5.4\,\text{ms}\pm180\,\mu\text{s}$ (mean$\pm$standard deviation). This low-variance latency permitted precisely timed ICMS feedback.

3.3.3 Stimulus isolation units

Four stimulator channels are assembled on a circuit board, providing independent and isolated monopolar or bipolar stimulation per electrode. Four of these boards can be stacked and serviced by one PCI-6533, for a total of 15 stimulation channels[1]. An overview of a single channel is shown in Figure 3.2.

There are four primary elements to each channel: the power supply, digital-

[1] The PCI-6533 has 32 digital input/output channels, and each channel requires two lines plus two common signals for all channels, hence only 15 channels can be controlled from one PCI-6533 card.

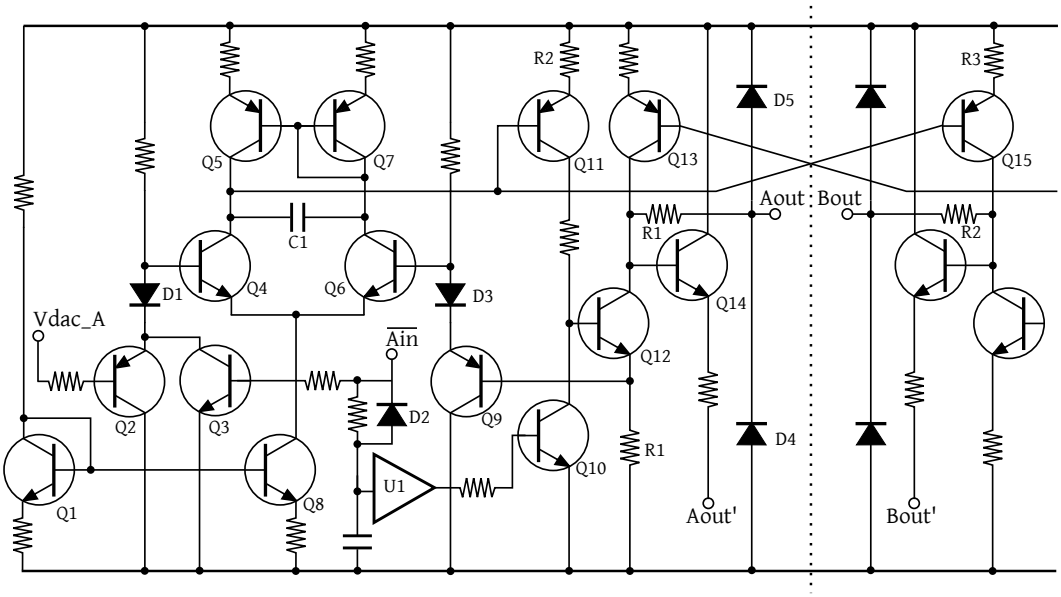

FIGURE 3.3: Detailed schematic of one-half of the voltage-controlled high-side current source. This topology is mirrored to provide a bipolar current source from one voltage supply. The mirror axis is shown by the dotted line.

to-analog converter (DAC), bipolar current regulator, and an isolated monitoring circuit. The isolated power supply uses two series 1 W miniature DC-DC converters to provide 40-160 V for high compliance / high impedance electrodes. An additional 1 W DC-DC converter is used to supply 5 V for the DAC and other circuitry. Current is commanded via the SPI DAC, with separate commands for the anodic and cathodic phases; the command signals for each DAC (clock, data, chip select, load output) are multiplexed with the anodic and cathodic pulse commands so only four signals need pass through the magnetic isolator. Stimulation is enabled with the inverted DAC chip select signal; current amplitude can hence be changed whenever stimulation pluses are absent. Chip select and DAC load output signals are common among all channels, thereby requiring the total number of digital control signals to be two plus twice the number of channels; in turn this means currents on all channels must be set (but not necessarily changed) at the same time.

The core of the stimulation unit is a voltage-feedback high-side current source,

shown in Figure 3.3. It is vital that the current source is high-side, as the topologically simpler low-side control alternative necessitates that during the anodic and cathodic phases the current needed to charge the stray capacitance from one channel to ground must pass through the output electrodes. Note the current source is a symmetric H-bridge, so for clarity only half is fully shown in the figure. Briefly, each half receives two inputs: a voltage command from the DAC into Vdac_A, and an inverted pulse command on Ain. Transistors Q2 and Q9 act as common-collector amplifiers to detect differences between voltage across the sense resistor, R1, and Vdac. Transistors Q4-Q7 act as a differential amplifier to set the current through Q11 and Q15. The latter directly controls the current into the opposite electrode in the pair, while the former supplies current to turn on the lower leg of the H-bridge, Q12. Note that base current into Q12 also goes through the sense resistor R1, so the current command is off by a fraction set by the ratio of resistors R2 and R3 * β_{Q15}. This offset is measured below and corrected in software. Capacitor C1 controls the slew rate of the Q4-Q7 pair, and prevents feedback oscillations. Finally, Q3 and Q10 serve to turn off the output stage when the control signal goes high; Q10 is essential for draining base charge on Q12 and returning the output to a high impedance condition. Buffer U1 serves to delay this command to Q10, allowing Q12 to remain on for about 4 μs longer so as to discharge any residual charge on the electrodes, and hence between the animal ground and isolated ground. As mentioned before, this is to minimize artifact on neighboring recording electrodes. Transistor Q3 is saturated on when output is disabled, which turns Q5 on through the current mirror, hence setting the base current of Q15 to zero; this means that stimulator leakage current is dominated by the off-state current mismatch through Q15 and Q12, which is measured to be less than 300 pA. It was chosen to make the output high-impedance when off rather than short-to-ground to further minimize noise injection.

For safety, diodes D4, D5 and their mirrors serve to protect the output stage from

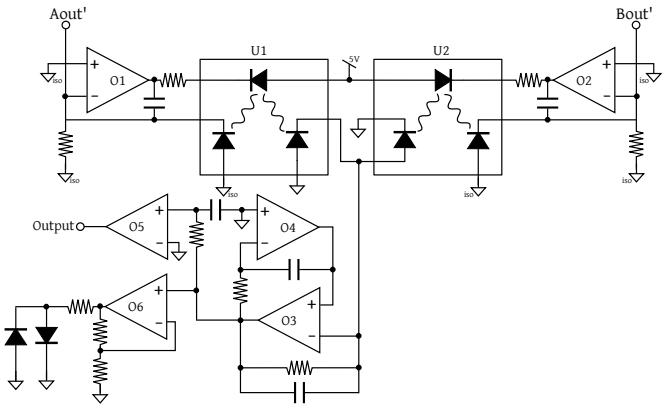

FIGURE 3.4: Isolated monitoring circuit.

ESD damage along with resistors R1 and R2. If this topology is used in a clinical setting, further protection will need to be added, as failure-to-short of any transistor can tie one half of the H-bridge to a supply rail, and failure of two transistors can permit unregulated DC current through the electrodes. In the implemented boards, all transistors are rated at 185 V or higher, while the supply voltage is typically 50 V; no semiconductor failures have observed in several years of operation, though one channel in one stimulator was disabled prior testing due to internal PCB delamination. This is best fixed by simply using a thicker medical-grade PCB. Finally, While there are no hardware limits on the duration of delivered current, we have observed no software failures leading to DC current applied to the animals. Transistor bias currents limit total current delivered per channel to 800 μA.

The isolated monitoring circuit stage is shown in Figure 3.4. Blocks U1 and U2 contain one infrared LED and two matched photodiodes. Opamps O1 and O2 regulate the LED current to match the photodiode current to that from inputs Aout' and Bout' (see Figure 3.3); this mirrors the current onto the non-isolated photodiode pairs. Opamp O3 converts the resulting non-isolated bipolar photodiode current to a voltage, and opamp O4 works to null DC differences due to photodiode imperfections. In turn, O6 drives indicator LEDs, and O5 the final output, which can be viewed on

an oscilloscope or digitized. Because the current command and resultant voltage are known, this circuit allows electrode resistance to be easily calculated.

3.3.4 Electrodes

The electrodes used in testing this system were fabricated in-house at the Duke University Center for Neuroengineering (DUCN). The electrodes work well for both chronic multisite neural ensemble recordings and for stimulation. The DUCN microelectrode arrays consist of tungsten or stainless steel microwires with teflon, SML, or HML insulation. The overall diameter of the microwires is in the range of 25-65 μm, and the separation of electrodes in the array is the range of 200-1000 μm, center to center, depending on the brain area targeted, the animal species, and the experimental protocol (Lehew G, 2008). For all testing and validation use of the system reported here, we stimulated between two of electrodes chosen from an arrays constructed with stainless steel microwires and HML insulation.

3.3.5 Assembly and Testing

Electrical schematics were designed in the open-source Kicad software suite; the PCB was designed in Kicadocaml then manufactured by Imagineering Inc. (Elk Grove, Illinois). We elected to use entirely discrete components in this device for manufacturing ease and cost; the current regulator and other parts could be integrated in a high-voltage bipolar process. The smallest components placed were 0402 chip resistors and capacitors, though the majority of the PCB is populated with 0603 scale resistors and transistors, only on the top of the board; this leads to a total PCB area for 4 channels of 187 cm^2 with a mass of 120 g. As mentioned in the introduction, this is much larger than comparable microstimulator ASICs designed for implantation, which are less than 1 cm^2, but the device meets its intended research purposes. Four PCBs can be stacked to obtain 15 stimulation channels. A photograph of the

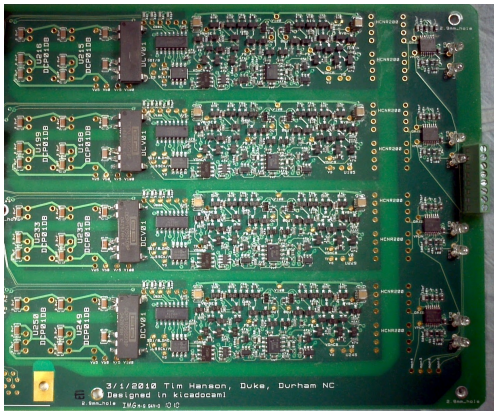

FIGURE 3.5: Photograph of a populated PCB featuring four bipolar channels; input is on the lower left, output on the right.

assembled PCB is shown in Figure 3.5.

3.4 Results

3.4.1 Bench-top testing

The system was first tested using resistive loads to verify proper circuit performance and timing. Figure 3.6 shows the output of the simulator through a 100 kΩ resistor and the resultant isolated monitoring output. The latter has a voltage attenuation of 25 to allow headroom for measuring large-amplitude signals or high-impedance electrodes. In practice, the waveforms have much lower slew rate due to the capacitance of the wire between electrode and microstimulator and the nonlinear charge/discharge profile of the electrode-tissue interface.

The implemented system is capable of a current range of 0-400 μA or 0-800 μA, depending on the DAC output scaling. Output currents larger than this will require different bias currents in the bipolar current regulator, hence a few component values would need to be changed. The stimulator features a measured maximum voltage compliance of 160V, and an output parallel resistance of greater than 10 MΩ. To characterize the slew rate of the current source, rise and fall times of the pulse output were measured across a 118 KΩ resistor for varying currents. Rise and fall times are

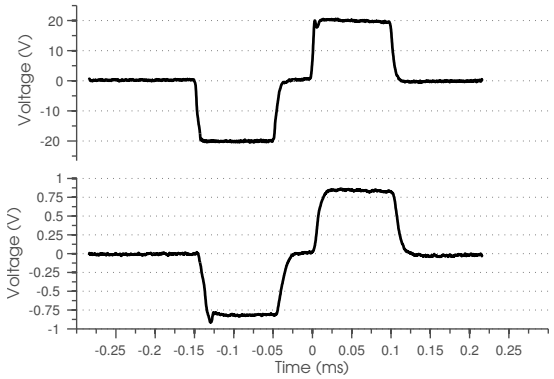

FIGURE 3.6: Top, output of microstimulator through a 100 kΩ resistor, current set at 200 μA, anodic and cathodic phases set to 100 μs, delay between pulses 50 μs. Bottom, simultaneous output of isolated monitoring circuit.

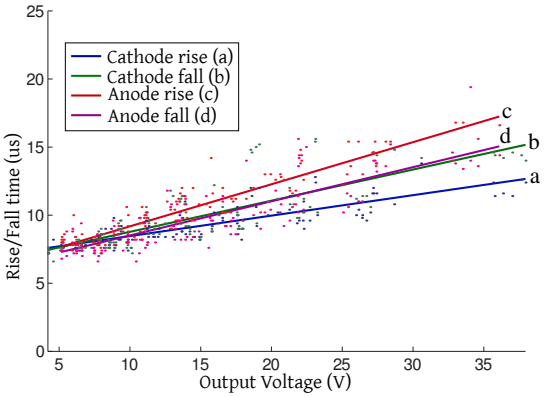

FIGURE 3.7: Rise and fall times for anodic and cathodic phases. Slight differences may be due to the fact that this was measured with one oscilloscope probe, hence the anodic pulse had to charge stray capacitance whereas the cathodic did not.

defined as the time for the voltage to increase from 10% to 80%, and to fall from 80% to 10% of the output amplitude, respectively. As can be seen in Figure 3.7, the rise and fall times ranged from 6-20 μs for output voltages of 5-38 V, with longer rise and fall times at higher output amplitudes. This corresponds to a slew rate of 5 V/μs at larger amplitudes; this may be decreased by increasing the value of capacitor C1 in Figure 3.3.

As mentioned above, the current output is less than the commanded output current by the base current of transistor Q12 in Figure 3.3. This current was set

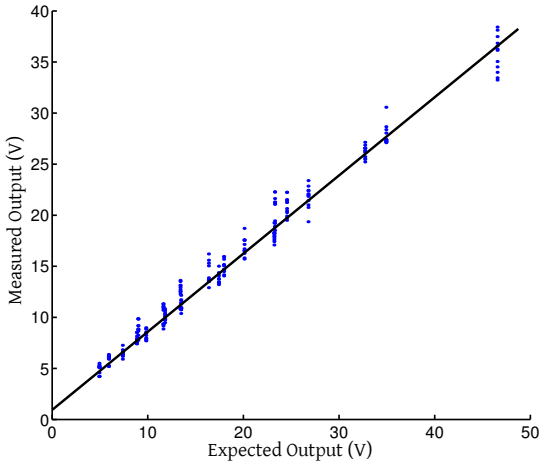

FIGURE 3.8: Expected vs. actual pulse amplitude for several current settings and resistive loads.

conservatively in the present implementation to allow higher output currents, hence must be corrected in software. To calibrate the device, we tested the output across 97, 120, 180, 240, 270, 330, and 470 kΩ resistors, with current amplitudes of 50, 75 and 100 μA. Figure 3.8 shows the result of this calibration, in which the trend line, found using linear regression, has slope of 0.745. The pulses measured in this test were deemed to have started when the voltage reached 50% of peak amplitude, and to have ended when the voltage dropped to 50% of peak amplitude. The output voltage amplitude is defined as the mean voltage during that interval.

Using these criteria, we also measured the distribution of pulse widths, shown in Figure 3.9. For a 100 μs command pulse, the distribution of measured pulse widths was found to have a mean of 92$\pm$1.3 μs. The charge balance of each stimulation pulse was calculated, and the distribution is shown to the right. The mean charge imbalance for commanded pulses was -0.094$\pm$0.56 nC. For comparison, the charge delivered in each phase is 5-10 nC, so this imbalance is only on the order of 1-2%.

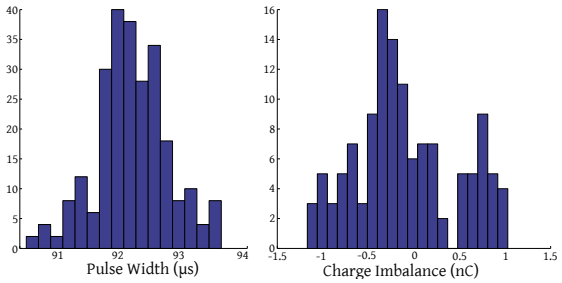

FIGURE 3.9: Left, distribution of measured pulse widths for a 100μs command pulse. Right, distribution of charge imbalance for pairs of anodic-cathodic pulses.

3.4.2 In Vivo testing

To characterize the stimulator in intended application, we examined the effects of ICMS in a rhesus monkey chronically implanted with multielectrode arrays bilaterally in motor and sensory cortices. In the first of these tests, we applied stimulus trains consisting of 150 μs long, 100 μA anodic and cathodic pulse pairs separated by a delay of 25 μs. Fifty of these pulse pairs were applied with an inter-pulse interval of 10 ms to electrodes spaced at 1 mm in the arm representation of the left primary motor cortex (M1). Simultaneously we recorded using a Plexon Inc. (Dallas, TX) Multi-acquisition processor (MAP) from electrodes implanted in the arm region of M1 of the opposite hemisphere, using standard spike (passband: 170 Hz-8 kHz, gain:1000) preamplifier boxes and custom headstages with a gain of 8 and one high-pass pole at 560 Hz.

In Figure 3.10, trace A was recorded from a blunt-cut 50 μm Teflon-insulated stainless electrode at +15.5 mm lateral the mid-line, +4.5 mm rostral the intra-aural line, or 32 mm from the center of the dipole created by the stimulating electrode. Trace B is from the same type of electrode, at +12 lateral, +10 rostral, making it 29.2 mm from the stimulating dipole; trace C is from a sharpened HML-insulated 65 μm stainless electrode +15 lateral, +6 rostral, hence 31.5 mm from stimulating dipole. Despite the fact that all three recordings were from about the same distance from

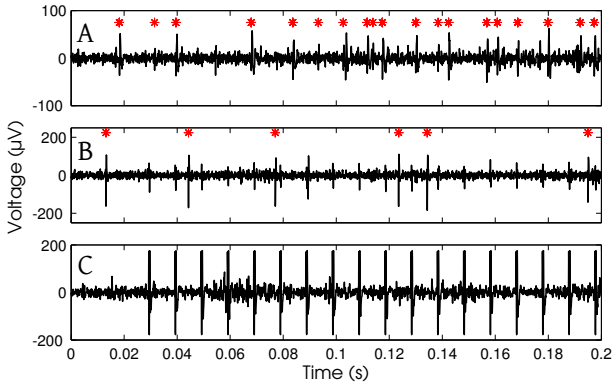

FIGURE 3.10: Three example voltage traces recorded from different electrodes in right M1 arm region of a rhesus macaque. Traces show varying amounts of stimulus artifact and simultaneous extracellular action potentials, as sorted in the Plexon software, indicated with red asterisks. Channels **A** and **B** were referenced to a reference electrode, hence have a smaller artifact. Channel **C** was referenced to animal ground.

the stimulating dipole, the top trace shows no stimulation artifact, the middle shows a small stimulation artifact, and the bottom shows a large stimulation artifact. The differences are likely due to different referencing for the three channels – channels A and B were referenced to electrodes in the microelectrode array functionally identical to the recorded electrode, while channel C was referenced to animal ground, which is connected to T-bolts implanted through the scull. In the Plexon preamplifier, reference channels are subtracted from individual electrode channels to cancel out common-mode noise; it can work well though better methods exist (Rolston et al., 2009b).

To further test the degree to which microstimulation interferes with neural recording, we needed to increase the artifact on channels A and B shown in Figure 3.10. As increasing the spacing between electrodes increases the size of the associated electric field, we made the distance between the stimulating electrodes as 5.6mm, as large as possible within one microelectrode array in the chronically implanted monkeys. Figure 3.11 shows the resulting traces, which indicate accordingly that the artifact

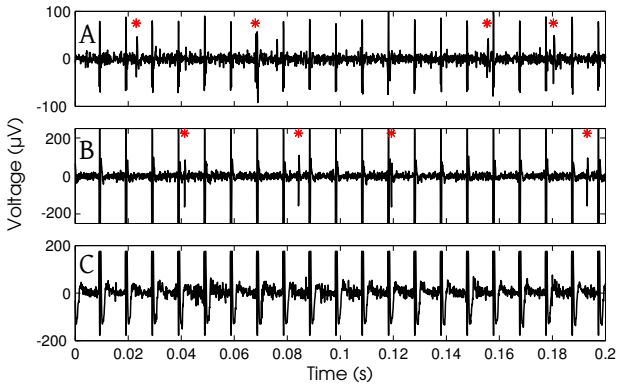

FIGURE 3.11: Three electrode traces recorded from right M1 arm region of a rhesus macaque. Stimulus artifact resultant 100 μs, 100 μA anodic and cathodic pulses separated by a delay of 100 μs. **A,B,C** as 3.10, only distance between stimulating pair was increased.

has increased as compared to figure 3.10.

Importantly, neuronal spikes are clearly still visible in between stimulus artifacts on Figure 3.11 traces A and B. Trace C shows a broader artifact that may occlude spikes. To accurately determine the width of these artifacts, we next recorded continuously for one hour, again from several microelectrodes located in the arm representation of M1 while stimulating the contralateral hemisphere with 100 μs, 100 μA anodic and cathodic pulses separated by a delay of 100 μs. These pulses were applied once a second (1Hz) to two electrodes spaced at 1 mm, the same electrodes as in Figure 3.10.

Figures 3.12 and 3.13 show the two extremes of the result of this test: Figure 3.12 shows a channel that was very minimally effected by the stimulus artifact, while Figure 3.13 shows the channel that was broadly affected. Figure 3.12 is consistent with only minor interference with spike detection and sorting, and only for those spikes whose duration spans the stimulus pulse. Figure 3.13, however, suggests that at least one part of the amplifier chain, most likely the high-gain preamplifier, is driven to saturation for the duration of the artifact; it is unlikely that the headstage

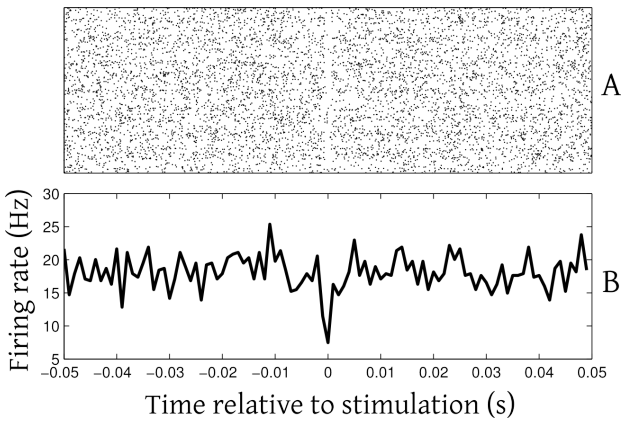

FIGURE 3.12: **A**, Rasterplot of spike times relative to the 1 Hz stimulation pulses; electrode and neuron were the same as shown in A of Figures 3.10 and 3.11. **B**, Peri-event time histogram (PETH) of the corresponding spike rate, binned at 1 ms. Artifact, while not visible in Figure 3.10, is visible here, and is ≈1 ms.

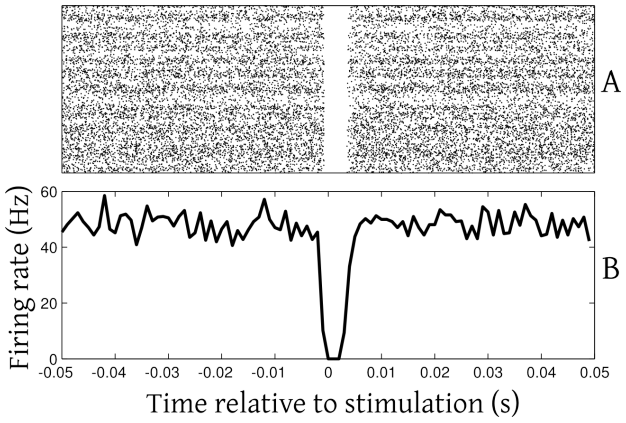

FIGURE 3.13: **A**, Rasterplot of spike times relative to the 1 Hz stimulation pulses; neuron was recorded from leg representation of right M1 @ +4.5 lateral, +2 rostral from 65 μm HML insulated stainless electrode, or 21 mm from the stimulating pair. **B**, Peri-event time histogram (PETH) of the corresponding spike rate, binned at 1 ms. Artifact was 6.5 ms and was the longest of those recorded in this session.

is driven to saturation, as then the result in Figure 3.12 would not be possible. These two channels, other than slight differences in distance from the stimulating pair, are only different in their referencing - the channel in Figure 3.13 was referenced to ground. These results show that it is possible to record with very minimal stimulus artifact with the described stimulation system, proper referencing, and centimeter

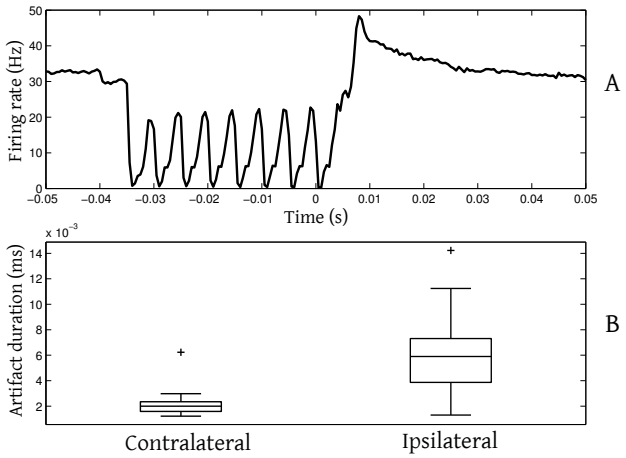

FIGURE 3.14: **A**, Mean aggregate firing rate of 190 neurons recorded from 112 electrodes in left and right motor cortex from a rhesus macaque. Stimulus was groups of 8 150 μa pulses separated by 5 ms. Note blanking due to stimulus artifact and rebound excitation after stimulus group. **B**, Boxplots of the stimulus artifact duration grouped by recording side. Box indicates 25% and 75% intervals, with the center line indicating mean duration, whiskers the distribution of all data, and '+' the duration of two outliers.

spacing between stimulating and recording electrodes. Note that no stimulation artifact suppression system was used.

To further characterize the duration of the artifact for much closer stimulation-recording distances, we examined the stimulus artifact on 112 channels during a closed-loop stimulation task with a rhesus macaque. Of the 112 recording electrodes, 32 were in motor cortex contralateral to stimulation, mean distance 36$\pm$1.7 mm from stimulating pair; the other 80 were ipsilateral, in the same array as the stimulating electrodes, mean distance 2.7$\pm$1.2 mm. Plotting stimulus artifact duration by absolute distance from stimulating pair did not yield any observable trends due to varying referencing and per channel gain, so the aggregate data is presented in Figure 3.14. Stimulus artifact in contralateral recording electrodes was 2.1$\pm$0.8 ms, and 5.8$\pm$2.3 ms for ipsilateral. Though the electrodes here are much closer to the stimulating pair than Figures 3.12 and 3.13, this is short enough that spikes can be recorded between stimulus pulses on many channels, as can be observed from

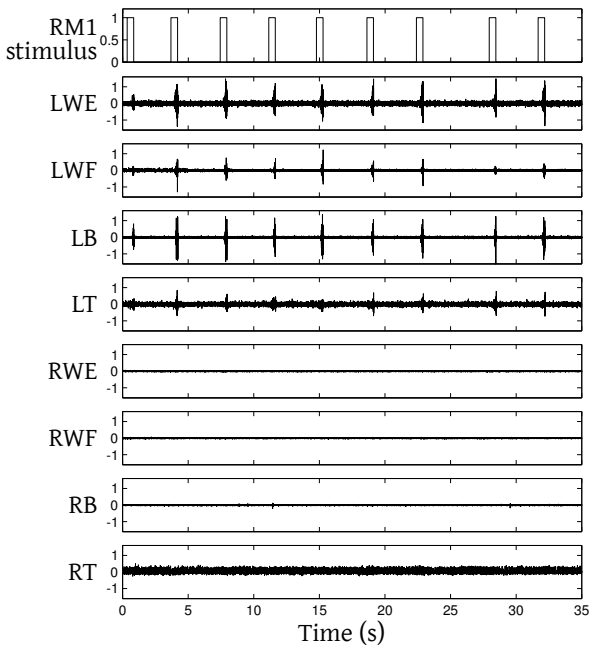

FIGURE 3.15: EMG responses to stimulation of right M1 cortex. Top trace shows the timing envelope of the stimulus; below that: LWE = left wrist extensor; LWF = left wrist flexor; LB = left biceps brachii; LT = left triceps brachii; RWE = right wrist extensor; RWF = right wrist flexor; RB = right biceps brachii; RT = right triceps brachii.

the aggregate firing rate in Figure 3.14 A.

3.4.3 Efficacy in Nervous Tissue

To demonstrate the efficacy of the stimulator in activating nervous tissue, we performed stimulation of the right arm representation of M1, with two stimulating electrodes consisting of HML insulated sharpened 65 μm stainless steel, centered +15mm lateral, +10mm rostral. These electrodes were the deepest of the array and penetrated the cortex by $\approx$3.4 mm. Stimulation pulses were 100 μs pulses of 75 μA, separated by 50 μs; fifty of such pluses were applied for each trial at 100 Hz. The results of this protocol are depicted in Figure 3.15.

The microstimulation had a gradually increasing effect on EMG during the half-second of duration of pulses, as is evident in the Figure. More immediate responses

and broader activations (including muscles of the torso) were obtained with higher currents - up to 175 μA. No other effects, harmful or otherwise, were observed in the monkey.

3.5 Conclusion

We have demonstrated the design of a multi-channel high-side digitally current regulated microstimulator, and verified its function on the bench as well as in an experimental animal. The design tries to minimize current injected as a result of parasitic capacitance between the microstimulator and animal ground, and as a result is capable of introducing only very short artifacts into simultaneous neuronal recordings – less than 1ms in some configurations – which, when combined in low-latency control, is suitable for experiments where neural recording and microstimulation are tightly interleaved. Our microstimulator offers a compliance of 50V or greater for stimulating high-impedance electrodes with a very small leakage current of 300pA or less. As such, the design is immediately applicable to experiential neurophysiology; indeed, in our lab we have been using three instances of the stimulator.

Several improvements are suggested by the results. Other than further reducing parasitic capacitance, it would be useful to provide a greater range to the output current. For example, if the feedback resistor (R1 in Figure 3.3) and bias currents are adjusted, the same stimulator topology can easily be used on muscles for functional electrical stimulation (FES). An alternative to the present H-bridge design is a bipolar supply totem-pole configuration with current mirroring rather than feedback stabilization, so there is no need for a feedback resistor an its attendant voltage offsets; however, this design can be susceptible to leakage current and charge imbalance, both which can damage electrodes. Even though the microstimulation artifact is short, active or forward cancellation schemes may be desired to reduce the artifact to below the noise level. Perhaps the most pressing concern, however, is size - if

microstimulation with simultaneous recording is to be clinically applied, stimulation channels and controller will need to be integrated onto one chip, consume less than 1mW, and likely share a common power supply rail with recording apparatus. We believe that the topology described herein represents a step forward in microstimulator design for experimental use, that the lessons in minimizing artifact are instructive to other practitioners, and that the same compact topology may be integrated and miniaturized into a ASIC for future clinical use.

3.6 Acknowledgment

The authors would like to thank D. Dimitrov for conducting the animal surgeries, G. Lehew and J. Maloy for constructing the electrodes, and T. Phillips, L. Oliveira and S. Halkiotis for invaluable technical support.

Animal procedures were performed in accordance with the National Research Council's Guide for the Care and Use of Laboratory Animals and were approved by the Duke University Institutional Animal Care and Use Committee.

4

Wireless recording system

4.1 Abstract

As a step towards fully implantable neuroprosthetic device for clinical applications, we have designed a wireless recording system for untethered large-scale recordings from primate brain. The system consists of digitizing headstages, transceiver, diversity receiver / ethernet bridge, and client software. Each headstage amplifies, multiplexes, and digitizes signals from 32 electrodes. The transceiver is connected to four headstages for a total of 128 channels per radio. The transceiver features a blackfin DSP which performs automatic gain control, LMS adaptive noise cancellation, 8 poles of high and lowpass filtering, two template comparisons per channel, data compression, and pipelined radio control, all in less than 80 instructions per sample. The transceiver transmits 1.3 Mbps full filtered analog trace of four channels and threshold match for both units on 128 channels; this is interleaved with 83 kbps reception, which allows the client to edit parameters on the transceiver. The radio protocol allows any memory location to be changed on the transceiver, and the transceiver streams from any location in memory, which is dangerous but

exceedingly powerful: any part of the signal chain may be edited and transmitted. The transceiver and wireless headstages consume approximately 264mw from a 3.7 V lithium battery, or 2 mW/channel, which allows to run for over 30 hours on a rechargeable cell. All parts for this system are commercially available (COTS) and up to 20 transmitters, or 2560 channels, may run at the same time. We have verified the operation of the system in a rhesus macaque implanted with multielectrode arrays in the areas of sensorimotor cortex representing both upper and lower extremities in both hemispheres. This monkey was trained to do one and two dimensional BMI tasks through the wireless system while he was in his home cage. Thus, our wireless system allows us to continuously record from unrestrained primates and allows unfettered access to the BMI or other research tasks.

4.2 Introduction

The most promising source of control signals for a neuroprosthetic device is populations of single units in the precentral or motor cortex. One limiting step in reliably obtaining these signals is the tissue-electrode interface; the other is the recording system. The latter ultimately will need to be high channel count for sufficiently precise volitional control and fully wireless to minimize the possibility of infection. Furthermore, there exists a need in neuroprosthetic and neuroscience research for a tool which allows unfettered, continuous real-time recording from primates. Wireless recording is essential for e.g. investigating social interactions, realistic motor control, or neural activity during sleep. The system described here solves these issues using relatively inexpensive COTS components and is a step toward an implantable neuroprosthetic.

4.3 Methods

The development of this device went through a number of cycles.

4.3.1 Revision 1

The first aim was to make a wireless recording system which digitized and transmitted signals from 32 electrodes. As this was conceived as a time and cost-sensitive project[1], it was decided that all components would be COTS. The critical factor here was, of course, the neural amplifiers, which need low input-referred noise, high gain, and a bandpass filter (highpass to remove low-frequency noise and electrode offset, and lowpass to remove high frequency noise). The best option at the time was Texas Instruments LMV1032 series of electret microphone preamplifiers, which are designed for microphones in commodity items like cell phones and Bluetooth headsets. They are tiny bumped bare silicon devices with a gain of 6, 15, or 25 dB, and a bandpass filter for the audio range 100 Hz - 20 kHz, and 100 μW power consumption from a unipolar 1.8 V supply. The SNR of the LMV1032-25 @ 1.7V is specified at 61 dB given an input tone of 18mV pk-pk at 1 kHz; this translates to 5.6 μ V_{rms} input-referred noise. Actual devices were measured to have 8 μ V_{rms} input-referred noise with a shorted input in a unshielded lab environment. Figure 4.1 shows LMV1032-6 amplifier response to a 1 mV test signal; passband is suitable for neural recording, and at the time the input-referred noise was also determined to be sufficient.

Neural signals range up to 1mV; the electret preamplifiers saturate at 1V pk-pk, hence a passband gain of 53.9db is desired, which was attained by cascading two of these 25 dB chipscale amplifiers. These were multiplexed into an Analog Devices ADG726, followed by a 2x gain through THS4281, then digitized at 12 bits and 1 Msps with an ADCS7476. ADC data was red into a Blackfin ADSP532 DSP, which simultaneously controlled the multiplexer and radio. At the time[2], the Blackfin offered the lowest power dual multiply-accumulate DSP architecture; on the board it was clocked at 240Mhz with a core/peripheral voltage of 0.8/2.7 V. The radio was

[1] At the outset – we shall see how many revisions were actually required

[2] and still!

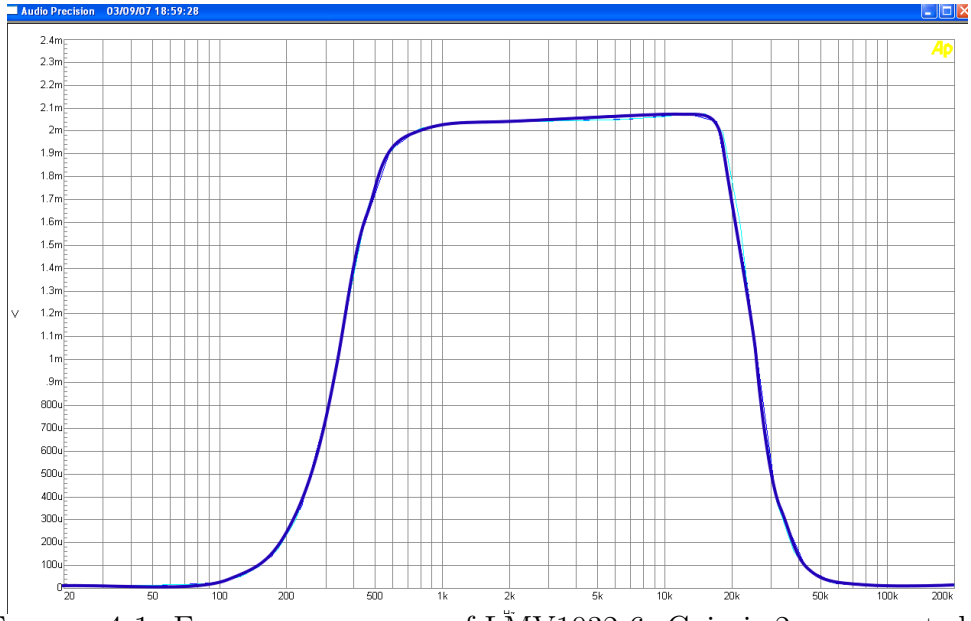

FIGURE 4.1: Frequency response of LMV1032-6. Gain is 2, as expected.

chosen to be an nRF24L01+, a commodity 2.4GHz FSK radio used in data-logging Nike shoes and similar. Other wireless biopotential systems utilize the same radio (Darmanjian et al., 2006; Thorbergsson et al., 2008). Though this was easier and simpler than a custom FSK or OOK radio as in (Miranda et al., 2010) control was not without difficulty. Bidirectional protocols proved to be tricky with this radio, as reading the received packet FIFO at an inopportune time or clearing status bits in the wrong order lead to corrupt data. The final bidirectional protocol is detailed in figure 4.2. For this revision, full waveform snippets surrounding threshold crossings were sent, which necessitated a fast clock rate as the Blackfin's jump and branch latencies are relatively high (5-9 cycles, depending on branch prediction). It also lead to a varying outgoing bandwidth and hence the possibility of dropped spikes, issues that have been carefully investigated in (Bossetti et al., 2004) and were to inform later designs.

The board was designed in Kicad, an open source EDA software, and hand assembled in my basement (At this time I was taking a leave of absence from the

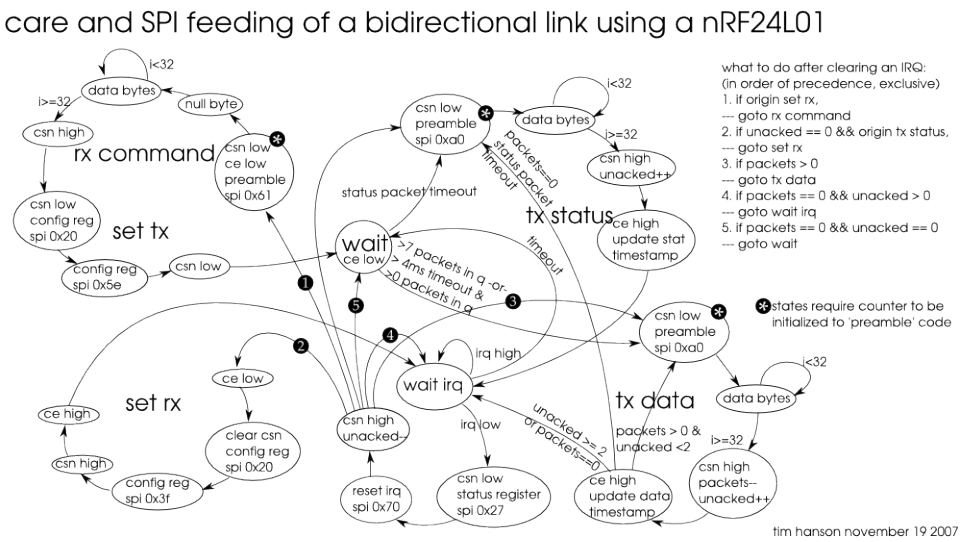

FIGURE 4.2: Flowchart detailing control of Nordic Semiconductor nRF24L01+ chip radios.

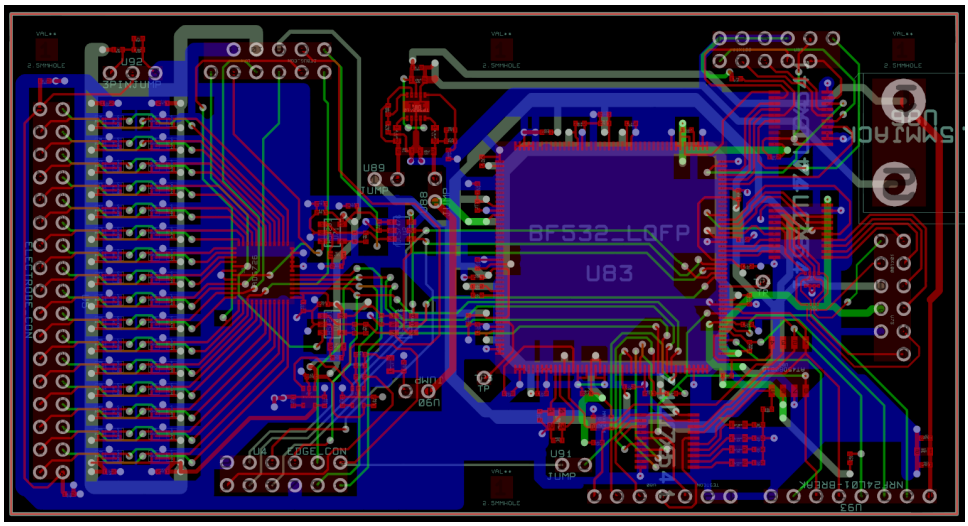

FIGURE 4.3: Layout of revision 1 of wireless headstage. Board is 4-layer standard-thickness FR4, 5 mil trace/space.

university). See Figures 4.3 and 4.4.

Testing of revision 1 proved instructive for the task. Four biquads of IIR filters were designed, but the canonical Direct form type II filter (Figure 4.5 proved not work with Blackfin's 1.15 signed fixed-point arithmetic. A biquad implements the transfer function:

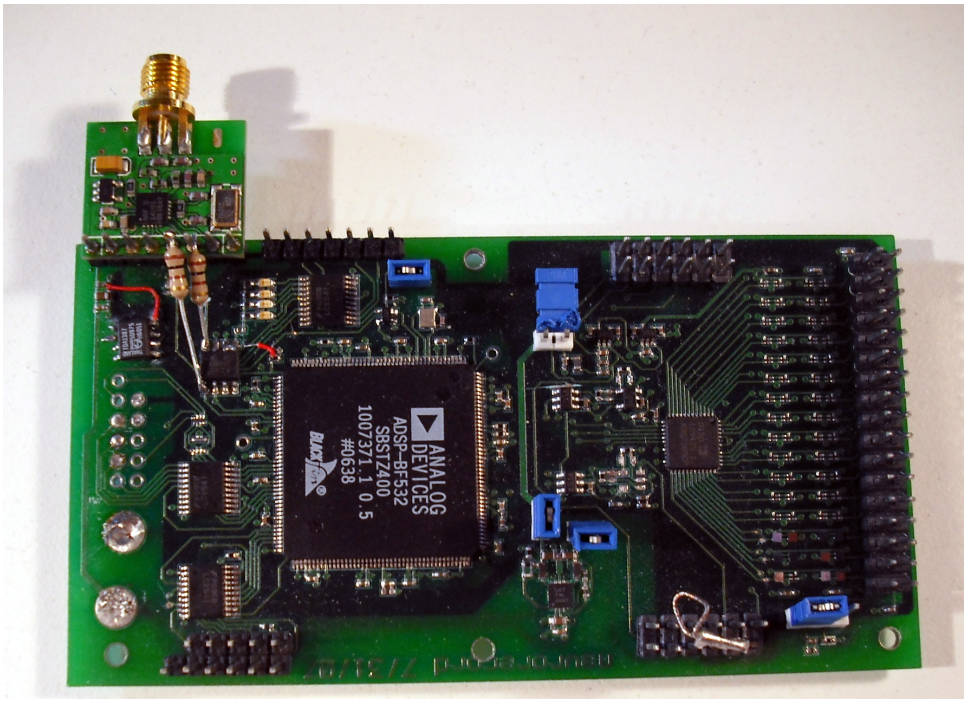

FIGURE 4.4: Assembled version 1 headstage. Sparkfun Nordic radio, without antenna, at top; electret amplifiers, the few that I could successfully hand-place, at bottom right. Resistors are to pull-down SPI lines. Philips chip below radio is a DAC off a SoundBlaster audio card and was used to verify IIR filtering performance. Device consumed 114 mW running radio and all filtering.

$$H(z) = \frac{b_0^1 + b_1^i z^{-1} + b_2^i z^{-2}}{1 + a_1^i z^{-1} + a_2^i z^{-2}}$$

When implemented with a minimum-delay Direct Form II 4.5, calculating the numerator before the denominator will saturate the fixed-point arithmetic (rounding and saturation occurs at the summation steps). Furthermore, most biquads demand denominator coefficients > 1, which cannot be represented in 1.15 fixed-point numbers.

The solution, as described by (Drutarovsky, 2005), is to use a Direct form I type filter with the additional *S2RND* flag for the MAC instruction. This flag causes accumulator results to be saturated and shifted left 1 bit (*2) prior moving to a

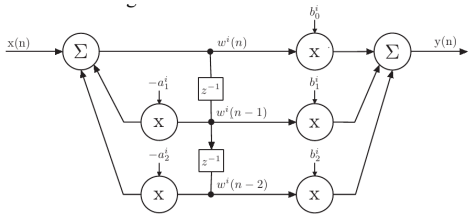

FIGURE 4.5: Direct form II implementation of an IIR biquad. This topology uses the minimum delays (2), but requires two rounding steps, the first of which usually saturates.

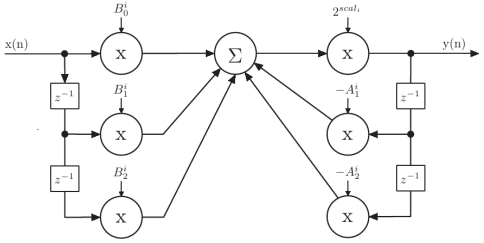

FIGURE 4.6: Direct form 1 with post-scaling by 2. Note delays for denominator (right) are shared with subsequent biquads.

16-bit register, hence all filter coefficients are pre-scaled by 0.5. See 4.6. Final filter was implemented in assembly and used ping-pong buffering, register preload, and shared delay taps to achieve near optimal processor utilization.

4.3.2 Revision 2

As this initial prototype proved that the strategy and components could work, the next revision was designed to be sufficiently small so as to fit on a monkey's head. Here three LMV1032 stages were employed (25, 15, and 15 dB), for a total of 55dB total gain (much closer to the design target of 54 dB) and a max input signal of 1.7 mV pk-pk. The board was designed in Kicad and Kicadocaml[3], and fabricated on 6-layer 63 mil FR4. A USB interface was added so that the same design could be both a transmitter and receiver, as well as EMG recording circuitry and debug interfaces (JTAG, RS232). These ancillary interfaces could be removed by simply

[3] An open-source PCB layout tool which I wrote.

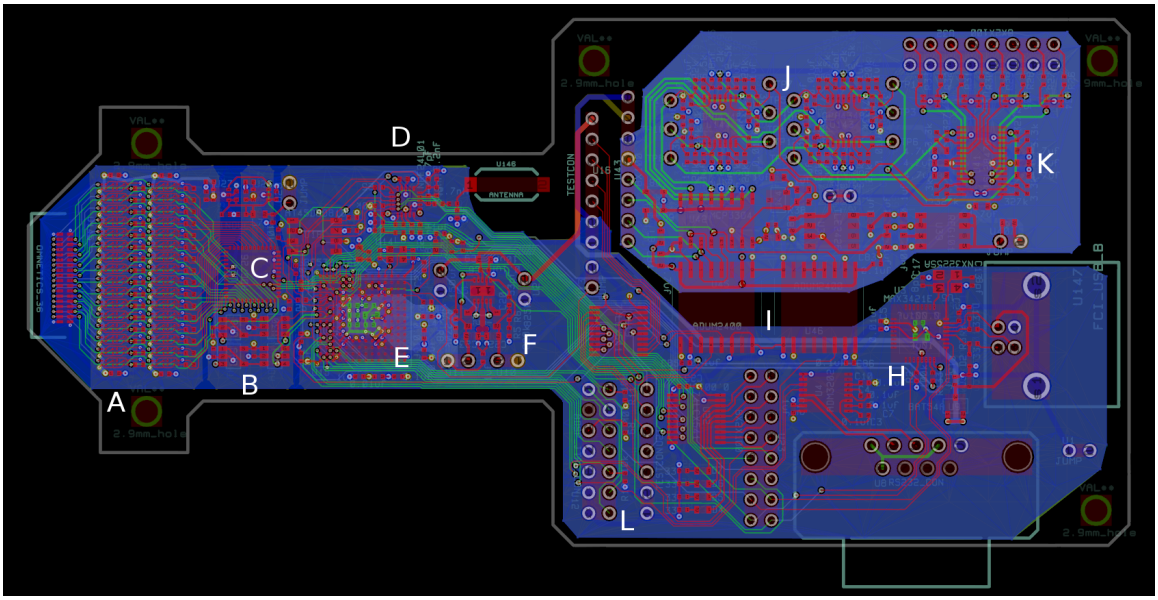

FIGURE 4.7: Design for revision 2 of the headstage. Most parts were placed on the top side of the PCB, making it much larger (13.46 x 6.35 cm) than successive designs. A, arrays of electret amplifiers, 96 in all. B, 2x gain and ADC. C, ADG726 multiplexer. D, Nordic nRF24L01+ radio, integrated rather than on an add-on board. E, Blackfin processor. F, TPS62410 two-channel switch-mode converter; voltage output 2.85V and 0.8V, the latter which supplied the DSP core. H, Maxim MAX3421E USB interface chip, controlled through SPI. I, Digital magnetic isolators to EMG circuitry. J, Four-pole multiple-feedback bandpass filter, highpass at 20 Hz to remove EKG, lowpass at 400 Hz, designed in LTSpice. K, Intersil ISL28470 instrumentation amplifier, gain of 40 dB with one highpass pole at 10 Hz. L, JTAG and flash programming headers.

cutting the board in two with a Dremel tool. Figure 4.7 shows the design.

While the radio and processor functioned well, the electret amplifiers did not. The bias voltage output of the first stage (500 mV) either forward biased ESD protection diodes in the subsequent stage, or pushed the input stage transconductance amplifier out of normal operating point. This effect was unexpected as the data sheet shows the input as being capacitively coupled, and led to 113 μ V_{rms} of input-referred noise, which rendered the prototype completely unsuitable for neural recording.

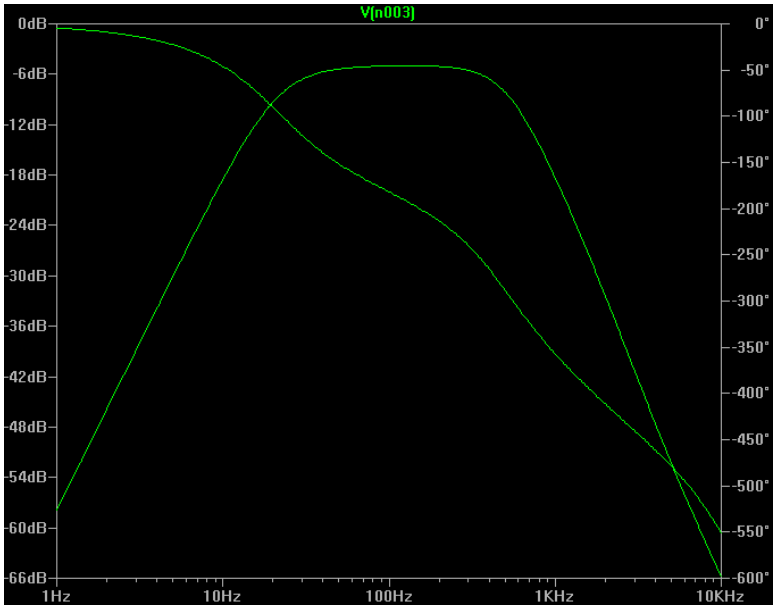

FIGURE 4.8: Simulated response for EMG filter chain, including front-end gain of 40 dB. Input is -60 dB; passband gain is +54 dB.

4.3.3 Revision 3

The obvious solution to the bias voltage problem was to properly capacitively couple individual stages of electret amplifiers. This was done using 0.1 μF 0201 package capacitors between each of the gain stages. To further minimize size, two 74HC4067BQ 16:1 muxes replaced the single ADG726, and components were placed on both the top and bottom of the board. See Figure 4.9. As before, one board was designed for multiple uses, including EMG and microstimulation (Fig. 4.10); this makes economic sense, as the primary cost of board is tooling and other non-recoverable engineering costs (NRE). One board was again designed to serve both the transmitter and receiver role via the inclusion of a SPI USB interface.

Power consumption for this device was 137 mW from a 3.7 V lithium ion battery; of this 96 amplifiers (powered through an LDO) consumed 22 mW, the radio condumed 37 mW, ADC and opamps 7 mW, 12 mW were lost in the buck converter, and the remaining 59 mW was consumed by the Blackfin. To test neural recording,

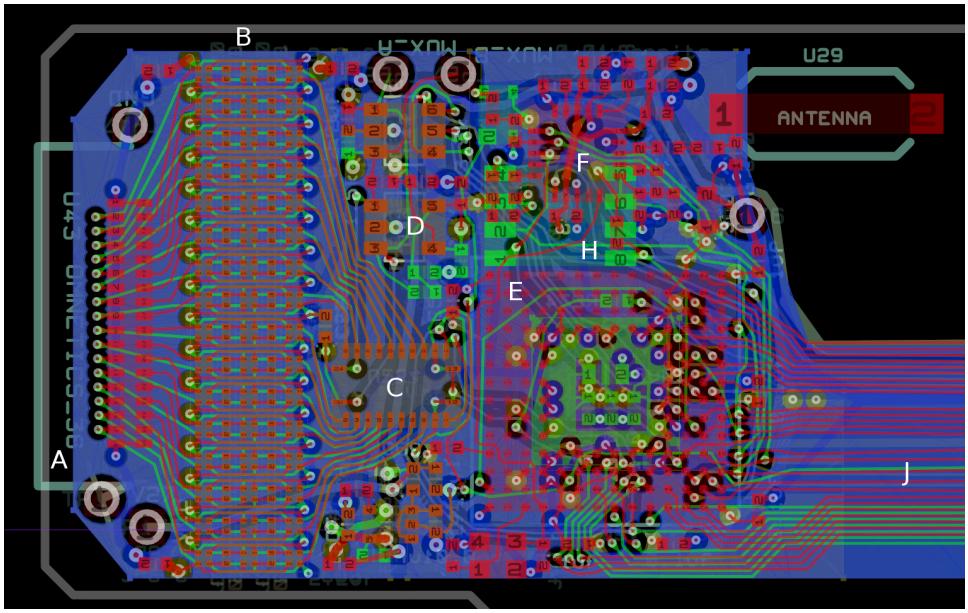

FIGURE 4.9: Revision 3 wireless headstage. A, Omnetics 36-pin connector. B, Array of 96 electret amplifiers coupled through 0201 capacitors. C, 16:1 multiplexer. D, Gain and ADC, 1 Msps at 12 bits → 31.25 kSPS per channel. E, Blackfin DSP. F, Nordic radio. H, 4 Mbit SPI boot flash. J, Connection to the rest of board for flash programming, EMG, and USB. Size of wireless section is 3.8 x 2.4 cm.

100 muV pk-pk 1kHz sine wave was input to the device through a 33k / 27 Ω divider circuit. Output-referred noise was 36 mV_{rms} (144 mV pk-pk on the scope) while the signal was 650 mV pk-pk; this equates to an input-referred noise of 6.5 μ V_{rms}, which agrees well with the measured values. Notably, this figure was only obtained when the amplifiers, which are bare silicon, are completely shielded from fluorescent lights in the lab; any near-infrared light is sufficient to activate or saturate the circuitry.

While the noise and power figures were acceptable for neural recording, none was ever attempted due to the great difficulty obtaining sufficient yield from this discrete analog front end. For all the channels to work fully 512 ≈ 10μL solder paste droplets must be well aligned, each must form a reliable solder joint, and 160 components must be within ±0.12 mm of their desired place, something which is impossible for human hands and difficult for my homegrown pick-and-place robot (the reason why

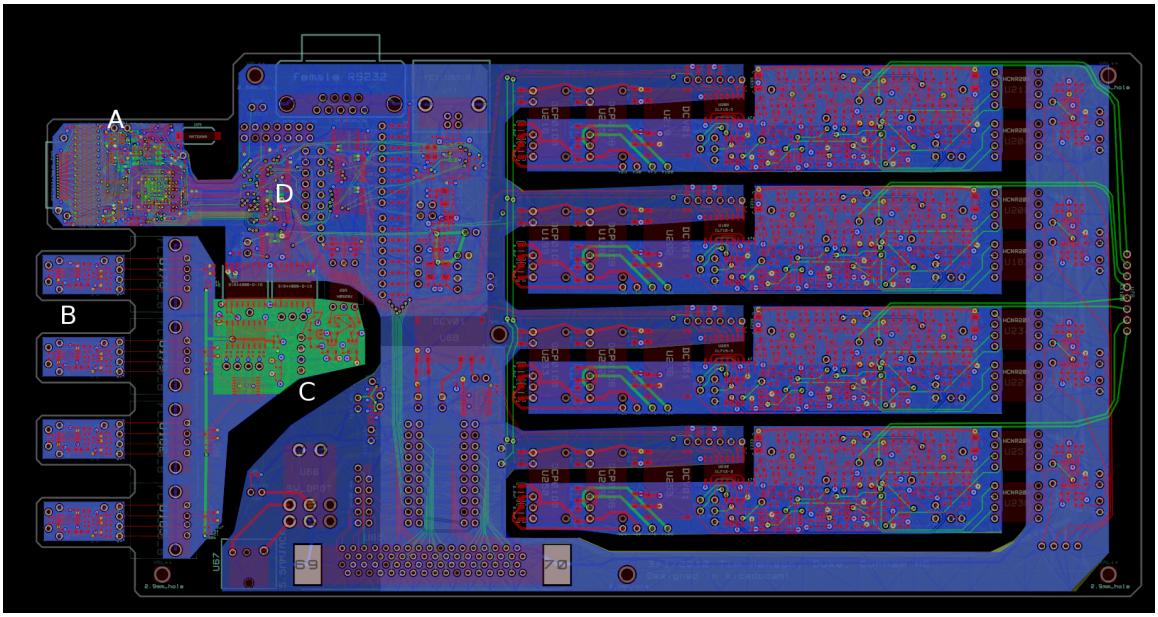

FIGURE 4.10: Revision 3 full PCB. A, wireless headstage. B, Active broadband EMG probes, as used in Delsys Bagnoli. Each includes a MAX4208 instrumentation amplifier G = 20 dB with one-pole highpass at 1.3 Hz, one-pole noise-reduction lowpass at 4.8 kHz, followed 2 successive HP/LP poles and an additional gain of 25 dB. C, isolated EMG digitization using a Microchip MCP3304 4-channel ADC. D, Interface buffers between 2.8 and 5V systems. The rest of the area is consumed by the microstimulator, as detailed in Chapter 3.

I built the device in the first place – see appendix B for a description).

Though the microstimulation section of this design has worked well in several experimental setups for well over a year, putting everything on one board is not without compromise. In order to keep the aspect ratio on the plated through vias underneath the 0.5 mm pitch ball-grid array DSP, the thickness of the board had to be reduced to 47 mil (1.2 mm). This permits the board to flex substantially more than normal 63 mil FR4, leading to a few traces to delaminate on some boards. Future revisions will be careful to preserve rigidity for larger designs.

4.3.4 Revision 4

At the time that it became obvious that the LMV1032 chips were not going to work because of mechanical issues, Intan technology under Reid Harrison announced

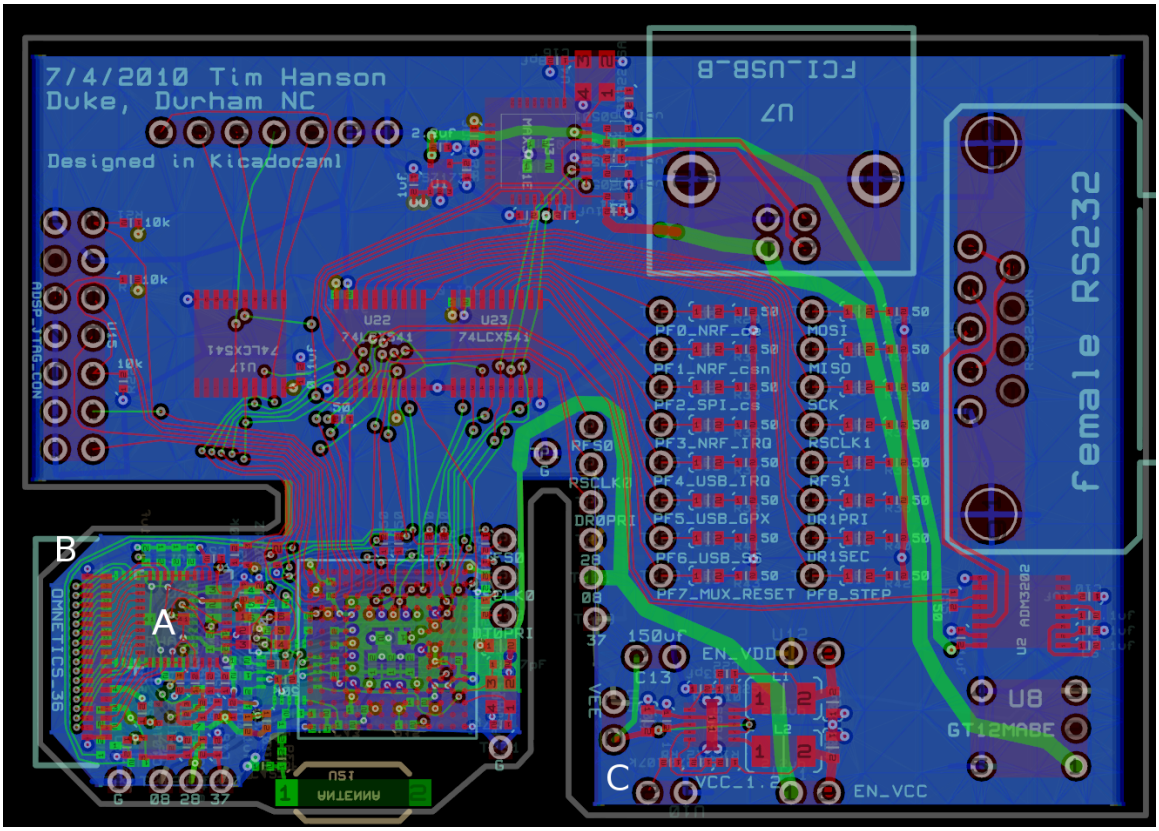

FIGURE 4.11: Revision 4 full PCB. A, Intan RHA2116 on top (red) and bottom (green) of board, not aligned. B, Poor routing choice. C, separate buck converter, to be mounted on the battery. Remainder of board is debug / program / interface. Total size = 7.36 x 5 cm; wireless size = 3.05 x 1.87 cm. Board made for high T_g FR4, 1.4 mm thickness, 6 layers, 5 mil trace/space.

commercial availability of their 16 channel integrated biopotential amplifiers. The wireless recording system was promptly redesigned (again) to feature two of these chips, each with an amplification of 200, variable band-pass filtering, and multiplexing. Figure 4.11 shows the resulting design, again with debug and programming circuitry that can be jettisoned via Dremel.

These devices worked well, finally, but were not without issues. Two high-speed serial lines used to read the firmware from the flash memory were routed around and within 5 mil of vias connecting the Omnetics connector to the amplifier on the back of the chip (Figure 4.11 B); because both the radio and flash memory were on the

same SPI bus, these lines were very active during transmission. The lines coupled to and corrupted electrode traces through capacitance and soldermask leakage currents. This particular problem was difficult to isolate, as it was my full expectation that RF energy was influencing the new Intan chips, much the same was that cell phone GSM signal, which is envelope modulated at 216 Hz, can be received by a poorly shielded stereo. The routing issue was fixed with a jumper.

One problem was never fixed. Through out these tests, the USB interface was set to emulate a serial port but could never be made to operate reliably.

4.3.5 Revision 5

USB was hence abandoned for ethernet; despite (or because of) the additional complexity, it is very reliable, and easier to write client software for as well. The design then split into both a transmitter (the wireless headstage) and wireless to wired bridge. The latter was based around a 600 Mhz Blackfin BF527, attached to a LAN8710A 10/100 ethernet PHY through the standard MII interface. To permit data buffering or more complicated tasks, 256 Mb of SDRAM was placed on the board (16 bits by 32 Mwords); as every good electrophysiologist uses his ears, an stereo audio output was also included. See Figure 4.12.

Revision 5 worked successfully, but the radio link proved to be highly unreliable in realistic environments, even when tuned to 2.524 Ghz[6] (the maximum possible using the nordic chip – and well away from the water absorption / WiFi / Bluetooth / ZigBee bands). The reason for this was twofold: multipath (RF reflecting off walls, metal objects) and linear polarization. Antenna diversity was chosen rather than circular antenna polarization as per (Miranda et al., 2010)– it is both simpler to design and more reliable. Furthermore it was realized that one Blackfin could control up to 128 channels with greater power and area efficiency, so the transmitter

[6] Actually, this band is owned by Sprint. oops.

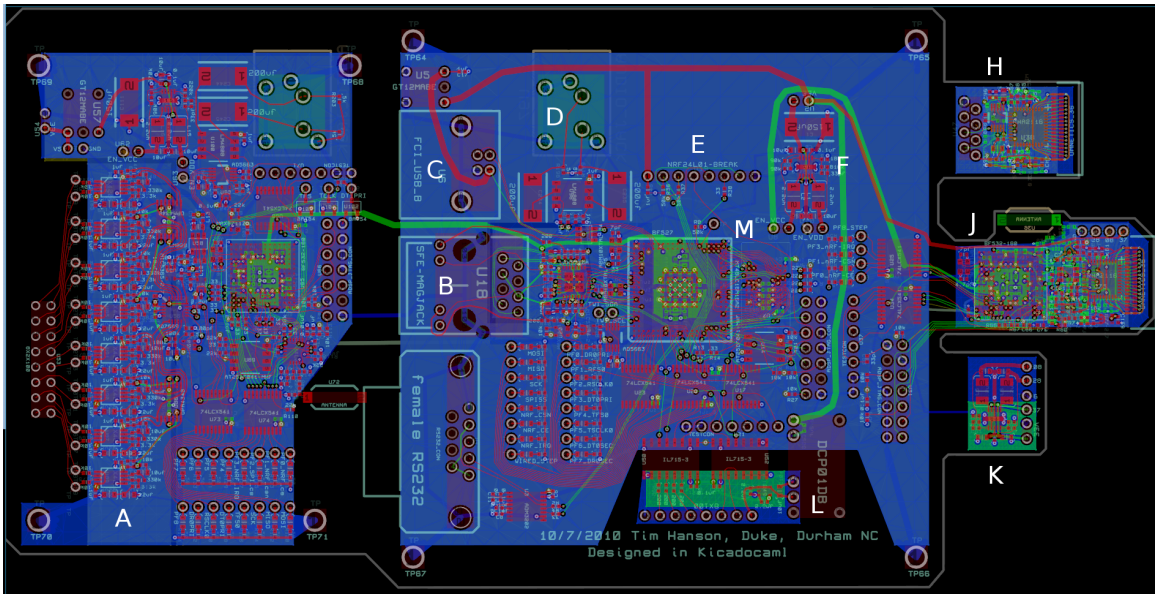

FIGURE 4.12: Revision 5 full PCB. A, Wireless EMG, 8 channels based around MAX4208 again, without active channels. Processing is done on a BF532, as in neural headstage, and uses the same Nordic radio. Device functions well. B, Ethernet jack with magnetics included. Immediately to the right (with 4 die ground pads) is the LAN8710A. C, USB port. The BF527 has support for full USB 2.0 high-speed (480 Mbps), but this has only been used for power. D, Audio output. Below is the DAC (AD5663) and headphone driver (LM4808). E, Header for Sparkfun nRF24L01+ radio subassembly, as used on revision 1. F, Buck converter, 5 V to 3.3 V and 1.2 V. H, Wired digitizing headstage. Works, but never used. J, wireless headstage, with routing errors fixed. K, Power supply for mounting on lithium-ion battery. L, Isolated interface for wired headstage. Used to eliminate ground loops[5] Total size = 19 x 9.5 cm. 63 mil thick, high T_g FR4, 6 layers.

was redesigned.

4.3.6 Revision 6

This is almost the final revision – see the description of the bridge in Figures 4.13, and the associated 128 channel wireless transceiver in Figure 4.14.

4.3.7 Revision 7

This is the most recent version. It fixes two major issues: (1) there was no way to re-flash the transceiver after debug circuitry had been removed, which is unfortunate as

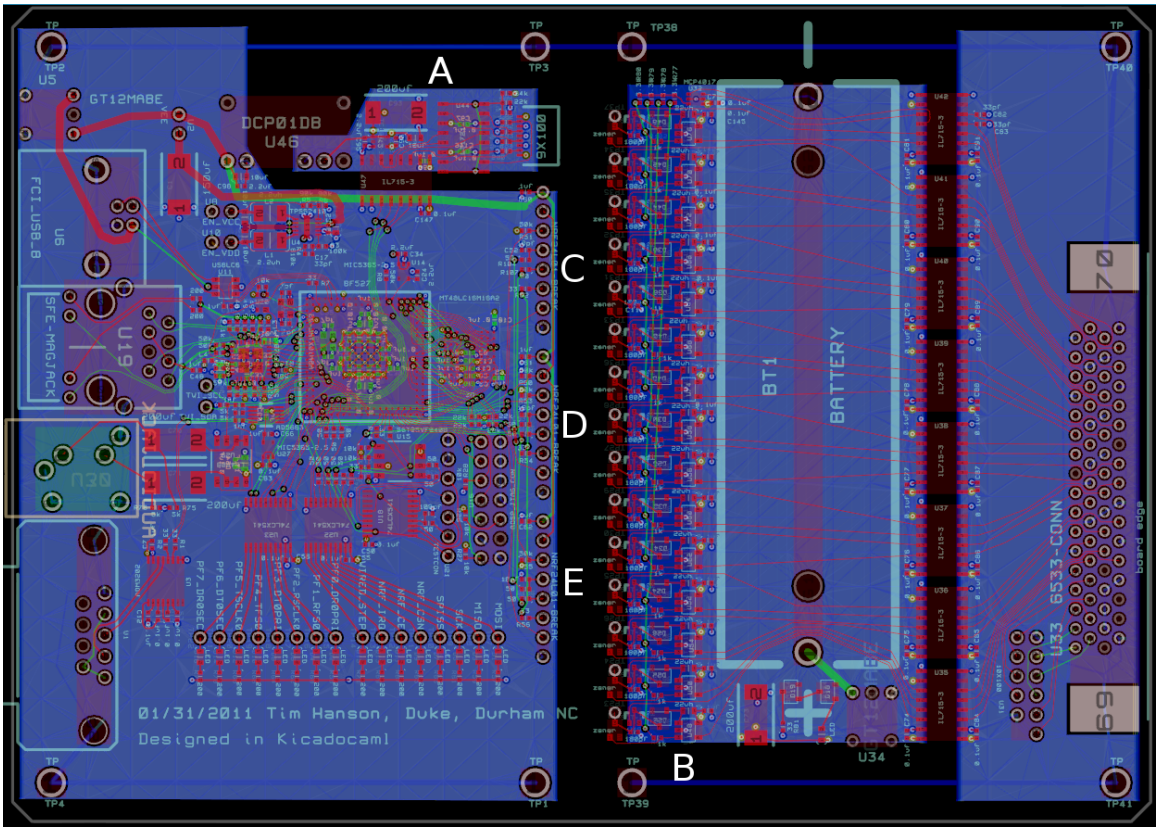

FIGURE 4.13: Revision 6 full 'Bridge' PCB. All but the same as revision 5, except for: A, High-speed impedance-matched isolated serial link, for use with the wireless transceiver in wired mode. B, Prototype wireless 16-channel microstimulator. Never fully investigated for lack of time / help. C,D,E: location of Nordic radio subassembly. Devices shared the SPI bus, barely not overloading it (rise/fall τ = 11 ns with a 10Mhz clock), with individual chip selects and IRQ lines. Total size = 14.7 x 10.6 cm.

the software is constantly changing and (2) Bridge was designed for remote operation (in the monkey rooms) via power-over-ethernet (PoE), and testing a commodity *unisolated* PoE adapter destroyed two bridges.

4.4 Software

A very appreciable segment of this project was the creation, testing, and inevitable rewrite of the software involved in recording system. There are 4 principal parts: transceiver firmware, bridge firmware, sorting client, and BMI software.

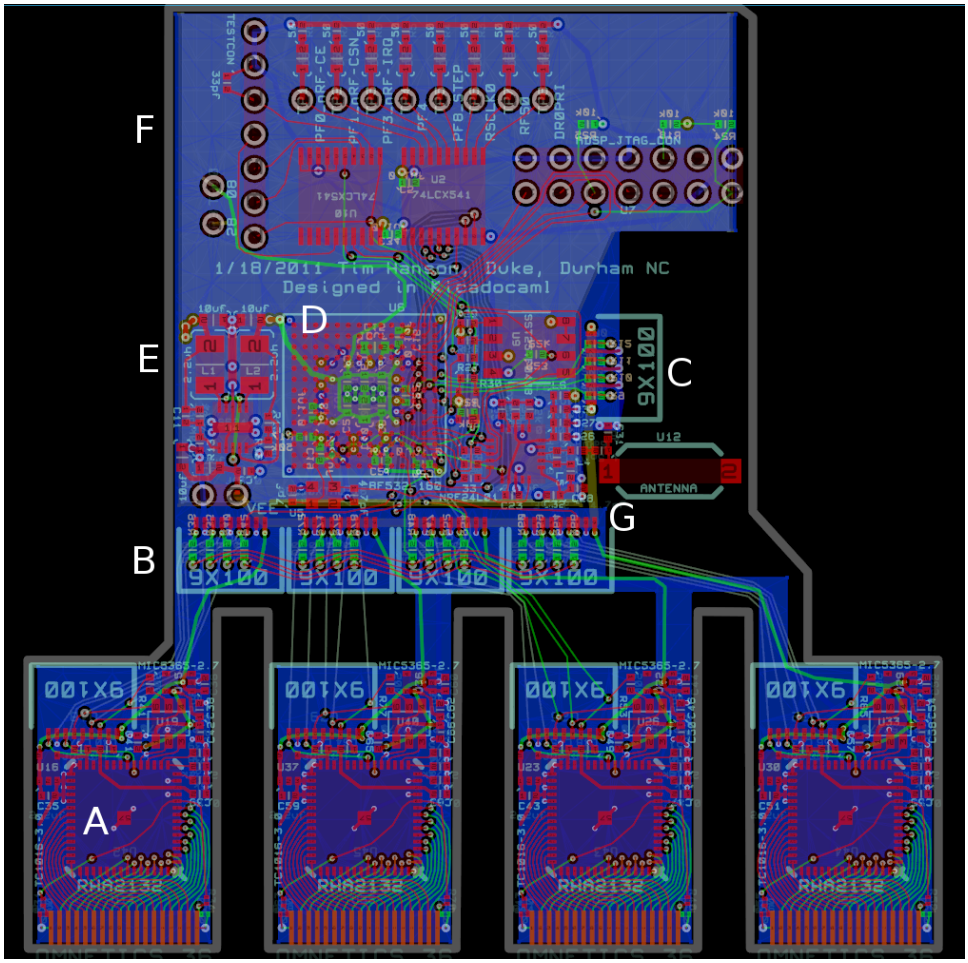

FIGURE 4.14: Revision 6 full 128 channel wireless PCB. A, Digitizing headstage using one Intan RHA2132 and a ADCS7476 ADC. Parts were mounted only on one side of board to permit stacking on tightly-arrayed electrode connectors. These connect to the processor through 9-pin (extra pins so that if orientation is wrong, nothing breaks) Omnetics nanominiature connectors, B, which were quite difficult to source and should be replaced. C, Connector for high-speed serial interface for wired use. D, Blackfin processor, here clocked at 400 Mhz at 0.95V. E, Buck power supply, properly integrated into headstage as opposed to the battery. F, Debug circuitry: JTAG and FLASH headers. G, Ground plane cut to avoid ground transients from interfering with digitizing headstages. Dimensions: Digitizing headstage, 1.37 x 2.15 x 0.16 cm, Processor and wireless, 4.3 x 2.1 x 0.34 cm. Fabricated on 0.68 mm thick, high T_g FR4, 6 layers.

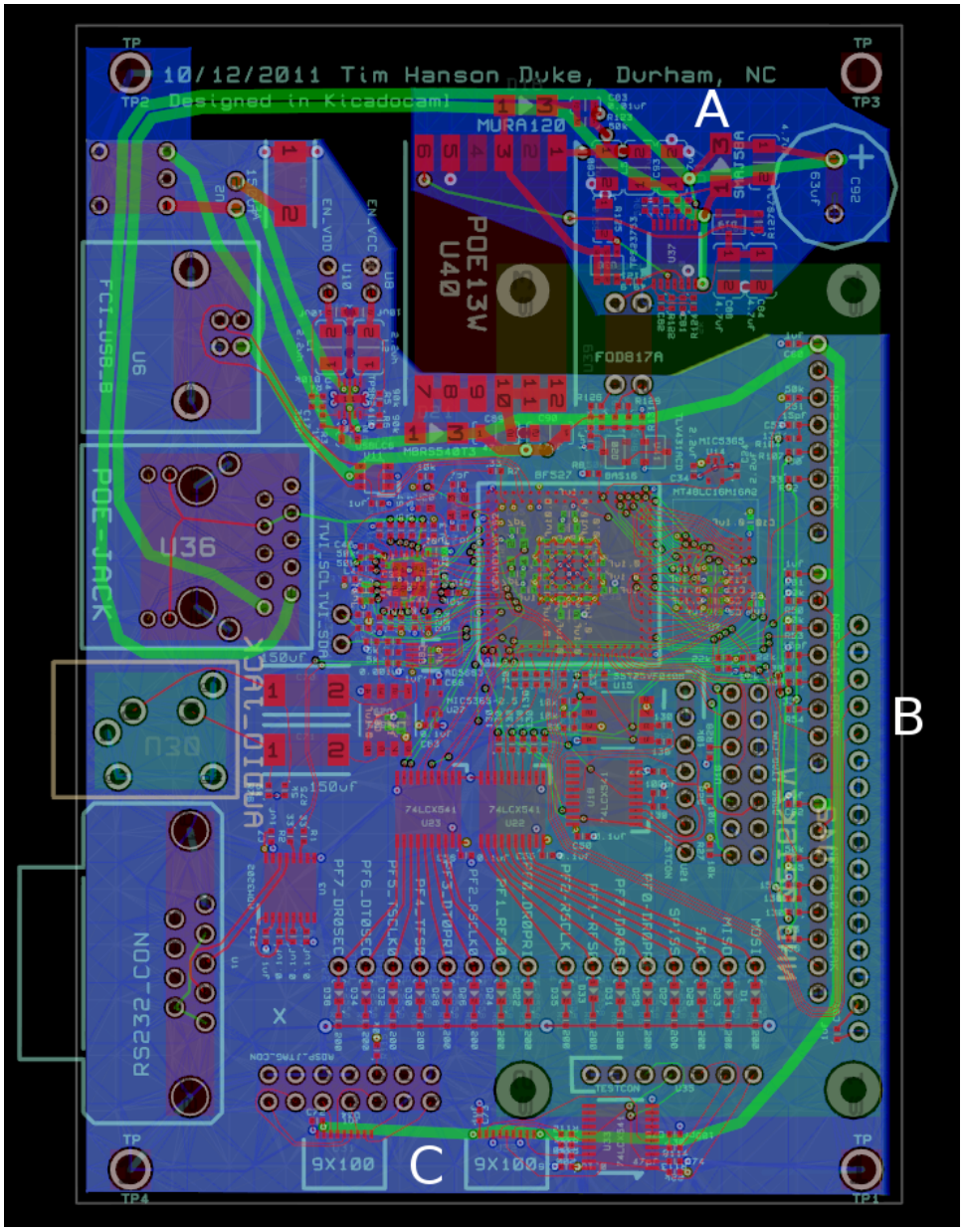

FIGURE 4.15: Revision 7 full 'Bridge' PCB. A, Power-over-ethernet circuitry, based around a Texas Instruments TPS23753. This is the first revision and stability of the optically-isolated feedback loop needs to be optimized a bit, along with switching EMI. B, Display was added to the backside of the board to present information, namely the IP address of a given bridge. This has been rendered irrelevant by the implementation of service location protocol (SLP) in the bridge firmware. C, JTAG and flash programming hardware, through Omnetics 9-pin nanominiature connectors. The remainder of the board is relatively unchanged from the previous revision. Total size: 7.7 x 11.0 cm.

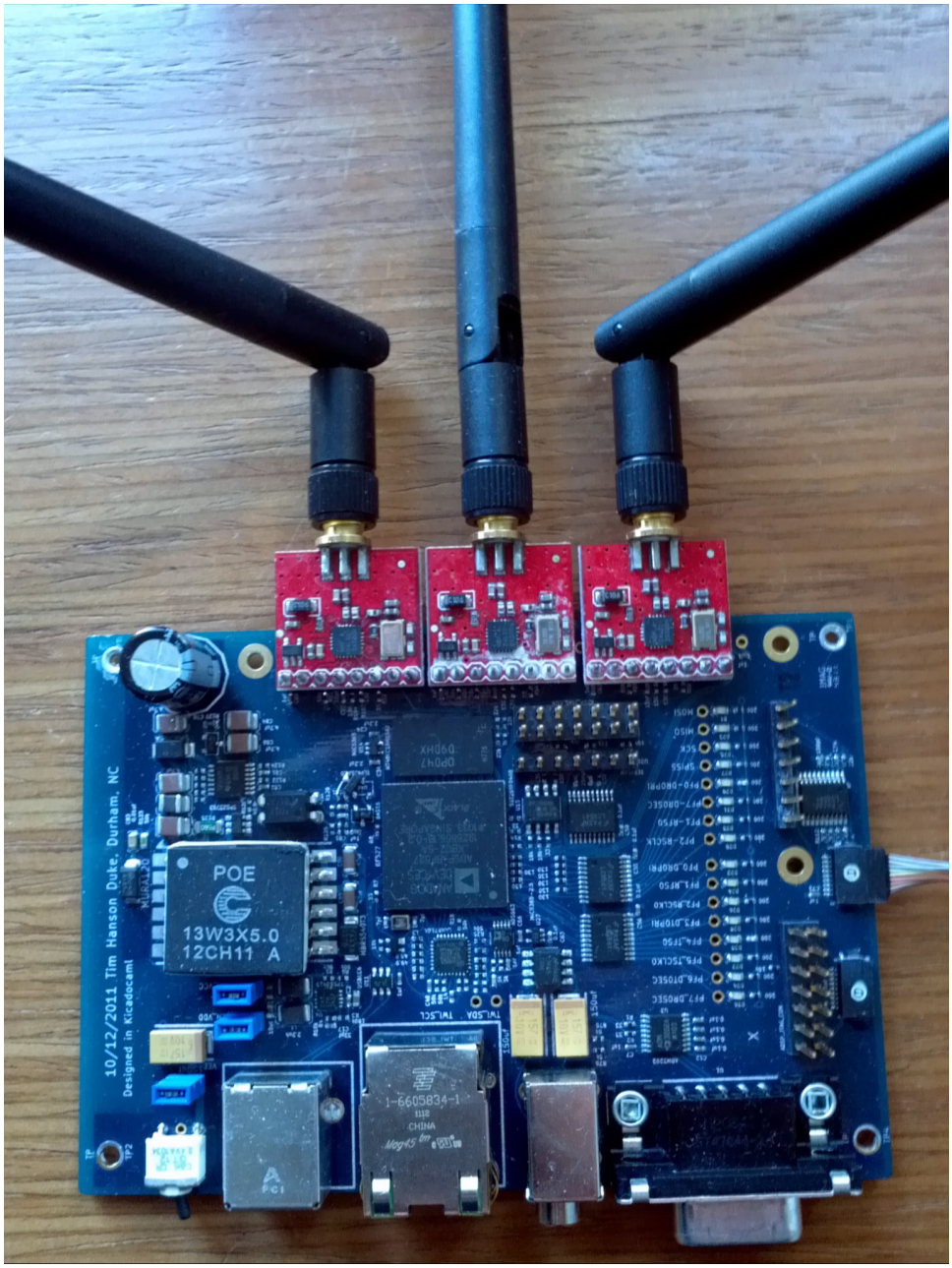

FIGURE 4.16: Revision 7 full 'Bridge' Assembled. Power consumption is 925 mW from a 5 V supply, 1.4 W from 36 V PoE.

4.4.1 Transceiver firmware

Firmware running on the transceiver was prototyped extensively in C with revisions 1, 2 and 3 hardware, and was converted to assembly for the remaining hardware

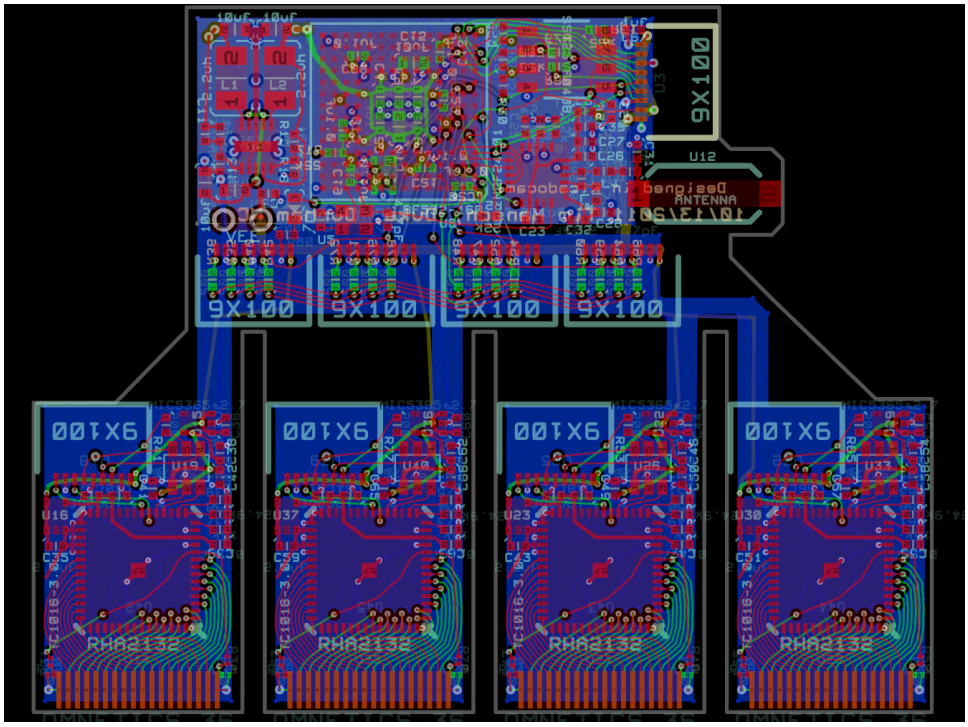

FIGURE 4.17: Revision 7 full transceiver PCB. A, Connectors for writing firmware to flash and JTAG, on top and bottom of board, respectively. JTAG connector is not normally populated. Digitizing headstages are identical to last revision. Power consumption is 264 mW from a 3.7V battery. Processor and wireless size: 4.06 x 2.1 x 0.34 cm.

revisions. The present firmware is 12.6 kB and fits easily in the 48 kB available, hence the processor has only a single-stage bootloader.

The firmware has effectively two threads: one for reading in samples from the ADCs, and one for handling radio transmission. The threads communicate via a 1024-byte, 32 packet circular buffer, and are interleaved using the program counter (PC) to hold state; all other registers are clobbered by the filtering routines. That is, the radio control program (which implements the protocol in 4.2), fills the SPI read or write registers and changes flags to the radio, then calls the ADC servicing routine, which blocks until a sample is read and has been fully processed; it returns via return-from-subroutine, which permits state to be saved in *code location* rather than variables or on the stack as with typical software threads. Provided the total

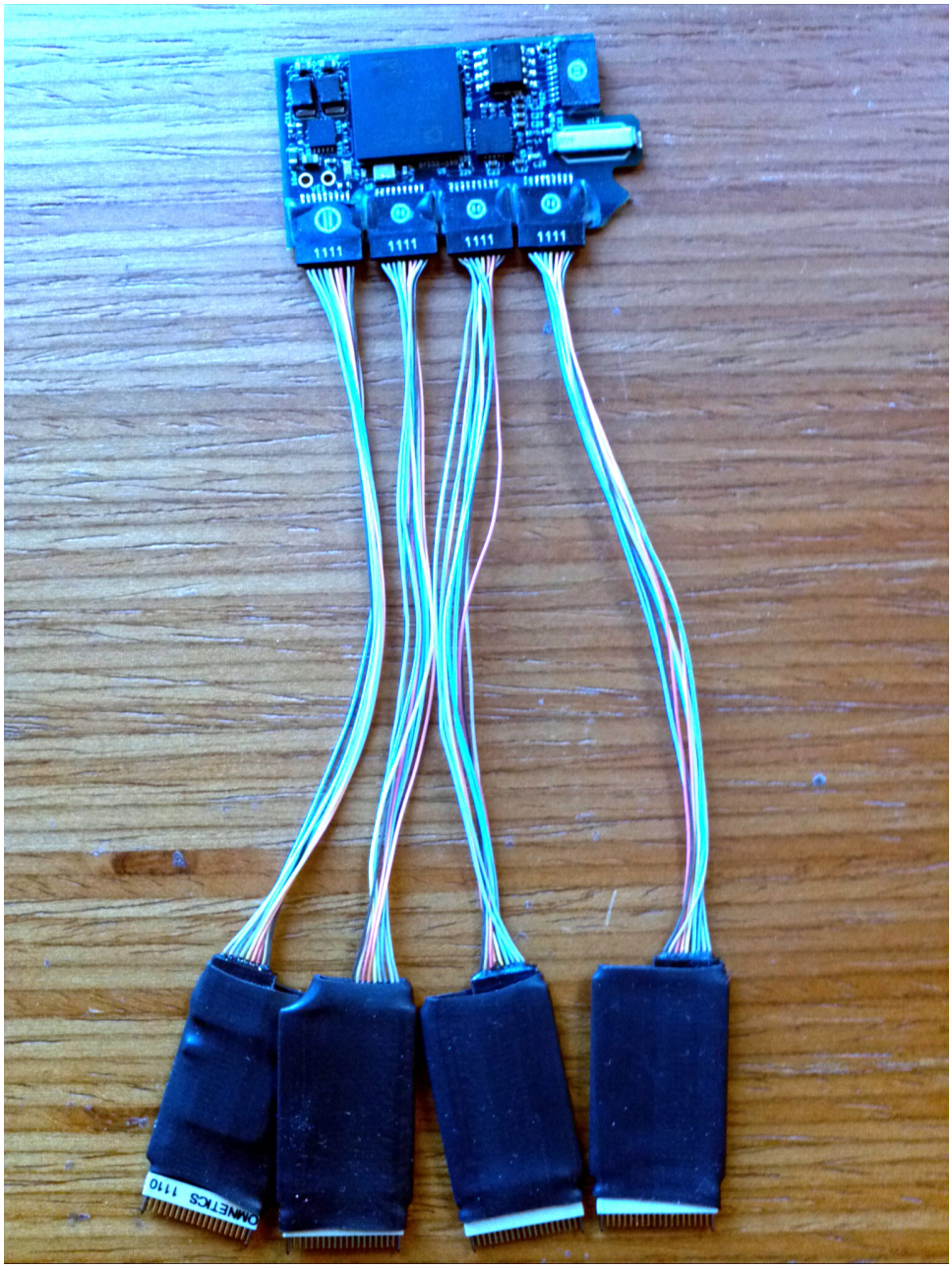

FIGURE 4.18: Revision 7 full wireless transceiver Assembled. Digitizing headstages are protected by heat-shrink tubing, and connected to the processor and radio through a 7.6 cm 9 conductor wire to better fit in the monkey's headcap.

codepath does not exceed 400 clocks (the processor is running at 400 Mhz, and the ADCs sample at 1 Mhz), everything proceeds lockstep at 1 μs increments, and little time is wasted. All persistent variables that do not have their own registers, such as

the number of packets enqueued, are stored in fixed offsets from the frame pointer to permit one-cycle access latency.

Four samples from each of the 4 ADCs are read at once; as the blackin works efficiently with two 16-bit samples at once, two samples (from two of the 4 headstages) are then processed at a time. These two come in at 12 bits unsigned, and must be converted to 1.15 signed fixed-point, which is done by pre-gain (usually 4) followed by an integrator highpass stage. The transfer function of the highpass stage is $H(z) = \frac{4(1-z^{-1})}{1+(mu-1)z^{-1}}$; the normal value of mu is 800/16384, which places the -3 dB cut at 250 Hz. This is followed by an AGC stage which applies a variable gain 0-128 in 7.8 fixed-point format; the absolute value of the scaled sample is compared to the AGC target (stored as the square root to permit 32-bit targets) and the difference is saturated at 1 bit plus sign[7]. This permits the gain to ramp from 0 to 127.999 in 2^{15} clocks, or about half a second, which is a bit too quick especially with very bursty neurons. In the future we may change the saturation behavior to permit slower attack / release on the AGC. This can, of course, be disabled once a suitable gain is found by setting AGC sat to zero. A diagram of this logic is in figure 4.19.

The next step is LMS adaptive noise cancellation see Figure 4.20. The delayed samples for the FIR part of the LMS filter is shared with the delays in the IIR filters, to be discussed below, which saves both time and space. As addressing is simply a fixed offset into the delay circular buffer this means that the last 7 channels scanned are used to predict the present channel (e.g. if the present MUX channel is 14, channels 7-13 are used for noise cancellation). Adaptive weight update proceeds in a pseudo-normalized LMS method: incoming samples are saturated following a variable gain and saved to the circular delay buffer; weights are decayed, then updated by the product of 1-bit saturated sign of the error, the saturated delayed sample, and

[7] As it is a 1-bit semi-stochastic weight update, AGC does not have an analytical transfer function; stability is not guaranteed, but has proven reliable over about a month of recording.

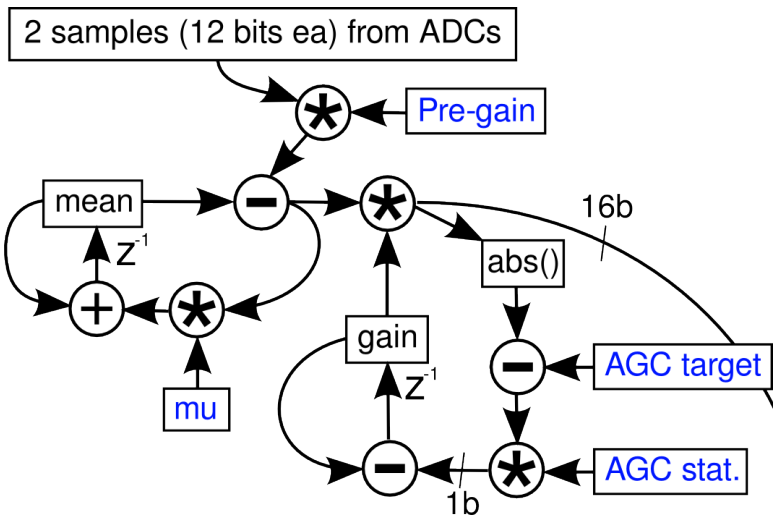

FIGURE 4.19: Integrator and AGC, first two steps in filtering pipeline. See text for details. In this figure and following all blue text indicates values that can be configured over the wireless link.

a small scaling factor (3). That is: if both the error and sample are the same sign, the weight increases (Hebb's rule). This permits the filter to be computed in 9 clocks, including register preload, and weight update to proceed in 15 clocks. Again, since this is involves saturation and 1-bit weight updates, it is not analytical, but in practice the filter settles to final weight values within 4 s. The filter offers 40 dB of noise rejection, and can be disabled by setting *decay* to 0.

LMS is followed by 8 poles of fully software-configurable IIR filtering. As mentioned above regarding revision 1, these are implemented as modified Direct Form I filters. As the 4 biquads run back-to-back, taps are shared between stages – see Figure 4.21. We've found that normal Butterworth filters are best for neural recording; although Elliptic and Chebychev filters have faster edge falloff and stop-band attenuation, they tend to ring and exhibit phase distortion, which is unacceptable when waveform shape is critical. By scaling the coefficients on the low-pass stages, it is possible to get further gain on the signal, which is useful when AGC gain is kept low by large EMG or microphonic contamination (subsequently removed by

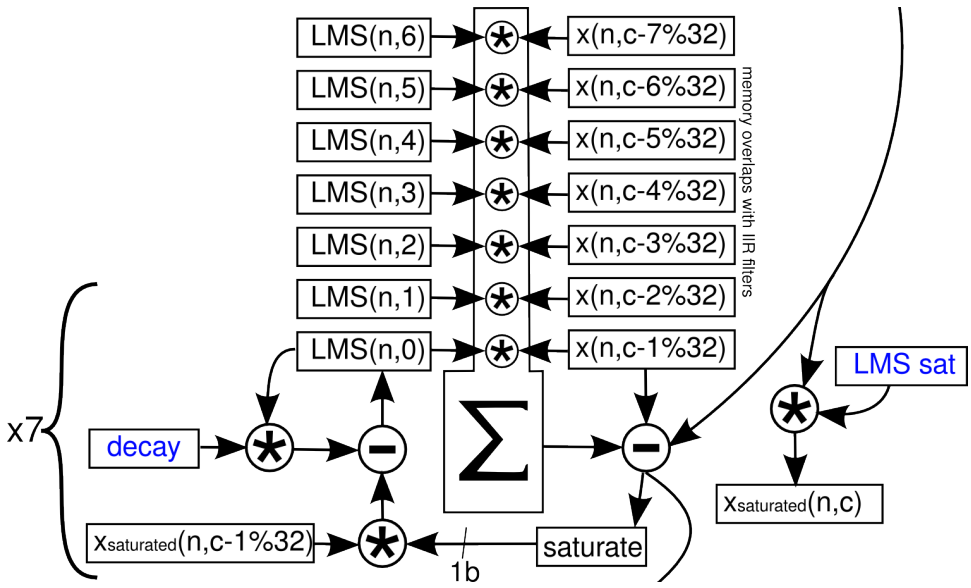

FIGURE 4.20: LMS noise cancellation filter. In the notation: n is the sample number, c is the channel number 0-31, % indicates modulus, and boxed values are stored in circular delay buffer. LMS update step in the bracket (decay, update with product of saturated sample and error) is repeated 7 times, but only one is shown for clarity.

LMS). The 4 stages take exactly 27 clocks and typically implement a bandpass with passband from 500 Hz to 6.7 kHz. They may be disabled by writing the appropriate filter coefficients, or more interestingly set to oscillate. This can be done by writing coefficients that satisfy $y(n) = (2-f)y(n-1) - y(n-2)$, or equivalently $0 = Y(z) - (2-f)Y(z)z^{-1} - Y(z)z^{-2}$, which has poles on the unit circle at angle $\omega = angle((2 - f \pm \sqrt{f^2 - 4f})/2)$, where ω is the frequency of oscillation, in radians/sample. This unintended feature has proved essential in debugging template matching, radio transmission, and other parts of the signal path; it is very obvious when a sample is dropped or misplaced in a sine wave, unlike in a neural trace.

As mentioned, two samples are operated at a time using the Blackfin's dual-MAC architecture, hence the signal path above (integrator → AGC → LMS → IIR) must be done twice to process all 4 simultaneous ADC samples. These 4 16-bit samples are then converted to unsigned 8-bit integers, packed into one 32 bit word, and written to the appropriate position within the circular delay buffer. Template

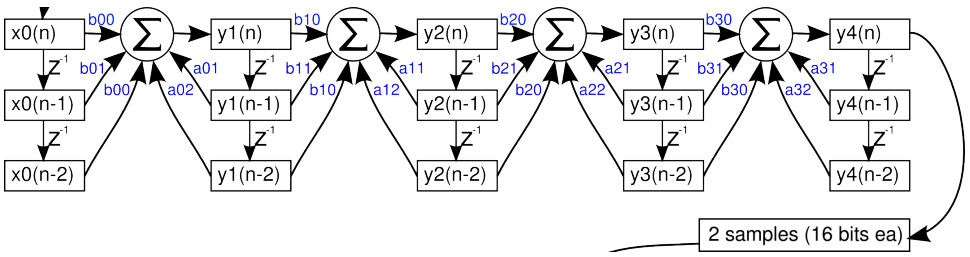

FIGURE 4.21: IIR filter, 4 biquads. Like the rest of the signal path, all coefficients are set individually for each of the 128 channels.

matching then uses the *SAA* instruction, which accumulates four different sums of absolute difference between vectors of unsigned bytes. SAA was explicitly designed for MPEG compression, where a critical step is measuring the per-pixel and per-color differences between video frames, but it works equally well for comparing neural waveforms to templates. The SAA instruction yields one value per channel, which is then compared to a software-defined aperture; spikes are accepted if the summed absolute difference is less than this aperture. Four templates on the four simultaneous channels are computed at the same time, which requires 22 clocks for a length 16 (512 μs) template, including bit manipulations to pack the template matches into "sticky" bits for radio transmission. Two templates are matched per channel per sample, hence each transceiver features 256 16-point 8-bit template vectors, all set by the user. Note that this is effectively convolution, and there is *no threshold* step; a rigorous study of how this compares to threshold-based sorting has yet to be done. Figure 4.22 graphically depicts this algorithm.

The next step is to collate and packetize the data into an outgoing radio stream. The Nordic radio features an over-the-air rate of 2 Mbps, but has a free-running PLL which loses sync after 4 ms, putting a limit on continuous transmission. Furthermore, the radio sends maximally 32-byte packets from a 3-deep transmit and receive FIFO. To fit within these constraints 6 samples from each of 4 channels (24 bytes) are packed with 8 bytes of template-match information. As 8 bytes corresponds to 64 template

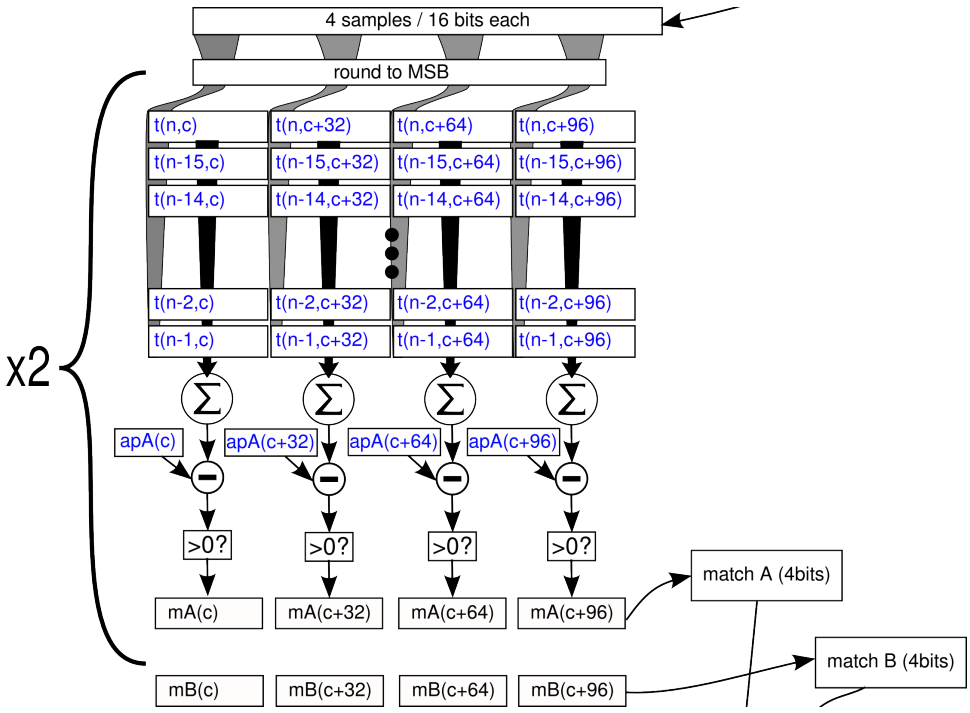

FIGURE 4.22: Template matching using the SAA instruction. Apertures and templates are set via client software and transmitted wirelessly. As there are two templates per channel, the algorithm runs twice.

matches out of 256, all template matches are transmitted every 4 packets, or 24 samples. With the ADCs running at 1 Msps, a new packet is produced every 192 μs, and all templates are sent (and their sticky bits cleared) every 768 μs, which is sufficiently higher than the maximum expected firing rate.

Sixteen packets are assembled into one frame, after which the transceiver goes into receive mode to listen for any commands from the control software. One frame lasts exactly 3.072 ms, which is less than the 4 ms PLL free-run time; the time to transmit these 16 packets, transition to receive mode, receive a packet, and transition back is 3.60 ms, hence the radio is being used at 99.6% of its maximum. This corresponds to an outgoing bandwidth of $1.33\bar{3}$ Mbps, and an incoming bandwidth of $83.3\bar{3}$ kbps.

To enable the bridge to time transmission of control packets properly, extra bits are needed within the transceivers packets. For this we make the simplification that,

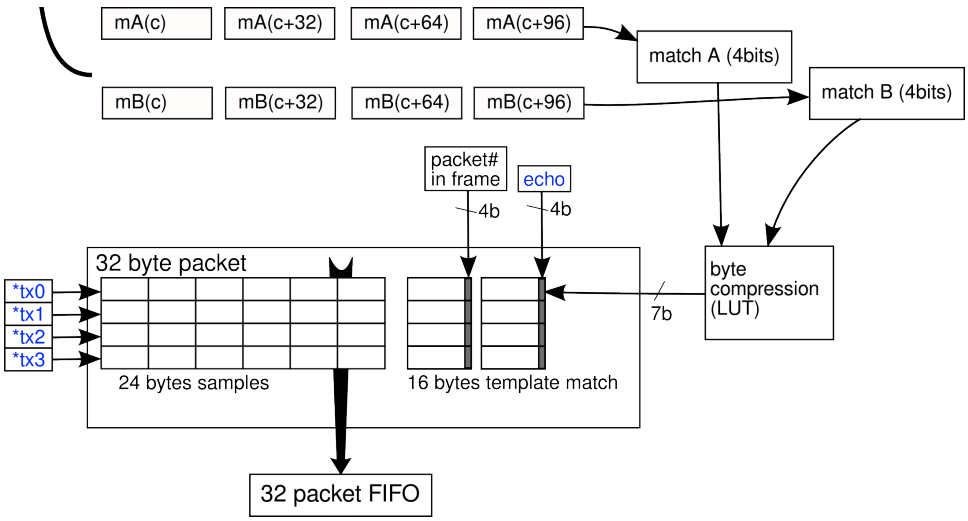

FIGURE 4.23: Transceiver outgoing packet structure. Match registers mA(), mB() are from bottom of figure 4.22. The pointers tx0 - tx3 are software set, along with the echo nibble. Byte compression is done via an in-assembly look-up table, which is itself written by a C program for calculating the lossy compression codes. Likewise, packet number in frame and echo are converted from nibbles to 0x80808080 masks via a LUT.

usually, two templates will not match one the same channel at the same time, and that usually neurons will not be firing. These assumptions allow lossy compression of 8 bits of template A/B match to 7 bits through a look-up table, thereby freeing up 8 extra bits in the 2 32-bit template match words. These 8 bits are used to transmit packet number in frame and a 4-bit echo. See Figure 4.23 for a graphical depiction.

As shown in Figure 4.23, 8-bit samples are sent from *arbitrary* pointers, which like the digital oscillator, has proven very useful in debugging the firmware. Four different streams of any delay taps, internal state, filter weights, etc. can be transmitted continuously at the sample rate via appropriate specification of the transmit pointers.

These transmit pointers as well as all the other values in blue in Figures 4.19 - 4.23 are set via packets from the bridge to the transceiver. The format here is similarly simple, and consists of four pairs of 28 bit addresses and 32 bit values; upon reception of these packets, the transceiver validates the addresses to lie within

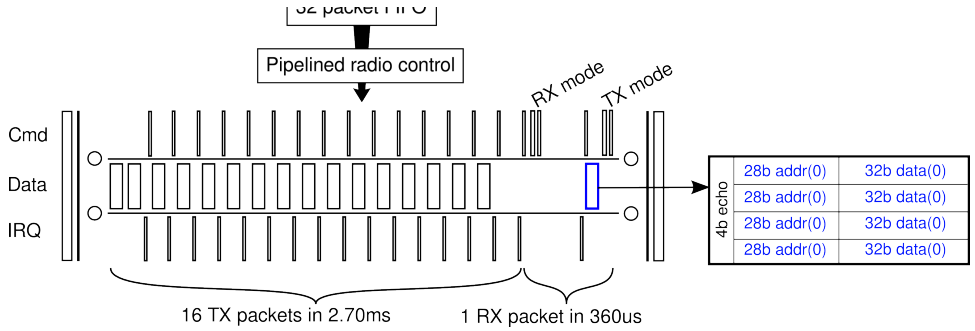

FIGURE 4.24: Schematic diagram of transceiver ↔ bridge packet framing, with the control packet highlighted in blue, and relevant SPI signals to the left of the repeat sign.

working memory range, and writes the value to that address. The upper nibble of the addresses is always 0xf, hence is replaced with 4 bits of echo value. This echo value is sent back as in Fig 4.23 when the transceiver applies the changes requested in the bridge's control packets, permitting SEQ-ACK like exchanges as in TCP. Bandwidth from the transceiver to the bridge features no such sequencing, as there is neither memory, bandwidth, nor processing time to re-send dropped packets. Control packets as shown in Fig. 4.24 are much more important and easy to re-send.

A final point to note is that the outgoing bandwidth is constant, which greatly simplifies the transceiver firmware. More importantly it allows a guaranteed latency to servicing samples for the ADC, because the code flow is fixed and can be analyzed for longest-path. As mentioned earlier, the Blackfin is not optimized for jumps or non-pipelined memory moves, both which would be required to send individual waveform snippets, nevermind the fact that waveform snippets from 128 channels would quickly overwhelm the 2 Mbps radio.

4.4.2 Bridge firmware

The bridge operates in a much less power and time constrained environment, hence the code is written most entirely in C, and is relatively straightforward. There is no OS, but unlike the transceiver, code runs from SDRAM and not L1 cache. Most of

the code manages the relevant networking protocols – ARP, IP, DHCP (to get an IP address on the network), ICMP (to shut down UDP stream when requested & to respond to PING), UDP (to send raw data stream), TCP (control packets and webserver), HTTP (webserver) and SLP (used to discover and configure bridges on a local network).

When the bridge boots, it first configures SDRAM refresh, sets clocks (600 Mhz core and 120 Mhz peripheral), and checks the SDRAM. Then the network interface is brought up, and a DHCP lease is requested. If a DHCP lease is granted, the bridge begins broadcasting its presence via SLP. If a client responds with the the correct code and a radio channel to these broadcasts, the bridge turns the three radios to this channel and pairs with the issuing IP address. It then remains in a tight loop, servicing the radio and buffering individual packets into 512 byte ethernet frames. Packets that do not match 16-bit CRC (as computed by the Nordic radio) are rejected. The radio that most recently received a valid packet transmits the most recent command packet when an end-of-frame packet is found (packet # = 15). No bit-averaging or error correction is presently employed, though there is plenty of processor headroom to do so. When recording from a monkey in a metal cage for 25 hours, including the normal range of movement, 1 in 3176 packets were rejected on average; assuming one bit error per packet, this equates to a bit error rate of 1.23e-6, or approximately one bit error per second. Efforts to reduce this have not been successful, but the system works acceptably presently.

Interruption-free audio output on the bridge proved a challenge in the face of these dropped packets, as pulses or breaks in the audio stream could be falsely interpreted by the ear as spikes. To prevent this, audio output is controlled by a PLL that switches between three resampling frequencies, one slightly higher, one at, and one slightly below the incoming sample rate. These two frequencies are toggled based on the fill status of a 512-sample circular buffer, with sufficient headroom to prevent

glitches following loss of 16 packets, or aggregate packet loss rates of 0.36% (> 10 times the observed packet loss rate). The three tones are separated by 7.25 cents each, which is very near the human threshold of detection of 6 cents for periodic signals, and hence switching is completely imperceptible with the normal stochastic signals.

The bridge is depicted in Figure 4.16; a schematic overview of the design to this point is in Figure 4.25.

The headstage timestamps each packet as it is received with a 32-bit slice of the 64-bit performance counter on the processor; it would be better to timestamp on the headstage, but there is insufficient radio bandwidth for that without sacrificing analog channels. This clock runs at 600 Mhz / 2^{16} = 9.1552734 kHz.

4.4.3 Sorting Client

The sorting client is written in C/C++ using the GTK2 GUI toolkit with OpenGL and HLSL for graphics, presently exclusively on Debian GNU/Linux. It consists of around 12600 lines of code, much for managing the GUI, displaying waveforms on the screen, maintaining persistent state (using sqlite3, ala Mail.app and Android), saving data, and communicating with clients.

Spike sorting on the client is very similar to that used by Plexon Inc's SortClient and OfflineSorter: raw traces are thresholded, waveforms are extracted around the threshold, and a PCA projection is computed of these waveform snippets. Unlike Plexon, threshold crossing can be moved in both *time* and *voltage* domains, which permits considerably greater flexibility when centering a waveform within the relatively narrow 16-sample template region. Threshold is currently positive-only, but negative thresholds can be realized by inverting per-channel gain. PCA projected waveforms are selected by the user via a polygonal lasso, and the mean and L1 norm of this sample is computed. The former is sent to the transceiver as the template,

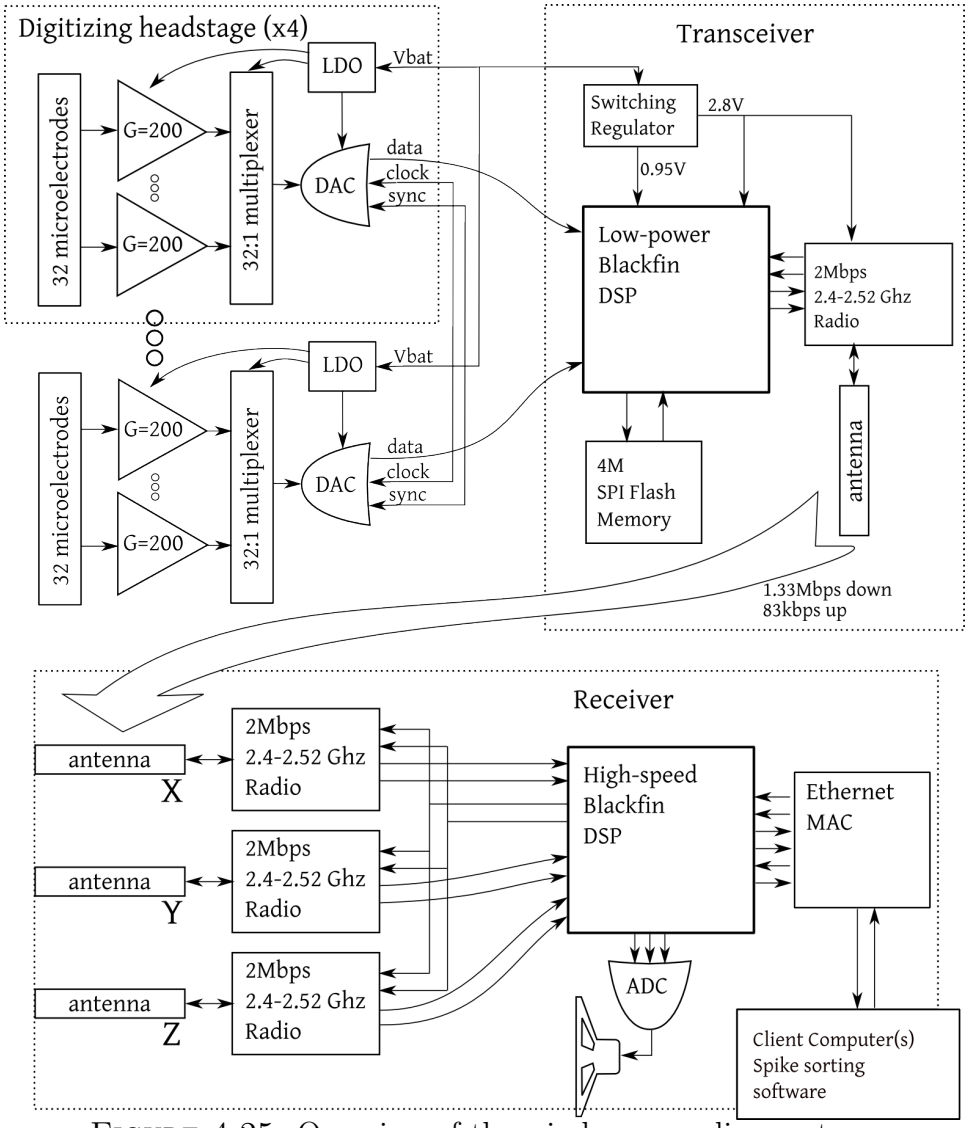

FIGURE 4.25: Overview of the wireless recording system.

and the latter sets a guess at the aperture. Aperture can later be updated manually by the user; as the aperture is changed, the GUI updates the color labels of the PCA projected points. Figure 4.26 shows the sorting GUI.

Sorting in the client is somewhat complicated by the fact that the transceiver does not specify which of the 24 possible set of samples matched a given template. To cross-check sorting between the transceiver and client, the latter convolves the known template with the last 24 continuously transmitted samples, finds the best,

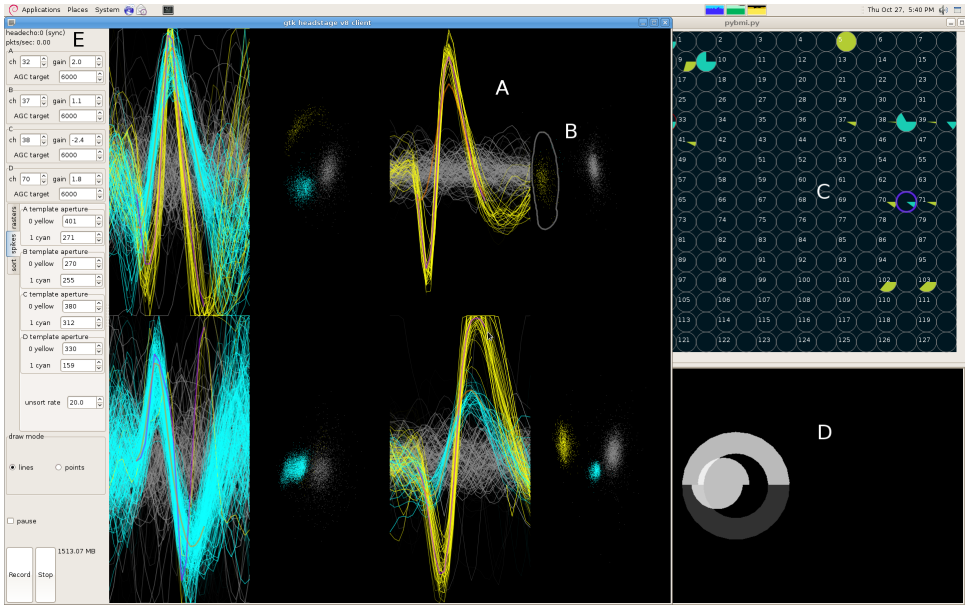

FIGURE 4.26: Screenshot showing client and BMI software. A, Waveform display; templates are lightly visible in purple and orange. Four channels may be sorted at the same time. B, PCA view with user lassoed cluster. C, BMI client for selecting units to be operantly conditioned. D, Local display of monkey's screen. E, GUI for setting parameters on transceiver. Channels 32, 37, 38, and 70 are currently selected, with varying post-LMS gain.

duplicates the SAA algorithm and verifies against the known aperture.

The client maintains an iterative estimate of the clock skew between the computer's performance counter and the timestamps received from the bridge using a standard PI controller. Interspike interval, binned at the 768 μs spike sample rate, is from this clock estimated and plotted on the screen. Likewise, bridge timestamps are recast to computer time for sending to clients. These timestamps are displayed in the bottom pane of Figure 4.27.

Packets coming from the transceiver are already sufficiently compressed, so these in addition to client clock and bridge clock are saved directly to file when recording. Outgoing packets are similarly saved in the file stream, along with ASCII versions of the commands. Commands to the transceiver are sufficiently complicated that it would be unreasonable to duplicate the code structure required to reinterpret them,

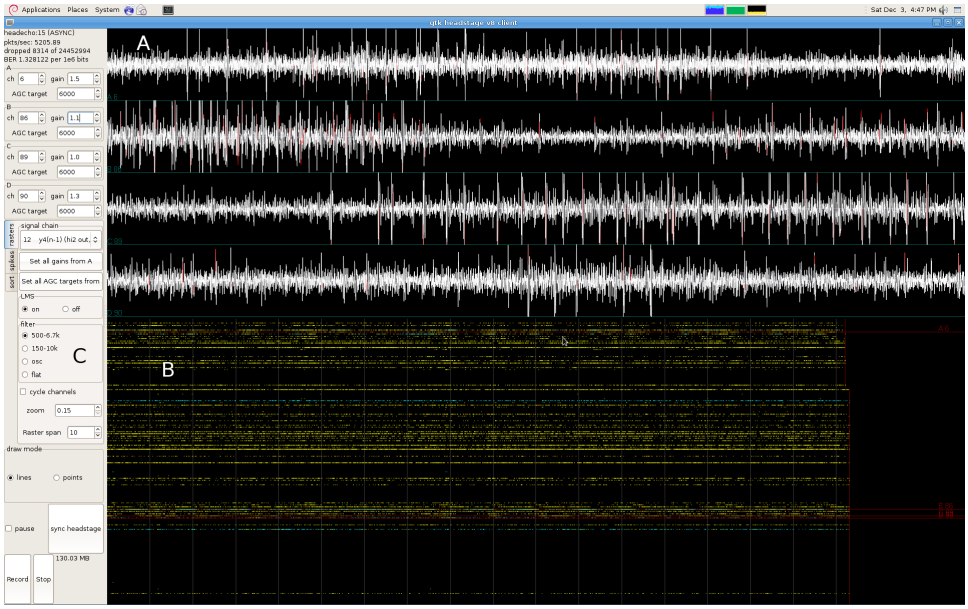

FIGURE 4.27: Screenshot showing client in rasters mode. A, Waveform of 4 continuously transmitted channels. B, Rasters of all 128 channels, two of which have been sorted for units A & B. C, GUI pane for setting the tap in the signal chain to examine, controlling gains, AGC, LMS, and filter bandwidth.

hence these human-readable messages are spliced into the stream.

The Sorting client optionally sends firing rates to requester through a TCP/IP socket. Firing rates are estimated by convolution with

$$x(t) = \gamma \frac{t}{t^4 + \alpha}$$

Where $\gamma = \frac{\pi}{4\sqrt{\alpha}}$. Typical values for $\alpha = 0.001$, resulting in the curve in Figure 4.28. This process is asynchronous so the BMI display may refresh as fast as the computer can run it.

4.5 Testing

The wireless recording system was mounted in a custom-designed headcap system (see Figure 4.29 and 4.30) and tested initially while the monkey was seated in a primate chair, then later while the monkey was in a custom-designed plastic cage.

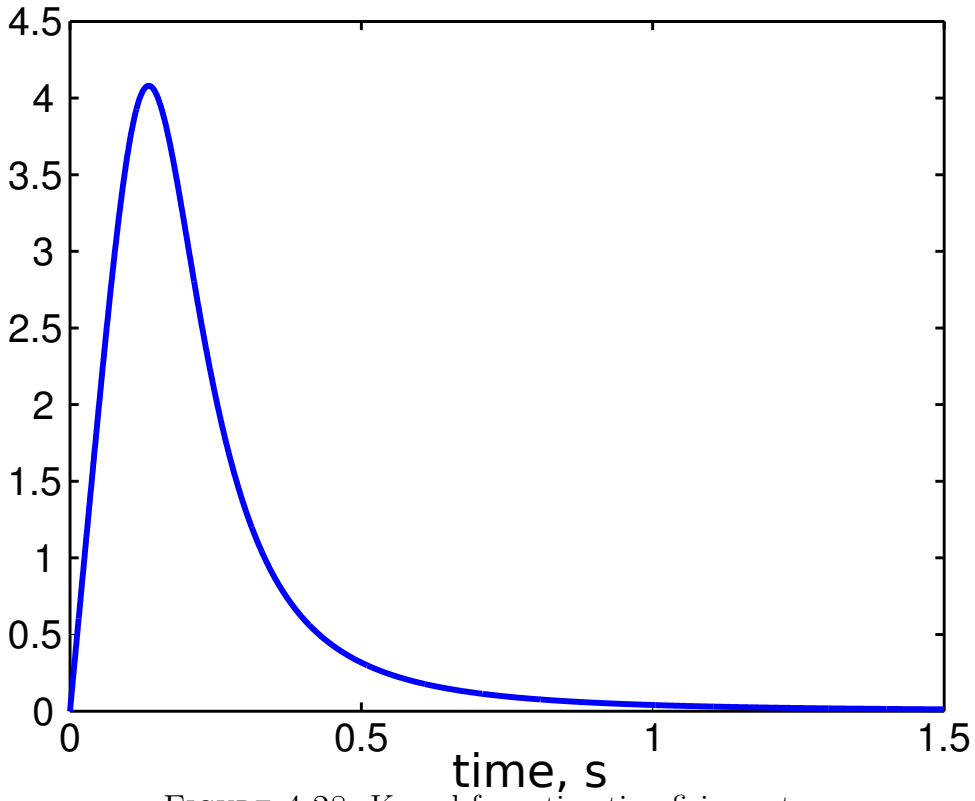

FIGURE 4.28: Kernel for estimating firing rate.

This was abandoned once it was realized that the radio worked acceptably well through the walls of the monkey's home cage (see Figure 4.31). An example recording session is shown in Figure 4.32; to date 14 days of recording have been made for 110 GB of compressed data.

4.5.1 1D BMI

The initial BMI tested was a simple 1D task, where the monkey had to modulate the firing rates of a few neurons to move the cursor left and right on the screen. This is operant conditioning as Fetz and Schmidt did decades ago, and as they discovered, it was not difficult for the monkey to learn. Figure 4.33 shows example behavior.

Both BMIs the monkey was in his home cage, with a juicer (powered by a General Motors windshield washer pump, with a backflow prevented by the valve from a squeegee bottle) mounted to the cage front. Positioned in front of the cage is the

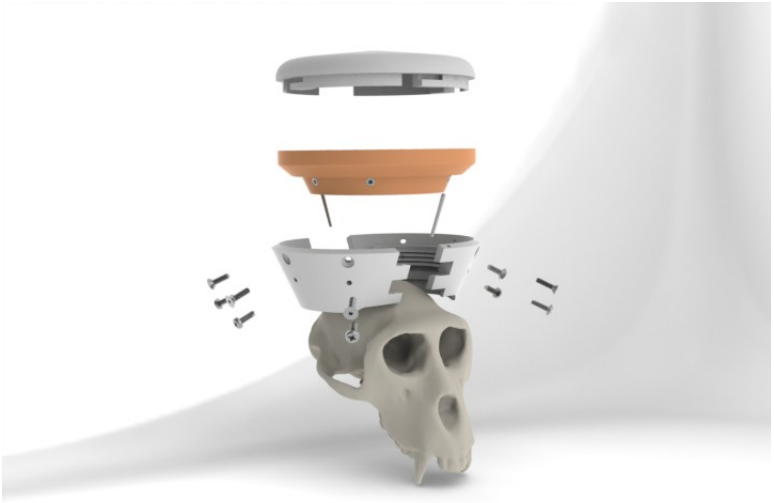

FIGURE 4.29: Headcap system for housing batteries and wireless system.

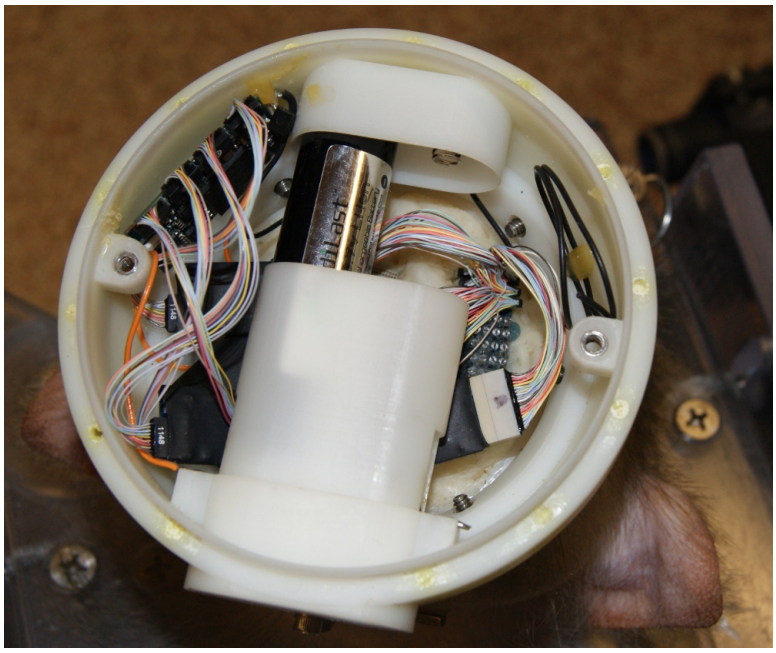

FIGURE 4.30: Wireless system mounted in headcap. Only one battery is used, but there is space for another. To replace the battery only one screw needs to be remove, which a trained monkey tolerates easily.

LCD monitor & computer setup, so that when the monkey is drinking from the juicer he has to face the screen. Cursor and target appear as circles on the screen, and the cursor must be held in the target for a variable length of time before juice is

FIGURE 4.31: Home cage wireless recording and behavioral setup. A, Bridge in a waterproof Pelican case;. B, Housing for monitor and computer. C, Webcams. D, Juice bottle case with pump. E, Juicer with IR detector.

rewarded. The juicer was instrumented with an IR detector so that when he was not attending to the game the juicer was disabled; the game itself continued, so as to provide control data. The monkey would routinely do 2500 to 3500 trials per day because this was his only source of water. Much of this work was done at night, when presumably there were no other distractions[8]. The experiment was monitored via webcams which streamed data to the downstairs office. Once the setup was working, all manipulations were done through the ethernet connection, and all that needed to be done was to refill the juice and replace the batteries once a day.

To determine if the monkey is actually controlling the cursor or merely waiting for it to spontaneously enter the target, latency and distance to target acquisition was measured, as well as cursor occupancy. See Figures 4.34, 4.35, and 4.36. Notably, to make these modulations the monkey initially learned to throw back his head,

[8] Upon observing this, the beeper for the juicer was turned off to avoid waking the other monkeys. The windshield wiper motor makes enough noise for the monkey to know when to expect juice.

presumably activating neck, shoulder, and hand muscles to keep himself from falling backwards in the cage. In later sessions, as shown in Figure 4.33, he learned to make isometric contractions that were not visible via webcam.

4.5.2 2D BMI

One the monkey achieved reasonable performance on the 1D BMI, control was transitioned to two dimensions. Unfortunately, there was only time to perform four days of training and behavioral shaping on this more difficult task, so the monkey only partially demonstrated convincing levels of cursor control. See Figure 4.37, 4.38, and 4.39.

In Figure 4.37 note relative higher occupancy for the lower right target – this was difficult for the monkey to hit, as it required increasing the firing rate of X group without increasing that of Y. For this experiment, the firing rates of 6 clearly isolated single units was summed to control the X axis, and a set of 6 others was used to control the Y axis. Biases are apparent in the upper left and right targets, but these proved to be nonsignificant once target size was accounted for.

There exists a chance that the significant result in Figure 4.39 is due to behavioral bias, as the monkey was likely to lose interest in trials that were taking too long, hence longer randomly-occurring trials were more likely to be unattended. If this were true, however, the same bias should be apparent in Figure 4.38. It is therefore likely that the monkey was starting to learn this new random coordination task.

4.6 Discussion

A wireless recording system has been designed through the course of several iterations, and is demonstrated with an operant conditioning task and a simple 2D BMI from and unrestrained primate from his normal metal home-cage. Though testing only includes one transceiver in one monkey, the system should easily scale to 256

Table 4.1: Wireless recording system specifications

Parameter	Value
Channels	128
Maximum # channels	2560
Sorting method	Templates
Templates per channel	2
Power consumption	264 mW
Battery life	> 30 hrs[9]
Input-referred noise	4.9 μ V_{rms}
Analog Gain	200
ADC resolution	12 bits
LSb of ADC	3.66 μV
Sampling rate	31.25 ksps / channel
Outgoing radio B/W	$1.33\bar{3}$ Mbps
Incoming radio B/W	$83.\bar{3}$ kbps
Size:	-
Digitizing headstages	1.37 x 2.15 x 0.16 cm
Processor and wireless	4.3 x 2.1 x 0.34 cm

channels and more; the radio itself, with 4 Mhz guard bands, is capable of supporting up to 20 simultaneous streams, or 2560 channels. The system features template based sorting on the transceiver itself, which greatly reduces required radio bandwidth, and is capable of transmitting 4 continuous channels alongside the template matches. Unlike many other neural recording systems, the radio is bidirectional so that the user and client computer may set parameters on the transceiver. The device is capable of running for over 30 hours on one commodity lithium-ion rechargeable battery. A list of the relevant specifications is in table 4.1.

The recording system offers a number of improvements and advantages for monkey electrophysiology.

- Easier – Requires only changing the batteries once a day.
- More data – The animals can work many hours a day.
- Better behavior – Animals are more relaxed and comfortable.

Table 4.2: Wireless power consumption breakdown

Component	Power	Percentage
Blackfin core	118 mW	44%
– static current	12.3 mW	4.7%
– dynamic current	106 mW	40%
Intan amplifiers[10]	60 mW	22%
Radio	34 mW	16.3%
Buck conversion loss	18 mW	6.8%
Misc. static currents[11]	13.3 mW	5%
Driving digital lines	12 mW	4.5%
ADCs	9 mW	3.4%

- More channels – The system is scalable to thousands of channels.
- Recording during sleep.
- Continuous recording – As neurons are recorded continuously their identity can be better assured.
- Higher quality recording – There are no ground loop problems, and 60 Hz / microphonic / EMG noise is adaptively removed by LMS.

All is not perfect, though: several immediate improvements are due. The primary is that of power. Table 4.2 lists the power consumption of the transceiver by component. Clearly, the largest component is the Blackfin; replacing it with an low-power FPGA may be a good alternative, though it may not as the heavily used multiply-accumulate units on the Blackfin are likely to be more power-efficient per operation than an unoptimized FPGA multiplier. Simplifying the software and lowering the clock rate and core voltage of the Blackfin may be a reasonable alternative; clocking the Blackfin at 320 Mhz at 0.85 V reduces the dynamic core power to 60 mW. This would reduce total power to 224 mW which is under the heat flux of 80 mW/cm^2 found to cause necrosis in muscles (Seese et al., 1998).

Training on the 2D BMI task proved sufficient to demonstrate recording system

functionality but little more; it seems likely that this is a matter of time. Ganguly and Carmena (2009) found that it took his monkeys 3-8 days to learn a fixed-transform consisting of a shuffled decoder, which is similar to (but perhaps more difficult than) the summed firing rate task employed here. However, their monkeys were well trained on the task; though the monkey here has been used in a number of experiments by Joseph O'Doherty, these were all with BMIs using supervised training from hand movements, hence the task of learning a transform *de novo* was new to him. Given how many tries to get the wireless system to an acceptable state, it is not surprising that the first pass of an many-neuron two dimensional operant-conditioning task did not succeed in the first 4 days. Future work will work out the problems; one promising avenue is to examine the correlative structure of the neurons over behaviorally relevant timescales (all neurons are correlated over long timescales (Jackson et al., 2007)), and select groups correspondingly.

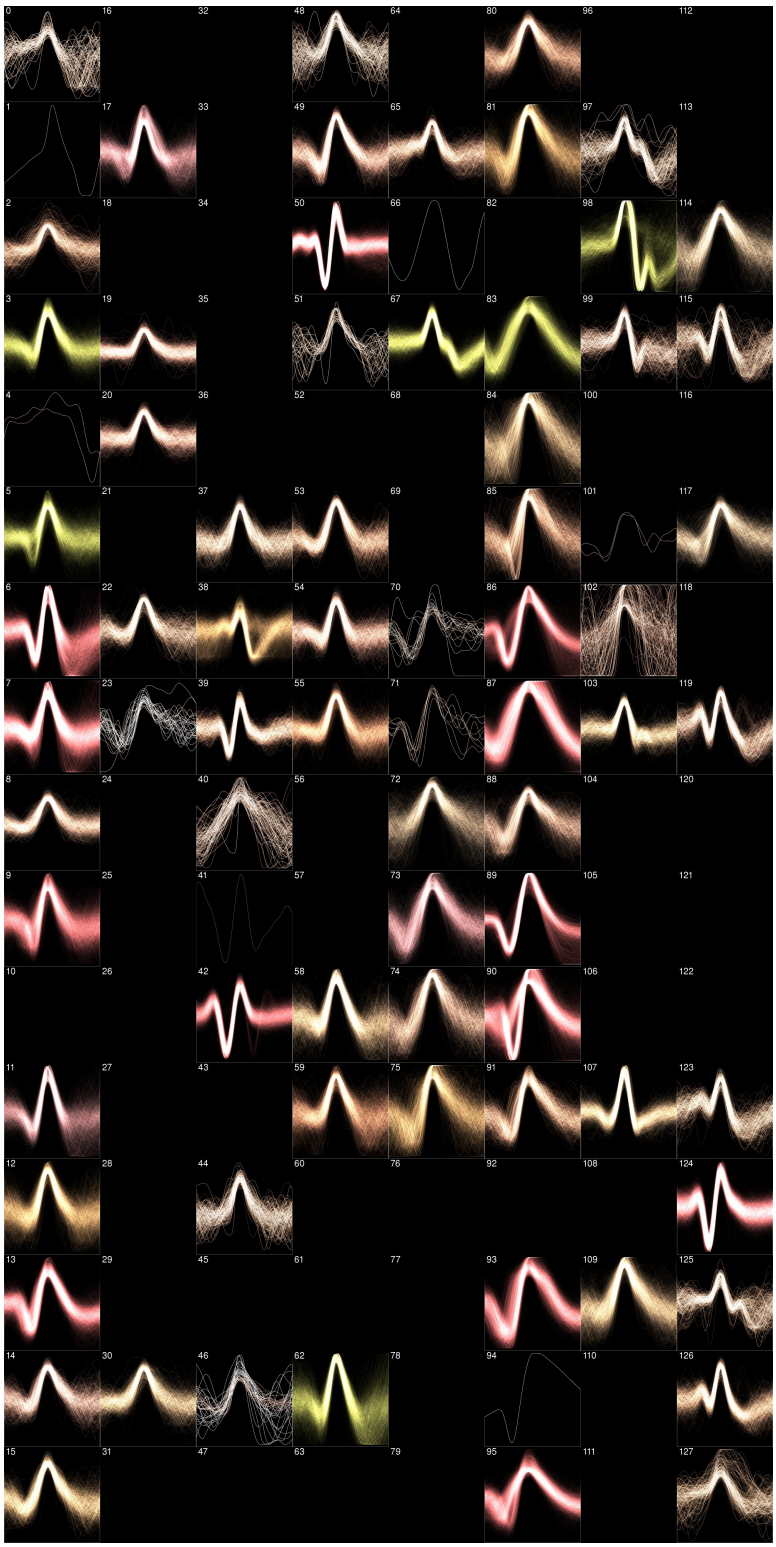

FIGURE 4.32: Waveforms from a 3.3 h 128 channel wireless recording session. Many single and multiunits are apparent.

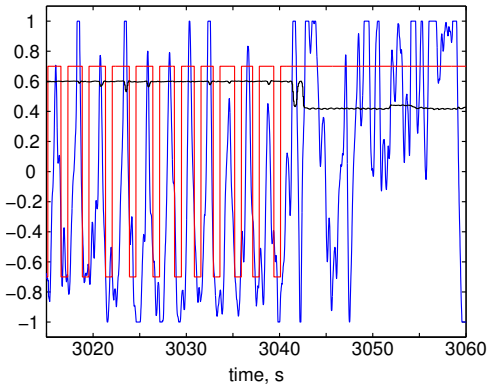

FIGURE 4.33: Example 1D BMI behavior. Blue = cursor, red = target, black = IR sensor on juicer. When the IR sensor is above 0.5 V the monkeys mouth is on the juicer. Note that to the left the monkey is controlling the cursor, and is making periodic left-right movements; to the right, he stops paying attention and the cursor is notably uncontrolled. In this experiment cursor position was the summed firing rates of two clear single units.

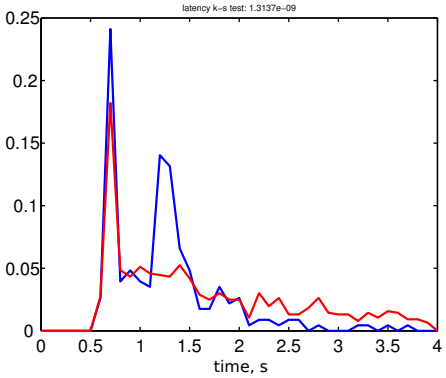

FIGURE 4.34: 1D BMI latency to target. Blue = monkey attending to task, red = not attending. Attending distribution is notably bimodal, as the monkey will attempt a second pulse if he misses (or does not hold long enough) the first time. Not-attending distribution has a peak shortly after the hold + reward time of 0.5 s, as firing rate modulations due to normal sleep and movement are sufficient to drive the cursor to target on occasion. Distributions different by K-S test, $p < 0.001$.

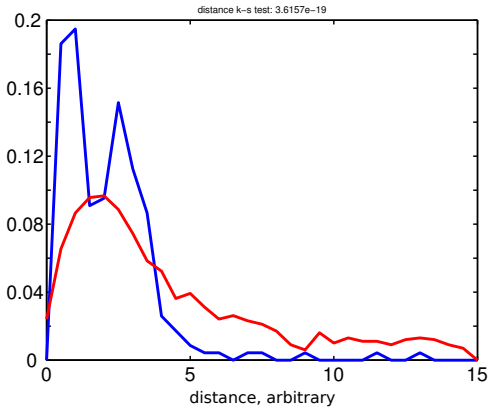

FIGURE 4.35: 1D BMI distance of path to target. Blue = monkey attending to task, red = not attending. Again, attending distribution is notably bimodal for try-again trials. Not attending distribution is broader and larger. Distributions different by K-S test, $p < 0.001$.

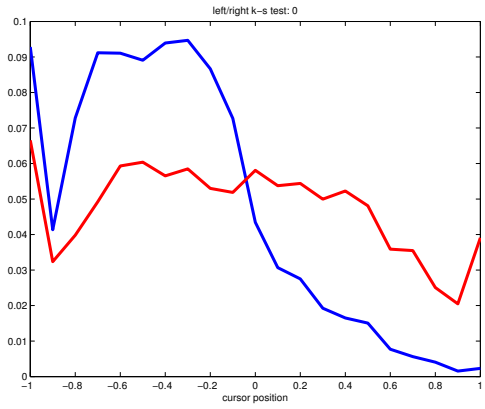

FIGURE 4.36: 1D BMI cursor occupancy. Blue, left target on screen; red, right target. Note for left target the monkey frequently pushes cursor against right wall. Distributions different by K-S test, $p < 0.001$.

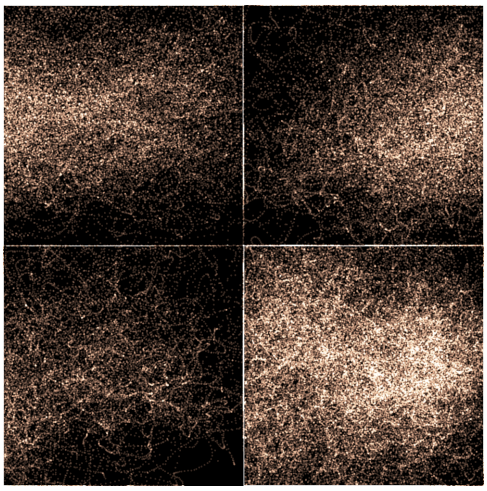

FIGURE 4.37: 2D BMI cursor occupancy. Each quarter corresponds to the time when the monkey was paying attention and the associated target was on the screen, e.g. lower left quarter is the occupancy when the lower left target was on the screen.

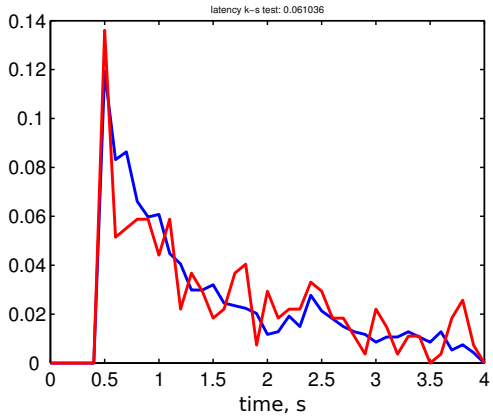

FIGURE 4.38: 2D BMI latency to target. Blue, time to target while the monkey was paying attention; red, time to target while not paying attention. Differences between distributions are not significant by K-S test, $p > 0.05$.

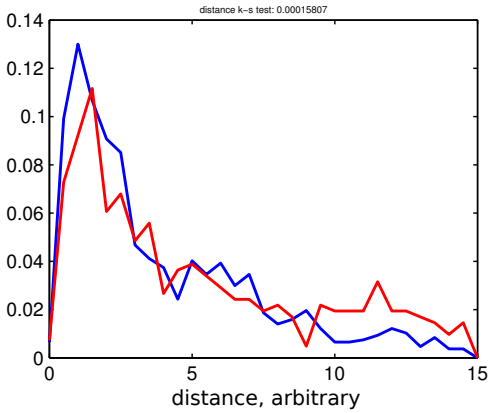

FIGURE 4.39: 2D BMI distance to target. Blue, distance to target while the monkey was paying attention; red, distance to target while not paying attention. Differences between distributions are significant by K-S test, $p < 0.001$.

5

Discussion

The work described here is, almost to a fault, highly iterative. Though it was not described, perfecting the microstimulator took many simulated designs and 5 full assembly-and-test cycles to get to the point of a workable 'product'; the same holds for the wireless recording system. Thorough iteration for the DBS work only occurred after the majority of recordings, which is perhaps why this was less successful. Data needs to be analyzed as soon as possible to correct for any errors in the experimental setup, or to improve recording quality, or to modify the stated purpose. The tighter this loop is brought the quicker structure can be built; I am certain there is math behind this, but I have not extensively searched for it.

Slightly less generally, the literature review of BMI technology related work has revealed a lot of redundant effort regarding recording systems, where each incompletely builds on others. (Commercially available technology and open-sourced hardware designs (Rolston et al., 2009a) are a notable exception to this.) This seems wasteful, since thousands of man-hours and public taxpayer dollars are put into this research, and in the case of physical designs rather than scientific results, much of the assembled structure is imperfectly represented in papers; it may not be, if the published

technologies are stepping stones to clinical or commercial application. All the utility of a scientific fact can be contained in a good paper; all the utility of a technology can be contained in a physical artifact. The lack of distribution of the latter[1] leads to dramatically slower structure-building[2].

As overviewed in Chapter 1, there is a lot of *very* good work that should be used in neurophysiology labs, but is not (Najafi's designs come to mind, or Rizk's system). To combat this and to prevent a technological stillbirth I've tried to make something that has utility beyond my own personal research interests; hopefully the lab, if not more people, can use it. Before I leave Duke I'll try to manufacture as many wireless systems as the robot can make, and iterate as needed from the feedback that experiments give.

Even less generally, there are vast possibilities for improvement to brain-machine interface technology. The primary is electrodes & recording methodologies. Optical methods, if tuned within the window that the brain is translucent to, would be optimal, as they are the least invasive communication path. Voltage-sensitive dies, two-photon imaging, or plasmonic gold particles (Zhang et al., 2009) offer promising avenues. In slightly longer wavelengths, backscatter sensing (Towe, 2007) would be impressive if the right RF band meta-materials could be made[3]. Beyond this, longer and shorter wavelength EM waves either require too large antennas or ionize tissue; that said, MRI uses quite long wavelengths and attains spatial precision through quantum-magnetic interactions, so nothing can be ruled out. For example, recent studies at Stanford show that biological tissue is relatively transparent to 1 GHz

[1] which capitalism solves

[2] Gregory Bateson astutely points out that communication, while typically focused on dealing with *non-redundant information* (if the receiver knows what the message is, or the message is redundant, there is no communication), actually makes the world *more redundant*: after communicating, both the transmitter and receiver have the same information. Hence communication reduces the open-system entropy.

[3] I tried proposing this to the Duke microwave 'invisibility cloak' lab, but they didn't bite.

frequencies, and very small antennas can be fabricated to receive the RF; while this has been applied to miniature swimming robots (Poon et al., 2007), it could easily be used in micro neural implants too.

Outside of EM, electrodes remain the best bet, and indeed literature suggests many possible avenues. The most glaring problem is the mechanical impedance mismatch between an electrode and the tissue it records. Electrodes need to be stiff to enter the brain without crumpling, though, which led Harris and colleagues (2011) to develop a nanocomposite electrode material which emulates sea cucumber skin. This composite, made of cellulose nanofibers embedded in a controllable polymer scaffold, undergoes a phase transition at physiological temperatures and becomes over 100 times less rigid once implanted. A much simpler solution to the problem is to make the electrodes so fine and so small that their rigidity is minimal. Indeed, polymer fibers smaller than 7 μm are effectively invisible to the immune system (Sanders et al., 2000) and to macrophage attachment (Bernatchez et al., 1996), which has lead Seymour and Kipke to design 'open architecture' electrodes where putative recording sites are spaced laterally off a penetrating shaft by 4 μm photoresist columns. This produced an decrease in encapsulation, though it was not complete, possibly because micromotion was still present, and the lithography did not permit actual recording sites on these lateral sites. Another method of inserting pliant electrodes is to attach the tip to a bit of steel, and accelerate it magnetically into the brain (Jaroch et al., 2009), or to attach the electrodes and a stiff insertion shuttle with a hydrophilic coating which releases after implantation (Kozai and Kipke, 2009), or to make the electrodes themselves amplifying carbon nanotube transistors (Tian et al., 2010).

I have spent much time and effort reviewing electrode technology literature as electrodes, more than anything else, are the limiting step. Thousands of neural channels seem required for proficient BMI control, probably due to the probabalistic nature of the brain (Deco et al., 2009), but thousands electrodes at current sizes

displace a large volume of tissue – they will need to get smaller. They should also get better, as excellent neural recording traces, as are possible with single sharpened glass insulated electrodes, make the task of amplification and sorting trivial, or at least well covered by existing technology. I do hope to work on this in the future, but in the meantime the recording system can be improved, by replacing the DSP with a FPGA as in (Zhang et al., 2011), reducing the noise and reducing amplifier current, simplifying the transceiver firmware, or employing a lower power radio (Liu et al., 2009). After extensive testing in the lab hopefully everything may be transitioned to a low-power implantable ASIC; indeed, fully implantable neurosystems are beginning to be available (Rouse et al., 2011). Implanting a wireless system would solve the final, and somewhat ignored, cause of implant failure: infection. One likely reason that the inverted or oblique electrode implantation technique (Kruger et al., 2010) works is that the path of infection was long and the immune system had plenty of space to prevent attack; likewise, acute recordings work because there is no time for infection. Many of the implants in the lab fail not because electrodes or connectors, but because of infection. While bulky, the system described *could* be implanted with the headstages on the head, wireless in the chest, and an inductive power link around the collar.

Regarding microstimulation, there are two areas that deserve investigation and development. The first is making the microstimulator wireless, work which has already started (see Figure 4.13, though far better approaches exist (Arfin et al., 2009)). The second is using out-of-band RF microstimulation below that needed to heat the tissue but sufficient to activate neurons. Because RF frequencies can be passively filtered and are actively ignored by the preamlifier, this makes true bidirectional recording and stimulation possible. The capacitive nature of metal electrodes is an advantage as well, as the impedance goes down with frequency hence only very low voltages are required. Radio frequency treatment of psychiatric disorders is common

in Russia (Richebe et al., 2005), and evidence shows that low AM band (500 kHz) RF stimulation is rectified by the membrane, hence able to activate neurons (Cosman and Cosman, 2005). Initial testing in humans has shown RF stimulation to elicit effects similar to DC microstimulation (Alberts et al., 1972), but given all the media fear regarding cell phone radiation affecting the brain, and other reports that RF energy below the threshold for heating can damage nerves (Hamann et al., 2006), caution must be exercised.

Around half of this dissertation was devoted to the Parkinson's disease, DBS, and in turn the basal ganglia; the other half to stimulating and recording technology, begging the question: how are they related? The two fields are converging, notably through closed-loop DBS, in which stimuulation is triggered on pathological activity, and more generally through the fact that learning to control a BMI, like much other motor learning, involves the basal ganglia. Jose Carmena, Rui Costa, and colleagues recently demonstrated this very fact by training rats and mice to perform a simple 1-D auditory feedback operant conditioning task, much like original rat BMI research (Gage et al., 2005)[4]. Whereas acurte NMDA receptor block did not affect BMI control, mice with cortico-striatal NMDA receptors were unable to learn to control the auditory cursor (Koralek et al., 2012).

This is perhaps a first step in determining how the brain learns and internalizes arbitrary associations, and how it develops new modes of sensorimotor control. BMI is a wonderful window for looking in on the brain as it learns, and I believe treating it as both a window and a clinical tool is the best future path for this subfield. Other aspects of BMI research have been discussed with respect to possible improvements and research avenues, but with the exception of electrodes, few directly offer new horizons: many groups are working on them, with diminishing returns. Improvement in decoder accuracy is one example – linear decoding captures at least 80% of

[4] Which they didn't seem aware of, or cite.

the variance with less than 20% of the algorithmic effort. New ideas beyond pure engineering optimization must be created; understanding how the brain coordinates behavior, or the function of e.g. the Piper rhythm, or the role of proprioceptive ventral-horn feedback, or if some neurons are more easily volitionally modulated [5], or if a vectoral proprioceptive signal can be provided to engage faster supervised learning (as in the cerebellum) – all these worthy venues of investigation.

Regarding DBS, the basal ganglia, and especially synchony and oscillation, there is tremendous need for both critical, controlled experiments (as opposed to simple open-ended observation studies [6]), and for comprehensive organization of the experimental results into competing hypotheses. The most recent 'vigorous tutor' theories behind basal ganglia function are convincing, but perhaps the same was thought of the rate models at the end of the 1980's; the theory needs to be cast in a critical light, especially in reference to the complicated etiology of Parkinson's and Huntington's disease. Furthermore, there is a large gap between intricate anatomical knowledge of the basal ganglia and the simple models used to understand their function; this needs to be remedied in the same way that complete models of the cortex are being developed. In terms of electrophysiology, true understanding waits for simultaneous recording of neurons in cortex, striatum, both sections of the pallidus, VA/VL and CM/Pf thalamus, and STN, ideally ones involved in the same pathway during a learning task. Progress on this front has recently been made (Feingold et al., 2011); the limitation is, again, recording technology.

As difficult as all the problems surrounding BMIs may be, there seems to be swelling interest, effort, and creativity toward making neuroprosthetics a reality, with

[5] The motor cortex is far more than an output structure. It computes something, and recording from the wrong set of neurons is perhaps like recording from the domino gates in an ALU of a computer, or the valve noise of an engine: you may know how 'much' of something is going on (arithmetic or acceleration, respectively), but you do not know exactly how that thing is computed.

[6] Hindsight is 20/20.

my own fractional incremental contribution here hopefully helping to move toward the goal.

Appendix A

Co-author papers

A.1 The muscle activation method: an approach to impedance control of brain-machine interfaces through a musculoskeletal model of the arm

For this paper, I performed recordings, helped create the musculoskeletal model in Matlab, and wrote the BMI software, hereafter referred to as BMI3 – it was the third revision of control software I had written, starting 2004-2005. Seven years later, it remains in heavy use.

The Muscle Activation Method: An Approach to Impedance Control of Brain-Machine Interfaces Through a Musculoskeletal Model of the Arm

Hyun K. Kim*, Jose M. Carmena, *Member, IEEE*, S. James Biggs, *Member, IEEE*, Timothy L. Hanson, Miguel A. L. Nicolelis, and Mandayam A. Srinivasan

***Abstract*—Current demonstrations of brain-machine interfaces (BMIs) have shown the potential for controlling neuroprostheses under pure motion control. For interaction with objects, however, pure motion control lacks the information required for versatile manipulation. This paper investigates the idea of applying impedance control in a BMI system. An extraction algorithm incorporating a musculoskeletal arm model was developed for this purpose. The new algorithm, called the muscle activation method (MAM), was tested on cortical recordings from a behaving monkey. The MAM was found to predict motion parameters with as much accuracy as a linear filter. Furthermore, it successfully predicted limb interactions with novel force fields, which is a new and significant capability lacking in other algorithms**

***Index Terms*—Brain-machine Interfaces, impedance control, musculoskeletal model, neuro-.**

I. Introduction

RESEARCH in brain-machine interfaces (BMIs) has flourished with recent technological advances in measuring electrical activity of populations of single cortical neurons through chronic implants. There have been numerous demonstrations of nonhuman primates controlling robots or graphical cursors in real-time through signals collected from cortical areas. These demonstrations can be divided largely into two categories: either continuous control of position [1]–[4] or discrete control of more abstract information such as intended targets, intended actions, and onset of movements [5], [6].

In BMI systems that use the continuous control of position strategy, much of the work thus far has treated the primate as a pure motion source. This makes intuitive sense considering that numerous studies show that much cortical activity is tuned broadly to higher level features of hand movement such as position [7] and velocity [8], [9]. Using this approach, neural recordings have been used to predict hand trajectory with reasonable accuracy [1]–[4]. This strategy has proved to be an appropriate first pass at BMI, confirming the potential for decoding movement features from cortical areas in order to drive neuroprostheses for paralyzed patients.

In this paper, we discuss the next logical step—impedance control of a brain machine interface. An introduction to impedance control can be found in [10]. For the newcomer, it can be briefly summarized as follows.

A motion source has infinite mechanical impedance. It is the complement of a force source, which has zero mechanical impedance. These ideal sources have behavior independent of the load they drive. However, the mammalian neuromuscular system is neither an ideal force source nor an ideal motion source, and its mechanical impedance is far from either of the two extremes. In fact, the neuromuscular system is highly adaptive and can modulate mechanical impedance. Numerous studies show that this modulation is essential for versatile interaction with the environment [10]–[12]. For example, when writing neatly on tax forms or soldering circuits, we increase the stiffness of our hand movements for precise position control. When catching an egg or handling delicate objects, we decrease the stiffness.

This stiffness along with the inertia and damping parameters determine the static and dynamic interaction with objects and are collectively referred to as the mechanical impedance of the manipulator. In prior work on BMIs this impedance information was lost. The decoding algorithms did not have mathematical forms that could capture these aspects of motor performance. The goal of the muscle activation method (MAM), which will be introduced below, is to decode mechanical impedance (intended inertia, damping and stiffness) from neural activity, so that impedance control [10] can be implemented on a slave robot, and the user's intended impedance can be displayed to the environment. If successful, this approach would give the neuroprosthesis user the sort of prosthesis control necessary to perform the wide range of tasks that interaction with objects demands, whether that task is filling out a tax form or catching an egg.

There are two general approaches to the problem of decoding impedance. The approach one takes depends on a deep-rooted argument in neuroscience about how motion is encoded in the cortex. Does the cortex only specify high-level movement features and leave the conversion of this relatively abstract representation into muscle commands for neurons downstream, or

Manuscript received April 28, 2006; revised December 10, 2006. This work was supported in part by the Defense Advanced Research Project Agency (DARPA) under Grant N66001-02-8022 and in part by the Christopher Reeve Paralysis Foundation, which supported JMC. *Asterisk indicates corresponding author.*

*H. K. Kim is with the Mechatronics and Manufacturing Technology Center, Samsung Electronics, Suwon, Korea (e-mail: hyunkim@mit.edu).

J. M. Carmena is with the Department of Electrical Engineering and Computer Sciecnes, and the Helen Willis Neuroscience Institute, University of California, Berkeley, CA 94720 USA (e-mail: carmena@eecs.berkeley.edu).

S. J. Biggs and M. A. Srinivasan are with the Touch Laboratory, Massachusetts Institute of Technology, Cambridge, MA 02139 USA (e-mail: jbiggs@mit.edu; srini@mit.edu).

T. L. Hanson and M. A. L. Nicolelis are with the Department of Neurobiology, Duke University, Durham, NC 27710 USA (e-mail: hanson@neuro.duke.edu; nicoleli@neuro.duke.edu).

Color versions of one or more of the figures in this paper are available online at http://ieeexplore.ieee.org.

Digital Object Identifier 10.1109/TBME.2007.900818

A.2 Primate reaching cued by multichannel spatiotemporal cortical microstimulation

For these experiments, I built the microstimulators used and wrote most of the microstimulation control software and associated software 'glue'.

Behavioral/Systems/Cognitive

Primate Reaching Cued by Multichannel Spatiotemporal Cortical Microstimulation

N. A. Fitzsimmons,[1,4] **W. Drake,**[1,4] **T. L. Hanson,**[1,4] **M. A. Lebedev,**[1,4] **and M. A. L. Nicolelis**[1,2,3,4]

Departments of [1]Neurobiology, [2]Biomedical Engineering, and [3]Psychological and Brain Sciences and [4]Center for Neuroengineering, Duke University, Durham, North Carolina 27100

Both humans and animals can discriminate signals delivered to sensory areas of their brains using electrical microstimulation. This opens the possibility of creating an artificial sensory channel that could be implemented in neuroprosthetic devices. Although microstimulation delivered through multiple implanted electrodes could be beneficial for this purpose, appropriate microstimulation protocols have not been developed. Here, we report a series of experiments in which owl monkeys performed reaching movements guided by spatiotemporal patterns of cortical microstimulation delivered to primary somatosensory cortex through chronically implanted multielectrode arrays. The monkeys learned to discriminate microstimulation patterns, and their ability to learn new patterns and new behavioral rules improved during several months of testing. Significantly, information was conveyed to the brain through the interplay of microstimulation patterns delivered to multiple electrodes and the temporal order in which these electrodes were stimulated. This suggests multichannel microstimulation as a viable means of sensorizing neural prostheses.

Key words: **microstimulation; brain–machine interface; primate; somatosensory; discrimination; neuroprosthetics**

Introduction

For more than a century, electrical stimulation has been used to probe brain circuitry and function in both humans (Penfield and Boldrey, 1937; Penfield and Rasmussen, 1950; Ransom, 1892) and animals (Fritsch and Hitzig, 1870; Ferrier, 1873, 1875). The effects of electrical stimulation depend on the location and parameters of stimulation. Stimulation of large brain areas typically hinders information processing (Pascual-Leone et al., 2000; Chambers and Mattingley, 2005; Kammer, 2006). Conversely, stimulation of small areas, termed microstimulation, can evoke motor and sensory effects that mimic the functional contribution of the stimulated area (Tehovnik, 1996; Graziano et al., 2002; Cohen and Newsome, 2004; DeAngelis and Newsome, 2004; Tehovnik et al., 2006). In the 1950s, neurobiologists began operantly conditioning animal behavior using electrical stimulation of the brain as a conditioned stimulus (Doty et al., 1956; Nielson et al., 1962; Doty, 1965, 1969) or a reinforcement (Olds and Milner, 1954). More recently, microstimulation of sensory areas has been shown to produce perceptual effects such as visual sensation (Bartlett et al., 2005), biasing the perception of visual motion (Salzman et al., 1990, 1992; Britten and van Wezel, 1998) or face recognition (Afraz et al., 2006), and mimicking the somatosensory perception of flutter (Romo et al., 1998, 2000; de Lafuente and Romo, 2005). Impressively, Talwar et al. (2002) used microstimulation of the rat barrel cortex to guide rats through a complex terrain. Although it is often difficult to prove that animals experience perceptions during microstimulation, microstimulation-induced perceptions have been demonstrated in humans (Penfield and Perot, 1963; Brindley and Lewin, 1968; Dobelle et al., 1976; Davis et al., 1998; Kiss et al., 2003; Ohara et al., 2004).

With the development of multielectrode implants (Nicolelis et al., 2003) and the concurrent advances of brain–machine interfaces (Chapin et al., 1999; Wessberg et al., 2000; Taylor et al., 2002; Carmena et al., 2003; Lebedev et al., 2005; Lebedev and Nicolelis, 2006), there is renewed interest in microstimulation as a means of providing the brain with an artificial sensory channel. Such a channel could recover sensation lost because of a neurological disorder or it could convey information from sensors of a prosthetic limb (Berger et al., 2005; Middlebrooks et al., 2005; Lebedev and Nicolelis, 2006; Wickelgren, 2006). Although this idea is intriguing, two critical issues must be addressed: (1) whether such artificial sensation can be improved by using multichannel microstimulation, and (2) whether microstimulation in this application is suitable for long-term usage. We explored the first issue by testing the capacity of owl monkeys to discriminate multichannel microstimulation of increasing complexity. We investigated the second issue by testing the long-term efficacy of microstimulation.

Two monkeys were previously trained in a reaching task in which target location was cued by vibrotactile stimuli (Sandler, 2005). Here, skin vibration was replaced by microstimulation of

Received Dec. 7, 2006; revised April 5, 2007; accepted April 9, 2007.

This work was supported by the Defense Advanced Research Projects Agency, Defense Science Office, and the Space and Naval Warfare Systems Center, San Diego Contracts N66001-02-C-8022 and N66001-06-C-2019 (M.A.L.N.) and by National Institutes of Health Grant NS40543 (M.A.L.N.). We thank Dragan Dimitrov for performing the implantation surgery; Gary Lehew for designing the electrode implants; Aaron Sandler, Laura Oliveira, and Parag Patil for surgical assistance; Ian Peikon for engineering and programming support; Steven Wise for reading the first draft of this manuscript and providing excellent suggestions; and Susan Halkiotis for manuscript preparation.

Correspondence should be addressed to M. A. L. Nicolelis, Department of Neurobiology, Bryan Research Building, Room 327E, Box 3209, Duke University Medical Center, 101 Research Drive, Durham, NC 27100. E-mail: nicoleli@neuro.duke.edu.

DOI:10.1523/JNEUROSCI.5297-06.2007

 0270-6474/07/275593-10$15.00/0

A.3 Unscented Kalman filter for brain-machine interfaces

I assisted with the experimental setup and recordings for this experiment. The unscented kalman filter Zheng Li created was implemented within the BMI3 framework.

OPEN ACCESS Freely available online

PLoS one

Unscented Kalman Filter for Brain-Machine Interfaces

Zheng Li[1], Joseph E. O'Doherty[2], Timothy L. Hanson[3], Mikhail A. Lebedev[3], Craig S. Henriquez[2,5], Miguel A. L. Nicolelis[2,3,4,5,6]*

1 Department of Computer Science, Duke University, Durham, North Carolina, United States of America, **2** Department of Biomedical Engineering, Duke University, Durham, North Carolina, United States of America, **3** Department of Neurobiology, Duke University, Durham, North Carolina, United States of America, **4** Department of Psychology and Neuroscience, Duke University, Durham, North Carolina, United States of America, **5** Duke Center for Neuroengineering, Duke University, Durham, North Carolina, United States of America, **6** Edmond and Lily Safra International Institute of Neuroscience of Natal, Natal, Brazil

Abstract

Brain machine interfaces (BMIs) are devices that convert neural signals into commands to directly control artificial actuators, such as limb prostheses. Previous real-time methods applied to decoding behavioral commands from the activity of populations of neurons have generally relied upon linear models of neural tuning and were limited in the way they used the abundant statistical information contained in the movement profiles of motor tasks. Here, we propose an n-th order unscented Kalman filter which implements two key features: (1) use of a non-linear (quadratic) model of neural tuning which describes neural activity significantly better than commonly-used linear tuning models, and (2) augmentation of the movement state variables with a history of *n-1* recent states, which improves prediction of the desired command even before incorporating neural activity information and allows the tuning model to capture relationships between neural activity and movement at multiple time offsets simultaneously. This new filter was tested in BMI experiments in which rhesus monkeys used their cortical activity, recorded through chronically implanted multielectrode arrays, to directly control computer cursors. The 10th order unscented Kalman filter outperformed the standard Kalman filter and the Wiener filter in both off-line reconstruction of movement trajectories and real-time, closed-loop BMI operation.

Citation: Li Z, O'Doherty JE, Hanson TL, Lebedev MA, Henriquez CS, et al. (2009) Unscented Kalman Filter for Brain-Machine Interfaces. PLoS ONE 4(7): e6243. doi:10.1371/journal.pone.0006243

Editor: Yann LeCun, New York University, United States of America

Received January 28, 2009; **Accepted** April 15, 2009; **Published** July 15, 2009

Funding: Funding from DARPA N66001-06-C-2019 and the Duke University Graduate School. The funders had no role in study design, data collection and analysis, decision to publish, or preparation of the manuscript.

Competing Interests: The authors have declared that no competing interests exist.

* E-mail: nicoleli@neuro.duke.edu

Introduction

Research on brain-machine interfaces (BMI) – devices that directly link the brain to artificial actuators [1,2,3] – has experienced rapid development during the last decade primarily because of the expectation that such devices may eventually cure severe body paralysis caused by injury or neurodegenerative disease [4,5,6,7,8]. A core component of BMIs is the computational algorithm that decodes neuronal activity into commands that drive artificial actuators to perform movements at the operator's will. Signal processing and machine learning techniques have been applied to the problem of inferring desired limb movements from neural recordings [9]. These include the population vector method [10,11,12,13,14,15,16], the Wiener filter [3,17,18,19,20], the Kalman filter [21,22,23,24], the particle filter [25,26,27,28], point process methods [29,30,31,32], artificial neural networks [18,33,34,35], and discrete state Bayesian approaches [18,36,37,38]. Decoding methods using linear models of the relationship between neural activity and limb movements, such as the Wiener filter and Kalman filter, are most commonly used in experimental research on BMIs. These methods cannot handle non-linear models, which describe neuronal modulations better but require more complex algorithms such as the particle filter [39], a non-parametric recursive Bayesian estimator. However, along with the power of particle filters comes a heavy computational cost, which makes this approach difficult to implement in real-time BMI systems. The space of possible non-linear models is vast, and selecting an appropriate model – one that offers significant improvement over a linear model while avoiding "over-fitting" of parameters [40] – is a non-trivial task. Combined with the more difficult software engineering involved, these factors explain the rarity of non-linear models in real-time BMI implementations.

We propose a new computational approach for BMIs, the n-th order unscented Kalman filter (UKF), to improve the extraction of motor commands from brain activity. Our experiments showed that this new approach offers more accuracy compared to methods which use linear models while remaining computationally light enough for implemention in real-time. This filter offers three improvements upon previous designs of BMI decoding algorithms. First, our filter allows the use of non-linear models of neuronal modulations to movements (*neural tuning models*). Our experiments demonstrate the increased accuracy of our quadratic model versus the previously-used linear model. Second, our filter takes advantage of the patterns of movements performed during the execution of tasks. For example, a prosthetic used to aid in feeding has to perform a stereotypical pattern of movements: the prosthetic actuator moves back and forth between the user's mouth and the food items placed on a tray. Our approach uses this stereotypic pattern to improve BMI output accuracy. Third, our filter allows the relationships between neural activity and arm movement at multiple time offsets to be used simultaneously.

These improvements were facilitated by extending the Kalman filter in two ways. First, the unscented Kalman filter [41], which uses a non-stochastic simulation method to approximate non-

A.4 A brain-machine interface instructed by direct intracortical microstimulation

I made the microstimulator, wrote a good section of the microstimulator control software (which Joseph O'Doherty extended considerably). This experiment also used the BMI3 software.

frontiers in
INTEGRATIVE NEUROSCIENCE

ORIGINAL RESEARCH ARTICLE
published: 01 September 2009
doi: 10.3389/neuro.07.020.2009

A brain-machine interface instructed by direct intracortical microstimulation

Joseph E. O'Doherty*[1,2], *Mikhail A. Lebedev*[2,3], *Timothy L. Hanson*[2,3], *Nathan A. Fitzsimmons*[2,3] *and Miguel A. L. Nicolelis*[1,2,3,4,5,6,7]

[1] *Department of Biomedical Engineering, Duke University, Durham, NC, USA*
[2] *Center for Neuroengineering, Duke University, Durham, NC, USA*
[3] *Department of Neurobiology, Duke University, Durham, NC, USA*
[4] *Department of Psychology and Neuroscience, Duke University, Durham, NC, USA*
[5] *Edmond and Lily Safra International Institute of Neuroscience of Natal, Natal, Rio Grande do Norte, Brazil*
[6] *Fellow, Center for Neuroprosthetics, Ecole Polytechnique Federale de Lausanne, Lausanne, Switzerland*
[7] *Blaise Pascal International Research Chair, École Supérieure de Physique et de Chimie Industrielles, Paris, France*

Edited by:
Sidney A. Simon, Duke University, USA

Reviewed by:
Marshall Shuler, Johns Hopkins University, USA
Rui M. Costa, Instituto Gulbenkian de Ciência, Portugal
Eberhard E. Fetz, University of Washington, USA

***Correspondence:**
Miguel A. L. Nicolelis, Department of Neurobiology, Duke University, Box 3209, Room 327E Bryan Research Building, 101 Research Drive, Durham, NC 27710, USA.
e-mail: nicoleli@neuro.duke.edu

Brain–machine interfaces (BMIs) establish direct communication between the brain and artificial actuators. As such, they hold considerable promise for restoring mobility and communication in patients suffering from severe body paralysis. To achieve this end, future BMIs must also provide a means for delivering sensory signals from the actuators back to the brain. Prosthetic sensation is needed so that neuroprostheses can be better perceived and controlled. Here we show that a direct intracortical input can be added to a BMI to instruct rhesus monkeys in choosing the direction of reaching movements generated by the BMI. Somatosensory instructions were provided to two monkeys operating the BMI using either: (a) vibrotactile stimulation of the monkey's hands or (b) multi-channel intracortical microstimulation (ICMS) delivered to the primary somatosensory cortex (S1) in one monkey and posterior parietal cortex (PP) in the other. Stimulus delivery was contingent on the position of the computer cursor: the monkey placed it in the center of the screen to receive machine–brain recursive input. After 2 weeks of training, the same level of proficiency in utilizing somatosensory information was achieved with ICMS of S1 as with the stimulus delivered to the hand skin. ICMS of PP was not effective. These results indicate that direct, bi-directional communication between the brain and neuroprosthetic devices can be achieved through the combination of chronic multi-electrode recording and microstimulation of S1. We propose that in the future, bidirectional BMIs incorporating ICMS may become an effective paradigm for sensorizing neuroprosthetic devices.

Keywords: brain–machine interface, primate, neuroprosthetics, cortical microstimulation, neuronal ensemble recordings

INTRODUCTION

During the last decade, considerable progress has been made in research on neuroprosthetics – devices that attempt to treat neurological impairments and limb loss by interfacing intact neural structures with artificial devices that enact motor or sensory functions (Nicolelis, 2003; Lebedev and Nicolelis, 2006; Schwartz et al., 2006; Fetz, 2007). Sensory neuroprosthetics, such as cochlear (Merzenich et al., 1974; Fallon et al., 2008) and visual (Dobelle et al., 1978; Dagnelie, 2008) implants, make use of electrical stimulation of sensory neural structures to recreate afferent input and perceptual experiences. Motor neuroprosthetics, often called BMIs (Nicolelis, 2001), transform neuronal activity recorded in motor areas into commands to move artificial actuators such as cursors (Serruya et al., 2002; Taylor et al., 2002) and robotic devices (Wessberg et al., 2000; Carmena et al., 2003; Velliste et al., 2008), and for the functional stimulation of muscles (Moritz et al., 2008).

Curiously, sensory and motor neuroprosthetics have developed largely in parallel, without attempts to build an integrated system with both motor and sensory capabilities. Normal interactions with the environment, however, require conjoint processing of sensory and motor signals (Witney et al., 2004; Crapse and Sommer, 2008). Thus, the neurophysiological mechanisms underlying voluntary motor control in mammals are critically dependent on the afferent innervation of the skin, muscles and joints (Ribot-Ciscar et al., 2003; James et al., 2007). Indeed, the paucity of sensory signals available in current BMIs could be a factor limiting their future clinical usefulness.

Here we propose that future clinical neuroprostheses could be based on a bi-directional system in which motor control signals are extracted from the brain, using multi-electrode arrays implanted in motor areas, while tactile, proprioceptive and other useful signals, are sent back to the brain through spatiotemporal patterns of intracortical microstimulation (ICMS) delivered to sensory areas (Lebedev and Nicolelis, 2006). To advance this goal, we added a direct intracortical input to a BMI, based on multi-electrode cortical microstimulation used by a rhesus monkey for enacting arm reaching movements (**Figure 1A**). This intracortical input instructed the direction of BMI-generated cursor movements.

A.5 Future developments in brain-machine interface research

This paper discusses much work done in the lab. I've been privileged to help my colleagues and co-authors with hardware / software / matlab analysis code.

Future developments in brain-machine interface research

Mikhail A. Lebedev,[I] Andrew J. Tate,[I,II] Timothy L. Hanson,[I,II] Zheng Li,[I,II] Joseph E. O'Doherty,[I,II] Jesse A. Winans,[I] Peter J. Ifft,[I] Katie Z. Zhuang,[I] Nathan A. Fitzsimmons,[I] David A. Schwarz,[I] Andrew M. Fuller,[I] Je Hi An,[I] Miguel A. L. Nicolelis[I,III]

[I] Neurobiology,Duke University, Durham, NC, USA. [II] Duke University Center for Neuroengineering, Duke University, Durham, NC, USA. [III] Edmond and Lily Safra International Institute of Neuroscience of Natal

Neuroprosthetic devices based on brain-machine interface technology hold promise for the restoration of body mobility in patients suffering from devastating motor deficits caused by brain injury, neurologic diseases and limb loss. During the last decade, considerable progress has been achieved in this multidisciplinary research, mainly in the brain-machine interface that enacts upper-limb functionality. However, a considerable number of problems need to be resolved before fully functional limb neuroprostheses can be built. To move towards developing neuroprosthetic devices for humans, brain-machine interface research has to address a number of issues related to improving the quality of neuronal recordings, achieving stable, long-term performance, and extending the brain-machine interface approach to a broad range of motor and sensory functions. Here, we review the future steps that are part of the strategic plan of the Duke University Center for Neuroengineering, and its partners, the Brazilian National Institute of Brain-Machine Interfaces and the École Polytechnique Fédérale de Lausanne (EPFL) Center for Neuroprosthetics, to bring this new technology to clinical fruition.

KEYWORDS: Brain-machine interface; Neuroprosthetic; Primate; Bipedal locomotion; Intracortical microstimulation; Sensory substitution.

Lebedev MA, Tate AJ, Hanson TL, Li Z, O'Doherty JE, Winans JA, Ifft PJ, Zhuang KZ, Fitzsimmons NA, Schwarz DA, Fuller AM, An JH, Nicolelis MAL. Future developments in brain-machine interface research. Clinics. 2011;66(S1):25-32.

Received for publication on January 28, 2011; **Accepted for publicaiton on** January 30, 2011

E-mail: nicoleli@neuro.duke.edu

Tel.: 919 684 4580

INTRODUCTION

Millions of people worldwide suffer from sensorimotor deficits caused by neurologic injuries, diseases or limb loss. According to recent data reported in Medical News Today, five million people in the USA alone currently suffer from some type of severe body paralysis.[1] Currently, there is no cure for such devastating cases of paralysis, for example complete spinal cord injury (SCI).[2] Meanwhile, treatment is only partially effective in less severe cases.[3] Neural prosthetic devices based on brain-machine interfaces (BMIs) hold promise to restore both partial and full body mobility in paralyzed patients.[4–10] BMIs bypass the site of the neural lesion and connect the remaining healthy motor areas of the brain, particularly the motor cortex, directly to assistive and prosthetic devices that can take the shape of, for example, robotic limbs or a full body exoskeleton. The main idea behind BMIs is to employ the activity of healthy motor brain areas, which in many cases of paralysis remain capable of generating motor commands despite being disconnected from the body effectors,[11] to control artificial tools that restore the patient's mobility.

During the last decade, the field of BMIs has experienced an explosive development.[7,9] Hence, it has generated high expectations among neuroscientists, physicians and patients alike, regarding its potential clinical applications. A number of BMI systems have been studied in rodents[12] and nonhuman primates.[13–17] BMI technology also entered human clinical research where both non-invasive EEG-based systems[5,18,19] and invasive BMIs based on brain implants[20–22] have been tested. Notwithstanding the success of these pioneering experiments, a number of issues need to be resolved before a fully functional practical neuroprosthetic for long-term use can be built.[7] These include: implant biocompatibility issues;[23] increasing the number of neural channels of the recording system; improving BMI decoding algorithms; building fully implantable systems; sensorizing neuroprosthetic limbs; and extending the BMI approach to a broader range of motor control tasks, especially tasks that require lower limb control: bipedal walking[24] and upright posture control.[25]

The Duke University Center for Neuroengineering (DUCN) has been at the forefront of BMI research on cortical prosthetic devices for motor rehabilitation since this field emerged about 12 years ago. At the DUCN, we have developed pioneering BMI systems that enact a wide range of motor functions, from arm reaching and grasping [13,17,26] to bipedal locomotion[24,27] in a variety of artificial actuators. DUCN researchers were also the first to incorporate artificial somatic sensation in BMIs.[28,29] Here, we review the most recent findings of the BMI initiative at the DUCN and discuss

Appendix B

Yushin

B.1 Description

Yushin is a scrapyard pick and place robot constructed for the original purpose of reliably mounting the 1.2 mm^2 LMV1032 amplifiers on the original wireless recording systems, as detailed Chapter 4. Its utility has extended beyond this, however, and I would not have been able to quickly assemble the many boards for the lab without it; humans have too much motor noise and fatigue too quickly to work with thousands of tiny parts that all look the same.

The four-axis robot is able to assemble boards with 0201 package components (0.6 mm x 0.3 mm) and locates parts via a arm-mounted video camera. Surface mount components to be placed are put within the robot workspace by double-sided taping them to the carrier tape they are packaged in to a large sheet of metal or plexiglas; placement does not need to be precise. On the arm is the vacuum pickup cannula, which is offset from the camera by 10 cm. Calibration of this cannula offset (all coordinates are camera-centric, like humans) is achieved either by a table-mounted camera which looks up to locate the position of the vacuum cannula, or through

a recursive sensory-motor loop. In the latter scheme, the robot locates the CoM of a part, picks it up, rotates it 180°, places it back down again, and re-assesses the CoM. Any translation should be twice the error in the camera-to-cannula offset, and hence is used to update the entries of the offset look up table. This table is indexed by 4th axis (cannula rotation), and should be sinusoidal but is not because of rotation-dependent static loading of the vacuum tube to the head.

B.2 Reflection

Some reflections are due following the creation of this device. With due respect for both connectionism and cybernetics, the whole project is really just a series of feedback loops: servo drive feedback from rotor encoders, camera feedback from part placement and part location on tape, feedback from the laser depth sensor; even within each step there are error-correcting feedback loops, e.g. EM algorithm for locating spots, simulated annealing for registering part locations. Each of these was put in place by the last loop of all: me. I don't think there was anything particularly incredible about each of the loops added, only that they were iterative and at times creative in locating or *creating* signals correlated with an error in question[1], hence permitting the error to be minimized under Newton-like linear methods. The particular example of this is optical part location, in which the robot moves following rough estimates of where 'register' thinks a part may be. There is no need to compensate for spherical aberration in the optics, or nonlinearities do to imperfect polishing of the ballscrews.

Throughout the designs outlined in the thesis, relatively little hard math was employed; even for the DBS paper, most tests were validated / corrected with simple

[1] Or alternately transforming the errors. An example of this would be if there was significant backlash in the ballscrews on the X and Y axes of the robot. If it were consistent backlash it could be removed by approaching each target endpoint with the same velocity and deceleration, thereby making the robot trajectories more complicated but transforming variable error into a constant error

bootstrapping. For example, to make the waveforms look nice in chapter 4, I emulated a massless, damped spring to upsample the 32-point waveforms, rather than more complicated curve fitting using splines. The algorithm is less than 25 lines of C, but achieves approximately the same result as splines without having to think very hard. There were many similar quick-and-dirty unscientific or un-mathematical hacks used in e.g. tuning the robot PID controllers (the actual inertia, winding inductance, K_d, damping, resonant modes, etc. were unknown for the motors that I had), but through guessing and parameter sensitivity testing the motors were made to work. It's all very "hackish" and non analytical, which makes me feel a little guilty, but I wonder if that is necessarily a bad thing.

The development of the wireless recording system proceeded in a similar, iterative 'fix the worst error' way, and, well, it seems to have worked. Humans are unique in that they can create and externalize these error-minimizing loops. One may hypothesize that certain loops within the brain work in the same way, namely the cortex → basal ganglia → thalamus → cortex, but this is almost too abstract to guide practical experiments. This hypothesis can also be approached from an engineering standpoint, in that the algorithms used to create feedback loops can be codified and automated, perhaps by copying the human sensory-cognitive-motor system.

B.3 Images

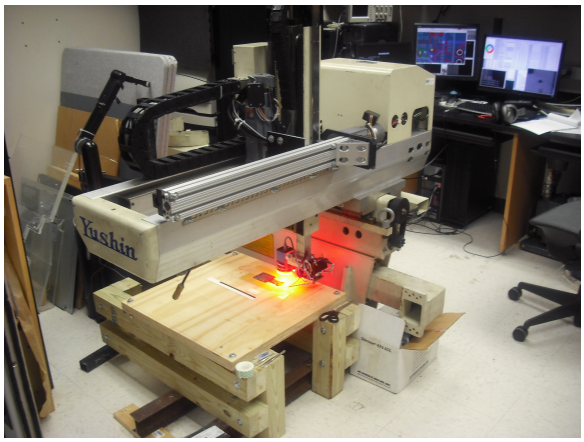

FIGURE B.1: Yushin pick and place robot. Device was purchased from a liquidated plastics molding company in Florida, and was sold on ebay for $100; the robot weighs $\approx$ 500 kg. Freight shipping was $400. Yushin is approximately as old as I am.

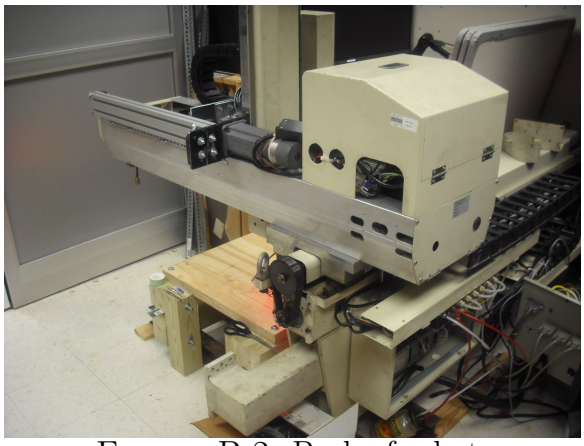

FIGURE B.2: Back of robot.

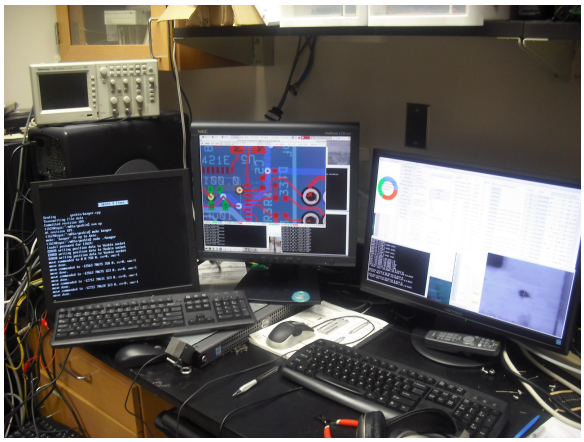

FIGURE B.3: Control computers. Left, realtime Linux servo control; center, board layout & source part location; right motion planner and computer vision.

FIGURE B.4: Robot was bolted to steel I-beams from a Durham scrapyard.

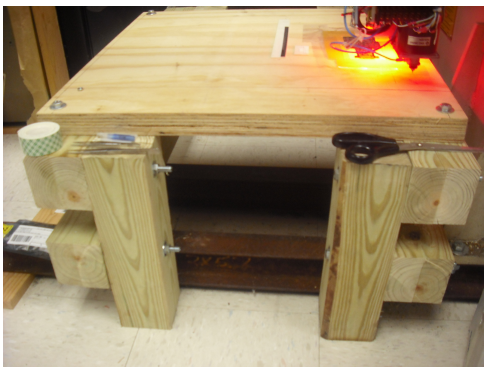

FIGURE B.5: Work table assembled of pressure-treated 4x4 lumber. Table tends to move with varying humidity and temperature, but system is stabilized by video feedback.

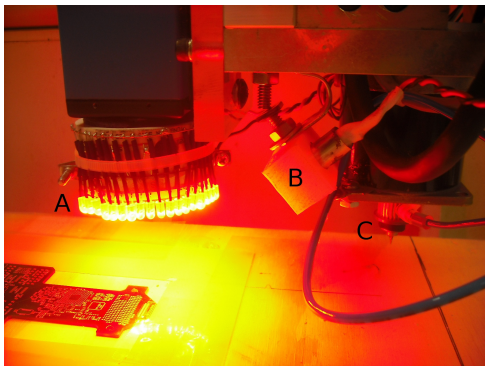

FIGURE B.6: A. Red ringlight for uniform illumination of parts. Right center in plastic block is a laser pointer recommissioned to measure height above part or PCB. In this scheme, laser it turned on, camera integrates 4 frames of image, laser is turned off, another 4 frames are integrated; 'on' and 'off' images are subtracted, resulting CoM of laser spot estimated through EM optimization. Height above table is then recursively estimated through sensory (laser) motor (Z-azis servo) loop, using a lightly damped Newton's method with stochastic guesses in cases with ambiguous gradient information. Right is stepper motor with 26 ga spring-mounted needle cannula for lifting and placing parts. Spring provides light setting force for picking and placing, and compliance for the inevitable errors from the laser depth-finder.

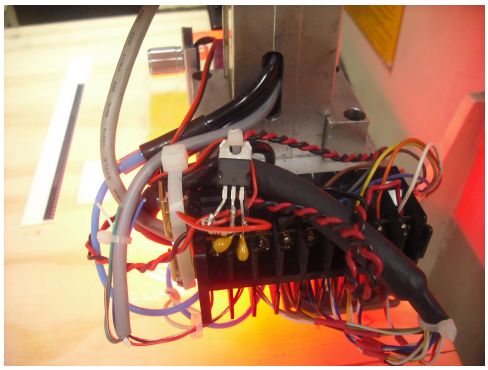

FIGURE B.7: View of head showing wiring (which was removed or cut by the factory liquidater), including the laser current regulator and stepper motor driver. Arm power supply varies as the stepper moves, hence the need for the regulator.

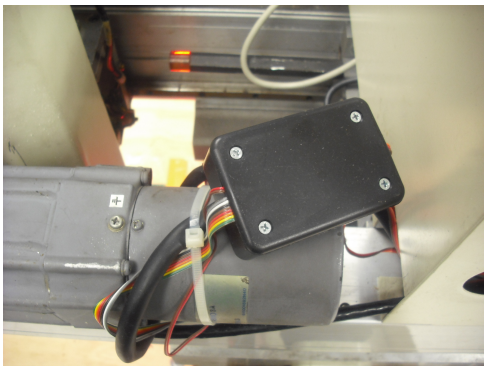

FIGURE B.8: Y-axis servo showing box for translating absolute encoder bus value to simulated hall-effect transducers to permit servo commutation.

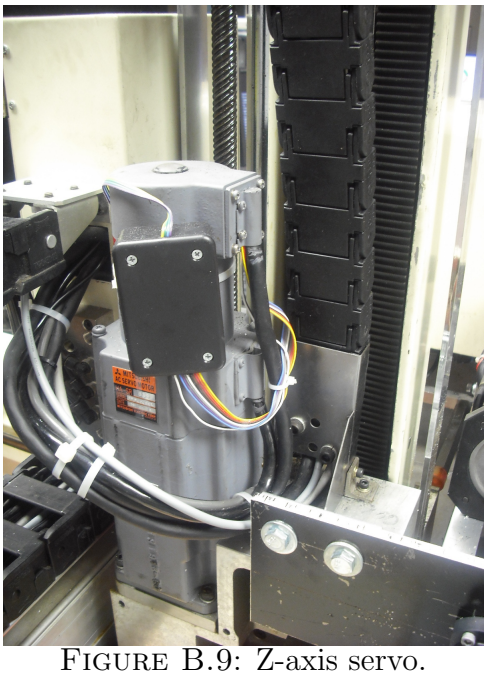

FIGURE B.9: Z-axis servo.

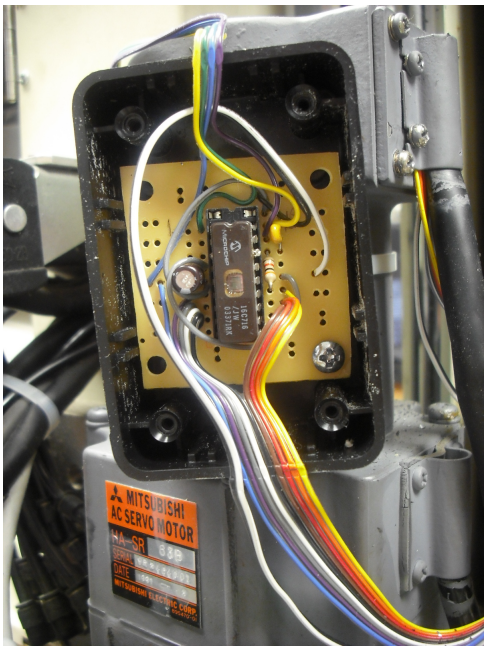

FIGURE B.10: Inside hall effect sensor simulator. Wires from the bottom are soldered to 8 bits of an internal bus on the absolute position encoders on each servo motor; wires to the top simulate hall-effect communtation sensors, and lead to the servo drives.

FIGURE B.11: Vacuum pump. $25.

FIGURE B.12: Vacuum manifold. $2

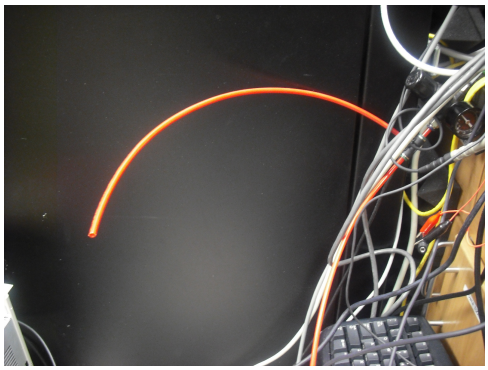

FIGURE B.13: In humid North Carolina air, small parts ($< 0.008g$) tend to stick to the tip of the vacuum cannula. To fix this, the line to the cannula was switched between full vacuum and slight positive pressure, the latter which is generated through a calibrated leak followed by a section of tube. The length of the section of tube determines the positive pressure.

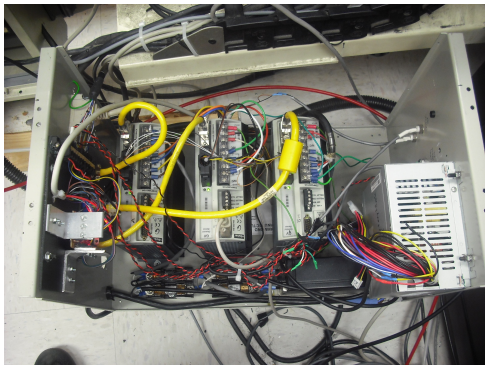

FIGURE B.14: Parker Automation servo controllers. Scrounged from other equipment in the lab.

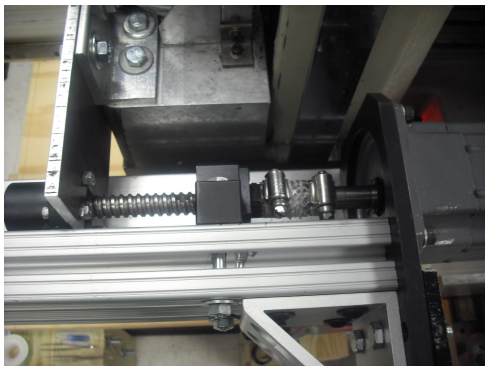

FIGURE B.15: Y axis on the original robot was actuated through a cogged polyethylene and kevlar belt, which proved to be both nonlinear and non-repeatable (pure anisotrphy of motion can be corrected for with the camera), and was replaced with a ballscrew purchased from ebay. Axial coupler was made with nylon-reinforced washing machine hose.

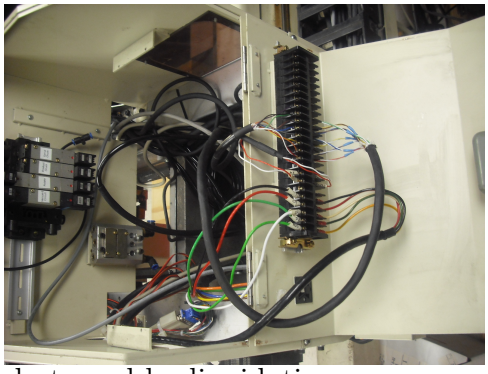

FIGURE B.16: Wires destroyed by liquidating crew were repaired or replaced.

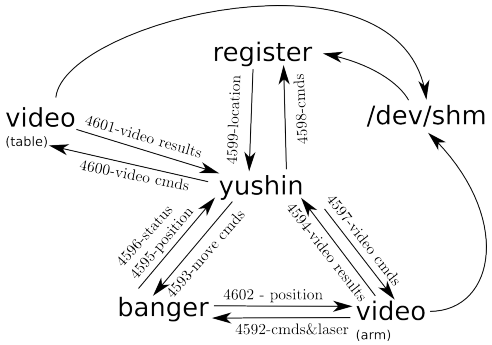

FIGURE B.17: Software control of robot. Yushin performs all high-level control and was written in Ocaml using functional reactive programming idioms; the unfortunately named banger was written in C and controls the servo drives ('banging' the bits out through paralell ports), register was written in CUDA and manages the computer vision tasks (part location), and the two running instances of video (written in C++) manage the table and arm mounted cameras. All programs communicated via TCP sockets, the port numbers of which are labeled on the arrows; video frames are shared using shared memory, /dev/shm.

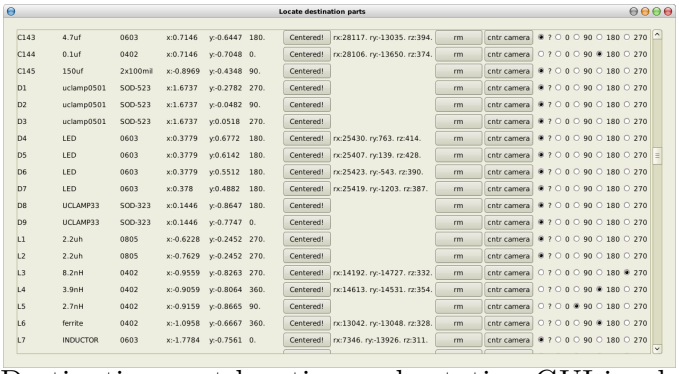

FIGURE B.18: Destination part location and rotation GUI in planning program.

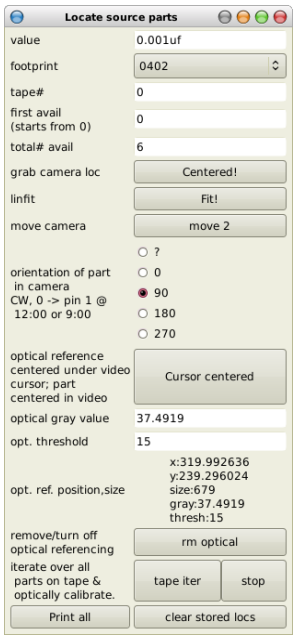

FIGURE B.19: Destination part location, rotation, and optical calibration GUI in Yushin.

Bibliography

Abosch, A., Hutchison, W. D., Saint-Cyr, J. A., Dostrovsky, J. O., and Lozano, A. M. (2002). Movement-related neurons of the subthalamic nucleus in patients with Parkinson disease. *J. Neurosurg.*, 97:1167–1172.

Aertsen, A. M., Gerstein, G. L., Habib, M. K., and Palm, G. (1989). . *J. Neurophysiol.*, 61:900–917.

Afraz, S. R., Kiani, R., and Esteky, H. (2006). Microstimulation of inferotemporal cortex influences face categorization. *Nature*, 442:692–695.

Akin, T., Najafi, K., and Bradley, R. (1995). An implantable multichannel digital neural recording system for a micromachined sieve electrode. In *Solid-State Sensors and Actuators, 1995 and Eurosensors Ix.. Transducers '95. The 8th International Conference on*, volume 1, pages 51 –54.

Akin, T., Najafi, K., and Bradley, R. (1998). A wireless implantable multichannel digital neural recording system for a micromachined sieve electrode. *Solid-State Circuits, Ieee Journal of*, 33(1):109 –118.

Alberts, W. W., Wright, E. W., Feinstein, B., and Gleason, C. A. (1972). Sensory responses elicited by subcortical high frequency electrical stimulation in man. *J. Neurosurg.*, 36:80–82.

Albin, R. L., Young, A. B., and Penney, J. B. (1989). The functional anatomy of basal ganglia disorders. *Trends Neurosci.*, 12:366–375.

Amirnovin, R., Williams, Z. M., Cosgrove, G. R., and Eskandar, E. N. (2004). Visually guided movements suppress subthalamic oscillations in Parkinson's disease patients. *J. Neurosci.*, 24:11302–11306.

Amtage, F., Henschel, K., Schelter, B., Vesper, J., Timmer, J., Lucking, C. H., and Hellwig, B. (2008). Tremor-correlated neuronal activity in the subthalamic nucleus of Parkinsonian patients. *Neurosci. Lett.*, 442:195–199.

Arfin, S. K., Long, M. A., Fee, M. S., and Sarpeshkar, R. (2009). Wireless neural stimulation in freely behaving small animals. *J. Neurophysiol.*, 102:598–605.

Ariano, M. A., Larson, E. R., Noblett, K. L., Sibley, D. R., and Levine, M. S. (1997). Coexpression of striatal dopamine receptor subtypes and excitatory amino acid subunits. *Synapse*, 26:400–414.

Ativanichayaphong, T., He, J. W., Hagains, C. E., Peng, Y. B., and Chiao, J. C. (2008). A combined wireless neural stimulating and recording system for study of pain processing. *J. Neurosci. Methods*, 170:25–34.

Awiszus, F. (1997). Spike train analysis. *J. Neurosci. Methods*, 74:155–166.

Bai, Q. and Wise, K. (2001). Single-unit neural recording with active microelectrode arrays. *Biomedical Engineering, Ieee Transactions on*, 48(8):911 –920.

Ballanger, B., Thobois, S., Baraduc, P., Turner, R. S., Broussolle, E., and Desmurget, M. (2006). is not a hallmark of Parkinson's disease but a general property of the motor system. *Mov. Disord.*, 21:1490–1495.

Bar-Gad, I., Morris, G., and Bergman, H. (2003). Information processing, dimensionality reduction and reinforcement learning in the basal ganglia. *Prog. Neurobiol.*, 71:439–473.

Barik, S. and de Beaurepaire, R. (1996). Evidence for a functional role of the dopamine D3 receptors in the cerebellum. *Brain Res.*, 737:347–350.

Bartels, J., Andreasen, D., Ehirim, P., Mao, H., Seibert, S., Wright, E. J., and Kennedy, P. (2008). Neurotrophic electrode: method of assembly and implantation into human motor speech cortex. *J. Neurosci. Methods*, 174:168–176.

Bartholow, R. (1874). Experimental investigations into the functions of the human brain. *The American Journal of the Medical Sciences*, 134:305–313.

Bartlett, J. R., DeYoe, E. A., Doty, R. W., Lee, B. B., Lewine, J. D., Negrao, N., and Overman, W. H. (2005). Psychophysics of electrical stimulation of striate cortex in macaques. *J. Neurophysiol.*, 94:3430–3442.

Barto, A. G. and Sutton, R. S. (1998). *Reinforcement Learning: An Introduction (Adaptive Computation and Machine Learning)*. A Bradford Book.

Basmajian, J. V. (1963). Control and training of individual motor units. *Science*, 141:440–441.

Batschelet, E. (1981). *Circular statistics in biology*. London ; New York: Academic Press.

Baunez, C., Amalric, M., and Robbins, T. W. (2002). Enhanced food-related motivation after bilateral lesions of the subthalamic nucleus. *J. Neurosci.*, 22:562–568.

Baunez, C. and Robbins, T. W. (1997). Bilateral lesions of the subthalamic nucleus induce multiple deficits in an attentional task in rats. *Eur. J. Neurosci.*, 9:2086–2099.

BeMent, S. L., Wise, K. D., Anderson, D. J., Najafi, K., and Drake, K. L. (1986). Solid-state electrodes for multichannel multiplexed intracortical neuronal recording. *Ieee Trans Biomed Eng*, 33:230–241.

Benabid, A. L., Chabardes, S., Mitrofanis, J., and Pollak, P. (2009). Deep brain stimulation of the subthalamic nucleus for the treatment of Parkinson's disease. *Lancet Neurol*, 8:67–81.

Benabid, A. L., Chabardes, S., and Seigneuret, E. (2005). Deep-brain stimulation in Parkinson's disease: long-term efficacy and safety - What happened this year? *Curr. Opin. Neurol.*, 18:623–630.

Benabid, A. L., Costecalde, T., Torres, N., Moro, C., Aksenova, T., Eliseyev, A., Charvet, G., Sauter, F., Ratel, D., Mestais, C., Pollak, P., and Chabardes, S. (2011). Deep brain stimulation: BCI at large, where are we going to? *Prog. Brain Res.*, 194:71–82.

Benabid, A. L., Pollak, P., Gervason, C., Hoffmann, D., Gao, D. M., Hommel, M., Perret, J. E., and de Rougemont, J. (1991). Long-term suppression of tremor by chronic stimulation of the ventral intermediate thalamic nucleus. *Lancet*, 337:403–406.

Benazzouz, A., Breit, S., Koudsie, A., Pollak, P., Krack, P., and Benabid, A. L. (2002). Intraoperative microrecordings of the subthalamic nucleus in Parkinson's disease. *Mov. Disord.*, 17 Suppl 3:S145–149.

Berardelli, A., Sabra, A. F., and Hallett, M. (1983). Physiological mechanisms of rigidity in Parkinson's disease. *J. Neurol. Neurosurg. Psychiatr.*, 46:45–53.

Bergman, H., Wichmann, T., and DeLong, M. R. (1990). Reversal of experimental parkinsonism by lesions of the subthalamic nucleus. *Science*, 249:1436–1438.

Bergman, H., Wichmann, T., Karmon, B., and DeLong, M. R. (1994). The primate subthalamic nucleus. II. Neuronal activity in the MPTP model of parkinsonism. *J. Neurophysiol.*, 72:507–520.

Bernatchez, S. F., Parks, P. J., and Gibbons, D. F. (1996). Interaction of macrophages with fibrous materials in vitro. *Biomaterials*, 17:2077–2086.

Bevan, M. D., Magill, P. J., Terman, D., Bolam, J. P., and Wilson, C. J. (2002). Move to the rhythm: oscillations in the subthalamic nucleus-external globus pallidus network. *Trends Neurosci.*, 25:525–531.

Birbaumer, N. and Cohen, L. G. (2007). Brain-computer interfaces: communication and restoration of movement in paralysis. *J. Physiol. (Lond.)*, 579:621–636.

Blankertz, B., Dornhege, G., Schafer, C., Krepki, R., Kohlmorgen, J., Muller, K. R., Kunzmann, V., Losch, F., and Curio, G. (2003). Boosting bit rates and error detection for the classification of fast-paced motor commands based on single-trial EEG analysis. *Ieee Trans Neural Syst Rehabil Eng*, 11:127–131.

Bossetti, C., Carmena, J., Nicolelis, M., and Wolf, P. (2004). Transmission latencies in a telemetry-linked brain-machine interface. *Biomedical Engineering, Ieee Transactions on*, 51(6):919 –924.

Boulet, S., Lacombe, E., Carcenac, C., Feuerstein, C., Sgambato-Faure, V., Poupard, A., and Savasta, M. (2006). Subthalamic stimulation-induced forelimb dyskinesias are linked to an increase in glutamate levels in the substantia nigra pars reticulata. *J. Neurosci.*, 26:10768–10776.

Boyden, E. S., Zhang, F., Bamberg, E., Nagel, G., and Deisseroth, K. (2005). Millisecond-timescale, genetically targeted optical control of neural activity. *Nat. Neurosci.*, 8:1263–1268.

Braak, H., Del Tredici, K., Rub, U., de Vos, R. A., Jansen Steur, E. N., and Braak, E. (2003). Staging of brain pathology related to sporadic Parkinson's disease. *Neurobiol. Aging*, 24:197–211.

Breit, S., Lessmann, L., Unterbrink, D., Popa, R. C., Gasser, T., and Schulz, J. B. (2006). Lesion of the pedunculopontine nucleus reverses hyperactivity of the subthalamic nucleus and substantia nigra pars reticulata in a 6-hydroxydopamine rat model. *Eur. J. Neurosci.*, 24:2275–2282.

Brindley, G. S. and Lewin, W. S. (1968). The sensations produced by electrical stimulation of the visual cortex. *J. Physiol. (Lond.)*, 196:479–493.

Britten, K. H. and van Wezel, R. J. (1998). Electrical microstimulation of cortical area MST biases heading perception in monkeys. *Nat. Neurosci.*, 1:59–63.

Brockwell, A. E., Rojas, A. L., and Kass, R. E. (2004). Recursive bayesian decoding of motor cortical signals by particle filtering. *J. Neurophysiol.*, 91:1899–1907.

Brodkey, J. A., Tasker, R. R., Hamani, C., McAndrews, M. P., Dostrovsky, J. O., and Lozano, A. M. (2004). Tremor cells in the human thalamus: differences among neurological disorders. *J. Neurosurg.*, 101:43–47.

Bronstein, J. M., Tagliati, M., Alterman, R. L., Lozano, A. M., Volkmann, J., Stefani, A., Horak, F. B., Okun, M. S., Foote, K. D., Krack, P., Pahwa, R., Henderson, J. M., Hariz, M. I., Bakay, R. A., Rezai, A., Marks, W. J., Moro, E., Vitek, J. L.,

Weaver, F. M., Gross, R. E., and DeLong, M. R. (2011). Deep brain stimulation for Parkinson disease: an expert consensus and review of key issues. *Arch. Neurol.*, 68:165.

Brown, P. (2000). Cortical drives to human muscle: the Piper and related rhythms. *Prog. Neurobiol.*, 60:97–108.

Brown, P. (2003). Oscillatory nature of human basal ganglia activity: relationship to the pathophysiology of Parkinson's disease. *Mov. Disord.*, 18:357–363.

Brown, P., Salenius, S., Rothwell, J. C., and Hari, R. (1998). Cortical correlate of the Piper rhythm in humans. *J. Neurophysiol.*, 80:2911–2917.

Brown, R. G., Jahanshahi, M., Limousin-Dowsey, P., Thomas, D., Quinn, N. P., and Rothwell, J. C. (2003). Pallidotomy and incidental sequence learning in Parkinson's disease. *Neuroreport*, 14:21–24.

Bures, J. and Buresova, O. (1967). Plastic changes of unit activity based on reinforcing properties of extracellular stimulation of single neurons. *J. Neurophysiol.*, 30:98–1.

Butovas, S. and Schwarz, C. (2007). Detection psychophysics of intracortical microstimulation in rat primary somatosensory cortex. *Eur. J. Neurosci.*, 25:2161–2169.

Byron, O. and Jennie, S. (2010). Evidence of a mechanism of neural adaptation in the closed loop control of directions. *International Journal of Intelligent Computing and Cybernetics*, 3:5–23.

Calabresi, P., Centonze, D., and Bernardi, G. (2000). Electrophysiology of dopamine in normal and denervated striatal neurons. *Trends Neurosci.*, 23:57–63.

Caparros-Lefebvre, D., Blond, S., Feltin, M. P., Pollak, P., and Benabid, A. L. (1999). Improvement of levodopa induced dyskinesias by thalamic deep brain stimulation is related to slight variation in electrode placement: possible involvement of the centre median and parafascicularis complex. *J. Neurol. Neurosurg. Psychiatr.*, 67:308–314.

Carlson, J. D., Cleary, D. R., Cetas, J. S., Heinricher, M. M., and Burchiel, K. J. (2010). Deep brain stimulation does not silence neurons in subthalamic nucleus in Parkinson's patients. *J. Neurophysiol.*, 103:962–967.

Carmena, J. M., Lebedev, M. A., Crist, R. E., O'Doherty, J. E., Santucci, D. M., Dimitrov, D. F., Patil, P. G., Henriquez, C. S., and Nicolelis, M. A. (2003). Learning to control a brain-machine interface for reaching and grasping by primates. *PloS Biol.*, 1:E42.

Carmena, J. M., Lebedev, M. A., Henriquez, C. S., and Nicolelis, M. A. (2005). Stable ensemble performance with single-neuron variability during reaching movements in primates. *J. Neurosci.*, 25:10712–10716.

Carpenter, M. B., Carleton, S. C., Keller, J. T., and Conte, P. (1981). Connections of the subthalamic nucleus in the monkey. *Brain Res.*, 224:1–29.

Cassidy, M., Mazzone, P., Oliviero, A., Insola, A., Tonali, P., Di Lazzaro, V., and Brown, P. (2002). Movement-related changes in synchronization in the human basal ganglia. *Brain*, 125:1235–1246.

Cassim, F., Labyt, E., Devos, D., Defebvre, L., Destee, A., and Derambure, P. (2002). Relationship between oscillations in the basal ganglia and synchronization of cortical activity. *Epileptic Disord*, 4 Suppl 3:31–45.

Centonze, D., Picconi, B., Gubellini, P., Bernardi, G., and Calabresi, P. (2001). Dopaminergic control of synaptic plasticity in the dorsal striatum. *Eur. J. Neurosci.*, 13:1071–1077.

Chae, M. S., Yang, Z., Yuce, M. R., Hoang, L., and Liu, W. (2009). A 128-channel 6 mW wireless neural recording IC with spike feature extraction and UWB transmitter. *Ieee Trans Neural Syst Rehabil Eng*, 17:312–321.

Chapin, J. and Moxon, K. (2000). *Neural Prostheses for Restoration of Sensory and Motor Function (Frontiers in Neuroscience)*. CRC Press.

Chapin, J. K., Moxon, K. A., Markowitz, R. S., and Nicolelis, M. A. (1999). Real-time control of a robot arm using simultaneously recorded neurons in the motor cortex. *Nat. Neurosci.*, 2:664–670.

Chestek, C. A., Batista, A. P., Santhanam, G., Yu, B. M., Afshar, A., Cunningham, J. P., Gilja, V., Ryu, S. I., Churchland, M. M., and Shenoy, K. V. (2007). Single-neuron stability during repeated reaching in macaque premotor cortex. *J. Neurosci.*, 27:10742–10750.

Chorover, S. L. and DeLuca, A. M. (1972). A sweet new multiple electrode for chronic single unit recording in moving animals. *Physiol. Behav.*, 9:671–674.

Collias, J. C. and Manuelidis, E. E. (1957). Histopathological changes produced by implanted electrodes in cat brains; comparison with histopathological changes in human and experimental puncture wounds. *J. Neurosurg.*, 14:302–328.

Cosman, E. R. and Cosman, E. R. (2005). Electric and thermal field effects in tissue around radiofrequency electrodes. *Pain Med*, 6:405–424.

Costa, R. M., Lin, S. C., Sotnikova, T. D., Cyr, M., Gainetdinov, R. R., Caron, M. G., and Nicolelis, M. A. (2006). Rapid alterations in corticostriatal ensemble coordination during acute dopamine-dependent motor dysfunction. *Neuron*, 52:359–369.

Crutcher, M. D. and DeLong, M. R. (1984a). Single cell studies of the primate putamen. I. Functional organization. *Exp Brain Res*, 53:233–243.

Crutcher, M. D. and DeLong, M. R. (1984b). Single cell studies of the primate putamen. II. Relations to direction of movement and pattern of muscular activity. *Exp Brain Res*, 53:244–258.

Csicsvari, J., Henze, D. A., Jamieson, B., Harris, K. D., Sirota, A., Bartho, P., Wise, K. D., and Buzsaki, G. (2003). Massively parallel recording of unit and local field potentials with silicon-based electrodes. *J. Neurophysiol.*, 90:1314–1323.

Dabrowski, W., Grybos, P., Hottowy, P., Skoczen, A., Swientek, K., Bezayiff, N., Grillo, A., Kachiguine, S., Litke, A., and Sher, A. (2003). Development of integrated circuits for readout of microelectrode arrays to image neuronal activity in live retinal tissue. In *Nuclear Science Symposium Conference Record, 2003 Ieee*, volume 2, pages 956 – 960 Vol.2.

Dagtekin, M., Liu, W., and Bashirullah, R. (2001). A multi channel chopper modulated neural recording system. In *Engineering in Medicine and Biology Society, 2001. Proceedings of the 23rd Annual International Conference of the Ieee*, volume 1, pages 757 – 760 vol.1.

Darmanjian, S., Cieslewski, G., Morrison, S., Dang, B., Gugel, K., and Principe, J. (2006). A reconfigurable neural signal processor (NSP) for brain machine interfaces. *Conf Proc Ieee Eng Med Biol Soc*, 1:2502–2505.

Darmanjian, S., Morrison, S., Dang, B., Gugel, K., and Principe, J. (2005). A portable wireless dsp system for a brain machine interface. In *Neural Engineering, 2005. Conference Proceedings. 2nd International Ieee Embs Conference on*, pages 112 –115.

Davidsen, J. and Schuster, H. G. (2002). Simple model for 1/f(alpha) noise. *Phys Rev E Stat Nonlin Soft Matter Phys*, 65:026120.

Deco, G., Rolls, E. T., and Romo, R. (2009). Stochastic dynamics as a principle of brain function. *Prog. Neurobiol.*, 88:1–16.

DeGiorgio, C. M., Shewmon, A., Murray, D., and Whitehurst, T. (2006). Pilot study of trigeminal nerve stimulation (TNS) for epilepsy: a proof-of-concept trial. *Epilepsia*, 47:1213–1215.

Delgado, J. (1971). *Physical control of the mind : toward a psychocivilized society*. Harper & Row, New York.

Delgado, J. M., Mark, V., Sweet, W., Ervin, F., Weiss, G., Bach-Y-Rita, G., and Hagiwara, R. (1968). Intracerebral radio stimulation and recording in completely free patients. *J. Nerv. Ment. Dis.*, 147:329–340.

Delgado, J. M. R. (1964). Personality, education, and electrical stimulation of the brain. *Innovation and Experiment in Modern Education: A report of the Tenty-Ninth Educational Conference*.

DeLong, M. R., Crutcher, M. D., and Georgopoulos, A. P. (1985). Primate globus pallidus and subthalamic nucleus: functional organization. *J. Neurophysiol.*, 53:530–543.

Delong, M. R., Georgopoulos, A. P., Crutcher, M. D., Mitchell, S. J., Richardson, R. T., and Alexander, G. E. (1984). Functional organization of the basal ganglia: contributions of single-cell recording studies. *Ciba Found. Symp.*, 107:64–82.

Denk, W., Strickler, J. H., and Webb, W. W. (1990). Two-photon laser scanning fluorescence microscopy. *Science*, 248:73–76.

Desmurget, M. and Turner, R. S. (2010). Motor sequences and the basal ganglia: kinematics, not habits. *J. Neurosci.*, 30:7685–7690.

Dethier, J., Gilja, V., Nuyujukian, P., Elassaad, S., Shenoy, K., and Boahen, K. (2011). Spiking neural network decoder for brain-machine interfaces. In *Neural Engineering (Ner), 2011 5th International Ieee/Embs Conference on*, pages 396 –399.

Deuschl, G., Bain, P., and Brin, M. (1998). Consensus statement of the Movement Disorder Society on Tremor. Ad Hoc Scientific Committee. *Mov. Disord.*, 13 Suppl 3:2–23.

Deuschl, G. and Elble, R. J. (2000). The pathophysiology of essential tremor. *Neurology*, 54:14–20.

Deuschl, G., Schade-Brittinger, C., Krack, P., Volkmann, J., Schafer, H., Botzel, K., Daniels, C., Deutschlander, A., Dillmann, U., Eisner, W., Gruber, D., Hamel, W., Herzog, J., Hilker, R., Klebe, S., Kloss, M., Koy, J., Krause, M., Kupsch, A., Lorenz, D., Lorenzl, S., Mehdorn, H. M., Moringlane, J. R., Oertel, W., Pinsker, M. O., Reichmann, H., Reuss, A., Schneider, G. H., Schnitzler, A., Steude, U., Sturm, V., Timmermann, L., Tronnier, V., Trottenberg, T., Wojtecki, L., Wolf, E., Poewe, W., and Voges, J. (2006). A randomized trial of deep-brain stimulation for Parkinson's disease. *N. Engl. J. Med.*, 355:896–908.

Dobelle, W. H., Mladejovsky, M. G., and Girvin, J. P. (1974). Artifical vision for the blind: electrical stimulation of visual cortex offers hope for a functional prosthesis. *Science*, 183:440–444.

Dorman, M., Prisbe, M., and Meindl, J. (1985). A monolithic signal processor for a neurophysiological telemetry system. *Solid-State Circuits, Ieee Journal of*, 20(6):1185 –1193.

Doty, R. W. (1965). CONDITIONED REFLEXES ELICITED BY ELECTRICAL STIMULATION OF THE BRAIN IN MACAQUES. *J. Neurophysiol.*, 28:623–640.

Doty, R. W. (1969). Electrical stimulation of the brain in behavioral context. *Annu Rev Psychol*, 20:289–320.

Doty, R. W., Larsen, R. M., and Ruthledge, L. T. (1956). Conditioned reflexes established to electrical stimulation of cat cerebral cortex. *J. Neurophysiol.*, 19:401–415.

Drutarovsky, M. (2005). An implementation of high performance iir filtration on 2-mac blackfin dsp architecture. *DSP-MCOM 2005, Kosice, Slovak republic*.

Elble, R. J. (1996). Central mechanisms of tremor. *J Clin Neurophysiol*, 13:133–144.

Eslamboli, A., Georgievska, B., Ridley, R. M., Baker, H. F., Muzyczka, N., Burger, C., Mandel, R. J., Annett, L., and Kirik, D. (2005). Continuous low-level glial cell line-derived neurotrophic factor delivery using recombinant adeno-associated viral vectors provides neuroprotection and induces behavioral recovery in a primate model of Parkinson's disease. *J. Neurosci.*, 25:769–777.

Eusebio, A. and Brown, P. (2009). Synchronisation in the beta frequency-band–the bad boy of parkinsonism or an innocent bystander? *Exp. Neurol.*, 217:1–3.

Evarts, E. V. (1968). Relation of pyramidal tract activity to force exerted during voluntary movement. *J. Neurophysiol.*, 31:14–27.

Fagg, A. H., Hatsopoulos, N. G., de Lafuente, V., Moxon, K. A., Nemati, S., Rebesco, J. M., Romo, R., Solla, S. A., Reimer, J., Tkach, D., Pohlmeyer, E. A., and Miller, L. E. (2007). Biomimetic brain machine interfaces for the control of movement. *J. Neurosci.*, 27:11842–11846.

Fan, D., Rich, D., Holtzman, T., Ruther, P., Dalley, J. W., Lopez, A., Rossi, M. A., Barter, J. W., Salas-Meza, D., Herwik, S., Holzhammer, T., Morizio, J., and Yin, H. H. (2011). A wireless multi-channel recording system for freely behaving mice and rats. *PloS One*, 6:e22033.

Fanselow, E. E., Reid, A. P., and Nicolelis, M. A. (2000). Reduction of pentylenetetrazole-induced seizure activity in awake rats by seizure-triggered trigeminal nerve stimulation. *J. Neurosci.*, 20:8160–8168.

Farshchi, S., Nuyujukian, P., Pesterev, A., Mody, I., and Judy, J. (2006). A tinyos-enabled mica2-basedwireless neural interface. *Biomedical Engineering, Ieee Transactions on*, 53(7):1416 –1424.

Feingold, J., Desrochers, T. M., Fujii, N., Harlan, R., Tierney, P. L., Shimazu, H., Amemori, K. I., and Graybiel, A. M. (2011). A system for recording neural activity chronically and simultaneously from multiple cortical and subcortical regions in non-human primates. *J Neurophysiol*.

Fellows, S. J., Kronenburger, M., Allert, N., Coenen, V. A., Fromm, C., Noth, J., and Weiss, P. H. (2006). The effect of subthalamic nucleus deep brain stimulation on precision grip abnormalities in Parkinson's disease. *Parkinsonism Relat. Disord.*, 12:149–154.

Fetz, E. E. (1969). Operant conditioning of cortical unit activity. *Science*, 163:955–958.

Fetz, E. E. (2007). Volitional control of neural activity: implications for brain-computer interfaces. *J. Physiol. (Lond.)*, 579:571–579.

Fetz, E. E. and Baker, M. A. (1973). Operantly conditioned patterns on precentral unit activity and correlated responses in adjacent cells and contralateral muscles. *J. Neurophysiol.*, 36:179–204.

Fetz, E. E. and Finocchio, D. V. (1971). Operant conditioning of specific patterns of neural and muscular activity. *Science*, 174:431–435.

Fetz, E. E. and Finocchio, D. V. (1972). Operant conditioning of isolated activity in specific muscles and precentral cells. *Brain Res.*, 40:19–23.

Fitzsimmons, N. A., Drake, W., Hanson, T. L., Lebedev, M. A., and Nicolelis, M. A. (2007). Primate reaching cued by multichannel spatiotemporal cortical microstimulation. *J. Neurosci.*, 27:5593–5602.

Flaherty, A. W. and Graybiel, A. M. (1994). Input-output organization of the sensorimotor striatum in the squirrel monkey. *J. Neurosci.*, 14:599–610.

Florio, T., Capozzo, A., Cellini, R., Pizzuti, G., Staderini, E. M., and Scarnati, E. (2001). Unilateral lesions of the pedunculopontine nucleus do not alleviate subthalamic nucleus-mediated anticipatory responding in a delayed sensorimotor task in the rat. *Behav. Brain Res.*, 126:93–103.

Frank, M. J., Samanta, J., Moustafa, A. A., and Sherman, S. J. (2007). Hold your horses: impulsivity, deep brain stimulation, and medication in parkinsonism. *Science*, 318:1309–1312.

Friston, K. (2002). Functional integration and inference in the brain. *Prog. Neurobiol.*, 68:113–143.

Fritsch, G. and Hitzig, E. (2009). Electric excitability of the cerebrum (Uber die elektrische Erregbarkeit des Grosshirns). *Epilepsy Behav*, 15:123–130.

Fuentes, R., Petersson, P., Siesser, W. B., Caron, M. G., and Nicolelis, M. A. (2009). Spinal cord stimulation restores locomotion in animal models of Parkinson's disease. *Science*, 323:1578–1582.

Gage, G. J., Ludwig, K. A., Otto, K. J., Ionides, E. L., and Kipke, D. R. (2005). Naive coadaptive cortical control. *J Neural Eng*, 2:52–63.

Ganguly, K. and Carmena, J. M. (2009). Emergence of a stable cortical map for neuroprosthetic control. *PloS Biol.*, 7:e1000153.

Ganguly, K., Dimitrov, D. F., Wallis, J. D., and Carmena, J. M. (2011). Reversible large-scale modification of cortical networks during neuroprosthetic control. *Nat. Neurosci.*, 14:662–667.

George, M. S., Nahas, Z., Bohning, D. E., Lomarev, M., Denslow, S., Osenbach, R., and Ballenger, J. C. (2000). Vagus nerve stimulation: a new form of therapeutic brain stimulation. *Cns Spectr*, 5:43–52.

Georgopoulos, A. P., DeLong, M. R., and Crutcher, M. D. (1983). Relations between parameters of step-tracking movements and single cell discharge in the globus pallidus and subthalamic nucleus of the behaving monkey. *J. Neurosci.*, 3:1586–1598.

Gesteland, R., Howland, B., Lettvin, J., and Pitts, W. (1959). Comments on microelectrodes. *Proceedings of the Ire*, 47(11):1856 –1862.

Ghovanloo, M. and Najafi, K. (2007). A wireless implantable multichannel microstimulating system-on-a-chip with modular architecture. *Neural Systems and Rehabilitation Engineering, IEEE Transactions on*, 15(3):449 –457.

Goldstein, S. R. and Salcman, M. (1973). Mechanical factors in the design of chronic recording intracortical microelectrodes. *Biomedical Engineering, Ieee Transactions on*, Bme-20(4):260 –269.

Gradinaru, V., Mogri, M., Thompson, K. R., Henderson, J. M., and Deisseroth, K. (2009). Optical deconstruction of parkinsonian neural circuitry. *Science*, 324:354–359.

Graybiel, A. M. (2005). The basal ganglia: learning new tricks and loving it. *Curr. Opin. Neurobiol.*, 15:638–644.

Grill, W. and Mortimer, J. (1995). Stimulus waveforms for selective neural stimulation. *Engineering in Medicine and Biology Magazine, IEEE*, 14(4):375 –385.

Grutzendler, J., Kasthuri, N., and Gan, W. B. (2002). Long-term dendritic spine stability in the adult cortex. *Nature*, 420:812–816.

Grutzendler, J., Yang, G., Pan, F., Parkhurst, C. N., and Gan, W. B. (2011). Transcranial two-photon imaging of the living mouse brain. *Cold Spring Harb Protoc*, 2011.

Gubellini, P., Salin, P., Kerkerian-Le Goff, L., and Baunez, C. (2009). Deep brain stimulation in neurological diseases and experimental models: from molecule to complex behavior. *Prog. Neurobiol.*, 89:79–123.

Guenther, F. H., Brumberg, J. S., Wright, E. J., Nieto-Castanon, A., Tourville, J. A., Panko, M., Law, R., Siebert, S. A., Bartels, J. L., Andreasen, D. S., Ehirim, P., Mao, H., and Kennedy, P. R. (2009). A wireless brain-machine interface for real-time speech synthesis. *PloS One*, 4:e8218.

Guillery, R. W. and Sherman, S. M. (2002). The thalamus as a monitor of motor outputs. *Philos. Trans. R. Soc. Lond., B, Biol. Sci.*, 357:1809–1821.

Guld, C. (1964). A GLASS-COVERED PLATINUM MICROELECTRODE. *Med Electron Biol Eng*, 2:317–327.

Guridi, J. and Obeso, J. A. (2001). The subthalamic nucleus, hemiballismus and Parkinson's disease: reappraisal of a neurosurgical dogma. *Brain*, 124:5–19.

Hagbarth, K. E., Jessop, J., Eklund, G., and Wallin, E. U. (1983). The Piper rhythm–a phenomenon related to muscle resonance characteristics? *Acta Physiol. Scand.*, 117:263–271.

Hamani, C., Saint-Cyr, J. A., Fraser, J., Kaplitt, M., and Lozano, A. M. (2004). The subthalamic nucleus in the context of movement disorders. *Brain*, 127:4–20.

Hamann, W., Abou-Sherif, S., Thompson, S., and Hall, S. (2006). Pulsed radiofrequency applied to dorsal root ganglia causes a selective increase in ATF3 in small neurons. *Eur J Pain*, 10:171–176.

Hanks, T. D., Ditterich, J., and Shadlen, M. N. (2006). Microstimulation of macaque area LIP affects decision-making in a motion discrimination task. *Nat. Neurosci.*, 9:682–689.

Hanson, T., Fitzsimmons, N., and J.E., O. (2008). Technology for multielectrode microstimulation of brain tissue. *In Nicolelis MAL (Ed.) Methods for neural ensemble recordings*, 2nd ed:47–55.

Hari, R. and Salenius, S. (1999). Rhythmical corticomotor communication. *Neuroreport*, 10:1–10.

Harris, J. P., Hess, A. E., Rowan, S. J., Weder, C., Zorman, C. A., Tyler, D. J., and Capadona, J. R. (2011). In vivo deployment of mechanically adaptive nanocomposites for intracortical microelectrodes. *J Neural Eng*, 8:046010.

Harris, L. J., Almerigi, J. B., and Bartholow, R. (2009). Probing the human brain with stimulating electrodes: the story of Roberts Bartholow's (1874) experiment on Mary Rafferty. *Brain Cogn*, 70:92–115.

Harrison, R. and Charles, C. (2003). A low-power low-noise cmos amplifier for neural recording applications. *Solid-State Circuits, Ieee Journal of*, 38(6):958 – 965.

Harrison, R., Kier, R., Chestek, C., Gilja, V., Nuyujukian, P., Ryu, S., Greger, B., Solzbacher, F., and Shenoy, K. (2009). Wireless neural recording with single low-power integrated circuit. *Neural Systems and Rehabilitation Engineering, Ieee Transactions on*, 17(4):322 –329.

Hashimoto, T., Elder, C. M., Okun, M. S., Patrick, S. K., and Vitek, J. L. (2003). Stimulation of the subthalamic nucleus changes the firing pattern of pallidal neurons. *J. Neurosci.*, 23:1916–1923.

Hassell, T., Jedlicka, S., Rickus, J., and Irazoqui, P. (2007). Constant-current adjustable-waveform microstimulator for an implantable hybrid neural prosthesis. In *Engineering in Medicine and Biology Society, 2007. EMBS 2007. 29th Annual International Conference of the IEEE*, pages 2436 –2439.

Hatsopoulos, N., Mukand, J., Polykoff, G., Friehs, G., and Donoghue, J. (2005). Cortically controlled brain-machine interface. *Conf Proc Ieee Eng Med Biol Soc*, 7:7660–7663.

Heimer, G., Rivlin, M., Israel, Z., and Bergman, H. (2006). Synchronizing activity of basal ganglia and pathophysiology of Parkinson's disease. *J. Neural Transm. Suppl.*, pages 17–20.

Helms Tillery, S. I., Taylor, D. M., and Schwartz, A. B. (2003). Training in cortical control of neuroprosthetic devices improves signal extraction from small neuronal ensembles. *Rev Neurosci*, 14:107–119.

Herzog, C. D., Dass, B., Holden, J. E., Stansell, J., Gasmi, M., Tuszynski, M. H., Bartus, R. T., and Kordower, J. H. (2007). Striatal delivery of CERE-120, an

AAV2 vector encoding human neurturin, enhances activity of the dopaminergic nigrostriatal system in aged monkeys. *Mov. Disord.*, 22:1124–1132.

Hikosaka, O. and Wurtz, R. H. (1983a). Visual and oculomotor functions of monkey substantia nigra pars reticulata. I. Relation of visual and auditory responses to saccades. *J. Neurophysiol.*, 49:1230–1253.

Hikosaka, O. and Wurtz, R. H. (1983b). Visual and oculomotor functions of monkey substantia nigra pars reticulata. II. Visual responses related to fixation of gaze. *J. Neurophysiol.*, 49:1254–1267.

Hikosaka, O. and Wurtz, R. H. (1983c). Visual and oculomotor functions of monkey substantia nigra pars reticulata. III. Memory-contingent visual and saccade responses. *J. Neurophysiol.*, 49:1268–1284.

Hilty, L., Jancke, L., Luechinger, R., Boutellier, U., and Lutz, K. (2011). Limitation of physical performance in a muscle fatiguing handgrip exercise is mediated by thalamo-insular activity. *Hum Brain Mapp*, 32:2151–2160.

Hochberg, L. R., Serruya, M. D., Friehs, G. M., Mukand, J. A., Saleh, M., Caplan, A. H., Branner, A., Chen, D., Penn, R. D., and Donoghue, J. P. (2006). Neuronal ensemble control of prosthetic devices by a human with tetraplegia. *Nature*, 442:164–171.

Hofstadter, D. R. (2007). *I Am a Strange Loop*. Basic Books.

Holgado, A. J., Terry, J. R., and Bogacz, R. (2010). Conditions for the generation of beta oscillations in the subthalamic nucleus-globus pallidus network. *J. Neurosci.*, 30:12340–12352.

Holleman, J. and Otis, B. (2007). A sub-microwatt low-noise amplifier for neural recording. In *Engineering in Medicine and Biology Society, 2007. Embs 2007. 29th Annual International Conference of the Ieee*, pages 3930 –3933.

Hollerman, J. R., Tremblay, L., and Schultz, W. (2000). Involvement of basal ganglia and orbitofrontal cortex in goal-directed behavior. *Prog. Brain Res.*, 126:193–215.

Hoogerwerf, A. and Wise, K. (1994). A three-dimensional microelectrode array for chronic neural recording. *Biomedical Engineering, Ieee Transactions on*, 41(12):1136 –1146.

Hua, S. E. and Lenz, F. A. (2005). Posture-related oscillations in human cerebellar thalamus in essential tremor are enabled by voluntary motor circuits. *J. Neurophysiol.*, 93:117–127.

Hubel, D. H. (1957). Tungsten Microelectrode for Recording from Single Units. *Science*, 125:549–550.

Hubel, D. H. and Wiesel, T. N. (1963). Shape and arrangement of columns in cat's striate cortex. *J. Physiol. (Lond.)*, 165:559–568.

Huber, D., Petreanu, L., Ghitani, N., Ranade, S., Hromadka, T., Mainen, Z., and Svoboda, K. (2008). Sparse optical microstimulation in barrel cortex drives learned behaviour in freely moving mice. *Nature*, 451:61–64.

Humphrey, D. R., Schmidt, E. M., and Thompson, W. D. (1970). Predicting measures of motor performance from multiple cortical spike trains. *Science*, 170:758–762.

Hurtado, J. M., Gray, C. M., Tamas, L. B., and Sigvardt, K. A. (1999). Dynamics of tremor-related oscillations in the human globus pallidus: a single case study. *Proc. Natl. Acad. Sci. U.S.A.*, 96:1674–1679.

Hyam, J. A., Owen, S. L., Kringelbach, M. L., Phd, N. J., Stein, J. F., Green, A. L., and Aziz, T. Z. (2011). Contrasting Connectivity of the Vim and Vop Nuclei of the Motor Thalamus Demonstrated by Probabilistic Tractography. *Neurosurgery*.

Iansek, R. and Porter, R. (1980). The monkey globus pallidus: neuronal discharge properties in relation to movement. *J. Physiol. (Lond.)*, 301:439–455.

Isoda, M. and Hikosaka, O. (2007). Switching from automatic to controlled action by monkey medial frontal cortex. *Nat. Neurosci.*, 10:240–248.

Isoda, M. and Hikosaka, O. (2008). Role for subthalamic nucleus neurons in switching from automatic to controlled eye movement. *J. Neurosci.*, 28:7209–7218.

Israel, Z. and Bergman, H. (2008). Pathophysiology of the basal ganglia and movement disorders: from animal models to human clinical applications. *Neurosci Biobehav Rev*, 32:367–377.

Jackson, A., Mavoori, J., and Fetz, E. E. (2007). Correlations between the same motor cortex cells and arm muscles during a trained task, free behavior, and natural sleep in the macaque monkey. *J. Neurophysiol.*, 97:360–374.

Jaroch, D. B., Ward, M. P., Chow, E. Y., Rickus, J. L., and Irazoqui, P. P. (2009). Magnetic insertion system for flexible electrode implantation. *J. Neurosci. Methods*, 183:213–222.

Jarosiewicz, B., Chase, S. M., Fraser, G. W., Velliste, M., Kass, R. E., and Schwartz, A. B. (2008). Functional network reorganization during learning in a brain-computer interface paradigm. *Proc. Natl. Acad. Sci. U.S.A.*, 105:19486–19491.

Ji, J. and Wise, K. (1992). An implantable cmos circuit interface for multiplexed microelectrode recording arrays. *Solid-State Circuits, Ieee Journal of*, 27(3):433 –443.

Jones, K. E., Campbell, P. K., and Normann, R. A. (1992). A glass/silicon composite intracortical electrode array. *Ann Biomed Eng*, 20:423–437.

Kane, M. J., Breen, P. P., Quondamatteo, F., and Olaighin, G. (2011). BION microstimulators: a case study in the engineering of an electronic implantable medical device. *Med Eng Phys*, 33:7–16.

Kawano, T., Harimoto, T., Ishihara, A., Takei, K., Kawashima, T., Usui, S., and Ishida, M. (2010). Electrical interfacing between neurons and electronics via vertically integrated sub-4 microm-diameter silicon probe arrays fabricated by vapor-liquid-solid growth. *Biosens Bioelectron*, 25:1809–1815.

Kelly, R. C., Smith, M. A., Samonds, J. M., Kohn, A., Bonds, A. B., Movshon, J. A., and Lee, T. S. (2007). Comparison of recordings from microelectrode arrays and single electrodes in the visual cortex. *J. Neurosci.*, 27:261–264.

Kennedy, P. R. (1989). The cone electrode: a long-term electrode that records from neurites grown onto its recording surface. *J. Neurosci. Methods*, 29:181–193.

Kennedy, P. R. and Bakay, R. A. (1998). Restoration of neural output from a paralyzed patient by a direct brain connection. *Neuroreport*, 9:1707–1711.

Kennedy, P. R., Bakay, R. A., Moore, M. M., Adams, K., and Goldwaithe, J. (2000). Direct control of a computer from the human central nervous system. *Ieee Trans Rehabil Eng*, 8:198–202.

Kennedy, P. R., Kirby, M. T., Moore, M. M., King, B., and Mallory, A. (2004). Computer control using human intracortical local field potentials. *Ieee Trans Neural Syst Rehabil Eng*, 12:339–344.

Kennedy, P. R., Mirra, S. S., and Bakay, R. A. (1992). The cone electrode: ultrastructural studies following long-term recording in rat and monkey cortex. *Neurosci. Lett.*, 142:89–94.

Kilgard, M. P. and Merzenich, M. M. (1998). Cortical map reorganization enabled by nucleus basalis activity. *Science*, 279:1714–1718.

Kim, H., Biggs, J., Schloerb, W., Carmena, M., Lebedev, M., Nicolelis, M., and Srinivasan, M. (2006). Continuous shared control for stabilizing reaching and grasping with brain-machine interfaces. *Biomedical Engineering, Ieee Transactions on*, 53(6):1164 –1173.

Kim, H. K., Carmena, J. M., Biggs, S. J., Hanson, T. L., Nicolelis, M. A., and Srinivasan, M. A. (2007). The muscle activation method: an approach to impedance control of brain-machine interfaces through a musculoskeletal model of the arm. *Ieee Trans Biomed Eng*, 54:1520–1529.

Kim, S., Bhandari, R., Klein, M., Negi, S., Rieth, L., Tathireddy, P., Toepper, M., Oppermann, H., and Solzbacher, F. (2009). Integrated wireless neural interface based on the Utah electrode array. *Biomed Microdevices*, 11:453–466.

Kinnier wilson, S. A. (1925). The croonian lectures on some disorders of motility and of muscle tone, with special reference to the corpus striatum. *The Lancet*, 206.

Koller, W. C., Lyons, K. E., Wilkinson, S. B., Troster, A. I., and Pahwa, R. (2001). Long-term safety and efficacy of unilateral deep brain stimulation of the thalamus in essential tremor. *Mov. Disord.*, 16:464–468.

Koralek, A. C., Jin, X., Long Ii, J. D., Costa, R. M., and Carmena, J. M. (2012). Corticostriatal plasticity is necessary for learning intentional neuroprosthetic skills. *Nature*.

Kordower, J. H., Emborg, M. E., Bloch, J., Ma, S. Y., Chu, Y., Leventhal, L., McBride, J., Chen, E. Y., Palfi, S., Roitberg, B. Z., Brown, W. D., Holden, J. E., Pyzalski, R., Taylor, M. D., Carvey, P., Ling, Z., Trono, D., Hantraye, P., Deglon, N., and Aebischer, P. (2000). Neurodegeneration prevented by lentiviral vector delivery of GDNF in primate models of Parkinson's disease. *Science*, 290:767–773.

Kordower, J. H., Herzog, C. D., Dass, B., Bakay, R. A., Stansell, J., Gasmi, M., and Bartus, R. T. (2006). Delivery of neurturin by AAV2 (CERE-120)-mediated gene transfer provides structural and functional neuroprotection and neurorestoration in MPTP-treated monkeys. *Ann. Neurol.*, 60:706–715.

Kozai, T. D. and Kipke, D. R. (2009). Insertion shuttle with carboxyl terminated self-assembled monolayer coatings for implanting flexible polymer neural probes in the brain. *J. Neurosci. Methods*, 184:199–205.

Krack, P., Dostrovsky, J., Ilinsky, I., Kultas-Ilinsky, K., Lenz, F., Lozano, A., and Vitek, J. (2002). Surgery of the motor thalamus: problems with the present nomenclatures. *Mov. Disord.*, 17 Suppl 3:2–8.

Krack, P., Kumar, R., Ardouin, C., Dowsey, P. L., McVicker, J. M., Benabid, A. L., and Pollak, P. (2001). Mirthful laughter induced by subthalamic nucleus stimulation. *Mov. Disord.*, 16:867–875.

Krack, P., Pollak, P., Limousin, P., Benazzouz, A., and Benabid, A. L. (1997). Stimulation of subthalamic nucleus alleviates tremor in Parkinson's disease. *Lancet*, 350:1675.

Kruger, J., Caruana, F., Volta, R. D., and Rizzolatti, G. (2010). Seven years of recording from monkey cortex with a chronically implanted multiple microelectrode. *Front Neuroeng*, 3:6.

Kuhn, A. A., Tsui, A., Aziz, T., Ray, N., Brucke, C., Kupsch, A., Schneider, G. H., and Brown, P. (2009). Pathological synchronisation in the subthalamic nucleus of patients with Parkinson's disease relates to both bradykinesia and rigidity. *Exp. Neurol.*, 215:380–387.

Kuiper, N. (1962). Tests concerning random points on a circle. *Proc Kon Ned Akad Wetensch*, pages 38–47.

Kumar, R., Lozano, A. M., Sime, E., and Lang, A. E. (2003). Long-term follow-up of thalamic deep brain stimulation for essential and parkinsonian tremor. *Neurology*, 61:1601–1604.

Lebedev, M. A., Denton, J. M., and Nelson, R. J. (1994). Vibration-entrained and premovement activity in monkey primary somatosensory cortex. *J. Neurophysiol.*, 72:1654–1673.

Lebedev, M. A. and Nicolelis, M. A. (2006). Brain-machine interfaces: past, present and future. *Trends Neurosci.*, 29:536–546.

Lebedev, M. A., Tate, A. J., Hanson, T. L., Li, Z., O'Doherty, J. E., Winans, J. A., Ifft, P. J., Zhuang, K. Z., Fitzsimmons, N. A., Schwarz, D. A., Fuller, A. M., An, J. H., and Nicolelis, M. A. (2011). Future developments in brain-machine interface research. *Clinics (Sao Paulo)*, 66 Suppl 1:25–32.

Leblois, A., Meissner, W., Bioulac, B., Gross, C. E., Hansel, D., and Boraud, T. (2007). Late emergence of synchronized oscillatory activity in the pallidum during progressive Parkinsonism. *Eur. J. Neurosci.*, 26:1701–1713.

Lee, H. S., Kim, S. W., Yoo, I. S., and Chung, S. P. (2005). Common causes of hemiballism. *Am J Emerg Med*, 23:576–578.

Lehericy, S., Benali, H., Van de Moortele, P. F., Pelegrini-Issac, M., Waechter, T., Ugurbil, K., and Doyon, J. (2005). Distinct basal ganglia territories are engaged in early and advanced motor sequence learning. *Proc. Natl. Acad. Sci. U.S.A.*, 102:12566–12571.

Lehew G, N. M. (2008). State-of-the-Art Microwire Array Design for Chronic Neural Recordings in Behaving Animals. *In Nicolelis MAL (Ed.) Methods for neural ensemble recordings*, 2nd ed:1–20.

Lemon, R. N., Hanby, J. A., and Porter, R. (1976). Relationship between the activity of precentral neurones during active and passive movements in conscious monkeys. *Proc. R. Soc. Lond., B, Biol. Sci.*, 194:341–373.

Lenz, F. A., Jaeger, C. J., Seike, M. S., Lin, Y. C., and Reich, S. G. (2002). Single-neuron analysis of human thalamus in patients with intention tremor and other clinical signs of cerebellar disease. *J. Neurophysiol.*, 87:2084–2094.

Lenz, F. A., Kwan, H. C., Dostrovsky, J. O., Tasker, R. R., Murphy, J. T., and Lenz, Y. E. (1990). Single unit analysis of the human ventral thalamic nuclear group. Activity correlated with movement. *Brain*, 113 (Pt 6):1795–1821.

Lenz, F. A., Kwan, H. C., Martin, R. L., Tasker, R. R., Dostrovsky, J. O., and Lenz, Y. E. (1994). Single unit analysis of the human ventral thalamic nuclear group. Tremor-related activity in functionally identified cells. *Brain*, 117 (Pt 3):531–543.

Lenz, F. A., Tasker, R. R., Kwan, H. C., Schnider, S., Kwong, R., Murayama, Y., Dostrovsky, J. O., and Murphy, J. T. (1988). with the 3-6 Hz component of parkinsonian tremor. *J. Neurosci.*, 8:754–764.

Levesque, M. and Parent, A. (2005). The striatofugal fiber system in primates: a reevaluation of its organization based on single-axon tracing studies. *Proc. Natl. Acad. Sci. U.S.A.*, 102:11888–11893.

Levy, R., Ashby, P., Hutchison, W. D., Lang, A. E., Lozano, A. M., and Dostrovsky, J. O. (2002). Dependence of subthalamic nucleus oscillations on movement and dopamine in Parkinson's disease. *Brain*, 125:1196–1209.

Levy, R., Dostrovsky, J. O., Lang, A. E., Sime, E., Hutchison, W. D., and Lozano, A. M. (2001). Effects of apomorphine on subthalamic nucleus and globus pallidus internus neurons in patients with Parkinson's disease. *J. Neurophysiol.*, 86:249–260.

Levy, R., Hutchison, W. D., Lozano, A. M., and Dostrovsky, J. O. (2000). High-frequency synchronization of neuronal activity in the subthalamic nucleus of parkinsonian patients with limb tremor. *J. Neurosci.*, 20:7766–7775.

Li, Z., O'Doherty, J. E., Hanson, T. L., Lebedev, M. A., Henriquez, C. S., and Nicolelis, M. A. (2009). Unscented Kalman filter for brain-machine interfaces. *PloS One*, 4:e6243.

Lilly, J. C. (1950). A method of recording the moving electrical potential gradients in the brain. the 25-channel bavatron and electro-iconograms. *A.I.E.E.-IRE Conf. on Electronic Instrumentation in Nucleonics and Medicine*, S-3:33–37.

Lim, H. H., Lenarz, M., and Lenarz, T. (2009). Auditory midbrain implant: a review. *Trends Amplif*, 13:149–180.

Lin, C. S., Nicolelis, M. A., Schneider, J. S., and Chapin, J. K. (1990). A major direct GABAergic pathway from zona incerta to neocortex. *Science*, 248:1553–1556.

Linderman, M. D., Gilja, V., Santhanam, G., Afshar, A., Ryu, S., Meng, T. H., and Shenoy, K. V. (2006). An autonomous, broadband, multi-channel neural recording system for freely behaving primates. *Conf Proc Ieee Eng Med Biol Soc*, 1:1212–1215.

Litvak, V., Jha, A., Eusebio, A., Oostenveld, R., Foltynie, T., Limousin, P., Zrinzo, L., Hariz, M. I., Friston, K., and Brown, P. (2011). Resting oscillatory cortico-subthalamic connectivity in patients with Parkinson's disease. *Brain*, 134:359–374.

Liu, X., McCreery, D., Bullara, L., and Agnew, W. (2006). Evaluation of the stability of intracortical microelectrode arrays. *Neural Systems and Rehabilitation Engineering, Ieee Transactions on*, 14(1):91 –100.

Liu, Y.-H., Li, C.-L., and Lin, T.-H. (2009). A 200-pj/b mux-based rf transmitter for implantable multichannel neural recording. *Microwave Theory and Techniques, Ieee Transactions on*, 57(10):2533 –2541.

Lohmann, E., Thobois, S., Lesage, S., Broussolle, E., du Montcel, S. T., Ribeiro, M. J., Remy, P., Pelissolo, A., Dubois, B., Mallet, L., Pollak, P., Agid, Y., Brice, A., Agid, Y., Bonnet, A. M., Borg, M., Brice, A., Broussolle, E., Damier, P., Destee, A., Durr, A., Durif, F., Lohmann, E., Martinez, M., Penet, C., Pollak, P., Rascol, O., Tison, F., Tranchant, C., Verin, M., Viallet, F., Vidailhet, M., and Warter, J. M. (2009). A multidisciplinary study of patients with early-onset PD with and without parkin mutations. *Neurology*, 72:110–116.

London, B. M., Jordan, L. R., Jackson, C. R., and Miller, L. E. (2008). Electrical stimulation of the proprioceptive cortex (area 3a) used to instruct a behaving monkey. *Ieee Trans Neural Syst Rehabil Eng*, 16:32–36.

Magarinos-Ascone, C. M., Figueiras-Mendez, R., Riva-Meana, C., and Cordoba-Fernandez, A. (2000). Subthalamic neuron activity related to tremor and movement in Parkinson's disease. *Eur. J. Neurosci.*, 12:2597–2607.

Magill, P. J., Bolam, J. P., and Bevan, M. D. (2001). Dopamine regulates the impact of the cerebral cortex on the subthalamic nucleus-globus pallidus network. *Neuroscience*, 106:313–330.

Magnin, M., Morel, A., and Jeanmonod, D. (2000). Single-unit analysis of the pallidum, thalamus and subthalamic nucleus in parkinsonian patients. *Neuroscience*, 96:549–564.

Mallet, N., Pogosyan, A., Marton, L. F., Bolam, J. P., Brown, P., and Magill, P. J. (2008a). Parkinsonian beta oscillations in the external globus pallidus and their relationship with subthalamic nucleus activity. *J. Neurosci.*, 28:14245–14258.

Mallet, N., Pogosyan, A., Sharott, A., Csicsvari, J., Bolam, J. P., Brown, P., and Magill, P. J. (2008b). Disrupted dopamine transmission and the emergence of exaggerated beta oscillations in subthalamic nucleus and cerebral cortex. *J. Neurosci.*, 28:4795–4806.

Marbach, W. D., Zabarsky, M., Hoban, P., and Nelson, C. (1982). Building the bionic man. *Newsweek*, 100:78–79.

Marks, W. J., Bartus, R. T., Siffert, J., Davis, C. S., Lozano, A., Boulis, N., Vitek, J., Stacy, M., Turner, D., Verhagen, L., Bakay, R., Watts, R., Guthrie, B., Jankovic, J., Simpson, R., Tagliati, M., Alterman, R., Stern, M., Baltuch, G., Starr, P. A., Larson, P. S., Ostrem, J. L., Nutt, J., Kieburtz, K., Kordower, J. H., and Olanow, C. W. (2010). Gene delivery of AAV2-neurturin for Parkinson's disease: a double-blind, randomised, controlled trial. *Lancet Neurol*, 9:1164–1172.

Marsden, J. F., Limousin-Dowsey, P., Ashby, P., Pollak, P., and Brown, P. (2001). Subthalamic nucleus, sensorimotor cortex and muscle interrelationships in Parkinson's disease. *Brain*, 124:378–388.

Marzullo, T. C., Lehmkuhle, M. J., Gage, G. J., and Kipke, D. R. (2010). Development of closed-loop neural interface technology in a rat model: combining motor cortex operant conditioning with visual cortex microstimulation. *Ieee Trans Neural Syst Rehabil Eng*, 18:117–126.

Marzullo, T. C., Miller, C. R., and Kipke, D. R. (2006). Suitability of the cingulate cortex for neural control. *Ieee Trans Neural Syst Rehabil Eng*, 14:401–409.

Maschietto, M., Mahmud, M., Stefano, G., and Vassanelli, S. (2009). A high resolution bi-directional communication through a brain-chip interface. In *Advanced Technologies for Enhanced Quality of Life, 2009. At-Equal '09.*, pages 32 –35.

McCreery, D. B., Agnew, W. F., Yuen, T. G., and Bullara, L. A. (1988). Comparison of neural damage induced by electrical stimulation with faradaic and capacitor electrodes. *Ann Biomed Eng*, 16:463–481.

McIntyre, C. C. and Grill, W. M. (2000). Selective microstimulation of central nervous system neurons. *Ann Biomed Eng*, 28:219–233.

McIntyre, C. C., Grill, W. M., Sherman, D. L., and Thakor, N. V. (2004). Cellular effects of deep brain stimulation: model-based analysis of activation and inhibition. *J. Neurophysiol.*, 91:1457–1469.

Mehring, C., Rickert, J., Vaadia, E., Cardosa de Oliveira, S., Aertsen, A., and Rotter, S. (2003). Inference of hand movements from local field potentials in monkey motor cortex. *Nat. Neurosci.*, 6:1253–1254.

Merrill, D. R., Bikson, M., and Jefferys, J. G. (2005). Electrical stimulation of excitable tissue: design of efficacious and safe protocols. *J. Neurosci. Methods*, 141:171–198.

Mink, J. W. (1996). The basal ganglia: focused selection and inhibition of competing motor programs. *Prog. Neurobiol.*, 50:381–425.

Miranda, H., Gilja, V., Chestek, C., Shenoy, K., and Meng, T. (2010). Hermesd: A high-rate long-range wireless transmission system for simultaneous multichannel neural recording applications. *Biomedical Circuits and Systems, Ieee Transactions on*, 4(3):181 –191.

Mohseni, P. and Najafi, K. (2004). A fully integrated neural recording amplifier with DC input stabilization. *Ieee Trans Biomed Eng*, 51:832–837.

Mojarradi, M., Binkley, D., Blalock, B., Andersen, R., Ulshoefer, N., Johnson, T., and Del Castillo, L. (2003). A miniaturized neuroprosthesis suitable for implantation into the brain. *Ieee Trans Neural Syst Rehabil Eng*, 11:38–42.

Monakow, K. H., Akert, K., and Kunzle, H. (1978). Projections of the precentral motor cortex and other cortical areas of the frontal lobe to the subthalamic nucleus in the monkey. *Exp Brain Res*, 33:395–403.

Moritz, C. T., Perlmutter, S. I., and Fetz, E. E. (2008). Direct control of paralysed muscles by cortical neurons. *Nature*, 456:639–642.

Morris, G., Nevet, A., and Bergman, H. (2003). Anatomical funneling, sparse connectivity and redundancy reduction in the neural networks of the basal ganglia. *J. Physiol. Paris*, 97:581–589.

Musallam, S., Corneil, B. D., Greger, B., Scherberger, H., and Andersen, R. A. (2004). Cognitive control signals for neural prosthetics. *Science*, 305:258–262.

Myers, F. B., Simpson, J. A., and Ghovanloo, M. (2006). A wideband wireless neural stimulation platform for high-density microelectrode arrays. *Conf Proc Ieee Eng Med Biol Soc*, 1:4404–4407.

Najafi, K. and Hetke, J. F. (1990). Strength characterization of silicon microprobes in neurophysiological tissues. *Ieee Trans Biomed Eng*, 37:474–481.

Najafi, K. and Wise, K. (1986). An implantable multielectrode array with on-chip signal processing. *Solid-State Circuits, Ieee Journal of*, 21(6):1035 – 1044.

Najafi, K., Wise, K., and Mochizuki, T. (1985). A high-yield ic-compatible multichannel recording array. *Electron Devices, Ieee Transactions on*, 32(7):1206 – 1211.

Narayanan, N. S., Kimchi, E. Y., and Laubach, M. (2005). Redundancy and synergy of neuronal ensembles in motor cortex. *J. Neurosci.*, 25:4207–4216.

Nicolelis, M. (2011). *Beyond Boundaries: The New Neuroscience of Connecting Brains with Machines—and How It Will Change Our Lives*. Times Books.

Nicolelis, M. A. (2001). Actions from thoughts. *Nature*, 409:403–407.

Nicolelis, M. A., Chapin, J. K., and Lin, R. C. (1992). Somatotopic maps within the zona incerta relay parallel GABAergic somatosensory pathways to the neocortex, superior colliculus, and brainstem. *Brain Res.*, 577:134–141.

Nicolelis, M. A., Dimitrov, D., Carmena, J. M., Crist, R., Lehew, G., Kralik, J. D., and Wise, S. P. (2003). Chronic, multisite, multielectrode recordings in macaque monkeys. *Proc. Natl. Acad. Sci. U.S.A.*, 100:11041–11046.

Nicolelis, M. A., Ghazanfar, A. A., Faggin, B. M., Votaw, S., and Oliveira, L. M. (1997). Reconstructing the engram: simultaneous, multisite, many single neuron recordings. *Neuron*, 18:529–537.

Nicolelis, M. A. and Lebedev, M. A. (2009). Principles of neural ensemble physiology underlying the operation of brain-machine interfaces. *Nat. Rev. Neurosci.*, 10:530–540.

Nicolelis, M. A. and Ribeiro, S. (2002). Multielectrode recordings: the next steps. *Curr. Opin. Neurobiol.*, 12:602–606.

Nielson, H. C., Knight, J. M., and Porter, P. B. (1962). Subcortical conditioning, generalization, and transfer. *J Comp Physiol Psychol*, 55:168–173.

Nowak, L. G. and Bullier, J. (1998a). Axons, but not cell bodies, are activated by electrical stimulation in cortical gray matter. I. Evidence from chronaxie measurements. *Exp Brain Res*, 118:477–488.

Nowak, L. G. and Bullier, J. (1998b). Axons, but not cell bodies, are activated by electrical stimulation in cortical gray matter. II. Evidence from selective inactivation of cell bodies and axon initial segments. *Exp Brain Res*, 118:489–500.

Obeid, I., Morizio, J., Moxon, K., Nicolelis, M., and Wolf, P. (2003). Two multichannel integrated circuits for neural recording and signal processing. *Biomedical Engineering, Ieee Transactions on*, 50(2):255 –258.

Obeid, I., Nicolelis, M. A., and Wolf, P. D. (2004a). A low power multichannel analog front end for portable neural signal recordings. *J. Neurosci. Methods*, 133:27–32.

Obeid, I., Nicolelis, M. A., and Wolf, P. D. (2004b). A multichannel telemetry system for single unit neural recordings. *J. Neurosci. Methods*, 133:33–38.

Obeso, J. A., Jahanshahi, M., Alvarez, L., Macias, R., Pedroso, I., Wilkinson, L., Pavon, N., Day, B., Pinto, S., Rodriguez-Oroz, M. C., Tejeiro, J., Artieda, J., Talelli, P., Swayne, O., Rodriguez, R., Bhatia, K., Rodriguez-Diaz, M., Lopez, G., Guridi, J., and Rothwell, J. C. (2009). What can man do without basal ganglia motor output? The effect of combined unilateral subthalamotomy and pallidotomy in a patient with Parkinson's disease. *Exp. Neurol.*, 220:283–292.

O'Doherty, J., Lebedev, M., Ifft, P., Zhuang, K., Shokur, S., Bleuler, H., and Nicolelis, M. (2011a). Active tactile exploration using a brainmachinebrain interface. *Nature advance online publication*, http://dx.doi.org/10.1038/nature10489.

O'Doherty, J., Lebedev, M., Li, Z., and Nicolelis, M. (2012). Virtual active touch using randomly patterned intracortical microstimulation. *Neural Systems and Rehabilitation Engineering, Ieee Transactions on*, 20(1):85 –93.

O'Doherty, J. E., Lebedev, M. A., Hanson, T. L., Fitzsimmons, N. A., and Nicolelis, M. A. (2009). A brain-machine interface instructed by direct intracortical microstimulation. *Front Integr Neurosci*, 3:20.

O'Doherty, J. E., Lebedev, M. A., Ifft, P. J., Zhuang, K. Z., Shokur, S., Bleuler, H., and Nicolelis, M. A. (2011b). Active tactile exploration using a brain-machine-brain interface. *Nature*, 479:228–231.

O'Driscoll, M., El-Deredy, W., and Ramsden, R. T. (2011). Brain stem responses evoked by stimulation of the mature cochlear nucleus with an auditory brain stem implant. *Ear Hear*, 32:286–299.

Ojakangas, C. L., Shaikhouni, A., Friehs, G. M., Caplan, A. H., Serruya, M. D., Saleh, M., Morris, D. S., and Donoghue, J. P. (2006). Decoding movement intent from human premotor cortex neurons for neural prosthetic applications. *J Clin Neurophysiol*, 23:577–584.

Olds, J. (1967). The limbic system and behavioral reinforcement. *Prog. Brain Res.*, 27:144–164.

Olds, J. and Milner, P. (1954). Positive reinforcement produced by electrical stimulation of septal area and other regions of rat brain. *J Comp Physiol Psychol*, 47:419–427.

Olsson, R.H., I. and Wise, K. (2005). A three-dimensional neural recording microsystem with implantable data compression circuitry. *Solid-State Circuits, Ieee Journal of*, 40(12):2796 – 2804.

O'Neill, D. E. (1980). man is now a scientific fact. *Rev Fed Am Hosp*, 13:22–23.

Oppenheim, A. and Schafer, R. (1975). *Digital signal processing*. Englewood Cliffs, N.J.,: Prentice-Hall.

Parent, A. and Hazrati, L. N. (1995a). Functional anatomy of the basal ganglia. I. The cortico-basal ganglia-thalamo-cortical loop. *Brain Res. Brain Res. Rev.*, 20:91–127.

Parent, A. and Hazrati, L. N. (1995b). Functional anatomy of the basal ganglia. II. The place of subthalamic nucleus and external pallidum in basal ganglia circuitry. *Brain Res. Brain Res. Rev.*, 20:128–154.

Parent, A., Sato, F., Wu, Y., Gauthier, J., Levesque, M., and Parent, M. (2000). Organization of the basal ganglia: the importance of axonal collateralization. *Trends Neurosci.*, 23:S20–27.

Parthasarathy, J., Hogenson, J., Erdman, A. G., Redish, A. D., and Ziaie, B. (2006). Battery-operated high-bandwidth multi-channel wireless neural recording system using 802.11b. *Conf Proc Ieee Eng Med Biol Soc*, 1:5989–5992.

Parush, N., Tishby, N., and Bergman, H. (2011). Dopaminergic Balance between Reward Maximization and Policy Complexity. *Front Syst Neurosci*, 5:22.

Patil, P. G., Carmena, J. M., Nicolelis, M. A., and Turner, D. A. (2004). Ensemble recordings of human subcortical neurons as a source of motor control signals for a brain-machine interface. *Neurosurgery*, 55:27–35.

Patil, P. G. and Turner, D. A. (2008). The development of brain-machine interface neuroprosthetic devices. *Neurotherapeutics*, 5:137–146.

Pawlak, V. and Kerr, J. N. (2008). Dopamine receptor activation is required for corticostriatal spike-timing-dependent plasticity. *J. Neurosci.*, 28:2435–2446.

Penfield, W. and Boldrey, E. (1937). Somatic motor and sensory representation in the cerebral cortex of man as studied by electrical stimulation. *Brain*, 60:389–443.

Penfield, W. and Perot, P. (1963). THE BRAIN'S RECORD OF AUDITORY AND VISUAL EXPERIENCE. A FINAL SUMMARY AND DISCUSSION. *Brain*, 86:595–696.

Penney, J. B. and Young, A. B. (1983). Speculations on the functional anatomy of basal ganglia disorders. *Annu. Rev. Neurosci.*, 6:73–94.

Perelman, Y. and Ginosar, R. (2007). An integrated system for multichannel neuronal recording with spike/LFP separation, integrated A/D conversion and threshold detection. *Ieee Trans Biomed Eng*, 54:130–137.

Plaha, P., Khan, S., and Gill, S. S. (2008). Bilateral stimulation of the caudal zona incerta nucleus for tremor control. *J. Neurol. Neurosurg. Psychiatr.*, 79:504–513.

Pollak, P., Benabid, A. L., Gervason, C. L., Hoffmann, D., Seigneuret, E., and Perret, J. (1993a). Long-term effects of chronic stimulation of the ventral intermediate thalamic nucleus in different types of tremor. *Adv Neurol*, 60:408–413.

Pollak, P., Benabid, A. L., Gross, C., Gao, D. M., Laurent, A., Benazzouz, A., Hoffmann, D., Gentil, M., and Perret, J. (1993b). [Effects of the stimulation of the subthalamic nucleus in Parkinson disease]. *Rev. Neurol. (Paris)*, 149:175–176.

Poon, A., O'Driscoll, S., and Meng, T. (2007). Optimal operating frequency in wireless power transmission for implantable devices. In *Engineering in Medicine and Biology Society, 2007. Embs 2007. 29th Annual International Conference of the Ieee*, pages 5673 –5678.

Porada, I., Bondar, I., Spatz, W. B., and Kruger, J. (2000). Rabbit and monkey visual cortex: more than a year of recording with up to 64 microelectrodes. *J. Neurosci. Methods*, 95:13–28.

Prescott, I. A., Dostrovsky, J. O., Moro, E., Hodaie, M., Lozano, A. M., and Hutchison, W. D. (2009). Levodopa enhances synaptic plasticity in the substantia nigra pars reticulata of Parkinson's disease patients. *Brain*, 132:309–318.

Prescott, T. J., Montes Gonzalez, F. M., Gurney, K., Humphries, M. D., and Redgrave, P. (2006). A robot model of the basal ganglia: behavior and intrinsic processing. *Neural Netw*, 19:31–61.

Quiroga, R. Q., Reddy, L., Kreiman, G., Koch, C., and Fried, I. (2005). Invariant visual representation by single neurons in the human brain. *Nature*, 435:1102–1107.

Raeva, S., Vainberg, N., Tikhonov, Y., and Tsetlin, I. (1999). Analysis of evoked activity patterns of human thalamic ventrolateral neurons during verbally ordered voluntary movements. *Neuroscience*, 88:377–392.

Raz, A., Vaadia, E., and Bergman, H. (2000). Firing patterns and correlations of spontaneous discharge of pallidal neurons in the normal and the tremulous 1-methyl-4-phenyl-1,2,3,6-tetrahydropyridine vervet model of parkinsonism. *J. Neurosci.*, 20:8559–8571.

Richebe, P., Rathmell, J. P., and Brennan, T. J. (2005). Immediate early genes after pulsed radiofrequency treatment: neurobiology in need of clinical trials. *Anesthesiology*, 102:1–3.

Rieke, F., Warland, D., de de Ruyter van Steveninck, R., and Bialek, W. (1999). *Spikes: Exploring the Neural Code (Computational Neuroscience)*. A Bradford Book.

Rizk, M., Bossetti, C. A., Jochum, T. A., Callender, S. H., Nicolelis, M. A., Turner, D. A., and Wolf, P. D. (2009). A fully implantable 96-channel neural data acquisition system. *J Neural Eng*, 6:026002.

Rizk, M., Obeid, I., Callender, S. H., and Wolf, P. D. (2007). A single-chip signal processing and telemetry engine for an implantable 96-channel neural data acquisition system. *J Neural Eng*, 4:309–321.

Roberts, W. W. and Kiess, H. O. (1964). Motivational properties of hypothalamic aggression in cats. *Journal of Comparative and Physiological Psychology*, 58:187–193.

Robinson, D. (1968). The electrical properties of metal microelectrodes. *Proceedings of the Ieee*, 56(6):1065 – 1071.

Rodriguez-Oroz, M. C., Lopez-Azcarate, J., Garcia-Garcia, D., Alegre, M., Toledo, J., Valencia, M., Guridi, J., Artieda, J., and Obeso, J. A. (2011). Involvement of the subthalamic nucleus in impulse control disorders associated with Parkinson's disease. *Brain*, 134:36–49.

Rodriguez-Oroz, M. C., Obeso, J. A., Lang, A. E., Houeto, J. L., Pollak, P., Rehncrona, S., Kulisevsky, J., Albanese, A., Volkmann, J., Hariz, M. I., Quinn, N. P., Speelman, J. D., Guridi, J., Zamarbide, I., Gironell, A., Molet, J., Pascual-Sedano, B., Pidoux, B., Bonnet, A. M., Agid, Y., Xie, J., Benabid, A. L., Lozano, A. M., Saint-Cyr, J., Romito, L., Contarino, M. F., Scerrati, M., Fraix, V., and Van Blercom, N. (2005). Bilateral deep brain stimulation in Parkinson's disease: a multicentre study with 4 years follow-up. *Brain*, 128:2240–2249.

Rodriguez-Oroz, M. C., Rodriguez, M., Guridi, J., Mewes, K., Chockkman, V., Vitek, J., DeLong, M. R., and Obeso, J. A. (2001). The subthalamic nucleus in Parkinson's disease: somatotopic organization and physiological characteristics. *Brain*, 124:1777–1790.

Rolston, J. D., Gross, R. E., and Potter, S. M. (2009a). A low-cost multielectrode system for data acquisition enabling real-time closed-loop processing with rapid recovery from stimulation artifacts. *Front Neuroeng*, 2:12.

Rolston, J. D., Gross, R. E., and Potter, S. M. (2009b). Common median referencing for improved action potential detection with multielectrode arrays. *Conf Proc Ieee Eng Med Biol Soc*, 2009:1604–1607.

Romo, R., Hernandez, A., Zainos, A., Brody, C. D., and Lemus, L. (2000). Sensing without touching: psychophysical performance based on cortical microstimulation. *Neuron*, 26:273–278.

Romo, R., Hernandez, A., Zainos, A., and Salinas, E. (1998). Somatosensory discrimination based on cortical microstimulation. *Nature*, 392:387–390.

Romo, R., Scarnati, E., and Schultz, W. (1992). Role of primate basal ganglia and frontal cortex in the internal generation of movements. II. Movement-related activity in the anterior striatum. *Exp Brain Res*, 91:385–395.

Rosin, B., Slovik, M., Mitelman, R., Rivlin-Etzion, M., Haber, S. N., Israel, Z., Vaadia, E., and Bergman, H. (2011). Closed-loop deep brain stimulation is superior in ameliorating parkinsonism. *Neuron*, 72:370–384.

Rousche, P. J. and Normann, R. A. (1998). Chronic recording capability of the Utah Intracortical Electrode Array in cat sensory cortex. *J. Neurosci. Methods*, 82:1–15.

Rouse, A. G., Stanslaski, S. R., Cong, P., Jensen, R. M., Afshar, P., Ullestad, D., Gupta, R., Molnar, G. F., Moran, D. W., and Denison, T. J. (2011). A chronic generalized bi-directional brain-machine interface. *J Neural Eng*, 8:036018.

Sage, J. R., Anagnostaras, S. G., Mitchell, S., Bronstein, J. M., De Salles, A., Masterman, D., and Knowlton, B. J. (2003). Analysis of probabilistic classification learning in patients with Parkinson's disease before and after pallidotomy surgery. *Learn. Mem.*, 10:226–236.

Salcman, M. and Bak, M. J. (1973). Design, fabrication, and in vivo behavior of chronic recording intracortical microelectrodes. *Biomedical Engineering, Ieee Transactions on*, Bme-20(4):253 –260.

Salcman, M. and Bak, M. J. (1976). A new chronic recording intracortical microelectrode. *Med Biol Eng*, 14:42–50.

Salin, P., Manrique, C., Forni, C., and Kerkerian-Le Goff, L. (2002). High-frequency stimulation of the subthalamic nucleus selectively reverses dopamine denervation-induced cellular defects in the output structures of the basal ganglia in the rat. *J. Neurosci.*, 22:5137–5148.

Salzman, C. D., Britten, K. H., and Newsome, W. T. (1990). Cortical microstimulation influences perceptual judgements of motion direction. *Nature*, 346:174–177.

Sanchez, J., Erdogmus, D., Nicolelis, M., Wessberg, J., and Principe, J. (2005). Interpreting spatial and temporal neural activity through a recurrent neural network brain-machine interface. *Neural Systems and Rehabilitation Engineering, Ieee Transactions on*, 13(2):213 –219.

Sanders, J. E., Stiles, C. E., and Hayes, C. L. (2000). Tissue response to single-polymer fibers of varying diameters: evaluation of fibrous encapsulation and macrophage density. *J. Biomed. Mater. Res.*, 52:231–237.

Santhanam, G., Linderman, M. D., Gilja, V., Afshar, A., Ryu, S. I., Meng, T. H., and Shenoy, K. V. (2007). HermesB: a continuous neural recording system for freely behaving primates. *Ieee Trans Biomed Eng*, 54:2037–2050.

Santhanam, G., Ryu, S. I., Yu, B. M., Afshar, A., and Shenoy, K. V. (2006). A high-performance brain-computer interface. *Nature*, 442:195–198.

Schalk, G., Wolpaw, J. R., McFarland, D. J., and Pfurtscheller, G. (2000). EEG-based communication: presence of an error potential. *Clin Neurophysiol*, 111:2138–2144.

Schmidt, E. M. (1980). Single neuron recording from motor cortex as a possible source of signals for control of external devices. *Ann Biomed Eng*, 8:339–349.

Schmidt, E. M. (1984a). Computer separation of multi-unit neuroelectric data: a review. *J. Neurosci. Methods*, 12:95–111.

Schmidt, E. M. (1984b). Instruments for sorting neuroelectric data: a review. *J. Neurosci. Methods*, 12:1–24.

Schmidt, E. M., McIntosh, J. S., Durelli, L., and Bak, M. J. (1978). Fine control of operantly conditioned firing patterns of cortical neurons. *Exp. Neurol.*, 61:349–369.

Schultz, W. and Romo, R. (1992). Role of primate basal ganglia and frontal cortex in the internal generation of movements. I. Preparatory activity in the anterior striatum. *Exp Brain Res*, 91:363–384.

Schwerdt, H., Xu, W., Shekhar, S., Abbaspour-Tamijani, A., Towe, B., Miranda, F., and Chae, J. (2011). A fully passive wireless microsystem for recording of neuropotentials using rf backscattering methods. *Microelectromechanical Systems, Journal of*, 20(5):1119 –1130.

Seese, T. M., Harasaki, H., Saidel, G. M., and Davies, C. R. (1998). Characterization of tissue morphology, angiogenesis, and temperature in the adaptive response of muscle tissue to chronic heating. *Lab. Invest.*, 78:1553–1562.

Serruya, M., Hatsopoulos, N., Fellows, M., Paninski, L., and Donoghue, J. (2003). Robustness of neuroprosthetic decoding algorithms. *Biol Cybern*, 88:219–228.

Serruya, M. D., Hatsopoulos, N. G., Paninski, L., Fellows, M. R., and Donoghue, J. P. (2002). Instant neural control of a movement signal. *Nature*, 416:141–142.

Shannon, R. V. (1992). A model of safe levels for electrical stimulation. *Ieee Trans Biomed Eng*, 39:424–426.

Sharott, A., Magill, P. J., Harnack, D., Kupsch, A., Meissner, W., and Brown, P. (2005). Dopamine depletion increases the power and coherence of beta-oscillations in the cerebral cortex and subthalamic nucleus of the awake rat. *Eur. J. Neurosci.*, 21:1413–1422.

Shink, E., Bevan, M. D., Bolam, J. P., and Smith, Y. (1996). The subthalamic nucleus and the external pallidum: two tightly interconnected structures that control the output of the basal ganglia in the monkey. *Neuroscience*, 73:335–357.

Shinkman, P. G., Bruce, C. J., and Pfingst, B. E. (1974). Operant conditioning of single-unit response patterns in visual cortex. *Science*, 184:1194–1196.

Skinner, B. (1938). *The behavior of organisms: an experimental analysis.* New York: Appleton-Century-Crofts.

Sodagar, A., Perlin, G., Yao, Y., Najafi, K., and Wise, K. (2009). An implantable 64-channel wireless microsystem for single-unit neural recording. *Solid-State Circuits, Ieee Journal of*, 44(9):2591 –2604.

Sodagar, A., Wise, K., and Najafi, K. (2006). A neural signal processor for an implantable multi-channel cortical recording microsystem. In *Engineering in Medicine and Biology Society, 2006. Embs '06. 28th Annual International Conference of the Ieee*, pages 5900 –5903.

Sodagar, A. M., Wise, K. D., and Najafi, K. (2007). A fully integrated mixed-signal neural processor for implantable multichannel cortical recording. *Ieee Trans Biomed Eng*, 54:1075–1088.

Song, Y.-K., Borton, D., Park, S., Patterson, W., Bull, C., Laiwalla, F., Mislow, J., Simeral, J., Donoghue, J., and Nurmikko, A. (2009). Active microelectronic neurosensor arrays for implantable brain communication interfaces. *Neural Systems and Rehabilitation Engineering, Ieee Transactions on*, 17(4):339 –345.

Song, Y. K., Patterson, W. R., Bull, C. W., Beals, J., Hwang, N., Deangelis, A. P., Lay, C., McKay, J. L., Nurmikko, A. V., Fellows, M. R., Simeral, J. D., Donoghue, J. P., and Connors, B. W. (2005). Development of a chipscale integrated microelectrode/microelectronic device for brain implantable neuroengineering applications. *Ieee Trans Neural Syst Rehabil Eng*, 13:220–226.

Starr, P. A., Rau, G. M., Davis, V., Marks, W. J., Ostrem, J. L., Simmons, D., Lindsey, N., and Turner, R. S. (2005). Spontaneous pallidal neuronal activity in human dystonia: comparison with Parkinson's disease and normal macaque. *J. Neurophysiol.*, 93:3165–3176.

Steiner, H. and Gerfen, C. R. (1998). Role of dynorphin and enkephalin in the regulation of striatal output pathways and behavior. *Exp Brain Res*, 123:60–76.

Sun, D. A., Yu, H., Spooner, J., Tatsas, A. D., Davis, T., Abel, T. W., Kao, C., and Konrad, P. E. (2008). Postmortem analysis following 71 months of deep brain stimulation of the subthalamic nucleus for Parkinson disease. *J. Neurosurg.*, 109:325–329.

Suner, S., Fellows, M. R., Vargas-Irwin, C., Nakata, G. K., and Donoghue, J. P. (2005). Reliability of signals from a chronically implanted, silicon-based electrode array in non-human primate primary motor cortex. *Ieee Trans Neural Syst Rehabil Eng*, 13:524–541.

Szuts, T. A., Fadeyev, V., Kachiguine, S., Sher, A., Grivich, M. V., Agrochao, M., Hottowy, P., Dabrowski, W., Lubenov, E. V., Siapas, A. G., Uchida, N., Litke, A. M., and Meister, M. (2011). A wireless multi-channel neural amplifier for freely moving animals. *Nat. Neurosci.*, 14:263–269.

Talwar, S. K., Xu, S., Hawley, E. S., Weiss, S. A., Moxon, K. A., and Chapin, J. K. (2002). Rat navigation guided by remote control. *Nature*, 417:37–38.

Tass, P., Smirnov, D., Karavaev, A., Barnikol, U., Barnikol, T., Adamchic, I., Hauptmann, C., Pawelcyzk, N., Maarouf, M., Sturm, V., Freund, H. J., and Bezruchko, B. (2010). The causal relationship between subcortical local field potential oscillations and Parkinsonian resting tremor. *J Neural Eng*, 7:16009.

Taylor, D. M., Tillery, S. I., and Schwartz, A. B. (2002). Direct cortical control of 3D neuroprosthetic devices. *Science*, 296:1829–1832.

Tehovnik, E. J., Tolias, A. S., Sultan, F., Slocum, W. M., and Logothetis, N. K. (2006). Direct and indirect activation of cortical neurons by electrical microstimulation. *J. Neurophysiol.*, 96:512–521.

Theodosopoulos, P. V., Marks, W. J., Christine, C., and Starr, P. A. (2003). Locations of movement-related cells in the human subthalamic nucleus in Parkinson's disease. *Mov. Disord.*, 18:791–798.

Thomas, C. A., Springer, P. A., Loeb, G. E., Berwald-Netter, Y., and Okun, L. M. (1972). A miniature microelectrode array to monitor the bioelectric activity of cultured cells. *Exp. Cell Res.*, 74:61–66.

Thorbergsson, P. T., Garwicz, M., Schouenborg, J., and Johansson, A. J. (2008). Implementation of a telemetry system for neurophysiological signals. *Conf Proc Ieee Eng Med Biol Soc*, 2008:1254–1257.

Tian, B., Cohen-Karni, T., Qing, Q., Duan, X., Xie, P., and Lieber, C. M. (2010). Three-dimensional, flexible nanoscale field-effect transistors as localized bioprobes. *Science*, 329:830–834.

Timmermann, L., Gross, J., Dirks, M., Volkmann, J., Freund, H. J., and Schnitzler, A. (2003). The cerebral oscillatory network of parkinsonian resting tremor. *Brain*, 126:199–212.

Towe, B. (2007). Passive backscatter biotelemetry for neural interfacing. In *Neural Engineering, 2007. Cne '07. 3rd International Ieee/Embs Conference on*, pages 144 –147.

Tropel, P., Platet, N., Platel, J. C., Noel, D., Albrieux, M., Benabid, A. L., and Berger, F. (2006). Functional neuronal differentiation of bone marrow-derived mesenchymal stem cells. *Stem Cells*, 24:2868–2876.

Turner, R. S. and Desmurget, M. (2010). Basal ganglia contributions to motor control: a vigorous tutor. *Curr. Opin. Neurobiol.*, 20:704–716.

Velliste, M., Perel, S., Spalding, M. C., Whitford, A. S., and Schwartz, A. B. (2008). Cortical control of a prosthetic arm for self-feeding. *Nature*, 453:1098–1101.

Ventura, V., Cai, C., and Kass, R. E. (2005a). Statistical assessment of time-varying dependency between two neurons. *J. Neurophysiol.*, 94:2940–2947.

Ventura, V., Cai, C., and Kass, R. E. (2005b). Trial-to-trial variability and its effect on time-varying dependency between two neurons. *J. Neurophysiol.*, 94:2928–2939.

Verloop, A. J. and Holsheimer, J. (1984). A simple method for the construction of electrode arrays. *J. Neurosci. Methods*, 11:173–178.

Vibert, J. F. and Costa, J. (1979). Spike separation in multiunit records: a multivariate analysis of spike descriptive parameters. *Electroencephalogr Clin Neurophysiol*, 47:172–182.

Vyssotski, A. L., Serkov, A. N., Itskov, P. M., Dell'Omo, G., Latanov, A. V., Wolfer, D. P., and Lipp, H. P. (2006). Miniature neurologgers for flying pigeons: multichannel EEG and action and field potentials in combination with GPS recording. *J. Neurophysiol.*, 95:1263–1273.

Wahnoun, R., He, J., and Helms Tillery, S. I. (2006). Selection and parameterization of cortical neurons for neuroprosthetic control. *J Neural Eng*, 3:162–171.

Wahnoun, R., Tillery, S. I., and He, J. (2004). Neuron selection and visual training for population vector based cortical control. *Conf Proc Ieee Eng Med Biol Soc*, 6:4607–4610.

Ward, M. P., Rajdev, P., Ellison, C., and Irazoqui, P. P. (2009). Toward a comparison of microelectrodes for acute and chronic recordings. *Brain Res.*, 1282:183–200.

Wattanapanitch, W., Fee, M., and Sarpeshkar, R. (2007). An energy-efficient micropower neural recording amplifier. *Biomedical Circuits and Systems, Ieee Transactions on*, 1(2):136 –147.

Weinberger, M., Hutchison, W. D., and Dostrovsky, J. O. (2009). Pathological subthalamic nucleus oscillations in PD: can they be the cause of bradykinesia and akinesia? *Exp. Neurol.*, 219:58–61.

Wessberg, J., Stambaugh, C. R., Kralik, J. D., Beck, P. D., Laubach, M., Chapin, J. K., Kim, J., Biggs, S. J., Srinivasan, M. A., and Nicolelis, M. A. (2000). Real-time prediction of hand trajectory by ensembles of cortical neurons in primates. *Nature*, 408:361–365.

Westby, G. W. and Wang, H. (1997). A floating microwire technique for multichannel chronic neural recording and stimulation in the awake freely moving rat. *J. Neurosci. Methods*, 76:123–133.

Wichmann, T., Bergman, H., and DeLong, M. R. (1994). The primate subthalamic nucleus. I. Functional properties in intact animals. *J. Neurophysiol.*, 72:494–506.

Wichmann, T. and Dostrovsky, J. O. (2011). Pathological basal ganglia activity in movement disorders. *Neuroscience*, 198:232–244.

Williams, J. C., Rennaker, R. L., and Kipke, D. R. (1999). Long-term neural recording characteristics of wire microelectrode arrays implanted in cerebral cortex. *Brain Res. Brain Res. Protoc.*, 4:303–313.

Williams, Z. M., Neimat, J. S., Cosgrove, G. R., and Eskandar, E. N. (2005). Timing and direction selectivity of subthalamic and pallidal neurons in patients with Parkinson disease. *Exp Brain Res*, 162:407–416.

Wilson, C. J. and Kawaguchi, Y. (1996). The origins of two-state spontaneous membrane potential fluctuations of neostriatal spiny neurons. *J. Neurosci.*, 16:2397–2410.

Wilson, C. L., Cash, D., Galley, K., Chapman, H., Lacey, M. G., and Stanford, I. M. (2006). Subthalamic nucleus neurones in slices from 1-methyl-4-phenyl-1,2,3,6-tetrahydropyridine-lesioned mice show irregular, dopamine-reversible firing pattern changes, but without synchronous activity. *Neuroscience*, 143:565–572.

Wingeier, B., Tcheng, T., Koop, M. M., Hill, B. C., Heit, G., and Bronte-Stewart, H. M. (2006). Intra-operative STN DBS attenuates the prominent beta rhythm in the STN in Parkinson's disease. *Exp. Neurol.*, 197:244–251.

Wise, K., Anderson, D., Hetke, J., Kipke, D., and Najafi, K. (2004). Wireless implantable microsystems: high-density electronic interfaces to the nervous system. *Proceedings of the Ieee*, 92(1):76 – 97.

Wise, K. D., Angell, J. B., and Starr, A. (1970). An integrated-circuit approach to extracellular microelectrodes. *Biomedical Engineering, Ieee Transactions on*, Bme-17(3):238 –247.

Won, D. S. and Wolf, P. D. (2004). A simulation study of information transmission by multi-unit microelectrode recordings. *Network*, 15:29–44.

Wood, F., Fellows, M., Donoghue, J., and Black, M. (2004). Automatic spike sorting for neural decoding. *Conf Proc Ieee Eng Med Biol Soc*, 6:4009–4012.

Worbe, Y., Epinat, J., Feger, J., and Tremblay, L. (2011). Discontinuous long-train stimulation in the anterior striatum in monkeys induces abnormal behavioral states. *Cereb. Cortex*, 21:2733–2741.

Wyler, A. R. (1985). Synchrony between cortical neurons during operant conditioning. *Brain Res.*, 341:66–72.

Wyler, A. R., Burchiel, K. J., and Robbins, C. A. (1980a). Operant control of precentral neurons: comparison of fast and slow pyramidal tract neurons. *Exp. Neurol.*, 69:430–433.

Wyler, A. R. and Fetz, E. E. (1974). Behavioral control of firing patterns of normal and abnormal neurons in chronic epileptic cortex. *Exp. Neurol.*, 42:448–464.

Wyler, A. R., Fetz, E. E., and Ward, A. A. (1975). Firing patterns of epileptic and normal neurons in the chronic alumina focus in undrugged monkeys during different behavioral states. *Brain Res.*, 98:1–20.

Wyler, A. R., Lange, S. C., Neafsey, E. J., and Robbins, C. A. (1980b). Operant control of precentral neurons: control of modal interspike intervals. *Brain Res.*, 190:29–38.

Wyler, A. R., Lange, S. C., and Robbins, C. A. (1980c). Operant control of precentral neurons: bilateral single unit conditioning. *Brain Res.*, 195:337–344.

Wyler, A. R. and Robbins, C. A. (1979). Operant control of precentral neurons: the role of reinforcement schedules. *Brain Res.*, 173:341–343.

Wyler, A. R. and Robbins, C. A. (1980). Operant control of precentral neurons: the role of audio and visual feedback. *Exp. Neurol.*, 70:200–203.

Wyrwicka, W. and Doty, R. W. (1966). Feeding induced in cats by electrical stimulation of the brain stem. *Exp Brain Res*, 1:152–160.

Zacksenhouse, M., Lebedev, M. A., Carmena, J. M., O'Doherty, J. E., Henriquez, C., and Nicolelis, M. A. (2007). Cortical modulations increase in early sessions with brain-machine interface. *PloS One*, 2:e619.

Zar, J. (1999). *Biostatistical analysis, 4th Edition*. Upper Saddle River, N.J.: Prentice Hall.

Zhang, F., Aghagolzadeh, M., and Oweiss, K. (2011). A low-power implantable neuroprocessor on nano-fpga for brain machine interface applications. In *Acoustics, Speech and Signal Processing (Icassp), 2011 Ieee International Conference on*, pages 1593 –1596.

Zhang, J., Atay, T., and Nurmikko, A. V. (2009). Optical detection of brain cell activity using plasmonic gold nanoparticles. *Nano Lett.*, 9:519–524.

Zirh, T. A., Lenz, F. A., Reich, S. G., and Dougherty, P. M. (1998). Patterns of bursting occurring in thalamic cells during parkinsonian tremor. *Neuroscience*, 83:107–121.

Biography

I was born July 27, 1981 in Holy Name Hospital, in Teaneck, NJ. During college I worked summers at DRS technologies, a military contractor in northern NJ, working on software, PCB design, and ethernet for their high-speed digital cameras. I graduated from Cornell with a bachelors in science of Electrical and Computer Engineering, Magnum Cum Laude, in 2003. Subsequent graduation I spent (or shall we say gained) a year in the lab of John Chapin, at SUNY Downstate. The city life got me down, so I moved to the Nicolelis lab summer of 2004. Fed up by lack of progress and poor neural recordings, I took a year leave of absence from the university 2007-2008, during which time my friend Jon Kuniholm and myself developed an open-source myoelectric processor, intended to be both a video game controller and prosthetic controller, thereby 'parasitizing' the much larger video game market to bring low-cost EMG processing to amputees. This work took much longer than the year I (and my savings) had allocated, but we are basically happy with performance now. Much of the recording system hardware and software is based on that year of hacking. Hopefully these projects can be either wrapped up or passed on to someone else.

B.4 Publications

- PMID-17694874 Kim HK, Carmena JM, Biggs SJ, Hanson TL, Nicolelis MA, Srinivasan MA. (2007) The muscle activation method: an approach to impedance

control of brain-machine interfaces through a musculoskeletal model of the arm. IEEE Trans Biomed Eng 54:8, 1520-9

- PMID-17522304 Fitzsimmons NA, Drake W, Hanson TL, Lebedev MA, Nicolelis MA. (2007 May 23) Primate reaching cued by multichannel spatiotemporal cortical microstimulation. J Neurosci 27:21, 5593-602

- Timothy Hanson, Nathan Fitzsimmons & Joseph E. O'Doherty. (2007) Methods For Neural Ensemble Recordings, Edited by Miguel A.L. Nicolelis. Chapter 3: Technology for Multi-electrode Micro-Stimulation of Brain Tissue. CRC Press.

- PMID-19603074 Li Z, O'Doherty JE Hanson TL Lebedev MA, Henriquez C, Nicolelis MAL. (2009 Jul 15) Unscented Kalman filter for brain-machine interfaces. PLoS One. 4(7):e6243

- United States Patent Application 11/677,582 (2007) Individual foot-skates for transportation, exercise, and sport

- PMID-19750199 O'Doherty JE, Lebedev MA, Hanson TL, Fitzsimmons NA, Nicolelis MA. (2009 Sep 1) A brain-machine interface instructed by direct intracortical microstimulation. Front Integr Neurosci. 2009;3:20.

- PMID-21779720 Lebedev MA, Tate AJ, Hanson TL, Li Z, O'Doherty JE, Winans JA, Ifft PJ, Zhuang KZ, Fitzsimmons NA, Schwarz DA, Fuller AM, An JH, Nicolelis MA. (2011) Future developments in brain-machine interface research. Clinics (Sao Paulo). 66 Suppl 1:25-32.

- Hanson TL, Omarsson B, O'Doherty JE, Peikon ID, Lebedev MA, Nicolelis MAL. High-side Digitally Current Controlled Biphasic Bipolar Microstimu-

lator Accepted to IEEE Transactions on Neural Systems and Rehabilitation Engineering.

- Hanson TL, Fuller AM, Lebedev MA, Turner DA, Nicolelis MAL. Population Analysis of Human Subcortical Neurons for Brain-Machine Interface Applications. Submitted to J Neurosci, in revision.

B.5 Poster Presentations

- Hanson TL, Carmena JM, Phelps EE, Nicolelis MAL. (2005) A suite of hardware and software for clinical brain-machine interfaces. Society for Neuroscience Abst 335.

- Hanson TL, Carmena JM, Nicolelis MAL. (2005) Predicting Arm Dynamics from Cortical Ensemble Activity in Primates via a Particle Filter. Society for Neuroscience, Abst 402.10.

- Grant BD, Hanson TL, O'doherty JE, Lebedev MA, Nicolelis MAL. (2007) Automated spike sorting of multiunit data for brain-machine interface applications. Society for Neuroscience Abst 319.1/KKK10.

- Peikon ID, Hanson TL, Fitzsimmons NA, Lebedev MA, Nicolelis MAL. (2007) Real-time three-dimensional video tracking system for kinematic analysis of animal behavior. Society for Neuroscience Abst 624.18/UU16.

- Li Z, O'Doherty JE, Hanson TL, Lebedev MA, Henriquez CS, Nicolelis MAL. (2007) N-th order Kalman filter improves the performance of a brain machine interface for reaching. Society for Neuroscience Abst 624.15/UU13.

- Hanson TL, Clayton D, Turner D, Nicolelis MAL. (2008) Properties of Subthalamic Nucleus and Ventral Intermediate Thalamus neurons in patients with

Essential Tremor and Parkinson's Disease. Society for Neuroscience Abst 34.

- Hanson TL, Lebedev MA, Nicolelis MAL. (2011) Wireless multichannel system for recording neuronal ensemble activity from the primate brain. Society for Neuroscience Abst 279.03/NN11.